

NANO-IONIC REDOX RESISTIVE RAM – DEVICE PERFORMANCE  
ENHANCEMENT THROUGH MATERIALS ENGINEERING,  
CHARACTERIZATION AND ELECTRICAL TESTING

by

Muhammad Rizwan Latif

A dissertation

submitted in partial fulfillment

of the requirements for the degree of

Doctor of Philosophy in Electrical and Computer Engineering

Boise State University

May 2014

© 2014

Muhammad Rizwan Latif

ALL RIGHTS RESERVED

BOISE STATE UNIVERSITY GRADUATE COLLEGE

**DEFENSE COMMITTEE AND FINAL READING APPROVALS**

of the dissertation submitted by

Muhammad Rizwan Latif

Dissertation Title: Nano-Ionic Redox Resistive RAM – Device Performance Enhancement Through Materials Engineering, Characterization and Electrical Testing

Date of Final Oral Examination: 03 April, 2014

The following individuals read and discussed the dissertation submitted by student Muhammad Rizwan Latif and they evaluated his presentation and response to questions during the final oral examination. They found that the student passed the final oral examination.

Maria I. Mitkova, Ph.D.	Chair, Supervisory Committee
William B. Knowlton, Ph.D.	Member, Supervisory Committee
Nader Rafla, Ph.D.	Member, Supervisory Committee
Vishal Saxena, Ph.D.	Member, Supervisory Committee
Patrick M. Lenahan, Ph.D.	External Examiner

The final reading approval of the dissertation was granted by Maria Mitkova, Ph.D., Chair of the Supervisory Committee. The dissertation was approved for the Graduate College by John R. Pelton, Ph.D., Dean of the Graduate College.

## DEDICATION

To My Parents and Family

## ACKNOWLEDGEMENTS

In the first place, I would like to express my deepest gratitude to my advisor, Dr. Maria Mitkova for her supervision, guidance, and advice during the entire course of this research work. She provided me with unflinching encouragement and support in various ways during all these years. I am truly indebted to her.

Further, I would like to thank Dr. Bill Knowlton, Dr. Nader Rafla, and Dr. Vishal Saxena for being on my dissertation committee despite their busy schedules. I would also like to thank the financial support from the Department of Electrical and Computer Engineering at Boise State University, Defense Threat Reduction Agency (DTRA), and the Idaho State Board of Education.

I gratefully thank Peter Miranda, Director Idaho Micro Fabrication Laboratory, for training me on the equipment and his readiness to help in every possible way. Also I would like to acknowledge Dr. Dmitri A. Tenne, for his support and guidance while I performed Raman studies. Many thanks to Dr. Paul Davis, Jasen Nielson, and Corey Efaw in the Surface Science Laboratory for training and guiding me while I performed AFM experiments. I would like to express my gratitude to Dr. Davis for his valuable discussion and time on designing the experiments to electrically characterize and image the cross-sectional areas of samples using AFM.

I would like to thank all the former and current members of the Nano-Ionic group. Their help and friendship made my stay at graduate school an enjoyable experience.

Especially, I would like to acknowledge Mahesh Ailavajhala for his continuous support and fruitful discussions, and Kasandra Wolf and Tyler Nichol for their willingness to help me with certain experiments. I would also like to acknowledge Dr. Ping Chen, Dr. Yoshifumi Sakaguchi, Steve Wald, Antonio Oblea, Steve Livers, and Bhes Pun for their advice and sharing thoughts with me, which were productive for shaping my ideas and research. I am lucky to have had some great friendships and bonds over the past few years. Without their physical and mental support, I would have not accomplished this. Thank you all!

I am extremely thankful to my parents for their boundless love and unwavering support. I would especially like to thank my Dad for his continuous encouragement during my graduate studies and my brothers for cheering me through hard times. Finally, I would like to express my deepest gratefulness and love to my wife, Asma, and my son, Subhan. Their patience, love, and sacrifice allowed me to pursue my dreams and made this dissertation possible.

## ABSTRACT

In recent years, Redox Conductive Bridge Memory (RCBM), which falls in the Resistive Random Access Memory (RRAM) category, has gained considerable attention as one of the promising candidates for future generation non-volatile memory due to its advantages over Flash memory as it offers high density, low operating power, fast read/write operation, and compatibility with conventional CMOS process. Currently research is being conducted to improve the reliability of the RCBM devices, which are comprised of an insulating material, also known as active layer, sandwiched between two metal electrodes. The main working mechanism of these devices is based on the resistance change induced by filament formation and dissolution through metal cations movement in the active film. The composition of these active films can vary from oxides to chalcogenides, among which we chose to work on Ge-containing chalcogenide glass films (i.e., Ge-S, Ge-Se, and Ge-Te), which are the most thermally stable among this family of materials, to get a broad perspective of the device performance as a function of the active film structures.

This work is focused on research related to new solutions for the active films to improve RCBM device performance. Application of two different deposition methods were investigated: Plasma-Enhanced Chemical Vapor Deposition (PECVD), which is not well studied for RCBM devices, and formation of nanostructures in the active film under oblique angle deposition by thermal evaporation method. Holding the sample surface at

an oblique angle to the arriving vapor flux resulted in a columnar morphology within the devices' active layer, which aided in improving the device performance by controlling the filament growth through these nanostructures. To minimize the radiant heating inside the evaporation chamber, a strict control over the evaporation current was required, which otherwise resulted in morphological changes of the nanostructure due to increased adatom diffusivity triggered by the thermal energy.

Study of the bare films provided insight into the active material average surface roughness and structural changes occurring in the layers by changing deposition temperature or deposition angle. These investigations were performed using Atomic Force Microscopy (AFM), Raman Spectroscopy, and Energy Dispersive X-ray Spectroscopy (EDS). The results demonstrated that for PECVD, low temperature deposited films with relatively low concentration of Ge had good relaxed structure. The surface roughness was also observed to be minimal with less frequency of hillocks while EDS studies yielded a compositional variation of ~1% for such films. For obliquely deposited films, Raman and EDS results revealed structural reorganization and compositional alterations with changing the deposition angle. Each of these respective results provided a partial view of the mechanisms that contribute to a reliable device performance. Since the RCBM device performance relies on silver diffusion in the chalcogenide matrix, the neutron reflectometry method was applied to study the silver kinetics.

After studying and considering active film material analysis, three types of devices were fabricated i.e., PECVD deposited devices, thermally evaporated devices under normal deposition angle and devices with obliquely deposited films. The devices

were electrically characterized by conducting current vs. voltage (IV) measurements, Read/Write voltage, the two resistive states, switching rate, and the reliability. The devices show greater than four orders of magnitude difference in the two resistive states, which can be detected using lower voltages, thus allowing RCBM devices to be used in low power memory applications.

By integrating the RCBM cells into a system, it can fulfill the essential role of memory with high storage density, precision, and access speed. As part of this research work, an array of RCBM devices were fabricated by non-conventional processing technique with individual cell addressing. The cells were electrically tested to enable application towards various memory architectures.

## TABLE OF CONTENTS

DEDICATION .....	iv
ACKNOWLEDGEMENTS .....	v
ABSTRACT .....	vii
LIST OF TABLES .....	xv
LIST OF FIGURES .....	xvi
LIST OF ABBREVIATIONS.....	xxv
CHAPTER ONE: INTRODUCTION .....	1
Flash Operating Mechanism .....	5
Application and Scaling Limitation of Flash Memory .....	7
Alternate Memory Technologies .....	8
Magneto Resistive Random Access Memory (MRAM).....	9
Ferroelectric Random Access Memory (FeRAM).....	11
Phase Change Random Access Memory .....	12
Resistive Switch Random Access Memory .....	14
Background and Literature Review .....	15
Principle of Resistance Switching Operation .....	16
Classification of the Switching Mechanism in RRAM.....	18
Illustration of Switching Mechanism in a Solid Electrolyte.....	23
Parameters for Evaluation of Memory Device Performance .....	30

Motivation of Study .....	35
Dissertation Organization .....	39
CHAPTER TWO: THIN FILM GROWTH AND OBLIQUE ANGLE DEPOSITION .....	40
Physical Structures of Thin Films.....	41
Oblique Angle Deposition .....	46
Formation of Columnar Structures .....	46
Columnar Structure Inclination and Shadowing Mechanism .....	49
Models for Column Structure Formation.....	51
Films Density .....	53
Application of Nano-Columnar Structure in RCBM .....	54
CHAPTER THREE: MASK DESIGNING AND DEVICE FABRICATION .....	56
Design of a Multilayered Mask.....	57
Device Fabrication Using Multilayered Mask.....	60
Process Flow for Development of RCBM Devices .....	61
Fabrication of RCBM Devices.....	63
Surface Cleaning.....	63
Substrate Preparation .....	64
Sputtering System .....	64
Optical Lithography .....	65
Etching Process .....	66
Deposition of Active Layer.....	67
Lift-Off Process .....	68
Formation of Anode Contact .....	68

Formation of Cathode Contact.....	68
PECVD Devices.....	69
Thermally Evaporated Devices.....	71
Normally Deposited Films.....	71
Improvement in Device Structure and COMSOL Simulation.....	73
Columnar Structured Devices.....	77
CHAPTER FOUR: MATERIALS RESEARCH RELATED TO ACTIVE FILMS.....	78
Analytical Methods for Film Study.....	78
Energy Dispersive X-ray Spectroscopy.....	78
Raman Spectroscopy.....	80
Atomic Force Microscopy (AFM).....	82
Scanning Electron Microscopy.....	83
Thin Film Analysis/Characterization.....	85
PECVD Deposited Active Film.....	86
PECVD Reactor.....	87
Material Characterization.....	88
Silver Diffusion Kinetics.....	94
Columnar Structure within Device Active Film.....	101
Experimental Results.....	103
Analysis of Columnar Structure.....	105
Cross-Sectional Study of Obliquely Deposited ChG Films.....	105
Surface Morphology of Obliquely Deposited Films.....	111
Compositional Analysis of Obliquely Deposited Films.....	114

Raman Analysis of Obliquely Deposited Films.....	117
Summary .....	125
CHAPTER FIVE: ELECTRICAL TESTING OF FABRICATED DEVICES .....	127
Quasi-Static Electrical Measurements .....	127
Electrical Testing of PECVD Devices .....	129
Thermally Evaporated Devices.....	135
Normally Deposited Film .....	135
Columnar Structured Devices .....	138
Higher Temperature Measurements.....	148
Retention Testing.....	151
Multilevel Switching Capability .....	154
Filament Growth through Columnar Structure - Atomic Level Switching ..	157
Summary .....	171
CHAPTER SIX: FORMATION OF THE MEMRISTIVE ARRAY.....	173
Lithography Free Formation of RCBM Array.....	174
Material Characterization of the Ion Bombarded Regions .....	175
Explanation .....	180
Electrical Testing of the Fabricated Devices .....	182
Summary .....	185
CHAPTER SEVEN: SUMMARY AND CONCLUSION.....	187
PECVD Devices.....	188
Column Structured Devices .....	188
Lithography-Free Array Formation .....	190

REFERENCES .....	192
APPENDIX A.....	216
Generation 1 Device's Process Flow .....	216
APPENDIX B.....	217
Matlab Code for calculating $V_{th}$ , LRS, HRS .....	217

## LIST OF TABLES

Table 1.1	Performance comparison of different memory technologies.....	9
Table 1.2	Resistive Switching Materials.....	23
Table 4.1	Process tool variable .....	88
Table 4.2	EDS Data for different Ge-S Composition .....	89
Table 4.3	Deposition and column angle growth for Ge-Se films (all units are in degrees).....	109
Table 4.4	Deposition and column angle growth for Ge-Te films (all units are in degrees).....	109
Table 6.1	EDS Results on Planar and Ion Bombarded regions for $\text{Ge}_x\text{Se}_{1-x}$ Films (where $x = 0.25, 0.3 \& 0.4$ ).....	176

## LIST OF FIGURES

Figure 1.1	Memory Classification (An Chen – Global Foundries) [4] .....	2
Figure 1.2	Structure of (a) SRAM and (b) DRAM .....	3
Figure 1.3	Flash memory and its floating gate structure .....	5
Figure 1.4	Programming a floating gate device by (a) Hot carrier injection and (b) Fowler-Nordheim Tunneling .....	6
Figure 1.5	Erasing a floating gate device by (a) FNT at source side and (b) FNT in channel .....	7
Figure 1.6	Schematic of a MRAM cell .....	10
Figure 1.7	(a) FeRAM Structure and (b) A polarization-electric field hysteresis loop .....	12
Figure 1.8	Phase Change Memory schematic with cell in Reset and Set state .....	13
Figure 1.9	ON and OFF State of RRAM.....	14
Figure 1.10	Two different resistance switching mode schematics (a) Unipolar and (b) Bipolar switching [35] .....	17
Figure 1.11	Resistive memory technology classification based on their operation [ITRS 2012] .....	18
Figure 1.12	X-ray fluorescence mapping after electroforming in Cr-doped SrTiO <sub>3</sub> showing distribution of oxygen vacancies between two electrodes [23]..	20
Figure 1.13	Electroforming process forming in TiO <sub>2</sub> by application of (a) Positive voltage/current and (b) Negative voltage/current [40].....	21
Figure 1.14	Barrier Modulation by oxygen accumulation along the interface representing (a) HRS corresponding to wide barrier and (b) LRS corresponding to narrow barrier [41] .....	22
Figure 1.15	Schematic illustration of Set (A-D) and Reset (E) operation for an RCBM cell [47] .....	25

Figure 1.16	Representation of the potential energy diagram of a charge transfer process. The black curves represent the initial state and the red curve results after applying an electric potential to the metal electrode. OHP is the outer Helmholtz plane [47] .....	27
Figure 1.17	Operating Voltage of RRAM Cell [31] .....	31
Figure 1.18	Retention of the ON state as measured before and after retention test ( $R_{OFF}$ stays above $10^{10}$ ohm) [57] .....	32
Figure 1.19	Endurance test of RRAM device with $10^5$ cycles [57] .....	33
Figure 1.20	Multilevel Switching in RRAM cell by changing the compliance current [58].....	34
Figure 1.21	Plot showing LRS and HRS of the RRAM cell with approximately 5 orders of magnitude difference between the two states [60] .....	35
Figure 1.22	ITRS 2012 requirement and performance chart for RCBM devices .....	36
Figure 1.23	Filament topographies reflecting multi-branching within the filaments during the growth process in (a) Pt/H <sub>2</sub> O/Ag system with no bias and biased conditions [44], (b) Cu/WO <sub>3</sub> /Pt system [64], (c-d) Ag/AgS/W system with different bias voltages [65], and (e) Ag/Ag <sub>2</sub> S <sub>3</sub> /Au system [66] .....	37
Figure 2.1	SEM images showing improvement in structures by GLAD [84].....	41
Figure 2.2	Evolution of Structure Zone Models [85].....	44
Figure 2.3	Evolutionary model for columnar thin film growth under low mobility conditions [91] .....	45
Figure 2.4	Obliquely angle deposition a) adatom diffusion stage, b) growth stage, and c) nano-columnar structure .....	47
Figure 2.5	$\alpha$ and $\beta$ definition for the columnar structure growth .....	47
Figure 2.6	Nano-Engineered morphologies formed by controlling different parameters (a) Zig Zag, (b) C-Shaped, and (c) S- Shaped [103] .....	48
Figure 2.7	Schematic representation of columnar growth by the arriving vapor flux ( $\alpha$ is the deposition Angles and $\beta$ is the columnar growth angle) .....	49
Figure 2.8	Shadowing mechanism in columnar structure growth.....	50

Figure 2.9	Columnar structure schematic of the films deposited under normal incidence angle.....	50
Figure 2.10	Variation of column angle $\beta$ with deposition angle $\alpha$ , obtained from the Tangent, Tait's and Lichter-Chen's expression .....	53
Figure 2.11	Schematic of (a) Real filament growth and (b) Ideal filament growth by providing pathways for its growth .....	55
Figure 3.1	Optical lithography process [127].....	56
Figure 3.2	Individual layers layout of the multilayered mask.....	58
Figure 3.3	Steps for using 3-in-1 mask (a) Patterning of Via layer, (b) Aligning Vias to Ag layer, and (c) Aligning W layer to Via/Ag layer.....	59
Figure 3.4	3 Layer layout of 3-in-1 mask.....	60
Figure 3.5	Process flow for fabrication of RCBM devices .....	62
Figure 3.6	Flow Chart for photolithography process .....	66
Figure 3.7	Top view of the vias under the optical microscope .....	67
Figure 3.8	SEM images of the vias (a) Top view of 2.1 $\mu$ m via, (b) Cross-sectional image of the 2.1 $\mu$ m, (c) Top view of 9.9 $\mu$ m via, and (d) Cross-sectional image of the 9.9 $\mu$ m via .....	67
Figure 3.9	Silver pad formation on top of vias.....	68
Figure 3.10	W pad formation top view on the sample .....	69
Figure 3.11	Vertical device structures after lithography steps.....	69
Figure 3.12	Lateral device structure.....	70
Figure 3.13	Optical schematic used to collimate beam.....	72
Figure 3.14	Geometry used for COMSOL simulations corresponding to (a) Gen. 1 and (b) Gen. 2 devices process flow .....	73
Figure 3.15	COMSOL simulations for Gen. 1 and Gen. 2 devices representing (a & b) Electric potentials, (c & d) Electric field, and (e & f) Electric energy density .....	75

Figure 3.16	Electric field distribution through via, Ag/chalcogenide/oxide (Gen. 1 devices) and Ag/oxide (Gen. 2 devices) interfaces.....	76
Figure 4.1	Raman Scattering .....	80
Figure 4.2	Illustration of SEM Working [147].....	84
Figure 4.3	Setup for thickness correction.....	85
Figure 4.4	Films stack for (a) PECVD deposited and (b) thermally evaporated chalcogenides (ChG).....	86
Figure 4.5	Raman Analysis of PECVD deposited $\text{Ge}_x\text{S}_{1-x}$ films.....	90
Figure 4.6	AFM result for $\text{Ge}_x\text{S}_{1-x}$ film deposition at different temperatures .....	91
Figure 4.7	Hillock formation and average surface roughness on the samples based on AFM scan of $5\mu\text{m}$ by $5\mu\text{m}$ area .....	92
Figure 4.8	SEM Images of $2\mu\text{m}$ device cross-section illustrating the smoothness of the PECVD Ge-S film with the corresponding layers composition determined through EDS.....	93
Figure 4.9	Schematic for measuring Neutron Reflectivity.....	96
Figure 4.10	Neutron reflectivity profiles before and after light exposure (a) Ag/ $\text{Ge}_{40}\text{S}_{60}$ and (b) Ag/ $\text{Ge}_{20}\text{S}_{80}$ films .....	97
Figure 4.11	Fourier Transform of the reflectivity data (a) Ag/ $\text{Ge}_{40}\text{S}_{60}$ and (b) Ag/ $\text{Ge}_{20}\text{S}_{80}$ films presented in Figure 4.10.....	98
Figure 4.12	Time evolution of neutron reflectivity of (a) Ag/ $\text{Ge}_{40}\text{S}_{60}$ and (b) Ag/ $\text{Ge}_{20}\text{S}_{80}$ films substrate film under light illumination.....	98
Figure 4.13	Fourier Transform of the time evolutionary reflectivity data of (a) Ag/ $\text{Ge}_{40}\text{S}_{60}$ and (b) Ag/ $\text{Ge}_{20}\text{S}_{80}$ .....	99
Figure 4.14	Fourier Transform of the time variation plots: (a) the position ( $\circ$ ) and the height ( $\bullet$ ) of the first peak in Ag/ $\text{Ge}_{40}\text{S}_{60}$ film and (b) the positions of the first ( $\circ$ ) and the second peaks ( $\Delta$ ) and the height of the first peak ( $\bullet$ ) in Ag/ $\text{Ge}_{20}\text{S}_{80}$ film.....	100
Figure 4.15	Electrochemical growth of the Ag dendrite in the Ag-Ge-Se electrolyte [166].....	101
Figure 4.16	Ideal RCBM device structure.....	102

Figure 4.17	(a) Schematic of thermal evaporation chamber illustrating incident vapor measuring method where $\alpha_1$ is the normally deposited film ( $\alpha_1 = 90^\circ$ ) and $\alpha_2$ is some angle less than $90^\circ$ ( $\alpha_1 < 90^\circ$ ) and (b) Semi-Knudsen Cell structure used for thermally evaporated films ..... 105
Figure 4.18	SEM cross-sectional images of (a) $\text{Ge}_{20}\text{Se}_{80}$ , (b) $\text{Ge}_{30}\text{Se}_{70}$ , and (c) $\text{Ge}_{40}\text{Se}_{60}$ under various incident vapor angles: (i) $\alpha = 90^\circ$ , (ii) $\alpha = 80^\circ$ , (iii) $\alpha = 70^\circ$ , (iv) $\alpha = 60^\circ$ , (v) $\alpha = 45^\circ$ , (vi) $\alpha = 30^\circ$ ..... 107
Figure 4.19	SEM cross-sectional images of (a) $\text{Ge}_{20}\text{Te}_{80}$ and (b) $\text{Ge}_{50}\text{Te}_{50}$ under various incident vapor angles: (i) $\alpha = 90^\circ$ , (ii) $\alpha = 80^\circ$ , (iii) $\alpha = 70^\circ$ , (iv) $\alpha = 60^\circ$ , (v) $\alpha = 45^\circ$ , (vi) $\alpha = 30^\circ$ ..... 108
Figure 4.20	Comparison of measured angles vs Tangent Rule and suggested correction for (a) Ge-Se system and (b) Ge-Te System..... 110
Figure 4.21	SEM images (a & b) of the obliquely deposited $\text{Ge}_{40}\text{Se}_{60}$ film and (c) EDS analysis performed on (a & b) to confirm the films under observation.. 111
Figure 4.22	AFM images for obliquely deposited (a) $\text{Ge}_{20}\text{Se}_{80}$ , (b) $\text{Ge}_{30}\text{Se}_{70}$ , and (c) $\text{Ge}_{40}\text{Se}_{60}$ films under various angles: (i) $\alpha = 90^\circ$ , (ii) $\alpha = 80^\circ$ , (iii) $\alpha = 70^\circ$ , (iv) $\alpha = 60^\circ$ , (v) $\alpha = 45^\circ$ , (vi) $\alpha = 30^\circ$ ..... 112
Figure 4.23	AFM images for obliquely deposited (a) $\text{Ge}_{20}\text{Te}_{80}$ and (b) $\text{Ge}_{50}\text{Te}_{50}$ films under various angles: (i) $\alpha = 90^\circ$ , (ii) $\alpha = 80^\circ$ , (iii) $\alpha = 70^\circ$ , (iv) $\alpha = 60^\circ$ , (v) $\alpha = 45^\circ$ , (vi) $\alpha = 30^\circ$ ..... 112
Figure 4.24	AFM images of the columnar structure by scanning on the sample cross-section of (a) $\text{Ge}_{20}\text{Se}_{80}$ at $\alpha = 70^\circ$ , (b) $\text{Ge}_{30}\text{Se}_{70}$ at $\alpha = 45^\circ$ , and (c) $\text{Ge}_{40}\text{Se}_{60}$ at $\alpha = 30^\circ$ ..... 113
Figure 4.25	AFM images of the columnar structure by scanning on the sample cross-section of (a) $\text{Ge}_{20}\text{Te}_{80}$ at $\alpha = 45^\circ$ and (b) $\text{Ge}_{50}\text{Te}_{50}$ at $\alpha = 45^\circ$ ..... 113
Figure 4.26	Average surface roughness observed in (a) $\text{Ge}_{20}\text{Se}_{80}$ , (b) $\text{Ge}_{30}\text{Se}_{70}$ , and (c) $\text{Ge}_{40}\text{Se}_{60}$ films under different depositions angles ..... 114
Figure 4.27	Average surface roughness observed in (a) $\text{Ge}_{20}\text{Te}_{80}$ and (b) $\text{Ge}_{50}\text{Te}_{50}$ films under various deposition angles..... 114
Figure 4.28	Compositional analysis of $\text{Ge}_x\text{Se}_{1-x}$ ( $x = 0.2, 0.3, 0.4$ ) films by altering the vapor flux angles..... 115
Figure 4.29	Compositional analysis of $\text{Ge}_x\text{Te}_{1-x}$ ( $x = 0.2, 0.5$ ) films by altering the vapor flux angles..... 116

Figure 4.30	Raman Spectra for obliquely deposited (a) $\text{Ge}_{20}\text{Se}_{80}$ , (b) $\text{Ge}_{30}\text{Se}_{70}$ , and (c) $\text{Ge}_{40}\text{Se}_{60}$ films under different angles .....	119
Figure 4.31	Variations in CS-mode as a function of obliqueness angle in (a) $\text{Ge}_{20}\text{Se}_{80}$ , (b) $\text{Ge}_{30}\text{Se}_{70}$ , and (c) $\text{Ge}_{40}\text{Se}_{60}$ .....	120
Figure 4.32	Raman intensity area ratio of (a) Se-Se and (b) ES/CS bonding for Ge-Se system as a function of obliqueness angle .....	121
Figure 4.33	Molar volume and packing fraction of Ge-Se glasses [189].....	122
Figure 4.34	Raman Spectra for obliquely deposited (a) $\text{Ge}_{20}\text{Te}_{80}$ and (b) $\text{Ge}_{50}\text{Te}_{50}$ ..	123
Figure 4.35	Variations in CS-mode as a function of obliqueness angle in (a) $\text{Ge}_{20}\text{Te}_{80}$ and (b) $\text{Ge}_{50}\text{Te}_{50}$ .....	123
Figure 4.36	Area ratio illustrating various bonds trends in (a) $\text{Ge}_{20}\text{Te}_{80}$ and (b) $\text{Ge}_{50}\text{Te}_{50}$ as a function of obliqueness angles .....	124
Figure 5.1	Step increase in the voltage with voltage sweep from $V_{\min}$ to $V_{\max}$ .....	128
Figure 5.2	IV curve of PECVD deposited lateral devices ( $\text{Ge}_{36.83}\text{S}_{63.17}$ ).....	130
Figure 5.3	Resistance vs Voltage Plot for lateral devices .....	131
Figure 5.4	IV curve of PECVD deposited lateral devices ( $\text{Ge}_{34.55}\text{S}_{65.45}$ ) .....	131
Figure 5.5	Non-uniform switching due to surface roughness at Chalcogenide/Ag interface.....	132
Figure 5.6	Standard free energy changes during an electrode reaction [53].....	134
Figure 5.7	IV Characteristics of RCBM devices with planar deposition and solid electrolyte formation.....	135
Figure 5.8	IV characteristic for the device not turning on after 1200 cycles .....	136
Figure 5.9	Schematic illustration of free volume in silver doped chalcogenides [195] .....	137
Figure 5.10	IV curves for $10^6$ cycles for (a) $\text{Ge}_{20}\text{Se}_{80}$ , (b) $\text{Ge}_{30}\text{Se}_{70}$ , and (c) $\text{Ge}_{40}\text{Se}_{60}$ having nano-columnar structure in the active films under various incident angles: (i) $\alpha = 90^\circ$ , (ii) $\alpha = 80^\circ$ , (iii) $\alpha = 70^\circ$ , (iv) $\alpha = 60^\circ$ , (v) $\alpha = 45^\circ$ , (vi) $\alpha = 30^\circ$ .....	139

Figure 5.11	IV curves for $10^6$ cycles for (a) $\text{Ge}_{20}\text{Te}_{80}$ and (b) $\text{Ge}_{50}\text{Te}_{50}$ layers having nano-columnar structure in the active films under various incident angles: (i) $\alpha = 90^\circ$ , (ii) $\alpha = 80^\circ$ , (iii) $\alpha = 70^\circ$ , (iv) $\alpha = 60^\circ$ , (v) $\alpha = 45^\circ$ , (vi) $\alpha = 30^\circ$	140
Figure 5.12	RV plot for $10^6$ cycles for (a) $\text{Ge}_{20}\text{Se}_{80}$ , (b) $\text{Ge}_{30}\text{Se}_{70}$ , and (c) $\text{Ge}_{40}\text{Se}_{60}$ films having nano-columnar structure in the active films under various incident angles: (i) $\alpha = 90^\circ$ , (ii) $\alpha = 80^\circ$ , (iii) $\alpha = 70^\circ$ , (iv) $\alpha = 60^\circ$ , (v) $\alpha = 45^\circ$ , (vi) $\alpha = 30^\circ$	142
Figure 5.13	RV plot for $10^6$ cycles for (a) $\text{Ge}_{20}\text{Te}_{80}$ and (b) $\text{Ge}_{50}\text{Te}_{50}$ films having nano-columnar structure in the active films under various incident angles: (i) $\alpha = 90^\circ$ , (ii) $\alpha = 80^\circ$ , (iii) $\alpha = 70^\circ$ , (iv) $\alpha = 60^\circ$ , (v) $\alpha = 45^\circ$ , (vi) $\alpha = 30^\circ$	143
Figure 5.14	Switching voltage dependence on the incident vapor angle for (a) $\text{Ge}_{20}\text{Se}_{80}$ , (b) $\text{Ge}_{30}\text{Se}_{70}$ , and (c) $\text{Ge}_{40}\text{Se}_{60}$ devices	144
Figure 5.15	Switching voltage dependence on the incident vapor angle for (a) $\text{Ge}_{20}\text{Te}_{80}$ and (b) $\text{Ge}_{50}\text{Te}_{50}$ devices	145
Figure 5.16	Switching voltage dependence on the Ge-Se active layer materials and incident vapor flux angle	146
Figure 5.17	Switching voltage dependence on the Te-Se active layer materials and incident vapor flux angle	147
Figure 5.18	Switching voltage dependence on active layer incident angle for (a) Ge-Se and (b) Ge-Te system	147
Figure 5.19	500 cycles of RV plots for (a) $\text{Ge}_{20}\text{Se}_{80}$ , (b) $\text{Ge}_{30}\text{Se}_{70}$ , and (c) $\text{Ge}_{40}\text{Se}_{60}$ films having nano-columnar structure in the active films under various incident angles	150
Figure 5.20	500 cycles of RV plots for (a) $\text{Ge}_{20}\text{Te}_{80}$ and (b) $\text{Ge}_{50}\text{Te}_{50}$ films with nano-columnar structure in the active films under various incident angles	151
Figure 5.21	Data retention of low resistive state of the devices written at a compliance current value of $10\mu\text{A}$ for (a) $\text{Ge}_{20}\text{Se}_{80}$ with $\alpha = 80^\circ$ , (b) $\text{Ge}_{30}\text{Se}_{70}$ with $\alpha = 60^\circ$ , (c) $\text{Ge}_{40}\text{Se}_{60}$ with $\alpha = 45^\circ$ , (d) $\text{Ge}_{20}\text{Te}_{80}$ with $\alpha = 30^\circ$ , and (e) $\text{Ge}_{50}\text{Te}_{50}$ with $\alpha = 30^\circ$ devices. The data for the written bit is read at voltage ranging from 0.3V to 0.5V	152
Figure 5.22	(a) Current-Voltage and (b) Resistance-Voltage curves with varying compliance current values for $\text{Ge}_{30}\text{Se}_{70}$ column-structured devices with deposition angle, $\alpha = 60^\circ$	156

Figure 5.23	Dependence of low resistive state on the compliance current value at room temperature .....	157
Figure 5.24	SEM image of the filament rupture caused by electron beam .....	158
Figure 5.25	Plots of Probe (Z position), Force and Current as a function of time during one PF-TUNA Cycle [209].....	160
Figure 5.26	Optical image (a) 1X zoomed and (b) 3X zoomed image of the cleaved sample for imaging using PF-TUNA.....	162
Figure 5.27	Experimental setup for imaging the growth of conductive path through the columnar structure in the active layer of the devices.....	163
Figure 5.28	PF-TUNA scans with No biasing and peak force set 10nN for (a) Ge <sub>20</sub> Se <sub>80</sub> with $\alpha = 70^\circ$ , (b) Ge <sub>30</sub> Se <sub>70</sub> with $\alpha = 45^\circ$ , and (c) Ge <sub>40</sub> Se <sub>60</sub> with $\alpha = 30^\circ$ where (i) the top view image of the cross-sectional area (ii) the side view of the cross-sectional area (iii) Tuna current measurement (iv) Peak Current measurement for each case .....	164
Figure 5.29	PF-TUNA scans with stage biased at -0.5V and peak force set 10nN for (a) Ge <sub>20</sub> Se <sub>80</sub> with $\alpha = 70^\circ$ , (b) Ge <sub>30</sub> Se <sub>70</sub> with $\alpha = 45^\circ$ , and (c) Ge <sub>40</sub> Se <sub>60</sub> with $\alpha = 30^\circ$ where (i-iv) the top scan view and the filament growth through the voids in the columnar structure (v) the top view image rotated by $90^\circ$ (vi-viii) the side scan view of the cross-sectional area and the filament growth through the voids in the columnar structure with corresponding current scale.....	166
Figure 5.30	PF-TUNA scans with stage biased at +5V and peak force set 10nN for Ge <sub>30</sub> Se <sub>70</sub> with $\alpha = 45^\circ$ where (i-iv) is the top scan view and the filament growth through the voids in the columnar structure (v) is the top view image rotated by $90^\circ$ (vi-viii) is the side scan view of the cross-sectional area and the filament growth through the voids in the columnar structure with corresponding current scales.....	168
Figure 5.31	Filament growth by applying a voltage bias of 25mV on Ge <sub>30</sub> Se <sub>70</sub> sample with $\alpha = 45^\circ$ .....	169
Figure 5.32	PF-KPFM scan (a) under unbiased and (b) biased condition with peak force set to 10nN for Ge <sub>30</sub> Se <sub>70</sub> film at $\alpha = 45^\circ$ .....	171
Figure 6.1	Schematic Illustration of RCBM Array .....	173
Figure 6.2	SNMS System configurations with sample stack .....	175
Figure 6.3	SEM image of the array formed by ion bombardment .....	176

Figure 6.4	EDS elemental mapping distribution of Ge-Se before and after ion bombardment .....	177
Figure 6.5	(a) Raman data and the corresponding mode assignment, (b) Area Ratios b/w ES and CS modes, and (c) Change in area ratio with different Ge concentrations .....	178
Figure 6.6	Formation of via in (a) Ge <sub>25</sub> Se <sub>75</sub> , (b) Ge <sub>30</sub> Se <sub>70</sub> , and (c) Ge <sub>40</sub> Se <sub>60</sub> films by Ar <sup>+</sup> ion bombardment .....	179
Figure 6.7	Surface morphology of Ge <sub>x</sub> Se <sub>1-x</sub> on a 25μm <sup>2</sup> area.....	179
Figure 6.8	Surface roughness RMS and peak hillocks in the vias of the cell .....	181
Figure 6.9	IV Curves of the single bit device.....	183
Figure 6.10	Resistance and threshold voltage plot of (a) Ge <sub>25</sub> Se <sub>75</sub> , (b) Ge <sub>30</sub> Se <sub>70</sub> , and (c) Ge <sub>40</sub> Se <sub>60</sub> in different cells of the array where 10 <sup>3</sup> cycles for cell 20 for each composition.....	184

## LIST OF ABBREVIATIONS

AFM	Atomic Force Microscopy
ALU	Arithmetic Logic Units
APM	Ammonium Peroxide Mixture
BOE	Buffered Oxide Etch
CG	Control Gate
ChG	Chalcogenide
CPU	Central Processing Unit
DRAM	Dynamic Random Access Memory
EDS	Energy Dispersive X-Ray Spectroscopy
FeRAM	Ferroelectric Random Access Memory
FG	Floating Gate
FNT	Fowler-Nordheim Tunneling
HCI	Hot carrier injection
HRS	High Resistive State
IML	Idaho Micro fabrication Laboratory
ITRS	International Technology Roadmap for Semiconductors
LRS	Low Resistive State
MIM	Metal Insulator Metal
MRAM	Magneto Resistive Random Access Memory
MTJ	Magnetic Tunnel Junction

NIM	Nano-ionic Memory
NVM	Non-volatile Memory
PCM	Phase Change Memory
PECVD	Plasma-Enhanced Chemical Vapor Deposition
PF-KPFM	Peak Force Kelvin Probe AFM
PF-TUNA	Peak Force Tunneling AFM
PMC	Programmable Metallization Cell
PVD	Physical Vapor Deposition
RBS	Rutherford Backscattering
RCBM	Redox Conductive Bridge Memory
RCM	Resistance Change Memory
RRAM	Resistive Random Access Memory
SEM	Scanning Electron Microscope
SRAM	Static Random Access Memory
TOF	Time of Flight
VLSI	Very Large Scale Integrated
VM	Volatile Memory

## CHAPTER ONE: INTRODUCTION

The last few decades in the semiconductor industry have seen tremendous growth, paving the way for better, faster, more cost effective, and energy efficient products, driven by intensive down-scaling of the devices based on Moore's Law [1, 2]. However, continued scaling over the years is now facing a dilemma as it has arrived at the point where device physics pose severe scaling challenges for future devices [3]. Therefore, to keep pace with Moore's Law, it is important to continue increasing the number of transistors on a chip by investigating new technologies. This will allow further scaling of devices at the rate predicted by Gordon Moore.

Memory is one of the essential components in today's electronics market. All modern electronic products have memory either embedded into the device itself or attached externally. In addition, advancements in personal electronic devices like laptops, smart phones, tablets, digital cameras, and other entertainment devices have resulted in a dramatic increase in the demand for memory. Improvements in current memory technologies are the main driving force for developing faster, smaller, and cheaper gadgets. Customers' consistent desire to have better and cheaper memory has motivated researchers to pursue continual developments in memory technology that offer higher storage density, faster speed, and lower power consumption.

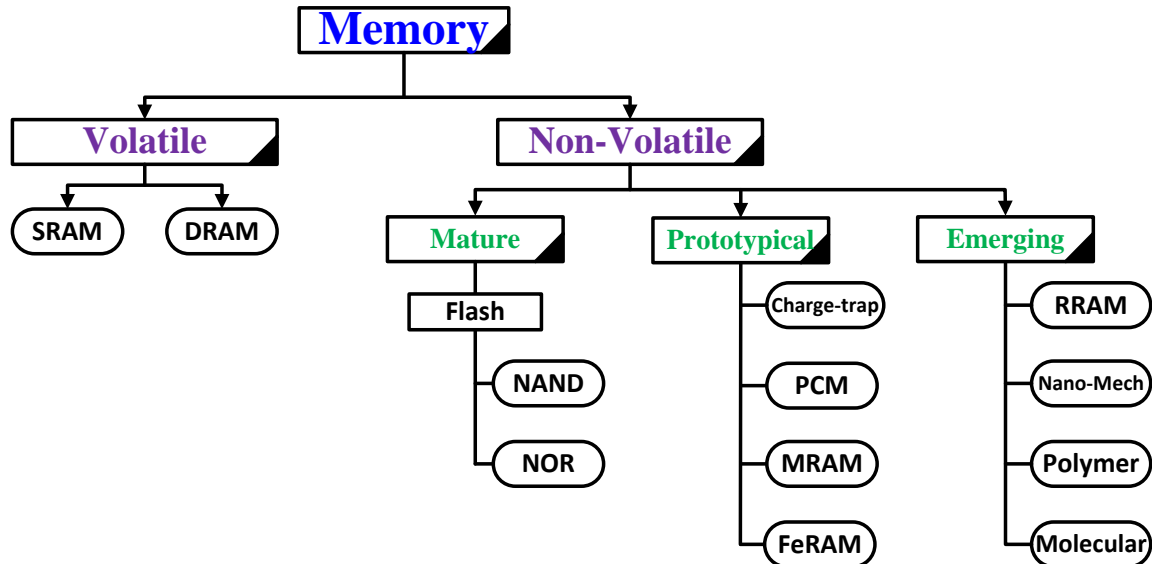


**Figure 1.1 Memory Classification (An Chen – Global Foundries) [4]**

Memory devices are classified broadly into two categories, based on their principle of operation as presented in Figure 1.1. One class is Volatile Memory (VM) and the other type is Non-Volatile Memory (NVM). A constant power supply must be connected during the entire operating period of the volatile memory. Once the power source is disconnected, all the stored information (bits) will be lost. The most popular volatile memories are: Static Random Access Memory (SRAM) and Dynamic Random Access Memory (DRAM). SRAM consists of six transistors for each memory element as shown in Figure 1.2a. It consists of two inverters with an access transistor attached at each input of the inverter. The structure of SRAM, involving six transistors per bit is relatively complex, which results in poor memory density and is very expensive regarding cost per bit. On the other hand, DRAM has a simple structure as depicted in Figure 1.2b. It consists of a transistor in series with a capacitor. The two states in DRAM are formed by: charging of the capacitor representing one state (binary 1), whereas a discharged state corresponds to the other state (binary 0).

Ideally, DRAM can hold the charge forever if there was no charge leakage through the capacitor and the information would remain stored in the DRAM cell even if the power is turned off. In reality, due to the charge leakage, periodic refreshment of capacitors are needed to keep the information. The additional circuitry and timing required to refresh the cells make DRAM memory slower than SRAM. Due to the simplicity of DRAM structure, it offers much higher density than SRAM. Because of this, DRAM has become the mainstream in computer main memory despite being slower than SRAM.

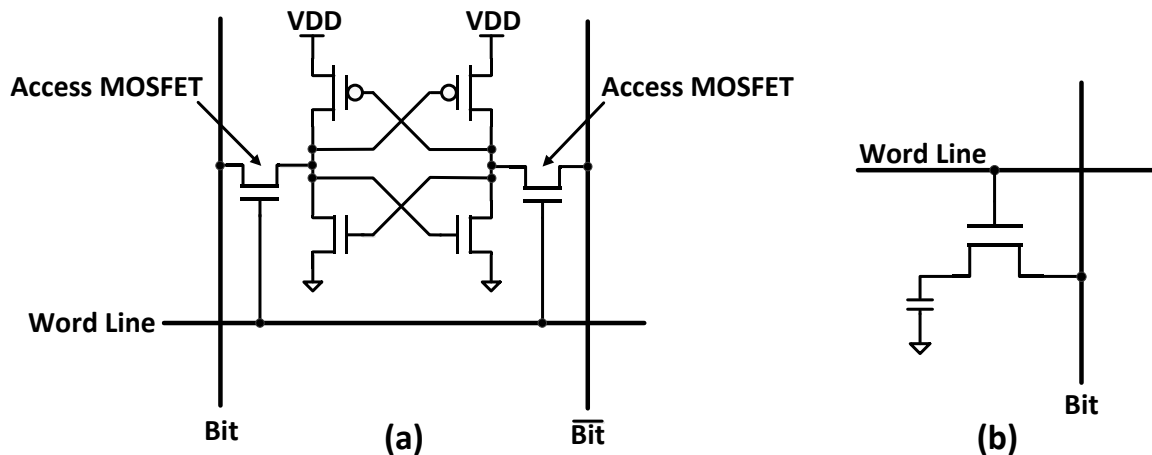


**Figure 1.2 Structure of (a) SRAM and (b) DRAM**

Non-volatile memory, on the other hand, retains the stored information even if the power supply is removed. Since NVM can sustain data even without a power supply, a question may arise, why do we still use volatile memory? The answer to this question is related to memory performance. Today's memory systems consist of a hierarchy of several devices, each having different requirements that cannot be easily incorporated within one single device. To support the instruction set commands and data in a CPU or ALU, a fast memory access has to be guaranteed. Despite being volatile memory, SRAM

is used in such devices where speed is more crucial than memory capacity. The most prominent use of SRAM is in the cache memory of processors where speed is very essential. Hard drives, optical drives, and other devices that need cache memory or buffers use SRAM modules. In contrast, DRAM, which has larger density and much lower cost per bit than SRAM, has slower speed and is used for RAM applications. However, the resulting power dissipation of these volatile memories is not economical or efficient, particularly in mobile applications. Traditional NVMs, such as Flash, have much larger storage density than both SRAM and DRAM, but operate at a slower speed than either of them.

Currently, the NVM market is worth billions of dollars, and is expected to keep growing in the future. The motivation to study other types of NVM is to further improve the memory density, which will also help to continue the trend of cheaper and more powerful electronic gadgets. Until now, Flash memory has dominated the NVM industry with a share above 90%. The rapid growth of Flash is attributed to two of its major properties that suit the electronics market [5]. The first is its reliability and the second is its non-volatile nature. Because of these features, Flash has become an ideal candidate for electronic devices that require mobility and miniaturization. Although, Flash memory is the most matured NVM technology, its floating gate structure possesses significant scaling challenges due to the limitations on tunneling oxide thickness [6].

In the following section, the working principle of Flash followed by the limitations affecting its future development are discussed.

### Flash Operating Mechanism

The basic Flash cell is shown in Figure 1.3a. As seen in the figure, the major difference between a Flash cell and a normal MOSFET is that the Flash cell has a second gate between the Control Gate (CG) and the substrate, which is not electrically connected, known as a Floating Gate (FG). A memory element is formed by trapping or removing the charge in FG.

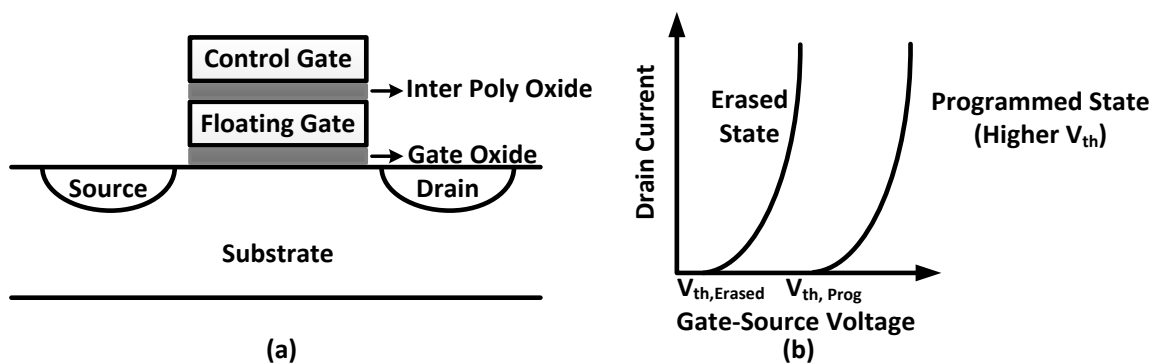


**Figure 1.3** Flash memory and its floating gate structure

The difference between the erased and the programmed state of a Flash cell is represented in Figure 1.3b. The erased state of the cell shows a normal MOSFET behavior, the device turns on and conducts a current above the threshold voltage ( $V_{th}$ ). However, when the cell is programmed, by injecting negative charge into the FG, it results in positive charge build up underneath the gate oxide. As a consequence, a larger CG voltage must be applied to turn the device on, as  $V_{th}$  of the cell increased.

Electrons can be trapped in the FG by either hot carrier injection (HCI) method or by Fowler-Nordheim Tunneling (FNT) technique. HCI is achieved by applying a large positive voltage ( $>10V$ ) to both the CG and the drain electrode, driving the transistor into the saturation region. As a result, a large electric field is created near the drain and

substrate junction. Electrons in this region gain significant kinetic energy and subsequently have energy large enough to overcome the oxide potential barrier, so that they traverse through the gate oxide and get trapped inside the floating gate, as illustrated in Figure 1.4a. In order to create enough hot carriers, a large drain current has to flow through the device, which results in poor power efficiency. On the other hand, positively biasing the CG and grounding the substrate while leaving the source and drain floating result in FNT. The strong transverse electric field between the channel and the CG enable electrons to tunnel from the inversion layer in the substrate directly into the FG, as shown in Figure 1.4b. The major advantage of this method is that it consumes much less power than HCI.

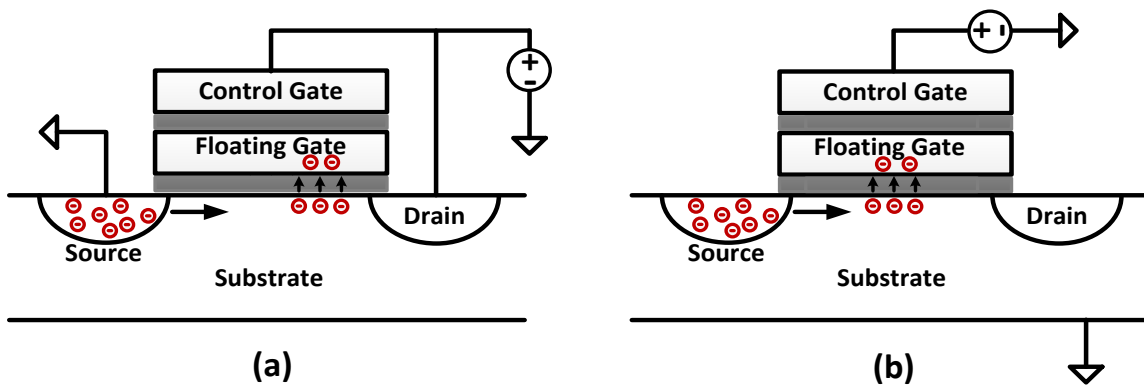


**Figure 1.4** Programming a floating gate device by (a) Hot carrier injection and (b) Fowler-Nordheim Tunneling

There are two ways, both FNT, to erase Flash cells. The first method is to apply a positive voltage on the source and to leave the CG grounded as illustrated in Figure 1.5a. Due to a high positive voltage present at the source side, the electrons tunnel back through the oxide into the source region. To prevent the breakdown of the cell, due to the application of large voltage, the doping concentration of the source cannot be too high. Another problem associated with this erase method is the shrinkage of overlap region between the FG and the

source region as the devices are becoming smaller and smaller. Thus the erase process gradually becomes less efficient. To overcome this problem, a second erase methodology has been developed as presented in Figure 1.5b. In this case, the substrate, instead of the source, is positively biased and the CG is grounded so the electrons can directly tunnel into the channel region. Furthermore, a symmetric source and drain configuration can be utilized.

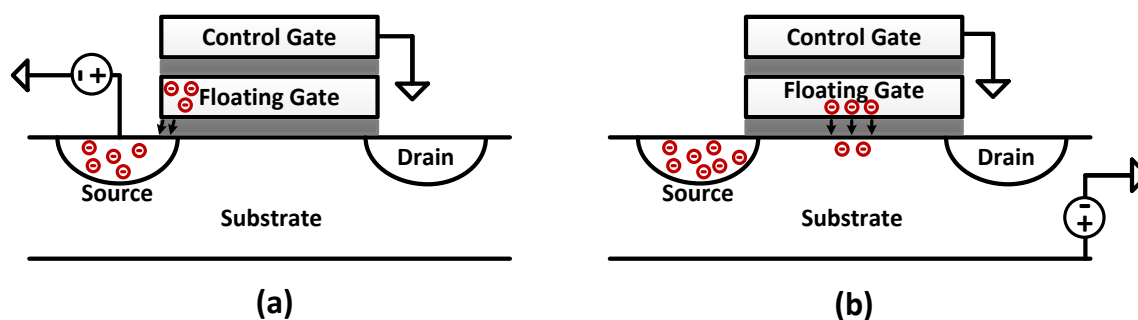


**Figure 1.5 Erasing a floating gate device by (a) FNT at source side and (b) FNT in channel**

### Application and Scaling Limitation of Flash Memory

Based on the fundamental operation mechanism of Flash, there are several limitations from both application and scaling perspectives. First, it is impossible to achieve properties like fast programming, quick access, and high memory density together with random access at same time. There are two topologies for Flash cell known as NAND and NOR. NAND Flash offers the advantages of faster programming and high density yet it does not have random access capability and the read speed is slow. NOR Flash has random access capability; however, it is inferior to NAND in all other aspects.

Scaling is another fundamental challenge to Flash technology for future NVM applications. Even though NAND Flash has higher density than NOR, it faces many difficulties to continue scaling down. It is generally believed that the feature size of traditional Flash cell is difficult to scale down below 20nm [7]. These limitations are

related to its fundamental operating principle. First, the inter-poly dielectric thickness must scale with gate oxide thickness to maintain adequate coupling of the applied voltage to the gate tunnel dielectric [8]. To ensure sufficient voltage can be applied to the FG during program and erase operations, the gate coupling ratio has to be greater than 0.6 [6]. As device dimensions scale down, the common gate needs to be wrapped around the FG to provide sufficient capacitance. However, it is very difficult to achieve such a structure when the bit line spacing becomes 20nm or less. In addition, there is a limitation on the thickness of the tunneling oxide. If the tunneling oxide is too thin, electrons, even without any external electric field, can easily tunnel back to the channel. Therefore, the device retention properties could be severely degraded. Furthermore, as the size of Flash cell decreases, the number of electrons stored in the FG will also decrease, causing severe random telegraph noise [9], resulting in reliability problems.

In general, continuous down scaling of the devices will result in additional physical problems. These problems will have to be avoided by more complex structures and materials. This complexity will result in a demand for advanced fabrication routes and tools, which is directly related to increase in lithography cost to obtain higher resolution. This will subsequently result in an increase of fabrication costs, which cannot be paid off by the increased memory/storage density, leading to an extremely high pricing for devices. These challenges raise the demand for alternative memory technology, combining high performance with non-volatility and low fabrication cost.

### **Alternate Memory Technologies**

As Flash memory approaches the scaling limit, new NVM solutions are being explored as a possible replacement. Among the new memory candidates, Magneto-

Resistive Random Access Memory (MRAM), Ferroelectric Random Access Memory (FeRAM), and Phase Change Memory (PCM) are in the prototype stage. These types of memories are used for various applications, though the number of commercialized products remains small due to the inherent technological problems. In addition to these memories, a memory solution that is being actively investigated is Redox Nano-Ionic Conductive Bridge Memristor (RCBM), commonly known as Resistive Random Access Memory (RRAM) or Resistive Change Memory (RCM).

RRAM will compete with the aforementioned memory technologies, as it offers non-volatility characteristics, providing an alternative to Flash memory. Table 1.1 summarizes the comparison of the performance of different memory technologies. They are, subsequently, briefly described and compared with matured technologies such as DRAM and Flash memory, illuminating the emerging demand for RRAM.

<b>Types</b>	<b>Flash Memory</b>	<b>MRAM</b>	<b>FeRAM</b>	<b>PCM</b>	<b>RRAM</b>
<b>Parameters</b>					
Writing time	~1µsec	~30ns	~150ns	~10ns	~10ns
Erasing time	~10msec	~30ns	~80ns	~50ns	~30ns
Reading time	~50nsec	~30ns	~60ns	~20ns	~20ns
Writing Power Consumption	High	Middle	Low	Material Dependent	Low

### Magneto Resistive Random Access Memory (MRAM)

A memory cell of an active MRAM device consists of a select transistor and a magnetic element, known as magnetic tunnel junction (MTJ), which is composed of a thin insulating film sandwiched between two ferromagnetic layers [10], as illustrated in

Figure 1.6. One layer has a pinned ferromagnetic polarity, whereas the other one can be changed by application of an external field. The MRAM device is positioned at the intersection of a bit line and a write word line. Both wires induce a directed and turning magnetic field that rotates the magnetic axis of the free layer with respect to the pinned layer.

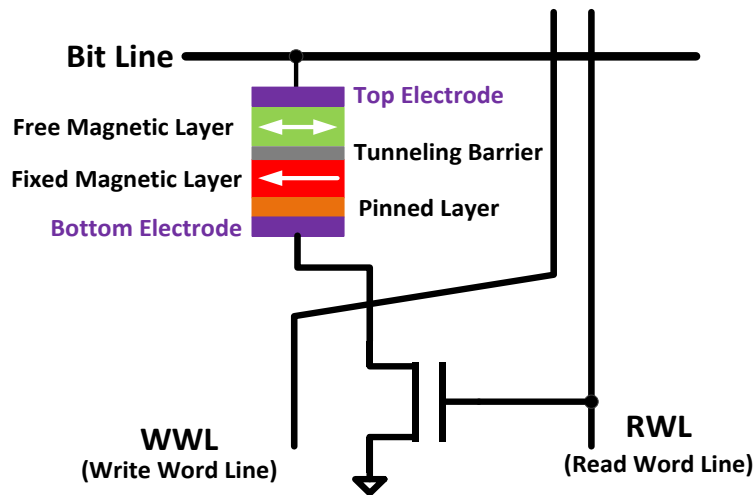


**Figure 1.6 Schematic of a MRAM cell**

When the polarity of the magnetic layer is the same, the electrons can tunnel easily through the tunnel barrier layer due to the magnetic tunneling effect, and the memory cell is in the Low Resistive State (LRS). On the other hand, tunneling is suppressed if the layers are aligned anti-parallel, and the cell is said to be in the High Resistive State (HRS). The state of the cells can be determined by the current through the bit line once the select transistor is opened by the read word line.

The writing and erasing speed of MRAM is faster compared to Flash with endurance comparable to DRAM. However, high current, which is necessary to program

the device, represents a disadvantage of this technology, and thus, limits its application in portable electronic devices.

### Ferroelectric Random Access Memory (FeRAM)

The structure of a FeRAM cell is very similar to DRAM [11], as it consists of an access transistor and a ferroelectric capacitor. Unlike DRAM, the data in FeRAM is stored by the remanent polarization ( $P_r$ ) of the ferroelectric film, which can be programmed by application of an electric field ( $E$ ) across the capacitor. The electric field dependent polarization nature of the ferroelectric material results in a hysteresis behavior with a positive and a negative remanent polarization as shown in Figure 1.7b, which is non-volatile in the absence of an electric field.

The polarization is switched either into the positive or negative direction depending on the applied voltage bias. A high amount of charge is shifted by a current flow if the polarization changes due to the voltage pulse. On the other hand, if the polarization already has the intended direction, only a small amount of charge is shifted because of the dielectric response of the ferroelectric material. The stored information can be read by detecting the voltage across the capacitor seen between the ferroelectric capacitance and the bit-line capacitance. Depending on the polarization state, the read voltage above or below a reference voltage, can be distinguished to define the stored state of the FeRAM element.

A significant feature of FeRAM is its low power consumption. An operation voltage of less than 2V is the greatest advantage against Flash cells, which require a voltage of 20V for a write or erase operation. Apart from a lower operating voltage, the current is also lower, resulting in less write energy in FeRAM compared with MRAM.

Additionally, in FeRAM, power is consumed only when a write and read operation is performed, contrary to DRAM where cells have to be refreshed continuously, which requires a continuous supply of power.

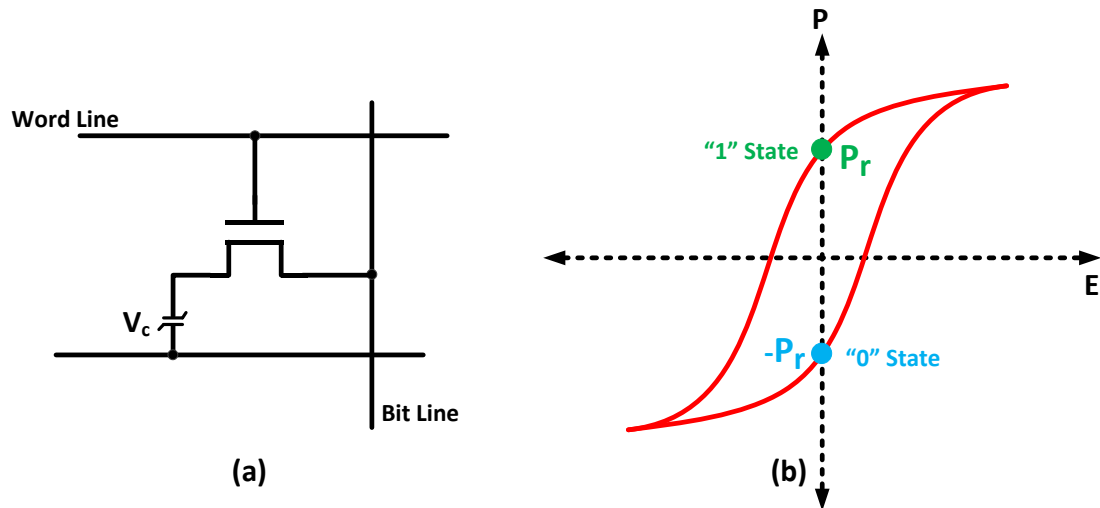


**Figure 1.7** (a) FeRAM Structure and (b) A polarization-electric field hysteresis loop

FeRAM is widely used as an embedded memory in a logic LSI for wireless cards, automobile equipment, and domestic electronic appliances. However, it remains a relatively small part of the overall semiconductor memory market as its cell structure is not suitable for scaling. The highest density reported for FeRAM is 128 Mb [12].

### Phase Change Random Access Memory

Phase change random access memory (PCM), like FeRAM, has a structure similar to DRAM [13]. Each cell consists of a select transistor and a memory element, which are arranged in a matrix of word and bit lines for addressing and operation, as presented in Figure 1.8. The key component is the memory element, which contains a chalcogenide (ChG) film, sandwiched between two electrodes that can be miniaturized easily.

Chalcogenide film is comprised by one or more elements of the sixteenth group (S, Se, and Te) in the periodic table, which in combination with other elements, for example, Ge, As, or Sb create a glassy solid state material.

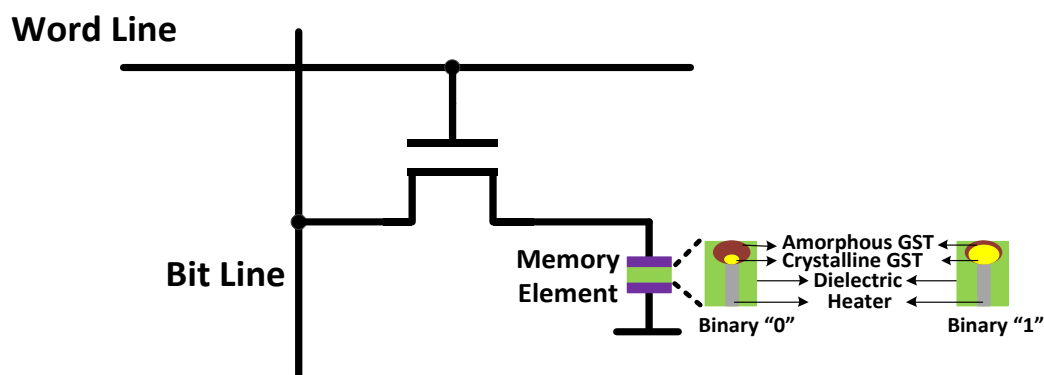


**Figure 1.8** Phase Change Memory schematic with cell in Reset and Set state

The operating principle of PCM is based on phase change of the ChG material from amorphous state to crystalline or vice versa by application of a small voltage. The amorphous state of the material is responsible for the high resistive state of the cell, while the crystalline one creates the low resistive state. The ChG material is sandwiched between two metal electrodes, which are used to induce time and amplitude controlled current pulses to transition between two states. A longer duration current pulse with a lower amplitude heats up the material above the crystallization temperature forming the crystalline state, enabling the low resistive state. In contrast, a fast pulse with a high current generates sufficient heat to exceed the crystallization temperature, but due to the small duration an under-cooled amorphous state is generated, making a HRS. The conduction of the PCM changes drastically as the material changes from amorphous to crystalline form. This effect is also used for rewriteable CD or DVD disks, where the corresponding state is determined optically by the reflectivity.

## Resistive Switch Random Access Memory

Resistive memory technology utilize the materials and structures where suitable voltages can change the memory state of the cells, allowing it to store binary data, similar to other NVM technologies. Over the last two decades and especially recently, there has been an increased interest in memristive system - resistor with memory as described by Leon Chua in 1971 [14]. He extended his description to memristive systems in 1976 and gave examples, such as thermistors, nerve axon membranes (as described by the Hodgkin-Huxley model) and discharge tubes [15]. Nevertheless, resistively switching thin films were not classified in this context for years. Certain types of materials have been observed to demonstrate a change in resistance based on the application of an external electrical field. These types of materials are ideal candidates for creating RRAM devices. The basic cell structure of a RRAM cell is shown in Figure 1.9.

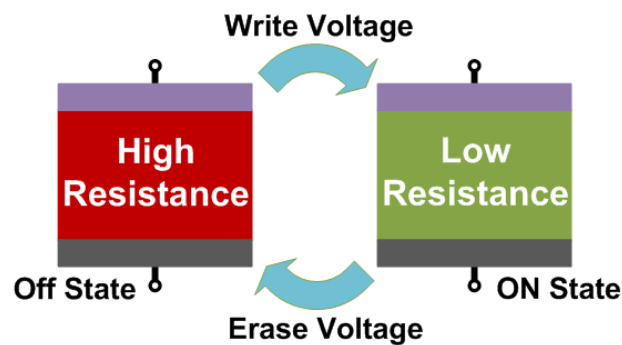


**Figure 1.9 ON and OFF State of RRAM**

The figure shown above is called metal insulator metal (MIM) structure, where the device switches between a high resistance state and low resistance state due the application of either Write or Erase voltage. HRS represents the OFF state while LRS represents the ON state of the device. In RRAM devices, resistance change occurs in response to charge flux by building up or dissolving a conductive molecular bridge

between two electrodes. The conductive bridge is formed and dissolved in the film sandwiched between the two metal electrodes and is termed active film in this work. In addition, the Write and the Erase voltages do not need to be applied continuously to maintain the state, thus classifying RRAM devices a NVM.

RRAM piques more and more interest as a promising candidate for the next generation of NVM, aimed to replace Flash memory due to the following reasons:

1. RRAM is compatible with current CMOS technology, which means that investment in new processing tools will be minimal.
2. RRAM has a simple capacitor like structure with two terminals, which is easy to fabricate and embed into VLSI circuits.
3. RRAM is operated, in many cases, under very low power.

High dense memories based on resistive switching have been proposed due to the simplicity of their structures and the possibility to scale them to nano-sized devices. However, RRAM still faces several challenges for practical applications. The problems being investigated are stability of the device performance and quantified analysis of the switching mechanism within these devices. Furthermore, device endurance requires further improvement to make RRAM devices commercially viable.

### **Background and Literature Review**

In recent years, various materials have successfully demonstrated the resistive switching effect, which includes binary and mixed-valence oxides [16-26], phase change material between the two electrodes [27, 28], and silver doped chalcogenides [29-31]. The switching phenomena can be different depending on the material. In terms of the

behavior, the resistive switching effect can be classified into two main types, unipolar and bipolar.

### **Principle of Resistance Switching Operation**

The most common characteristic of this type of non-volatile memory devices is the demonstration of the hysteretic current voltage characteristic in which resistance change occurs between two stable states, namely LRS and HRS. This resistance switching is controlled by either current or voltage. Switching of the device from LRS to HRS is called the RESET process, while switching from HRS to LRS is called the SET process.

The operation of resistance switching is distinguished by two different schemes depending on the biasing, as shown in Figure 1.10a. To distinguish between a SET state and a RESET process, a current limit and certain voltage amplitude are required.

When either the SET or RESET switching takes place at the same voltage or current polarity, the switching is referred to as unipolar switching (i.e., the switching process is independent of polarity). Thus, in unipolar switching, the applied voltage or current should be precisely controlled. In such type of switching, change in the resistance state occurs (HRS to LRS) by a threshold voltage accompanied by compliance current (CC), which is required to protect the device from thermal breakdown or immediate reset. Once the device turns ON, resetting of the device to HRS occurs at a lower voltage than the writing voltages.

The nature of the unipolar mechanism offers an advantage of operation with a single polarity and simplifies the triggering for an external control circuit considerably.

The switching effect can be explained by the fuse-antifuse effect in which the formation or rupture of a conducting path, due to an electric field and thermal impact results in change of state of the device. Several transition metal oxides including NiO and Nb<sub>2</sub>O<sub>5</sub> exhibit unipolar switching [19, 32-34].

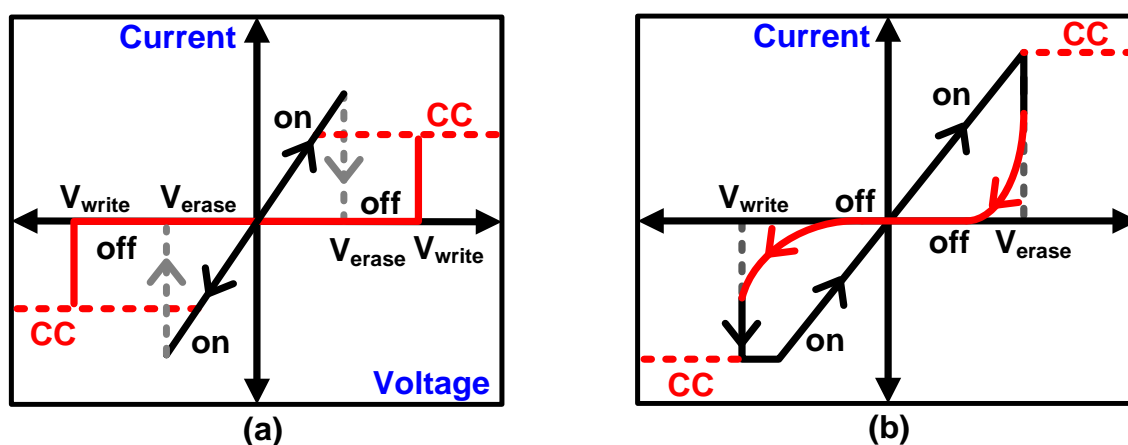


**Figure 1.10** Two different resistance switching mode schematics (a) Unipolar and (b) Bipolar switching [35]

A typical current response for a bipolar double voltage sweep is illustrated in Figure 1.10b. Bipolar switching shows a voltage polarity dependency for either SET or RESET process. Unlike unipolar switching, in bipolar switching if, for example, SET state occurs at positive voltage, then the RESET switching is obtained at a negative voltage. The asymmetry of the switching curve is normally caused by an asymmetry of the memory element. This can be caused by different electrode materials for the top and bottom electrode or a directed treatment during the electroforming process.

In both types of switching modes, the resistance states are distinguished by a small read out voltage, less than SET or RESET voltages. Therefore, the read operation has no influence on the resistance state. Different switching modes are explained by

different mechanisms and the switching criteria depend on the materials and measurement methods.

### Classification of the Switching Mechanism in RRAM

One of the challenging issues in the RRAM field is the switching mechanisms that govern the resistance change within the active material. Several mechanisms have been proposed to explain the switching phenomena in RRAM based on different materials. The International Technology Roadmap for Semiconductors (ITRS) roadmap suggests 5 types of RRAM devices that are based on different switching mechanisms as illustrated in Figure 1.11.

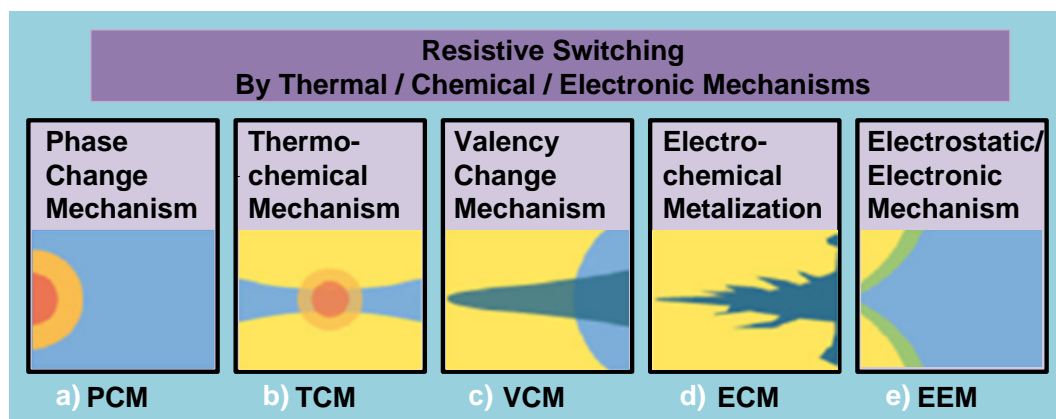


**Figure 1.11 Resistive memory technology classification based on their operation [ITRS 2012]**

The *first* switching mechanism, Figure 1.11a, is due to the phase change within the material, which results in different resistance states. The underlying mechanism of Phase Change Memory is explained in the *Phase Change Random Access Memory* section. The most reliable active material that is currently being applied in Phase Change Memory is  $\text{Ge}_2\text{Sb}_2\text{Te}_5$  (GST) [36, 37].

The *second* switching classification, Figure 1.11b, is based on thermo-chemical mechanism also known as fuse-antifuse switching. The application of an applied voltage induces a partial breakdown of the switching material, thus creating a fuse between the two electrodes enabling the device in LRS. The conductive filament path is disrupted by joule heating caused by high current density through the filament enabling HRS. An example of this type of RRAM material is NiO, which exhibits filamentary conduction [38].

The *third* type of switching method, Figure 1.11c, is based on valence change mechanism. This mechanism is referred to as anion migration induced redox switching [39, 40]. In this mechanism, anions, typically oxygen vacancies in many transition metal oxides, drift towards and accumulate at the cathode, therefore an oxygen deficient region begins to grow and expand towards the anode. Oxygen vacancies reduce the valence state of anions, turning oxide into a metallic phase, resulting in the formation of a metallic conductive channel. Thus, the conduction path is composed of highly oxygen deficient non-stoichiometric phase, which shows higher conductivity than normal phase. A region with a high oxygen vacancy concentration between anode and cathode is shown in Figure 1.12 obtained by X-ray absorption near edge spectroscopy (XANES) spectra [23]. This shows the importance of oxygen vacancy actions in transition metal oxides, which plays a significant role in resistive switching. Materials such as  $\text{TiO}_2$ ,  $\text{SrTiO}_3$  and  $\text{Pr}_{0.7}\text{Ca}_{0.3}\text{MnO}_3$  demonstrate this switching mechanism.

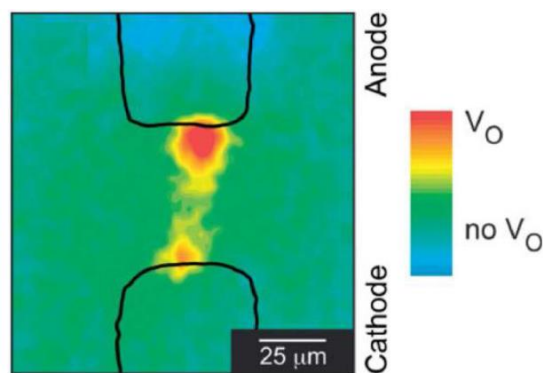


**Figure 1.12 X-ray fluorescence mapping after electroforming in Cr-doped SrTiO<sub>3</sub> showing distribution of oxygen vacancies between two electrodes [23]**

Models demonstrating the generation of conductive path by oxygen vacancies are described by Jeong et al. [40], Zhirnov and Cavin [41], and Yang et al. [42]. Jeong et al. made their observations on a symmetric stack of Pt/TiO<sub>2</sub>/Pt on the basis of the electroforming process in both vacuum and ambient atmosphere. During the electroforming process, the accumulation of oxygen gas at the anode hinted at the source of oxygen. Jeong et al. assumed that TiO<sub>2</sub>/Pt interface generates the dopant. The chemisorption of oxygen by Pt results in PtO\* and production of oxygen vacancies as illustrated in Figure 1.13. Due to the applied voltage field and the concentration gradient electric field, the positively charged vacancies drift towards the cathode. At cathode, they start to form a conductive path consisting of reduced TiO<sub>2-x</sub>, growing towards the anode. An opposite polarity creates oxygen vacancies, which close the path or shifts the existing vacancies towards the upper electrode. This serves as an explanation for the requirement of a bipolar electroforming process, which requires dual sweep with different polarities to either turn on the device or to turn it OFF.

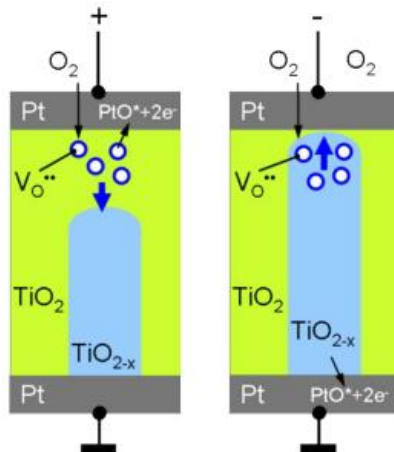


**Figure 1.13** Electroforming process forming in  $\text{TiO}_2$  by application of (a) Positive voltage/current and (b) Negative voltage/current [40]

The Zhirnov models of anions behavior is based on an interface effect rather than a bulk mechanism [41]. According to this model, if the oxygen atom is removed from its lattice position and the uncompensated valence of the nearby Ti atom creates an oxygen vacancy, the material becomes semi-conductive [41]. An electric field biases the vacancies in the material, which is assumed to be reduced constantly. As a result, they are pushed towards or pulled away from the metal electrode by the electric field. The Pt/ $\text{TiO}_2$  interface between the metal electrode and the bulk oxide represents a Schottky-barrier. The consequence of the field and the attending shift of the vacancies is an expansion or shrinkage of this barrier, which is presented in Figure 1.14. The current flow becomes less when the barrier expands, permitting LRS, and minimizes the tunneling probability. On the other hand, the current is increased when the barrier width decreases, enabling HRS. A bidirectional voltage sweep with a correspondingly high voltage leads to a hysteretic current response by changing the Schottky barrier twice within a loop. Yang et al. [42] in their model, presented the influence of metal/oxygen interface based on the memristive model presented by Strukov et al. [43].

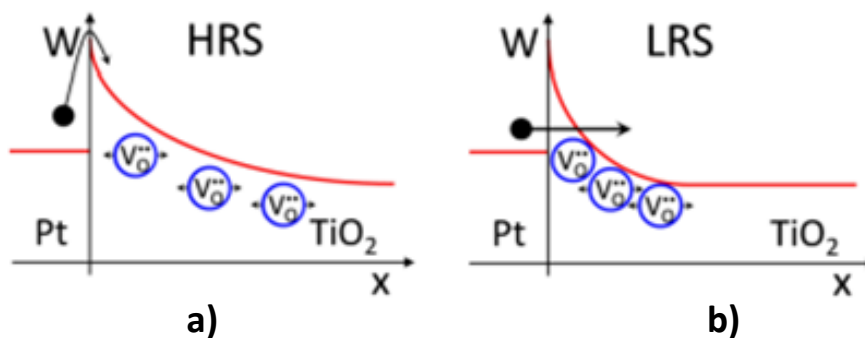


**Figure 1.14 Barrier Modulation by oxygen accumulation along the interface representing (a) HRS corresponding to wide barrier and (b) LRS corresponding to narrow barrier [41]**

The fourth type of switching method, shown in Figure 1.11d, is referred to as a redox induced cation migration mechanism. During the electroforming process, oxidation of a metal electrode occurs at the anode interface. The positively charged metal cations migrate to the inert cathode and are reduced at the interface. The reduced metal atoms accumulate at the cathode and grow a metallic bridge towards the anode, forming a metallic conductive filament. The device is in the ON state when the filament bridges the cathode and anode. The application of a reverse bias voltage results in the dissolution of the metal atoms at the interface of the anode, resulting in OFF state. Silver (Ag) or copper (Cu) [44, 45] are typically used as the oxidizable anode with Ge<sub>x</sub>Se<sub>1-x</sub> [31] as a switching material. Details about this switching mechanism are discussed in the following section.

The last switching process, Figure 1.11e, is based on an electrostatic/electronic mechanism. Electronic charges are injected and trapped at the interface of defect sites, which affects the Schottky barrier and changes the resistance of the active material. Some perovskite materials like PMCO (Pr<sub>0.7</sub>Ca<sub>0.3</sub>MnO<sub>3</sub>) function using these principles [46].

<b>Material</b>	<b>Composition</b>
Binary Oxides	TiO <sub>2</sub> , CuO, NiO, MnO <sub>2</sub> , ZrO <sub>2</sub> , HfO <sub>2</sub> , WO <sub>3</sub> , Ta <sub>2</sub> O <sub>5</sub> , VO <sub>2</sub> , Nb <sub>2</sub> O <sub>5</sub> , Fe <sub>3</sub> O <sub>4</sub> , Al <sub>2</sub> O <sub>3</sub> , SiO <sub>2</sub> , GdO <sub>x</sub> , etc.
Perovskites	LCMO (La <sub>1-x</sub> Ca <sub>x</sub> MnO <sub>3</sub> ), PCMO (Pr <sub>0.7</sub> Ca <sub>0.3</sub> MnO <sub>3</sub> ), YBCO (YBa <sub>2</sub> Cu <sub>3</sub> O <sub>7-x</sub> ), BSCFO (Ba <sub>0.5</sub> Sr <sub>0.5</sub> Co <sub>0.8</sub> Fe <sub>0.2</sub> O), Sr <sub>1-x</sub> La <sub>x</sub> TiO <sub>3</sub> , La <sub>1-x</sub> Sr <sub>x</sub> Fe <sub>3</sub> , La <sub>1-x</sub> Sr <sub>x</sub> CoO <sub>3</sub> , SrFeO <sub>2</sub> , YBa <sub>2</sub> Cu <sub>3</sub> O <sub>7</sub> , SrZrO <sub>3</sub> Cr, LaMnO <sub>3</sub> , etc.
Chalcogenides	Ge <sub>x</sub> Se <sub>1-x</sub> (Ag, Cu, Te doped), Ag <sub>2</sub> S, Cu <sub>2</sub> S, Cd <sub>2</sub> S, ZnS, etc.

A significant research work is currently being performed to investigate new materials that exhibit resistive switching. A number of materials that have successfully demonstrated resistive switching behavior are summarized in Table 1.2. Due to the high number of materials that have already demonstrated resistive switching behavior, it is important to narrow down the list to few possible candidates that show reliable device performance as well as have the capability for being applicable to commercial products.

Among the various types of the memory effects shown above, we focused our studies on the devices using redox based electrochemical cation migration. It has been a subject of studies for a relatively short time, but the fact that it requires low power consumption, scaling to atomic size, high switching rate, and storage of multiple bits controlled by a compliance current, has made these devices the front runner in the race to dominate the next generation NVM market.

### **Illustration of Switching Mechanism in a Solid Electrolyte**

Among several mechanisms, the formation of a conductive bridge filament is the most intriguing and highly researched mechanism for resistive switching. Cation-based

switching occurs when one of the two electrodes is an electrochemically active electrode (anode) metal, such as Ag or Cu, while the other is an electrochemically inert electrode (cathode) metal, for example, Pt, W, Ni, etc., and a thin film of solid electrolyte (or a dielectric) sandwiched between both electrodes. Solid electrolyte is formed by either thermal or photo diffusion of silver into the chalcogenide matrix, thus making it an ion conducting medium. The switching ON of the cell is due to an electrochemical formation of a metallic conductive bridge in the ion conducting chalcogenide medium, whereas the switching OFF is triggered by the dissolution of this filament. The electrochemically active electrode provides the source of metal ions, which after realization of the electrochemical process allows the formation of a conductive bridge filament. Figure 1.15 illustrates the principle of operation of redox conductive bridge cell in conjunction with a current-voltage (IV) switching cycle using a quasi-static triangular voltage source with silver (Ag) as an oxidizable electrode and platinum (Pt) as an inert electrode. Initially, the cell resistance is high (OFF-state) and no electrodeposit of Ag is present on the inert electrode (Pt). When a sufficiently positive voltage is applied to the Ag electrode, the switching process (filament formation) consists of the following steps:

- i) Metallic Ag atom originating from Ag electrode is oxidized to create  $\text{Ag}^+$  ion at the Ag electrode/solid electrolyte (Ag-ChG) interface according to the following reaction:



- ii) Due to the applied voltage bias, which consequently creates an internal electric field between the two electrodes, the  $\text{Ag}^+$  ion is attracted to the

inert electrode and migrates through the solid electrolyte towards the Pt electrode.

- iii)  $\text{Ag}^+$  ions are reduced back to metallic silver at the Pt electrode/solid electrolyte interface according to the following reaction:

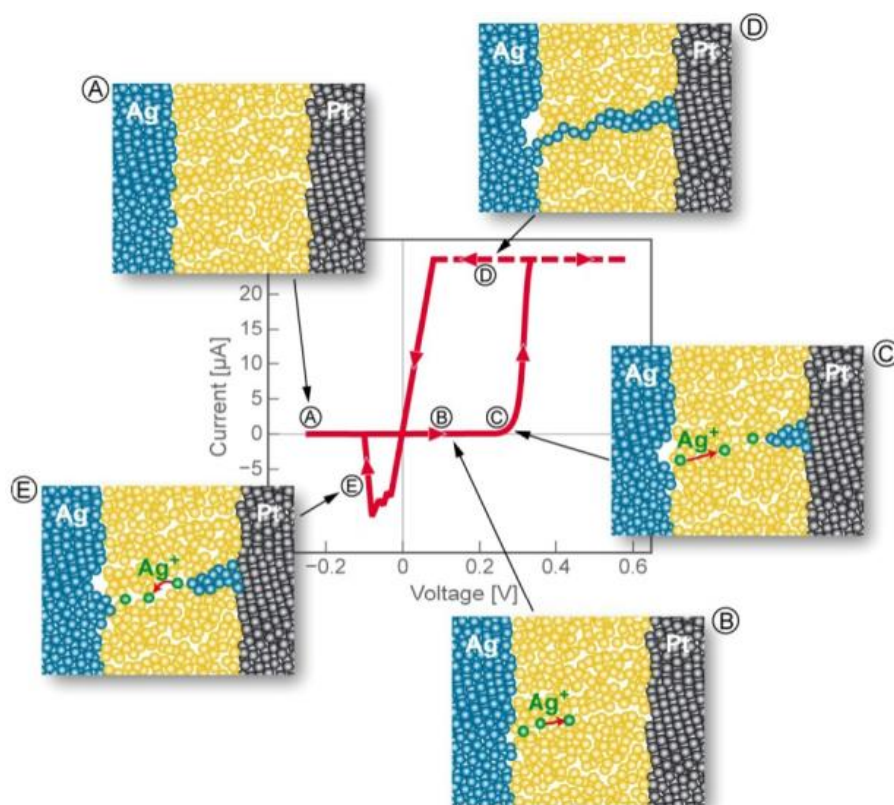
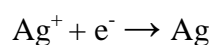


**Figure 1.15** Schematic illustration of Set (A-D) and Reset (E) operation for an RCBM cell [47]

This newly deposited Ag atom is a preferred growth site for the next silver atom. Due to the electrodeposition of Ag at the Pt electrode, the distance between the two electrodes reduces, creating a stronger electric field at the new Ag site. The filament continues to grow from this site (Figure 1.15C). Due to multiple redox reactions and electric field distribution between the two electrodes, a filament consisting of Ag atoms

grows from the Pt electrode towards the Ag electrode. The moment when the front most Ag dendrite makes contact with the solid Ag electrode, the device transitions from high resistance state to low resistance state (Figure 1.15D). When the filament reaches the Ag electrode, the device switches from HRS to LRS by short-circuiting the two electrodes. Upon reversal of the voltage polarity, electrochemical dissolution of the filament takes place, resulting in resetting the system into the OFF state (Figure 1.15E).

Different names have been given to the cation migration based resistive switching devices, such as programmable metallization cell [31], nano- bridge [48], solid-state atomic switch [49], electrolyte memory [50], conductive bridging RAM [51], and so on. Since the filament formation and dissolution in the Ge-Se system is based on an oxidation and reduction reaction, it is referred as Nano Ionic Redox Conductive Bridge Memory (RCBM) in this dissertation.

The electrochemical behavior of a RCBM cell is a function of thermodynamics and kinetics parameters, which are discussed in the following section. The process of filament formation involves the kinetics of electrode reactions (formation and dissolution of the filament) at both electrodes.

#### Charge Transfer Kinetics

The kinetics of the electrode reactions (either at anode or at cathode) can limit the overall reaction rate and the switching performance of the RCBM cell. The quantity that limits the electrode reaction rate is the overpotential ( $\Delta\varphi$ ) defined as  $\Delta\varphi = V_o - V_i$ , where  $V_o$  is the potential measured at equilibrium and  $V_i$  is the externally applied potential. The  $\Delta\varphi$  contributing parts can be further expressed as:  $\Delta\varphi = \Delta\varphi_{crystal} + \Delta\varphi_{charge} +$

$\Delta\varphi_{diff}$ . The current limitation due to the activation enthalpy  $\Delta G$  required for the initial nucleation process is represented by crystallization overpotential [52]. The electrochemical potential of the electrons ( $\eta_e$ ) is shifted by the applied electric potential that changes the activation barrier height. A schematic presentation is shown in Figure 1.16, where  $\Delta\vec{G}'^\ddagger, \vec{G}'^\ddagger, \Delta\vec{G}^\ddagger, \vec{G}^\ddagger$  are the activation free enthalpies for the forward and backward reactions, respectively, without and with applied voltage. The change in activation energy is proportional to the applied voltage, as shown in Figure 1.16. Part of the applied voltage that is being used to lower the activation barrier is the proportionality factor, known as transfer coefficient ( $\alpha$ ). The transfer coefficient for the anodic and cathodic reactions must sum up to one.

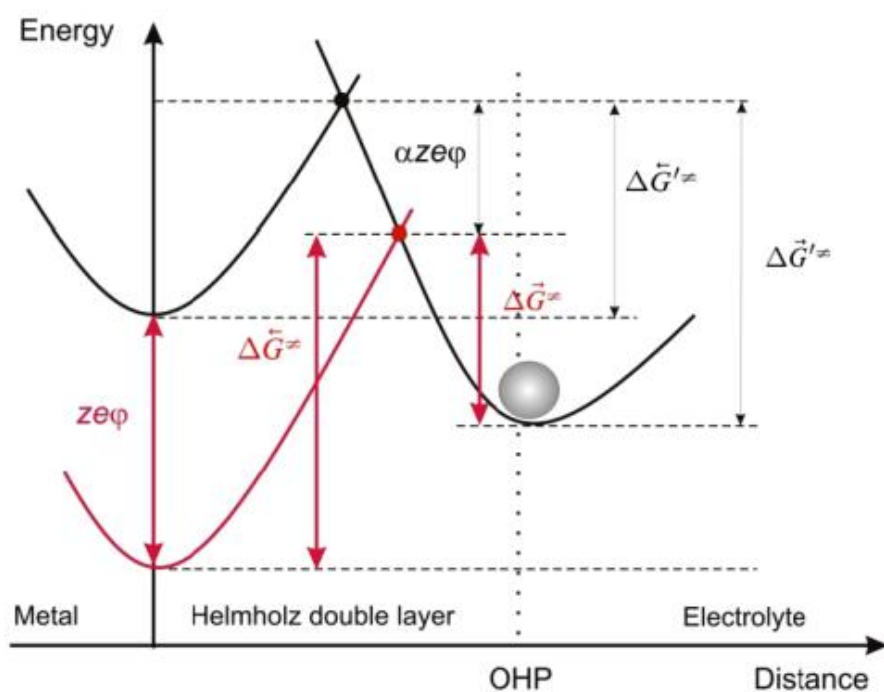


**Figure 1.16** Representation of the potential energy diagram of a charge transfer process. The black curves represent the initial state and the red curve results after applying an electric potential to the metal electrode. OHP is the outer Helmholtz plane [47]

The current voltage dependence for an electrode process controlled by the charge transfer at steady state conditions is given by the Butler-Volmer equation [53, 54]:

$$i = i_o \left[ \exp\left(\frac{1-\alpha Z_i e}{k_B T} \Delta\varphi_{charge}\right) - \exp\left(-\frac{\alpha Z_i e}{k_B T} \Delta\varphi_{charge}\right) \right] \quad (1.1)$$

where  $i$  is the current density,  $i_o$  is the exchange current density,  $\alpha$  is the transfer coefficient,  $Z_i$  is the number of exchanged electrons. The first term in equation 1.1 represents the anodic process while the second term shows the cathodic process. The overvoltage has a positive sign convention for anode process and negative for cathodic ones. The exchange current density, an important parameter, is defined as the current density at equilibrium that is a measure for the catalytic activity of the electrode toward a particular electrode reaction given as [47]:

$$\begin{aligned} i_o = \vec{i}_o = \overleftarrow{i}_o &= -ze\vec{k}c_{ox} \exp\left(-\frac{\alpha ze}{k_B T} V_{eq}\right) \\ &= ze\overleftarrow{k}c_{red} \exp\left(\frac{(1-\alpha)ze}{k_B T} V_{eq}\right) \end{aligned} \quad (1.2)$$

In equation 1.2,  $\vec{k}$  and  $\overleftarrow{k}$  are the rate constants of the cathodic and anodic reactions respectively. The exchange current density may also be used as a stability criterion for the stability of the active electrode against chemical oxidation.

Equation 1.1 is derived by taking into account a single step electron without considering additional concentration effect, double layer effects, multi-step processes, etc. In the case of an RCBM cell, one electron transfer reaction without considering additional terms may be applied to achieve a boundary condition in the following manner:

In the case of small overpotentials  $\left(|\Delta\varphi| \ll k_B T/e\right)$ , that is, close to equilibrium,

both terms in equation 1.1 should be considered. Equation 1.1 can be approximated to the linear dependence [47]:

$$i = \frac{i_0 z e}{k_B T} \Delta\varphi_{charge} = \frac{1}{R_p} \Delta\varphi_{charge} \quad (1.3)$$

where  $R_p$  is known as polarization resistance and has the units of ohms.

For large overpotentials  $\left(|\Delta\varphi| > k_B T/e\right)$ , by increasing the voltage one of the

term in equation 1.1 becomes very small and can be neglected. Under these conditions, the overpotential can be derived as:

$$\Delta\varphi_{cathodic} = \frac{k_B}{\alpha z e} \ln \frac{i_0}{i} \quad (1.4)$$

Equation 1.4 is widely used to study the kinetics of the charge transfer limited process. In the case of the Ge-Se/Ag system, the charge transfer process of Ag deposition determines the reaction rate [55], and, hence the switching speed of the cell during the Set process. Hence, the charge transfer limitation is an important parameter for RCBM devices where switching is based on the ionic conduction. For such systems, the diffusion process will be fast because of smaller diffusion length and higher diffusion coefficients. Therefore, the most probable limitation will be the electron transfer at the Ag electrode/electrolyte interface in accordance with the Butler-Volmer equation.

### Diffusion Limited Kinetics

The reaction is diffusion limited if the diffusion of the reactants and the byproducts towards the electrode/electrolyte interface limits the overall reaction rate and

the overvoltage is referred to as diffusion overvoltage ( $\Delta\phi_{diff}$ ). In this case, the steady state current-voltage dependence is given as [47]:

$$\Delta\phi_{diff} = \frac{k_B T}{ze} \ln \left( 1 - \frac{i}{i_d} \right) \quad (1.5)$$

where  $i_d$  is the diffusion limited current, which is independent of the increasing voltage.

The diffusion current  $i_d$  depends on the concentration of reacting species and their diffusion coefficient and is expressed as [47]:

$$i_d = z_i e D_i \frac{c_i - c_i^s}{\delta} \quad (1.6)$$

where  $c_i^s$  is the surface concentration given in  $\text{cm}^3$ . The condition of constant diffusion limited current is reached when the surface concentration drops to zero. For Ge-Se/Ag system, it has been proposed that the charge transfer reaction is the rate limiting factor for the electrochemical reaction. The diffusion limited process will be of importance for systems in which the materials have low ion conductivity or larger thickness. In oxide based materials, since metal ions cannot enter the dielectric, the diffusion limited process is dominant.

### **Parameters for Evaluation of Memory Device Performance**

The fabricated devices can be systematically evaluated using the following parameters:

#### **1. Non-volatility:**

Memory devices are classified into two types; volatile and non-volatile memories.

A device is considered volatile if the stored information is lost after removing the electrical power from the memory cell while a non-volatile device keeps the

information even after the electrical power is removed. SRAM and DRAM falls in the category of volatile memory while Flash memory is non-volatile.

## 2. Operating voltage:

Operation voltage is elucidated as the necessary bias required for Writing/Erasing/Reading a memory cell. Large operation voltage not only negatively influences reliability, but also increases the complexity of external circuits. One of the negative points of Flash memory is its large operating voltage. Figure 1.17 depicts the working voltage of RRAM devices. These devices are written at much lower voltage compared to the 20V/-20V used for writing/erasing the Flash cell.

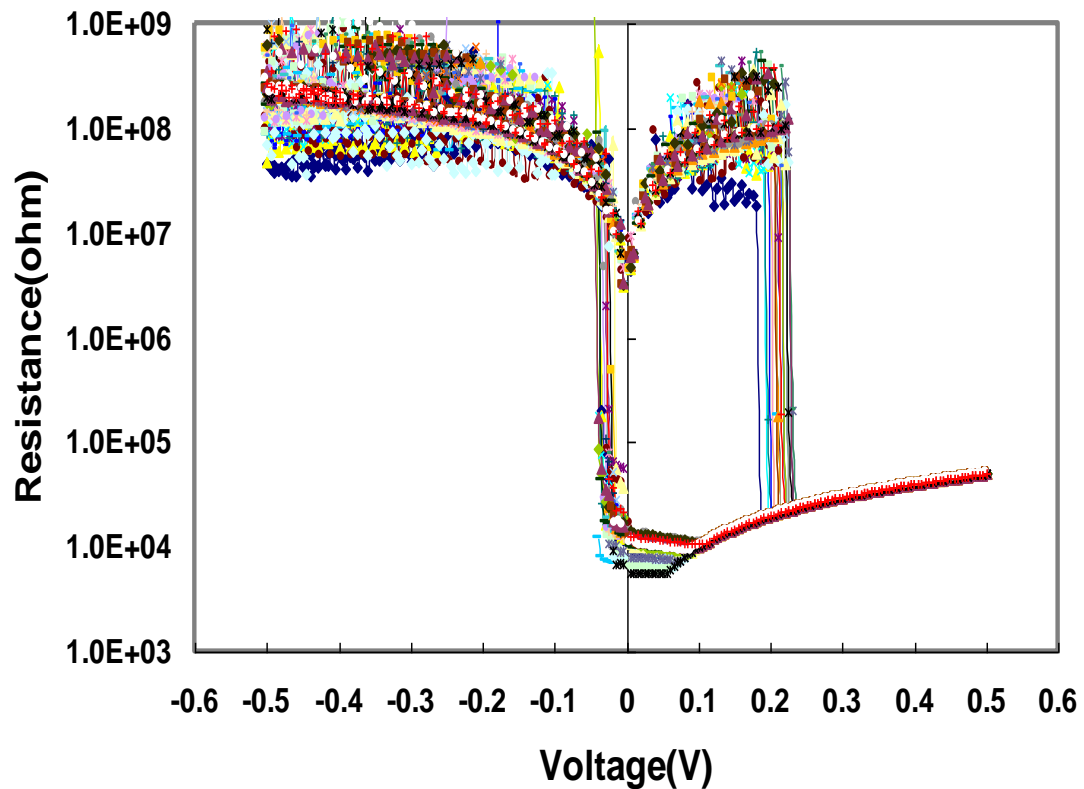
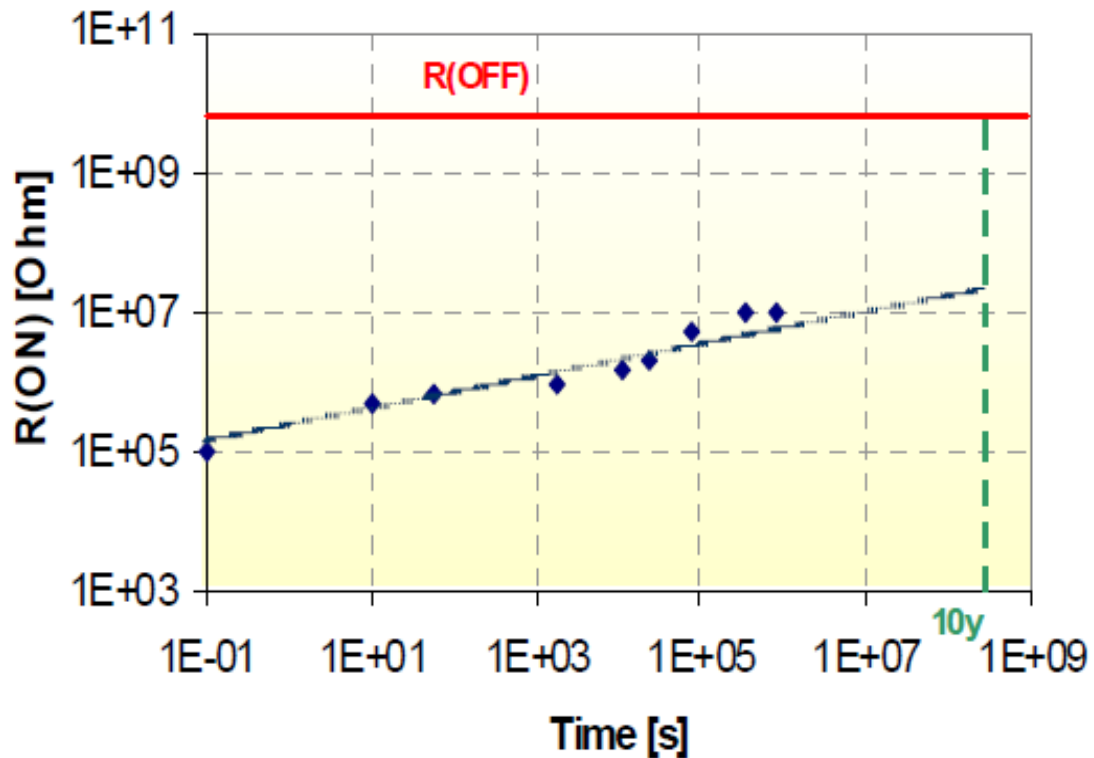


Figure 1.17 Operating Voltage of RRAM Cell [31]

### 3. Retention:

Retention is defined as the time duration for which the devices can retain the programmed values. Memory is classified as non-volatile, if the programmed value is retained for around 10 years. Even though Flash memory shows good retention (>10 years [56]), it is becoming more of a concern as the Flash cells are being scaled down. On the contrary, RRAM devices show excellent retention properties as shown in Figure 1.18.



**Figure 1.18** Retention of the ON state as measured before and after retention test ( $R_{OFF}$  stays above  $10^{10}$  ohm) [57]

### 4. Endurance:

Endurance is related to the number of times the device can be written and erased before failure. For non-volatile memory,  $10^4$  switching cycles is considered an

acceptable value. There is ongoing research aimed at improving the endurance of RRAM cells and current endurance capability is presented in Figure 1.19.

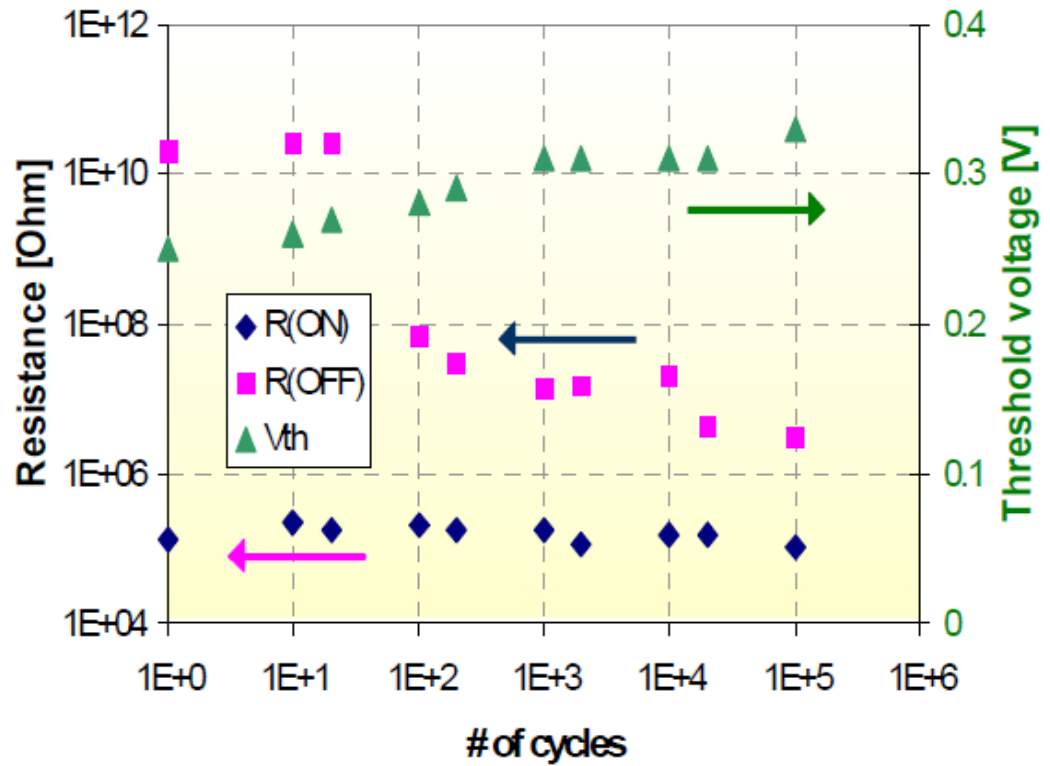


**Figure 1.19** Endurance test of RRAM device with  $10^5$  cycles [57]

##### 5. Multilevel storage:

Multilevel storage indicates the device has more than two programmable states, which improves the storage density. Thus, compared to binary state, a multilevel device can represent more than two states. Flash memory has a capability of storing fewer states compared to RRAM cells, making RRAM suitable for highly dense memory. An example of multilevel switching in RRAM is presented in Figure 1.20.

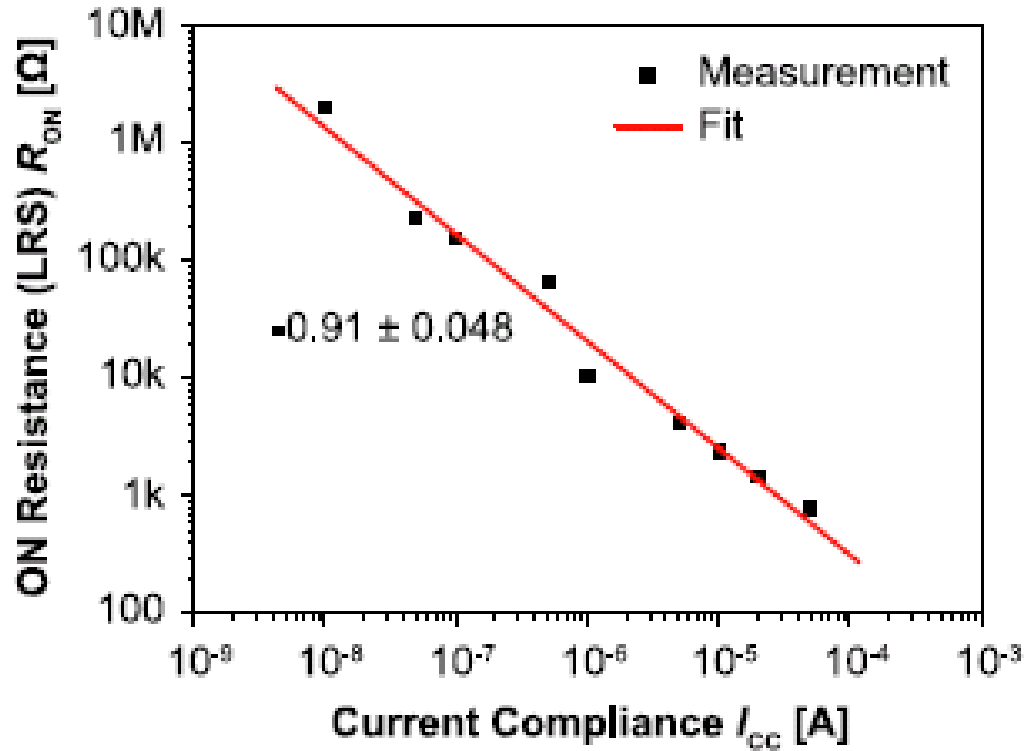


**Figure 1.20** Multilevel Switching in RRAM cell by changing the compliance current [58]

#### 6. Write/Erase time:

Write/Erase time are important parameters for evaluating memory performance.

The write/erase time of Flash memory is in the order of  $10^{-6}$  seconds to  $10^{-3}$  seconds. On the other hand, the write/erase time of RRAM can be achieved in the orders of 10 to 100ns [59].

#### 7. Memory Window:

It represents the ratio of HRS to LRS, which may be considered as figure of merit for comparing RRAM technologies. Figure 1.21 represents these two distinctive states. Higher ON/OFF ratio results in better memory since a small ratio will lead to more read error bits.

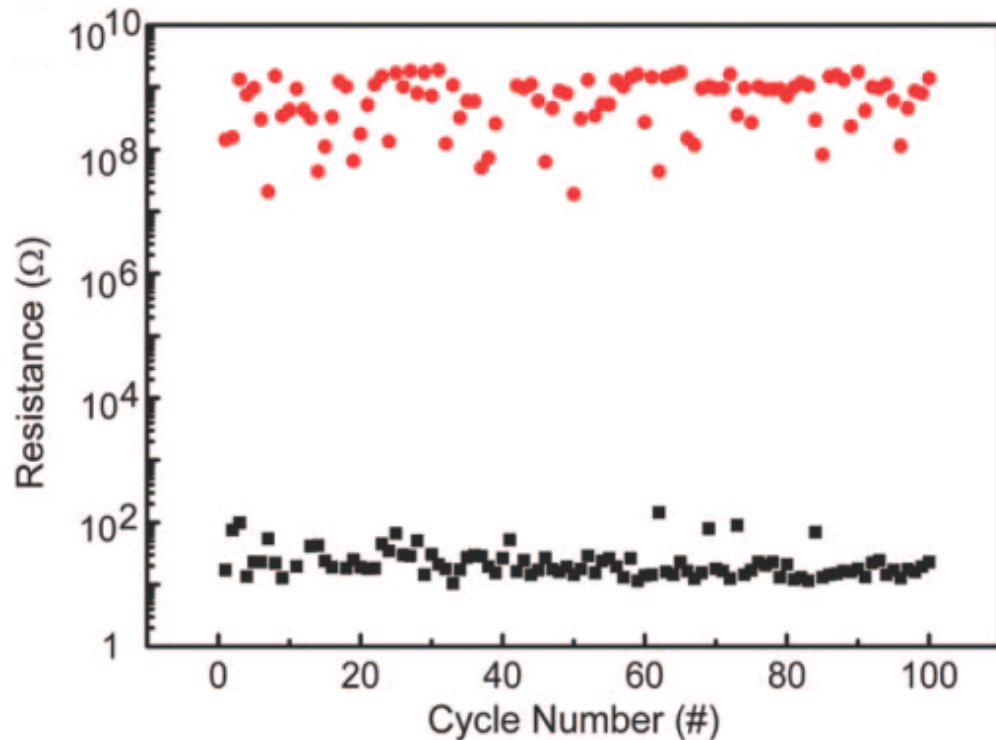


**Figure 1.21** Plot showing LRS and HRS of the RRAM cell with approximately 5 orders of magnitude difference between the two states [60]

#### 8. Scaling:

Scaling refers to the potential of decreasing the device dimension without sacrificing its performance. RRAM studies have demonstrated excellent scalability properties, thus making it a suitable candidate for future NVM applications.

#### Motivation of Study

The ITRS data for nano ionic redox conductive bridge memory devices' improvement and progress, since 2007 is presented in Figure 1.22. The performance of the devices improve as we move radially outward along the octagonal path in the figure. The performance parameters mentioned on the octagonal suggests that the RCBM

devices meet all the requirements, except for the reliability parameter hindering the devices from being commercialized.

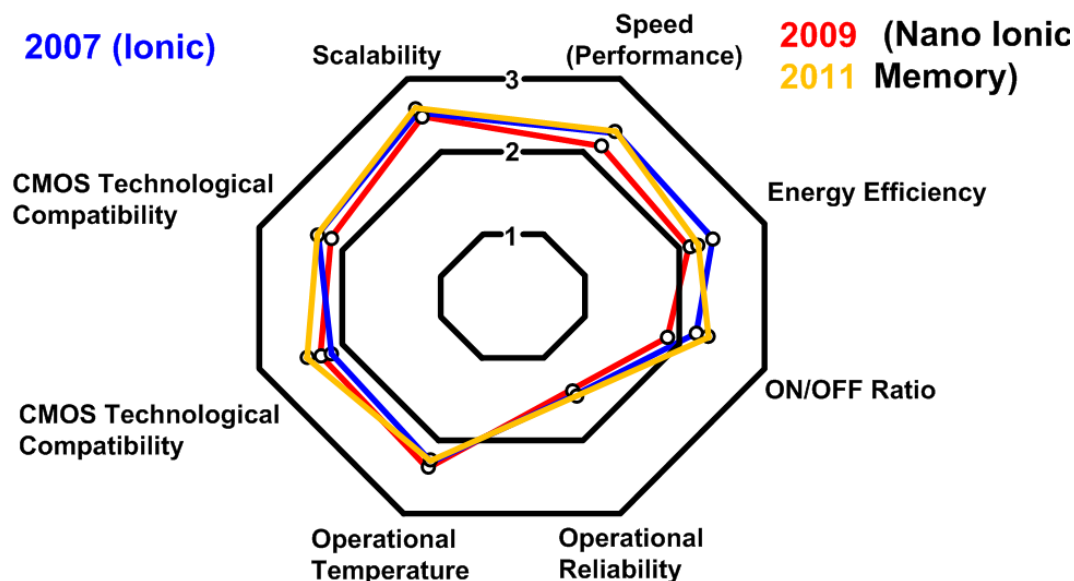


**Figure 1.22 ITRS 2012 requirement and performance chart for RCBM devices**

Operational reliability is one of the most important parameters for the emerging memory solutions. Reliability of the devices include both the endurance and retention properties as well as uniform and repeatable switching voltage for each cycle. Having a uniform switching voltage is an important parameter for using the RCBM devices in logic circuits, neuromorphic computing, and analog applications.

The process of filament formation and dissolution results in an RCBM cell to switch states between LRS and HRS. Few studies [61-63] have been conducted to investigate the morphology of the metal filament growth and its dimension. Unequivocal evidence of the filament growing in various directions having multiple branches is illustrated in Figure 1.23, which results in non-uniform switching (unreliable) of the devices.

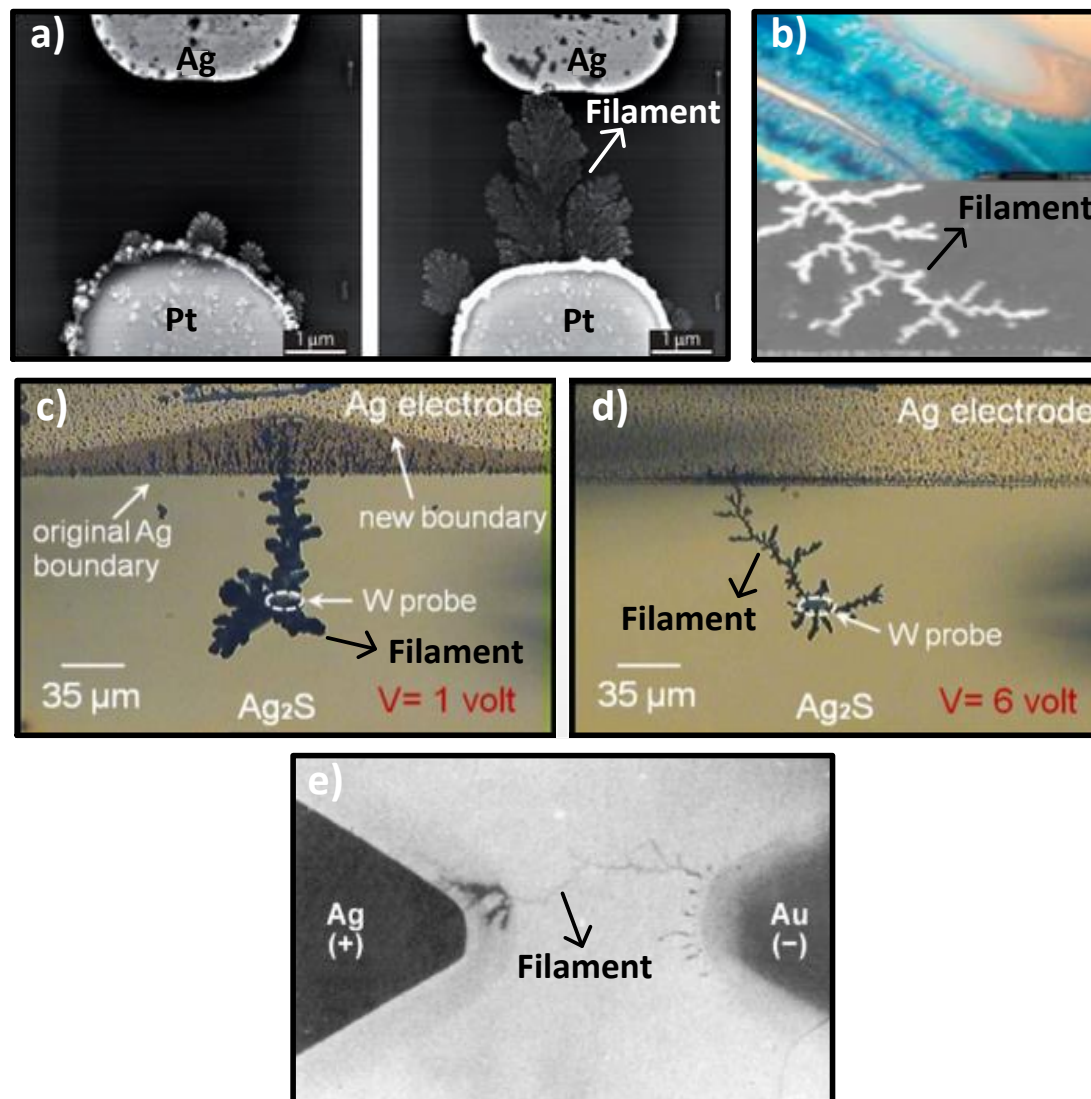


**Figure 1.23** Filament topographies reflecting multi-branching within the filaments during the growth process in (a) Pt/H<sub>2</sub>O/Ag system with no bias and biased conditions [44], (b) Cu/WO<sub>3</sub>/Pt system [64], (c-d) Ag/AgS/W system with different bias voltages [65], and (e) Ag/Ag<sub>2</sub>S<sub>3</sub>/Au system [66]

Once the filament is formed with multiple branches, causing the device to be in LRS, it has several connections at the bottom electrode (Figure 1.23 a, b, and e). Once the voltage polarity is reversed, it will stay in LRS till the last branch of the filament is dissolved. To ensure that the device switches from LRS to HRS, the bias has to be applied for a long enough time so that the filaments and all its branches are dissolved.

Since dissolving of the bridge is not a self-sustaining process, the filament may not be dissolved completely when the device is switched back to HRS (Figure 1.23a). The non-dissolved part of the filament becomes the preferential site for the filament growth in subsequent switching cycles, and therefore results in non-uniform switching performance of the device.

The work presented in this dissertation is aimed to improve the RCBM device performance through profound materials research regarding the active film formation and by nano-engineering the columnar structures growth within the device active layer. Multi-branching within the filament can be avoided by either having a very smooth (planar) surface for the active layer so that there is no preferred site for the filament to grow or by defining specific nano-pathways within the active film for the filament to grow. For planar deposition of active film, Ge-S devices were studied by Plasma-Enhanced Chemical Vapor Deposition (PECVD) method, which allowed good control over the deposited chalcogenide composition in a dynamic environment. The nano-columnar structures were created by obliquely depositing the active films with no additional cost in the existing fabrication line. The devices' performance with nano-columnar structures in  $\text{Ge}_x\text{Se}_{1-x}$  ( $x = 0.2, 0.3, 0.4$ ) and  $\text{Ge}_x\text{Te}_{1-x}$  ( $x = 0.2, 0.5$ ) active films under six different deposition angles were studied. Also a novel, CMOS compatible method for formation of RCBM arrays was investigated that could be embedded into the current semiconductor processes. In addition to various device fabrication techniques, the materials and electrical characterization of the fabricated devices were also studied to demonstrate the improvement achieved with the proposed techniques.

## **Dissertation Organization**

The dissertation organization up is structured as following: Chapter 2 describes the background of columnar structures. Mask designing and device fabrication details are presented in Chapter 3. In Chapter 4, the results regarding the research conducted on PECVD deposited films and thermally evaporated obliquely deposited films are presented. Electrical testing of the fabricated devices is discussed in Chapter 5. A method for fabricating lithography free RCBM array and its electrical characterization is discussed in Chapter 6. The research summary and findings are presented in Chapter 7.

## CHAPTER TWO: THIN FILM GROWTH AND OBLIQUE ANGLE DEPOSITION

Nanotechnology is interdisciplinary by nature and precise control over the morphology, porosity, and crystal structure is essential to significantly improve the properties of the engineered nano-structures. Thin films in nano-world involve working with scales that lie in the range of 1-100nm. Phenomena occurring at nano-scales are of interest to many researchers, making it a frontier in materials science research.

Nano-columnar structures, achieved by oblique angle deposition technique, have been of interest for decades owing to enhancement of properties such as dichroism, birefringence, and anisotropic resistivity [67-69]. These nano-structures are porous in nature, which gives rise to interesting properties. Nano-columnar structures are believed to be an important building block for the assembly of integrated nano-electrical, nano-optical, and nano-mechanical systems [70]. Recently, nano-structures within the thin films are becoming increasingly important as their electrical, optical, and magnetic properties can be tuned for many promising applications, including nano-electronics [71], photonic crystal [72], nano-optics [73], gas sensors [74], and field emitters [75]. Apart from nano-structured applications, high porous nano-voids in thin film materials have fascinated many researchers in various fields due to their potential in applications, like multilayer dielectric structures [76, 77], optical micro-resonators [78], and optical interconnects [79].

In this work, the formation of nano-columnar structures in Ge-Se and Ge-Te thin films is investigated and applied to RCBM devices for improving their reliability. Inclined isolated nano-columnar structures were preferred in this work due to the inherent porous nature associated with this geometry. The symmetric nature of the pores helped the conductive filament within the device to grow in a directional manner.

The nano-columnar structures using oblique angle deposition was first demonstrated by Kundt [80] and later by others [81, 82]. Thin films nano-structure on rotating substrate was demonstrated by Robbie et al. [83] at extreme vapor incidence angles ( $\geq 10^\circ$  with respect to substrate normal) and it was termed glancing angle deposition (GLAD). Figure 2.1 presents structures produced by GLAD technique. Modern GLAD implementations use real-time feedback system aided with computer controlled programs to control the substrate angle.

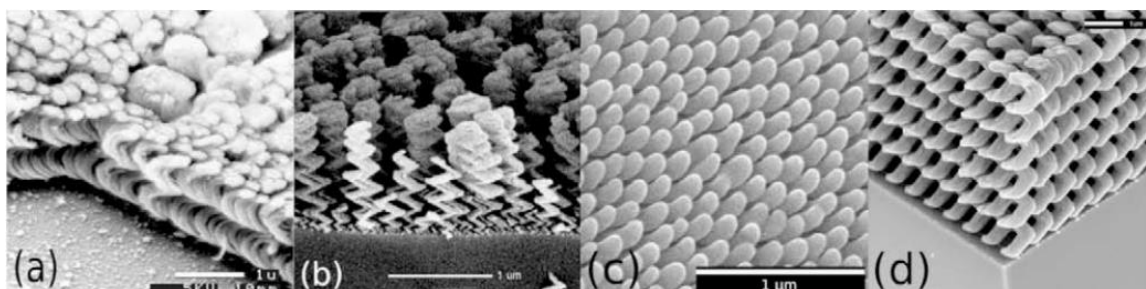


**Figure 2.1** SEM images showing improvement in structures by GLAD [84]

### Physical Structures of Thin Films

Thin film growth by Physical Vapor Deposition (PVD) technique is a non-equilibrium process due to high concentrations of impurity atoms and non-uniform substrates. Because of this, the number of extrinsic and intrinsic defects in thin films may exceed the defects found in the bulk material by a few orders of magnitude, signifying

that the deposited film consists of defect rich crystalline grains, separated by impurity enriched grain boundaries. For this reason, thin film properties differ significantly from bulk properties [85].

The real structure of thin film is determined by the following processes:

- a) *Shadowing*: A phenomenon arising from geometric constraint imposed by the roughness of the growing film and the line of sight impingement of the arriving atoms. This effect is dominant at low substrate temperatures ( $T_S$ ).
- b) *Surface diffusion*: It determines the mobility of adatoms or admolecules at the surfaces and interfaces of the deposit material. The surface diffusion phenomenon is dominant at medium,  $T_S$ .
- c) *Bulk diffusion*: It governs the mobility of adatoms or admolecules in the volume of grains, which is dominant at high,  $T_S$ .
- d) *Recrystallization*: Phase transition because of complete change of crystal orientation that is dominant at large film thickness, which is dominant at high  $T_S$ .

These properties result in a particular crystallographic orientation, relative to substrate, in the growing films. Different structural morphologies are exhibited by these processes as a function of the material melting temperature ( $T_M$ ) and the substrate temperature ( $T_S$ ). This is the basis of Structure Zone Models [86-88], which have been devised to characterize thin film and coating grain structures. Based on the  $T_S/T_M$  ratio, structures were classified as belonging to one of the three zones.

According to this model [86], for  $T_S/T_M < 0.3$ , the structures fall in zone 1, which are columnar in nature consisting of inverted cone like covers and separated by voided

boundaries that are several nanometers wide. These structures arise because of very limited adatom movement and shadowing effects. The surface of the films is quite rough for the films falling in this zone. For  $0.3 < T_S/T_M < 0.5$ , the structures are also columnar in nature with well-defined column boundaries, which are approximately 0.5nm wide. Surface or grain boundary diffusion plays a role in the evolution of this structure. The effect of shadowing decreases by greater adatom mobility, which results in dense films. As a result the adatoms spread more uniformly over the surface and the film surface becomes relatively smooth.  $T_S/T_M > 0.5$  falls in zone 3 where the bulk diffusion is the dominant factor owing to high temperatures. In this case, recrystallization can occur. The crystals are rather large and their boundaries are randomly oriented with respect to substrate resulting in a smooth surface in this zone.

In 1974, Thornton [87] extended the Structure Zone Model by defining a fourth zone, transition zone, T, between zone 1 and zone 2. This zone was characterized by the densely packed fibrous grains morphology. Compared to zone 1, the surface mobility is characterized with less shadowing effect, higher density and smoother surface. In this zone, the morphology is directly related to sputtering gas pressure and inversely to the energetic particles generated by bombardment. Movchan and Thornton models were developed for relatively thick films at higher deposition rates.

An improvement in the model was suggested by Messier et al. [88, 89] in 1984, for regions with  $T_S/T_M$  below 0.5, to accommodate both the evolution of morphology with decreasing the film thickness. Additionally, Grovenor et al. [90] investigated the influence of substrate morphology into consideration and examined the granular size for a

number of evaporated metals with thickness of 100 nm. Comparison of all models is presented in Figure 2.2.

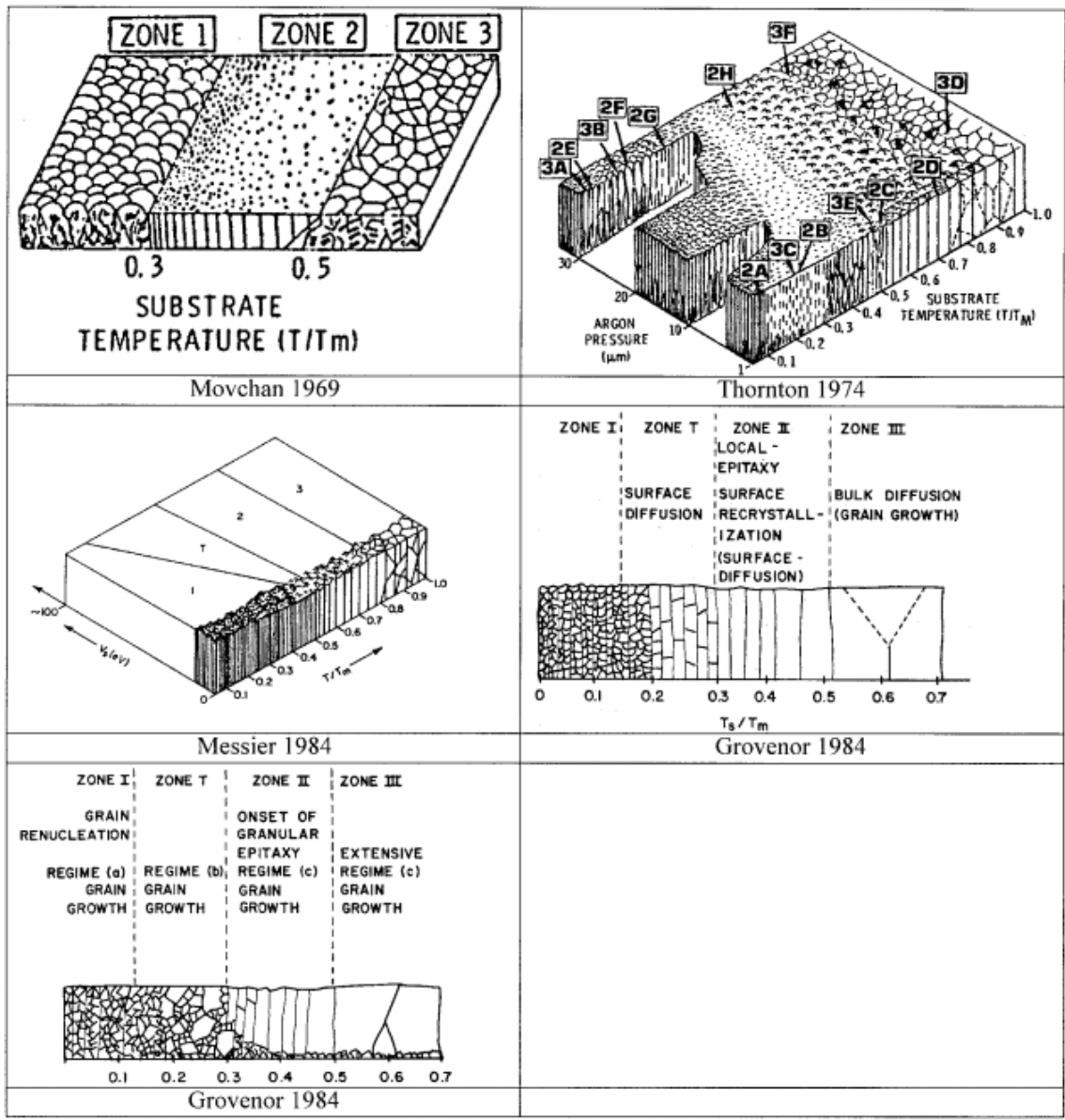
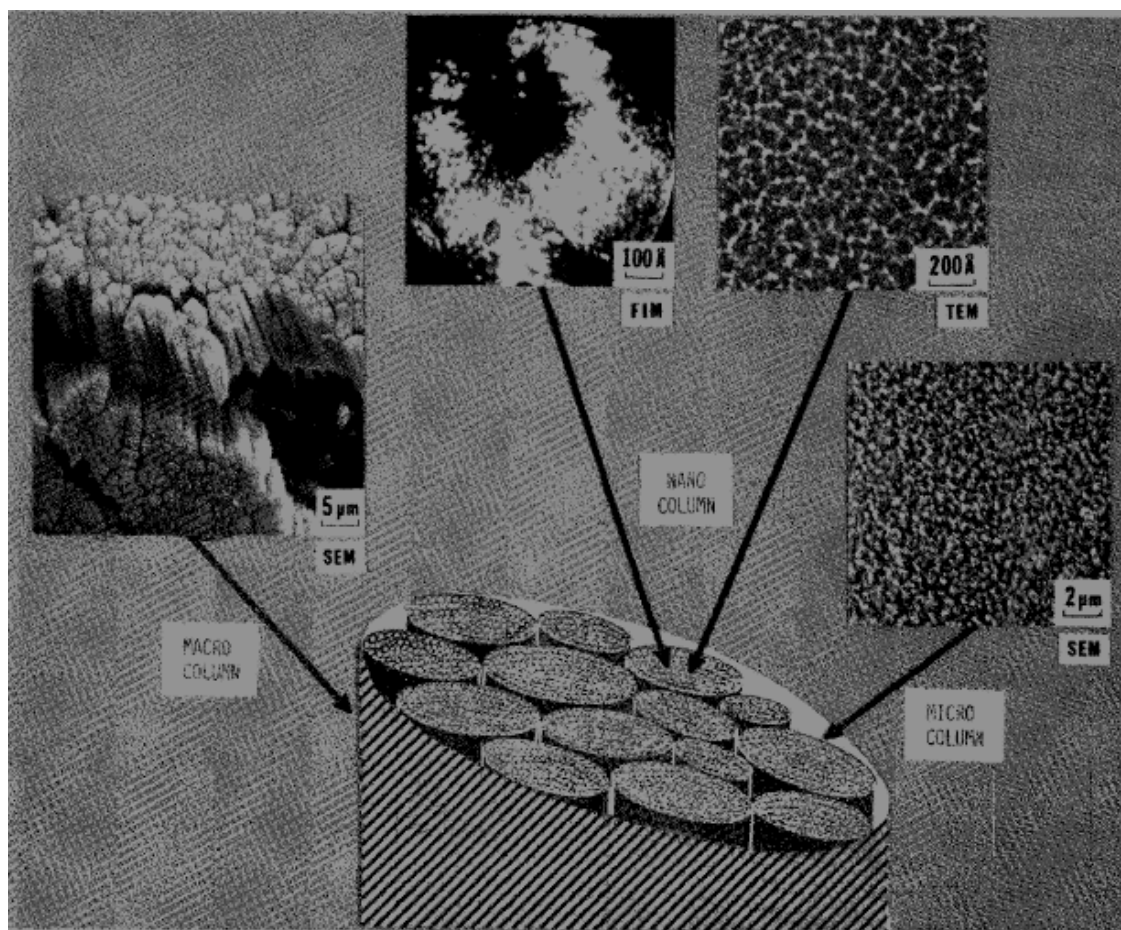


Figure 2.2 Evolution of Structure Zone Models [85]

Messier explained his findings with an evolutionary model of column growth in zone 1. According to his model, three general structural units were recognized; nano, micro, and macro columns and the associated nano, micro, and macro voids [91]. Figure

2.3 illustrates the schematic representation of these interrelated structural units along with representative micrographs of amorphous Ge (a-Ge) films. A given column is composed of smaller columns stacked together that are themselves composed of sub columns. The typical size of the columns ranged from 1 to 3nm for the thin films (15nm) and approximately 300nm for the thick films (10 $\mu$ m) [88]. Separate nano-columns are developed in thin films as the film growth continues. These columns cluster together, forming a larger column, which eventually bundles together to form an even larger column, leading to the structural hierarchy depicted in Figure 2.3.



**Figure 2.3** Evolutionary model for columnar thin film growth under low mobility conditions [91]

## Oblique Angle Deposition

Even though early work recognized that obliquely deposited thin films exhibit properties that are different to normally deposited thin films, it was not until 1966 that the morphology of these films was proven to be made up of columns [92] that were tilted and grown in the direction of the arriving vapor flux stream.

In obliquely deposited films, a flow of atoms or molecules (vapor flux) in a gas phase impinge on a substrate under some angle, which results in a columnar morphology of the deposited material because of shadowing. The angle of incidence controls the tilt of the columns and affects the degree of shadowing and thus the porosity of the film. A porous film consisting of isolated evenly spaced columns has already been demonstrated using an oblique angle technique [93]. If the substrate rotates around the substrate normal axis, the morphology of the film changes dramatically.

### Formation of Columnar Structures

Columnar growth is attributed to a seeding and self-shadowing mechanism at the substrate surface [94, 95]. In the initial stage of a normal vapor deposition process, the vapor adatoms condense on the substrate to form molecular islands. When the substrate is held at an oblique position, condensed molecular islands act as barriers for the subsequent vapor flux, preventing them from depositing on the shadowed areas of the surface [96]. In this manner, the molecular islands capture the vapor and continue to have tilted growth towards the incident vapor direction as illustrated in Figure 2.4, where  $\alpha$  is defined as the incident vapor angle of the material being deposited and  $\beta$  is angle under which the columnar profile grows (inclination angle). These definitions are elaborated in Figure 2.5.

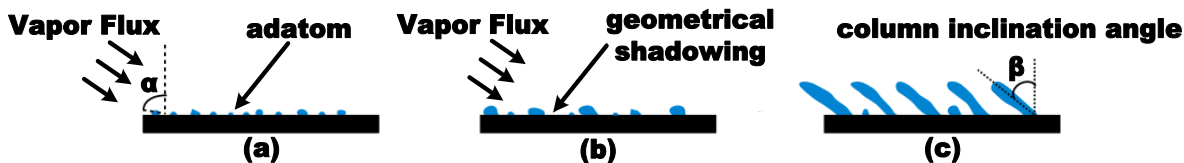


**Figure 2.4** Obliquely angle deposition a) adatom diffusion stage, b) growth stage, and c) nano-columnar structure

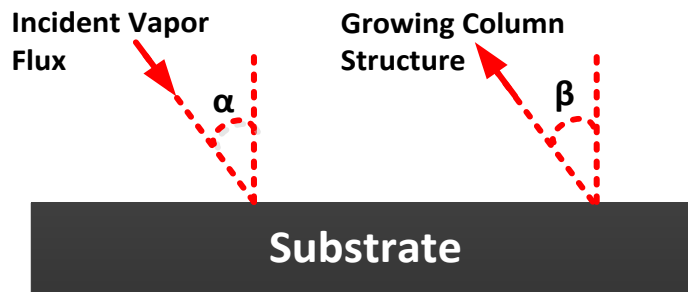


**Figure 2.5**  $\alpha$  and  $\beta$  definition for the columnar structure growth

Moreover, the self-shadowing effect together with limited adatom diffusion during film growth allows producing of anisotropic and porous thin films. The anisotropy and porosity are strongly dependent on vapor flux incidence angle, material, and deposition conditions. In the obliquely deposited films, the morphology of the columnar structure depends on the incident vapor flux angle, substrate rotational speed, and the growth rate. A wide variety of nano-engineered morphologies, with controlled porosity, such as inclined columns, vertical columns, zigzags, chevrons, C-shapes, S-shapes, helices, super helices, square spirals, etc. can be achieved by controlling these parameters [97-102]. Figure 2.6 illustrates a few of the nano-engineered structures produced by controlling the aforementioned parameters.

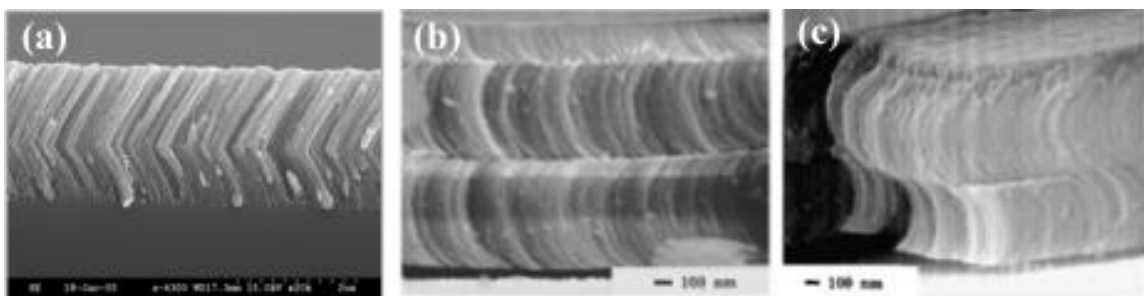


**Figure 2.6 Nano-Engineered morphologies formed by controlling different parameters (a) Zig Zag, (b) C-Shaped, and (c) S- Shaped [103]**

The thin film morphologies are evolved under conditions of shadowing dominated aggregation due to oblique incidence vapor flux and limited adatom diffusion on the substrate due to low substrate temperature ( $T_S/T_M < 0.3$ ), which favors zone 1 columnar growth, where a columnar morphology develops. In addition, the variations in the flux arrival angular distribution has to be considered as it affects the thin film growth. The extension of zone 1 structure to higher  $T_S/T_M$  ratios for high argon pressure, in the sputtering zone model proposed by Thornton, is a direct consequence of the increase in the angular distribution of the vapor flux due to randomizing collisions with the transport gas. More vapor flux arrives at an oblique angle, creating more atomic shadowing and resulting in a more porous film structure. A non-uniform and rough substrate surface will enhance the atomic shadowing with oblique incident flux resulting in more voided and porous film structures. An oblique deposition film on the stationary stage, shown in Figure 2.7, results in different shadowing characteristics parallel and perpendicular to the deposition plane, which results in structural morphology of the deposited films [104].

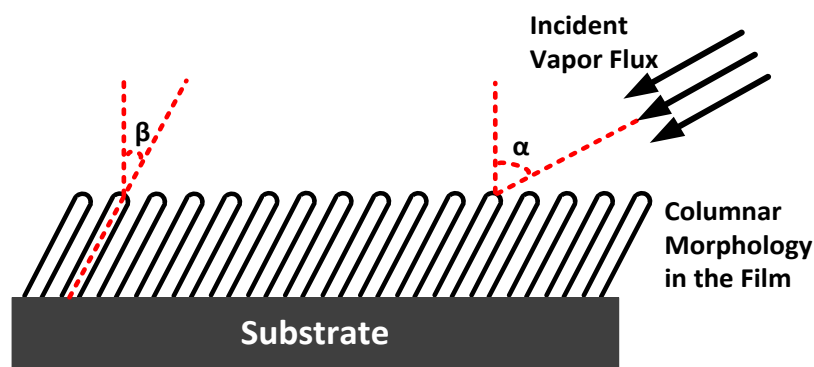


**Figure 2.7** Schematic representation of columnar growth by the arriving vapor flux ( $\alpha$  is the deposition Angles and  $\beta$  is the columnar growth angle)

### Columnar Structure Inclination and Shadowing Mechanism

If the film is deposited under the condition of limited adatom surface diffusion with the vapor flux arriving normal to the substrate (zone 1) columnar micro/nano structures are formed [105]. This is due to the atomic shadowing that dominates adatom diffusion. The principle of the shadowing mechanism is based on nucleation of the evaporated material on the substrate as the regions that are shadowed by random agglomerated nuclei or grains do not receive any additional vapor flux. The atomic shadowing mechanism is enhanced when the substrate is tilted in such a way such that incident vapor fluxes arrive at an oblique angle to the substrate normal. The film growth occurs on the faces of the domed column tops facing the vapor source, which results in the columnar structure characteristics for zone 1. In particular, at extremely oblique flux incidence angles, the resulting film is highly porous in nature and composed of isolated nano-columnar structure inclined toward the vapor source [106]. The shadowing mechanism and directional column growth is illustrated in Figure 2.8.

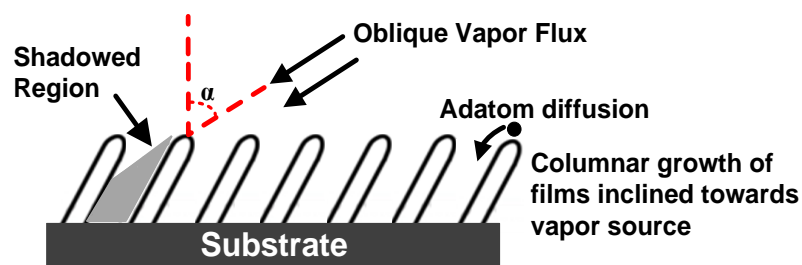


**Figure 2.8 Shadowing mechanism in columnar structure growth**

Ideally, shadowing effects can be enhanced by limiting adatom diffusion into the shadowed areas, which will lead to columnar film structures where the boundaries or voids between columns cannot receive vapor flux. The resulting film is normally composed of cylindrical shaped columns of material, separated by voids as shown in Figure 2.8. Such morphologies are difficult to achieve with standard deposition methods as the adatom nucleation will start to occur at all places on the substrate surface, resulting in amorphous structures. When the vapor flux arrives normal to the substrate, the flux distribution is symmetrical and anisotropic effects are produced by shadowing, whereas under oblique angle deposition, the vapor flux distribution at the surface is not symmetrical that results in asymmetry shadowing. A special control over the deposition rate is required to achieve such structures.

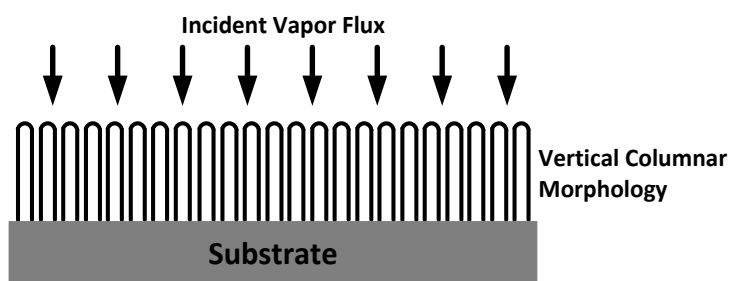


**Figure 2.9 Columnar structure schematic of the films deposited under normal incidence angle**

A main requirement for columnar growth is a collimated vapor source; the degree of collimation will determine the homogeneity in the diameter of the columns. Therefore, all methods for physical vapor deposition techniques are well suited for this type of process. The surface diffusion of the molecules over the substrate material also plays an important role in determining the growth parameters of column width, separation, and tilt. Hence, a low substrate temperature is required to be maintained to minimize surface diffusion arising due to thermal energy.

### Models for Column Structure Formation

There have been many studies that have tried to predict the geometry of the columns as well as the relationship between the vapor direction  $\alpha$  and the substrate tilting angle  $\beta$ . Relating orientation of columnar nano-structures to various deposition parameters was a primary focus of early research [107]. Simple geometry rules such as tangent and cosine laws do not apply to the obliquely deposited films. The relationship is believed to be based on a combination of factors, including the vapor directions, surface diffusion of the arriving vapor on the substrate, properties of the material being deposited, kinetic energy of the arriving vapor, and vacuum pressure [94]. Various attempts have been made to qualitatively and/or quantitatively explain the column tilt angle,  $\beta$ . An empirical rule, known as the Tangent Rule [108], was proposed that defines the relationship between  $\alpha$  and  $\beta$  as:

$$\tan\beta = \frac{1}{2} \tan\alpha \quad (2.1)$$

This relation was not derived by any basic principles but rather was found to correlate well with the experimental results. According to this rule, the columnar tilt angle,  $\beta$ , is less than the deposition angle,  $\alpha$ .

A ballistic model, known as Tait's Rule, for orientation of columnar growth was proposed to overcome the empirical Tangent Rule. The geometric analysis of this model was based on the fact that when being shadowed by a neighboring column, the exposed surface is not symmetric around the deposition axis. Rather, the mean direction of growth is inclined towards the substrate normal [109], resulting in the following expression:

$$\beta = \alpha - \sin^{-1} \left( \frac{1 - \cos \alpha}{2} \right) \quad (2.2)$$

Another model developed by Lichter-Chen for relating the tilted columnar structures and the deposition angle was derived by using a continuum model approach as [110]:

$$\tan \beta = \frac{2}{3} \frac{\tan \alpha}{(1 + \emptyset \tan \alpha \sin \alpha)} \quad (2.3)$$

where  $\emptyset$  depends on diffusivity and deposition rate.

The expressions, equation 2.1 to equation 2.3, are plotted in Figure 2.10 for comparison (with  $\emptyset=0.2$  for experimental conditions). A fitting parameter  $E$  was defined to generalize the tangent rule [111]

$$\tan \beta = E \tan \alpha \quad (2.4)$$

Due to the sensitivity of the columnar structure on deposition conditions and material dependent properties, all materials behave differently and accurate predictions are difficult. However, experimental results tend to follow the trends predicted by these equations [109].

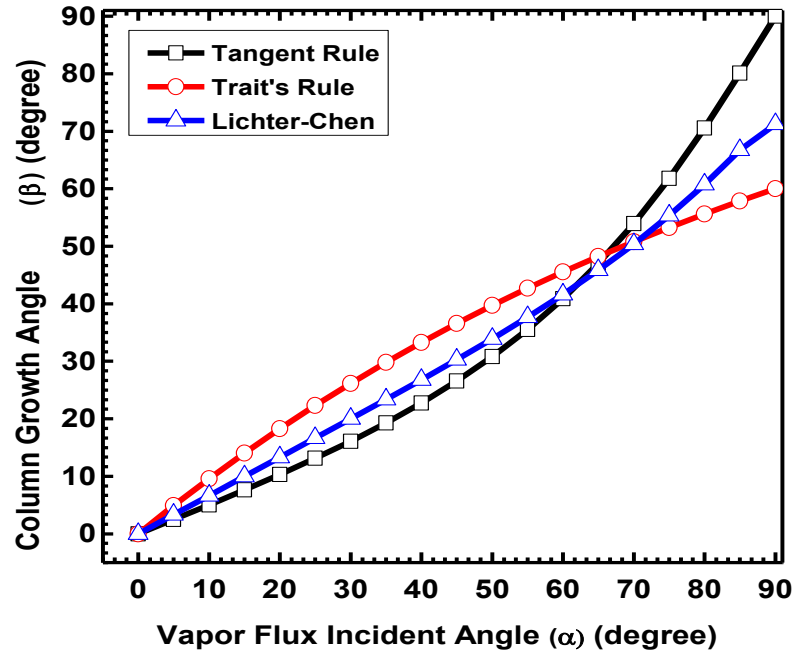


**Figure 2.10** Variation of column angle  $\beta$  with deposition angle  $\alpha$ , obtained from the Tangent, Tait's and Lichter-Chen's expression

### Films Density

The nano-columnar structures in thin films cause film porosity and, therefore, degrade stability against environmental influence [112]. The density of films with columnar morphologies, expressed in terms of  $\rho_0$  at  $\alpha=0$ , is defined as:

$$\rho = \rho_0 \frac{2 \cos \alpha}{1 + \cos \alpha} \quad (2.5)$$

Column density decreases with film density [113] and is closely related to column width [114]. Increasing the substrate temperature results in decreasing the columnar density [115] that also varies with film thickness, deposition angle and material, and must be evaluated for any given application [116].

### **Application of Nano-Columnar Structure in RCBM**

While oblique angle deposition technique implications have been employed for various applications over the years, the dominant use of this technique has been in optics applications as it provides a unique ability to produce an engineered index grading with the same material in a one-step deposition process.

The exciting application of obliquely deposited films is extended to RCBM technology, in this work. Many studies have suggested RRAM to be one of the promising candidates for future studies because of its brilliant features such as non-volatility [117], simple structure [118, 119], and high speed response [120, 121]. However, the poor reproducibility of switching voltages constricts the practical use of these devices [122, 123]. The variation of switching voltage is thought to happen owing to random filament growth and multi-branching causing deviation in resistivity [124, 125]. Naturally question arises, how can the variations in switching voltage be reduced/controlled? On the basis of filament growth mechanism, the diminishment in multiple filament growth or multi branches within the same filament would be an effective way for improving the reproducibility of the switching voltage. As presented in Figure 2.11a, in reality, the conductive filaments are formed with many branches as they approach the bottom electrode where they seem to have wide spread distribution. However, if nano-channels (nano-columnar structures) are created within the device active layer having an opening width comparable to the filament size, it becomes an ideal scenario where only one filament is permitted to grow through each opening as illustrated in Figure 2.11b. Such a structure will remove/reduce multi-branching within the filament as well as the bottom of the electrode, therefore, allowing uniformity in the switching voltage. This provides a

novel way to increase the reliability of the RRAM devices, without involving any increase in the devices' fabrication cost.

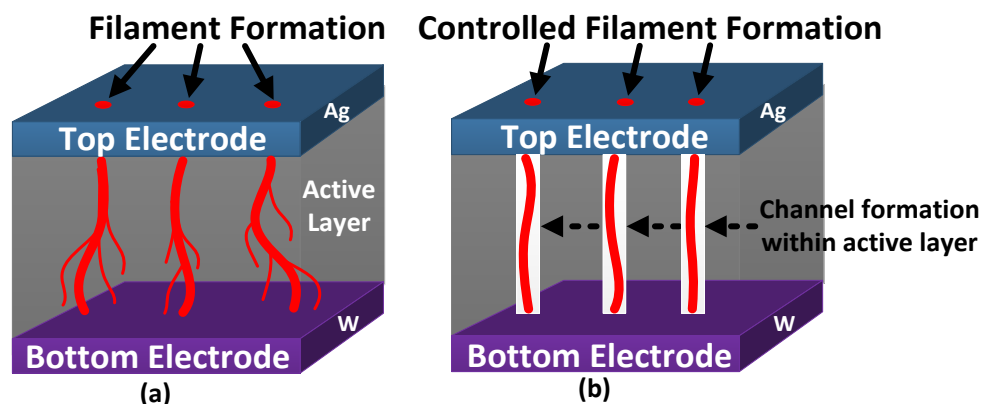


**Figure 2.11** Schematic of (a) Real filament growth and (b) Ideal filament growth by providing pathways for its growth

The nature of a RCBM cell is characterized by its randomness due to the cation-based electrochemical process. As the device operation involves chemical reaction and movement of ions for filament formation, it causes randomness in the device performance at the atomic scale. The experimental details regarding the deposition of planar Ge-S active film with the aid of PECVD and formation of Ge-Se columnar structure within the devices' active film to counter these problems are discussed in the following chapters, preceded by the mask designing and process flow for the devices' fabrication.

### CHAPTER THREE: MASK DESIGNING AND DEVICE FABRICATION

Optical microlithography, a process similar to photographic printing, is used to transfer circuit patterns onto the silicon wafers, which forms a critical step in integrated circuits fabrication [126]. The schematic for transferring the pattern to silicon wafers is illustrated in Figure 3.1.

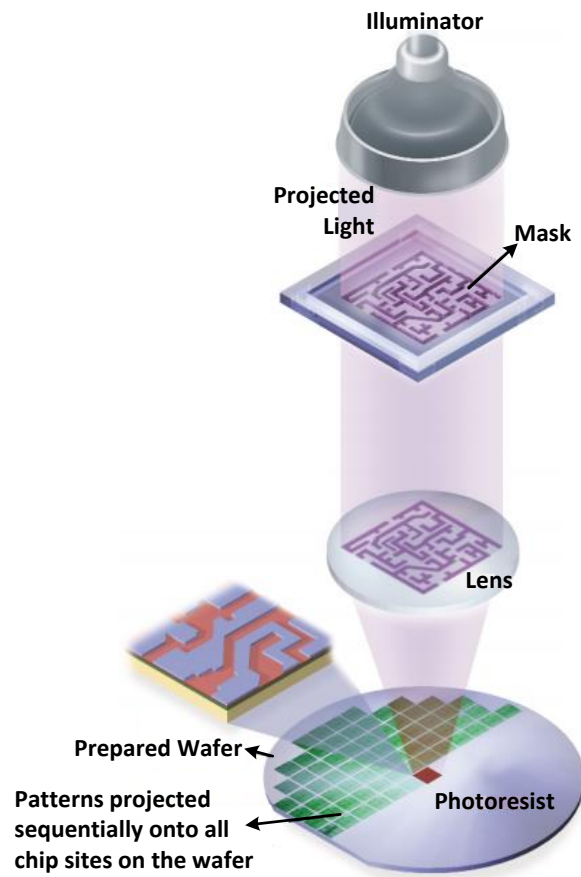


**Figure 3.1** Optical lithography process [127]

The pattern to be replicated on the wafer is carved on a reticle (mask or photo-mask), which is composed of quartz with a layer of chrome. Clear quartz areas allow light to pass while chrome regions block the light. A two or three dimensional layout of the entire fabrication process for an integrated process is outlined on the mask. A UV source (illuminator) shines light through the mask, producing an image of the pattern onto a photoresist coated wafer using a projection system. The photoresist, being chemically sensitive to light, acts as the recording medium for the above imaging system. The photoresist, upon interaction with UV light, undergoes a bleaching action that results in breaking or formation of new chemical bonds in the exposed region, depending on the usage of either a positive photo resist or a negative photoresist, thereby changing the dissolution properties. The photoresist is finally developed, leaving behind a replicated pattern of the reticle onto the wafer.

### **Design of a Multilayered Mask**

The mask is an important component that is used in the semiconductor fabrication process. The application of the photolithography technology allows plotting of fine patterns on the wafer, which are not possible by mechanical means. The device critical dimensions are miniaturizing on integrated circuits, which is putting stringent requirements on the photolithography process, primarily the mask design. This results in a large financial and design pressure on mask designing and device fabrication engineers [128].

In the silicon fabrication industry, one mask is generally used for patterning each layer such as Poly, Metal1, or Contact. The design and creation of the mask for each step requires significant amount of time and cost when compared to the cost of a single silicon

wafer. In this research work, the mask cost is reduced by designing a special multilayered mask structure (also referred to as a 3-in-1 mask in this dissertation). The downside of using a single mask for fabricating RCBM devices is that it limits the number of fabricated devices per chip. However, for small-scale fabrication, reducing the cost of the mask by 1/3 outweighs the downside of the number of fabricated devices.

The mask was designed using the Electric VLSI Design System, version 8.11. Electric VLSI Design System is a power CAD system for designing layouts. The individual layer layout of the 3-in-1 mask is shown in Figure 3.2. Open windows within the mask were designed to aid the alignment of the respective layers.

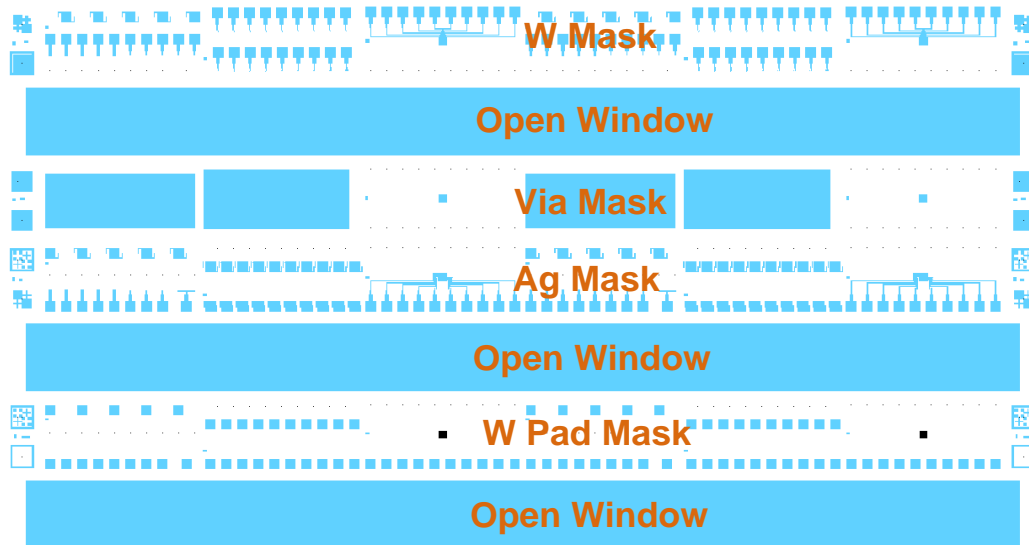


**Figure 3.2 Individual layers layout of the multilayered mask**

The procedure for using the 3-in-1 mask is outlined below and pictorial illustration of the outlined steps are presented in Figure 3.3.

- a. Pattern the **Via Mask Layer** onto the wafer.

- b. Align the **Ag Mask Layer** on the mask to the **Via Mask Layer** on the wafer and pattern the Ag Mask Layer.
- c. Align the **W Pad Layer** on the mask to the combined **Via/Ag Mask Layer** on the wafer and pattern the W Pad Layer.

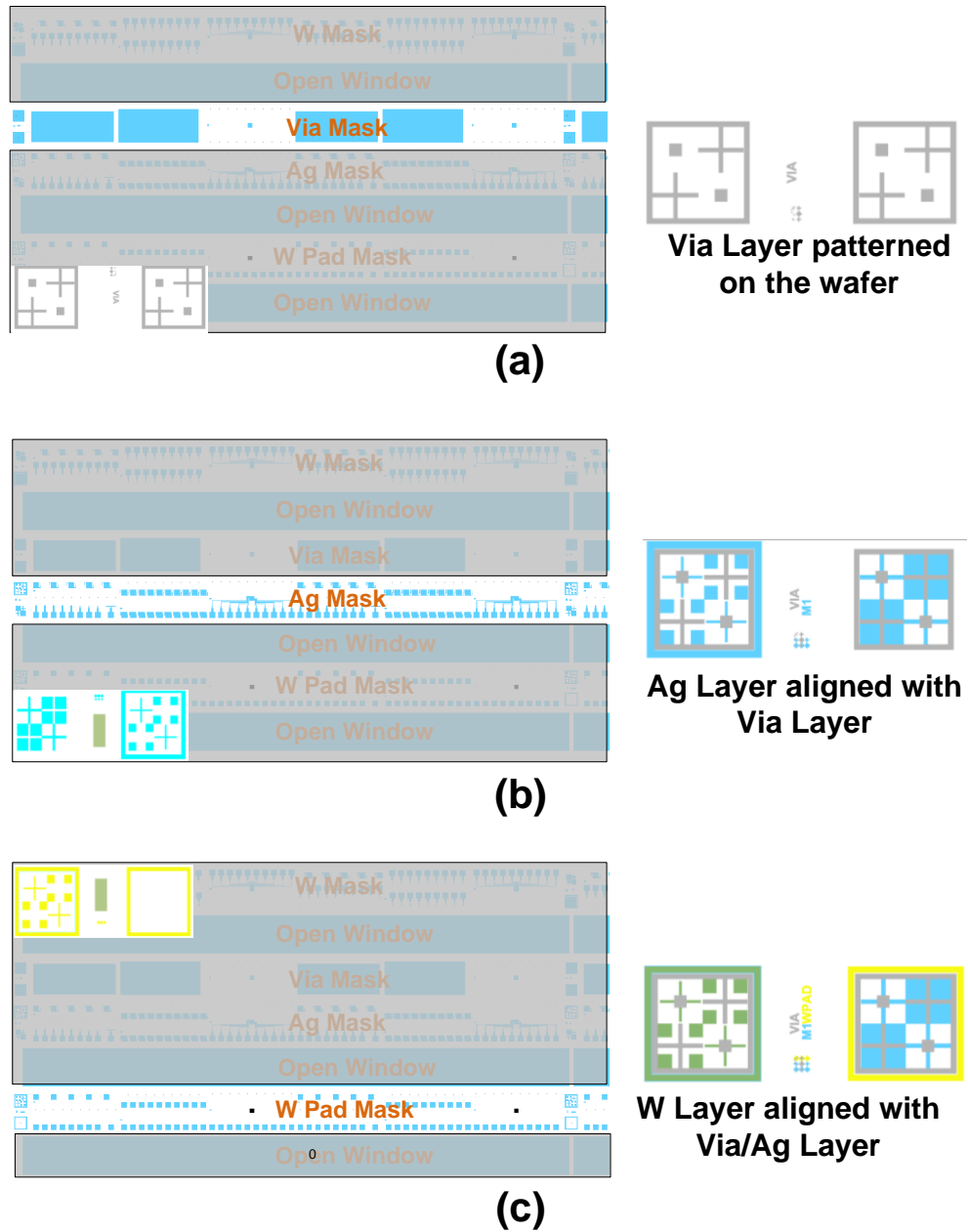


**Figure 3.3** Steps for using 3-in-1 mask (a) Patterning of Via layer, (b) Aligning Vias to Ag layer, and (c) Aligning W layer to Via/Ag layer

The mask was designed with multiple vias dimensions that could be patterned using a single step. This allowed the flexibility to establish the device performance as a function of via size. Final layout of the devices created by using the 3-in-1 mask is presented in Figure 3.4 with via, metal 1 and metal 2 shown in gray, magenta, and green, respectively. In addition, the alignment markers after all three alignment steps are shown on the left of the device layout in Figure 3.4.

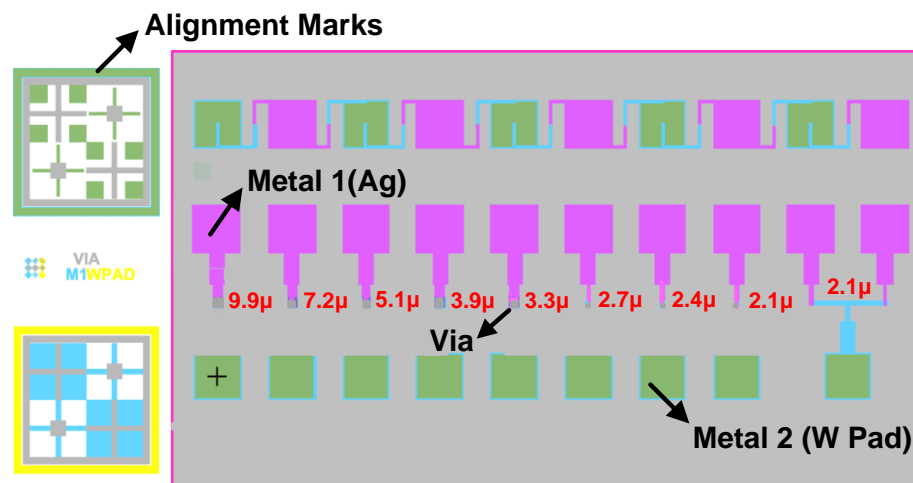


**Figure 3.4** 3 Layer layout of 3-in-1 mask

Running more layers on a single mask in a similar manner will nearly double the area for each new layer, consequently quickly making the scheme impractical. However, a full process flow can be divided into few steps like this scheme, saving researchers money with the non-production device fabrication experiments.

### Device Fabrication Using Multilayered Mask

The following section describes the fabrication processes for different layers related to the RCBM metal insulator metal structure. The RCBM cells with multiple via

dimensions were fabricated by the 3-in-1 mask using optical lithography. The studied active layer within RCBM vias were deposited by:

- I. PECVD method
- II. Thermally Evaporated method with
  - a. Normally deposited films
  - b. Obliquely deposited films

### **Process Flow for Development of RCBM Devices**

A CMOS compatible process flow was developed to fabricate the vertical devices using optical lithography, as presented in Figure 3.5. This process flow was developed such that the deposited ChG active layer does not come in direct contact with basic nature of the solutions, which are used in conventional lithography, since the ChG films are soluble in such solutions. Devices fabricated by means of optical lithography involve three steps:

- I. Formation of Via (Via Mask) and deposition of active layer (Figure 3.5a-d)
- II. Formation of Anode (Metal 1 Mask) (Figure 3.5e-h)
- III. Formation of Cathode (Metal 2 Mask) (Figure 3.5i-k)

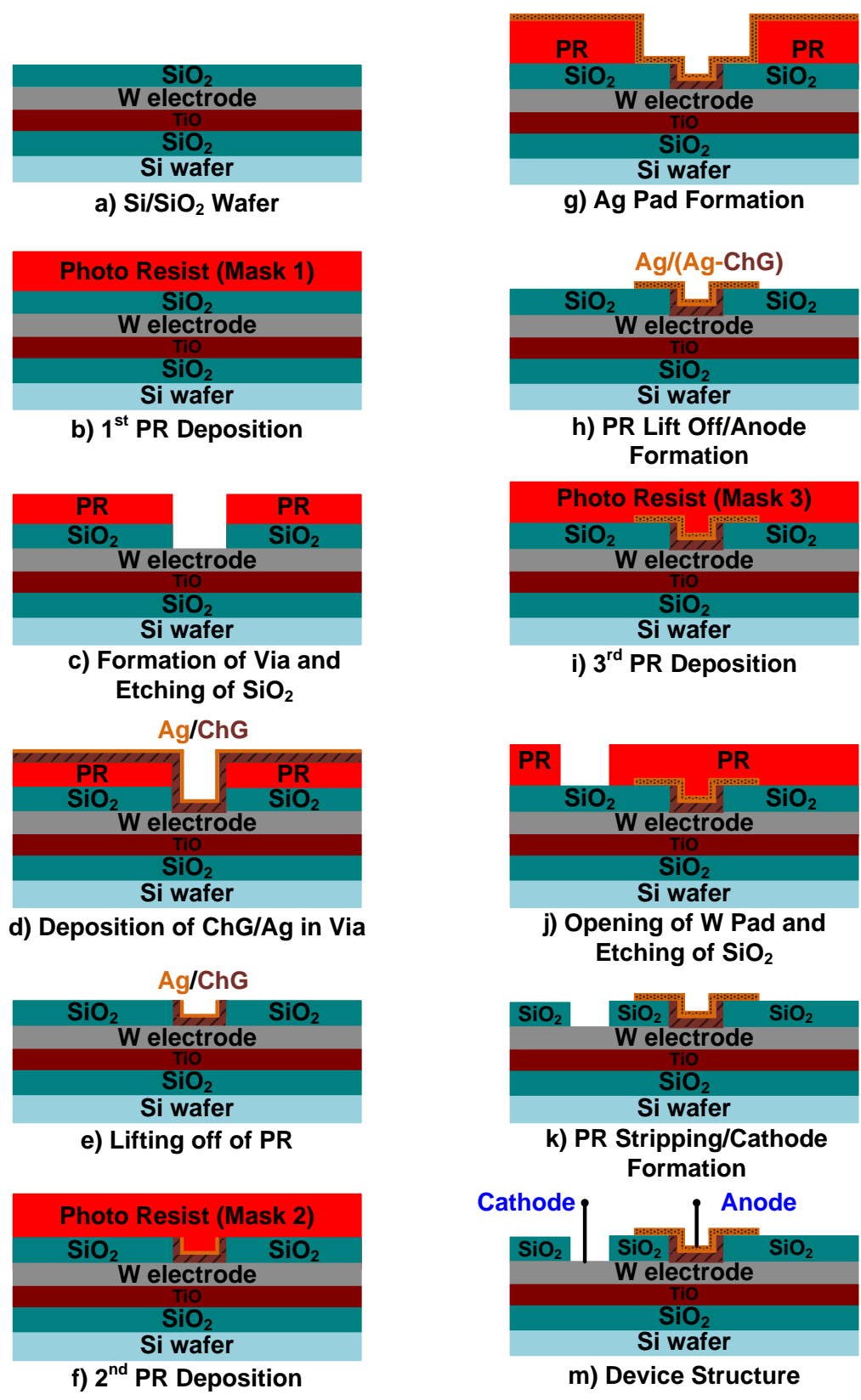


Figure 3.5 Process flow for fabrication of RCBM devices

The multilayered structure of the RCBM is evident from the process flow, consisting of the bottom (inert) electrode, active material and top (oxidizable) electrode. Individual devices are separated by Silicon Dioxide ( $\text{SiO}_2$ ) dielectric layer. Silver photo-diffusion process was used to form the solid electrolyte, which increases the ionic conductivity of the ChG film for the devices created using the PECVD deposition process. The dynamics of silver diffusion in the ChG matrix was studied and analyzed using neutron Reflectometry. The photo-diffusion step was eliminated for column structured devices since the nano-engineered column structures provide the pathways for the metallic filament to grow.

### **Fabrication of RCBM Devices**

The final structure of the RCBM device is presented in Figure 3.5m. The width of the via in  $\text{SiO}_2$  dielectric layer separating the top and bottom electrodes define the device active area and is referred to as device size. RCBM devices were prepared at the Idaho Micro Fabrication Lab (IML) at Boise State University. The details regarding the device formation steps for fabricating the devices are elucidated below.

#### Surface Cleaning

Si wafer cleaning is critically important in the era of VLSI and ULSI nano-technology. Over 50% of yield losses in integrated circuit fabrication are generally accepted to be due to micro-contamination [129], such as metal contamination, organic contamination, ionic contamination, etc. Si wafers were treated with an ammonium peroxide mixture (APM), which is composed of  $\text{H}_2\text{O}_2$  and  $\text{NH}_4\text{OH}$  ( $\text{H}_2\text{O}_2\text{-NH}_4\text{OH-H}_2\text{O} = 1:1:5$ ) to remove the organic residues. The wafers were rinsed thoroughly with DI (de-

ionized) water. The oxide formed during the APM processing was removed by drenching the wafer into a diluted HF solution (HF-H<sub>2</sub>O = 1:30). The wafers were cleaned by DI water again to neutralize the reaction. The removal of native SiO<sub>2</sub> was verified using the hydrophobic property of Si [130] as no water deposits were observed on the wafer top surface.

### Substrate Preparation

The devices were prepared on Silicon (Si) substrate having a thickness of 380μm and a diameter of 4” with <100> orientation. The Si wafers were Boron doped (p-type) with single side polished. Since the Si wafers have a resistivity of  $1^{-10} \frac{\Omega}{cm^2}$ , which is significantly small, therefore, to isolate the devices from the Si substrate, a 200-300nm SiO<sub>2</sub> layer was thermally grown on top of the substrate with a standard oxide furnace at 1100 °C for 20 minutes. A 30nm thick film of Titanium Oxide (TiO) was used as an adhesion promoter and diffusion barrier, followed by a deposition of 100nm of Tungsten (W) film that was used as the inert electrode for the devices. The individual devices were separated by a sputtered 100nm of SiO<sub>2</sub> dielectric layer that also served as an encapsulation of the device. The cross-sectional schematic of the base wafer is shown in Figure 3.5a.

### Sputtering System

Sputtering is used in micro fabrication processes to deposit a variety of metal and metal alloys [131]. The inert electrode, W and top SiO<sub>2</sub> layer for encapsulating the devices were deposited by AJA Orion 5 Sputter Machine (Model No.: ATC ORION 5 Sputtering System). The sputtered material was deposited at a pressure of  $6 \times 10^{-6}$  mbar. A

DC input power of 200W was utilized for W deposition with a rate of 1.20 Å/second. The material transported was unidirectional and isotropic due to the larger diameter (2 inch) of the target and the small distance between the target and the sample. This effect was also strengthened by comparably high working pressure, resulting in a high collision rate of the sputtered material. The W electrode deposition was followed by sputtering a 100nm of SiO<sub>2</sub>, having a deposition rate of 0.66 Å/seconds, using a RF source to avoid any charge build up on the target during film growth. Both films were deposited without breaking the vacuum to prevent the introduction of interlayer contaminants. The deposition conditions were programmed using the AJA International Phase II J Computer control built-in software.

### Optical Lithography

The optical lithography procedure was repeated three times to complete the RCBM devices fabrication as shown in the process flow (Figure 3.5b to Figure 3.5k). The application of the 1<sup>st</sup> lithography step formed the openings, which are the future location of the device via. Anode contacts were made during the second lithography step, while the last lithography step created the openings to the underlying W layer.

Figure 3.6 illustrates the procedure for the performing the lithography steps. About 3-4ml of Hexamethyldisilazane (HMDS), an adhesion promoter, was applied to one quarter of the wafer. The HMDS was spun with a Headway Spin Coater (Model: PWM 32-PS-R 790) at 5000 rpm for 35 seconds followed by the application of 2-3ml of positive photoresist (SPR-220), which was then spun at 6000 rpm for 35 seconds. The photoresist coated wafers was baked at 115°C for 90 seconds to drive off excess moisture in the photoresist, which is called the pre-baking process. The contact

aligner, equipped with high intensity UV light ( $22\text{mW}/\text{cm}^2$ ), was used to transfer the 3-in-1 mask patterns onto the photoresist coated wafer. The exposed wafer was then developed in a MF-26A developer for 40 seconds followed by a post-baking step for 90 seconds to solidify the remaining photoresist for wet chemical etching.

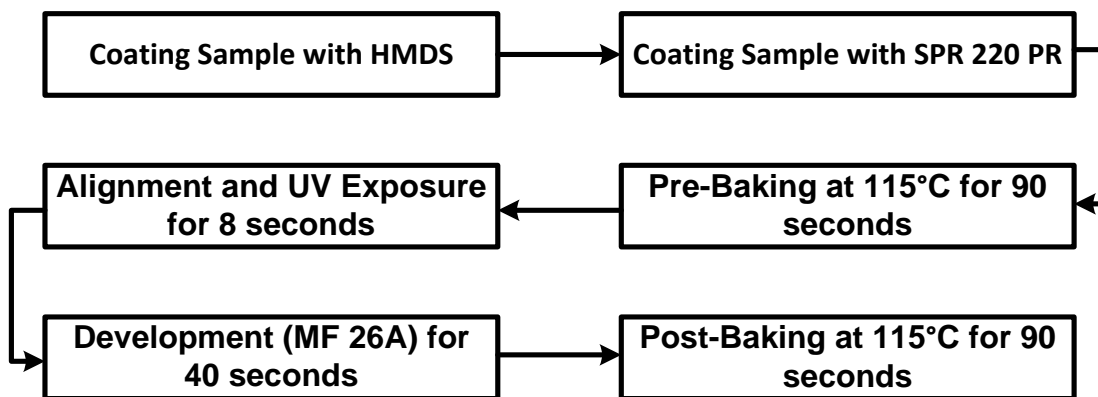


**Figure 3.6** Flow Chart for photolithography process

### Etching Process

The wet etch process was preferred due to its simplicity and time efficiency over the dry etching method. The oxide in the vias was etched using 20:1 Buffered Oxide Etch (BOE) at a rate of  $8 \text{ \AA}/\text{second}$  for 2 minutes. BOE is a mixture of Ammonium Fluoride and Hydrofluoric Acid and performs a very selective etch. The etched vias opening under the optical microscope are presented in Figure 3.7. To ensure that the wet etch process was not causing any undercutting in the oxide layer, SEM analysis was performed by cleaving and studying the cross-section of the etched via. The cleaved sample was sputtered with Pt to have a good contrast and the results are presented in Figure 3.8, with no significant undercutting in the vias. The side walls of the photoresist seem to be rough, which might be due to the long exposure ( $\sim 2$  minutes) of the sample in the BOE solution.

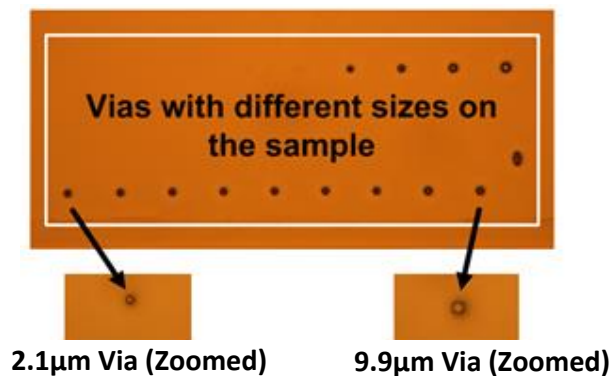


**Figure 3.7** Top view of the vias under the optical microscope

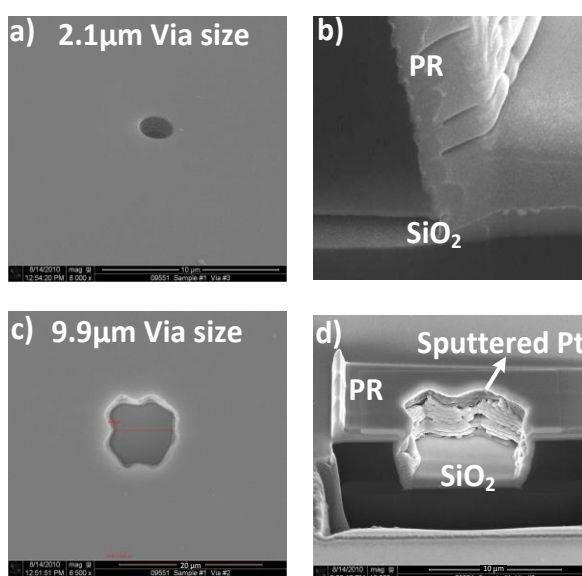


**Figure 3.8** SEM images of the vias (a) Top view of 2.1µm via, (b) Cross-sectional image of the 2.1µm, (c) Top view of 9.9µm via, and (d) Cross-sectional image of the 9.9µm via

### Deposition of Active Layer

The active layer of the film was deposited by both the PECVD and thermal evaporation methods. For PECVD deposition, the reactor was equipped with a vapor drawn precursor delivery system and a RF plasma network, while the Cressington 308R Vacuum System was used for thermally evaporated films. Details about the deposition systems are explained later in this chapter along with the complete device structure.

### Lift-Off Process

Lift-off is a conventional technique to pattern metal or dielectric films in the  $\mu\text{m}$  or sub- $\mu\text{m}$  range. Etching the vias and deposition of the chalcogenide film was followed by the lift-off process using a 1165 micro-stripper. The micro-stripper solution was heated to  $65^\circ\text{C}$  for lift-off purposes. The sample was dipped in the solution for 2 minutes, with continuous stirring to avoid photo resist re-deposition.

### Formation of Anode Contact

The lift-off process was followed by the 2<sup>nd</sup> lithographic step using the Ag mask to form the Ag contact to the vias. The Ag contact was patterned by aligning the via alignment mark on the sample to the alignment mark on the mask with great care since any misalignment would result in the contact pad not overlapping with the appropriate via forming a non-functional device. The Ag contact pad on top of the via, under the optical microscope, is shown in Figure 3.9.

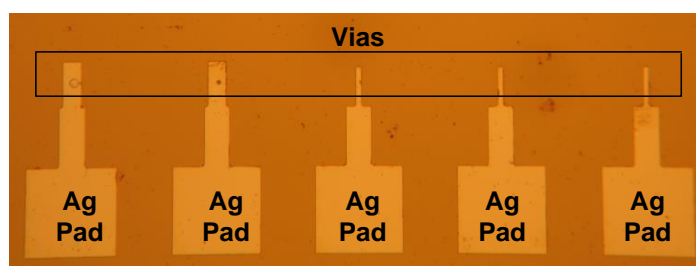


**Figure 3.9** Silver pad formation on top of vias

### Formation of Cathode Contact

The Ag contact step was completed by lifting off the extra Ag from unwanted regions of the wafer by using a 1165 micro-stripper. The lift-off step was followed by the 3<sup>rd</sup> lithography step to form the W pads by aligning the W alignment mark on the mask to

anode alignment marks on the sample. Formation of the W pad, Figure 3.10, was completed by etching the SiO<sub>2</sub> layer with the wet etch method.



**Figure 3.10** W pad formation top view on the sample

The complete structure of the fabricated devices, with the process flow as presented in Figure 3.5, is shown in Figure 3.11. The electrical performance of the devices was tested by probing the Ag and W electrodes with correct biasing.

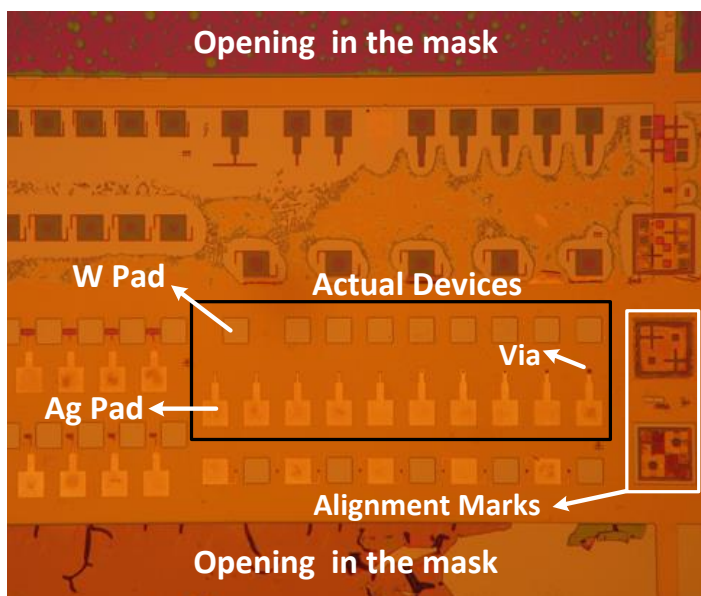


**Figure 3.11** Vertical device structures after lithography steps

### PECVD Devices

Smooth film, with the PECVD technique, was obtained at deposition temperature of 120°C and pressure of 0.2-0.3 torr within the reaction chamber. This condition however, contradicts some of the requirements for photolithography, since the

conventional photoresist is stable up to 115°C. Because of this, the lift off procedure for creating vertical devices with PECVD deposited  $\text{Ge}_x\text{S}_{1-x}$  film was not successful. The reason for this is unclear but it is believed that there are two underlying causes for this behavior. One cause is that the photoresist reacts with sulfur radicals in the PECVD environment causing it to be non-reactive to the micro-stripper solution. During the photoresist lift off process, the bonds within the resist need to be broken to make the photoresist soluble in the solvent. Another cause for the lack of efficiency of the lift off process is that in the PECVD process a slight increase in molecular weight of the resist may make it completely insoluble in the applied solvents. This can be due to the thermal cross-linking of the photoresist molecules in case the reactor temperature is too high or the chemical reactions in the reactor are causing the molecular weight to increase.

To demonstrate the applicability of the PECVD technique for fabricating RRAM devices, a lateral device structure was created and the devices exhibited the characteristic switching behavior of the RCBM. Ag was deposited using shadow mask on a stack of Ge-S/ $\text{SiO}_2$ /Si followed by thermal evaporation of Aluminum (Al) to form the inert electrode. The lateral device structure is presented in Figure 3.12.

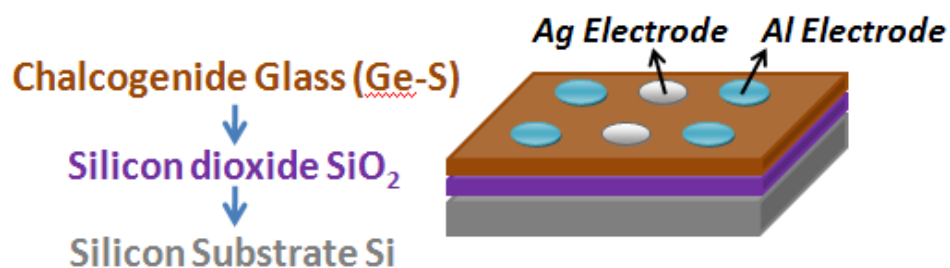


**Figure 3.12** Lateral device structure

### **Thermally Evaporated Devices**

Only lateral RCBM devices could be created by the PECVD method, whereas the advantage of using RCBM cells exists in the creation of nano-scaled devices.

Demonstration of a vertical RCBM device is more advantageous for nano-scaled devices and these types of devices were successfully fabricated using the thermal evaporation technique. The benefits for controlling the composition of the active material using PECVD can also be achieved using thermal evaporation, but not in a dynamic manner. Normal deposition of the active material hinders the ability to control the filament growth; therefore, the conductive filament can grow in different direction and vary the device performance. The active layer with planar and columnar structures were created using the Cressington 308R Vacuum System, which allowed the wafer stage to be rotated  $360^\circ$  around its axis, and enabled a wide range of angular depositions.

### Normally Deposited Films

The devices, called Generation 1 (Gen. 1) devices, were initially fabricated at normal deposition angle with the process flow presented in Appendix A. The difference in the Generation 1 and Generation 2 (Gen. 2) devices (fabricated with process flow presented in Figure 3.5) can be observed in the 2<sup>nd</sup> lithography step. For Gen 1. devices, the active material and Ag pad were created in one lithography step so that the entire area under the Ag pad and within the vias formed the solid electrolyte with photo diffused Ag in ChG glass [132, 133]. Ag diffusion into the chalcogenide film is unique since silver diffusion profile resembles a step-like concentration change.

The diffusion front is thought to progress continuously under light till it reaches the saturation point or the silver source is exhausted. The optical arrangement used to

collimate the beam and formation of solid electrolyte is shown in Figure 3.13. A UV lamp having an intensity of  $1.5\text{W}/\text{cm}^2$  is used for the photo diffusion step. Photo diffusion was preferred over thermal diffusion as saturation of Ag within the chalcogenide matrix could be achieved much faster [134].

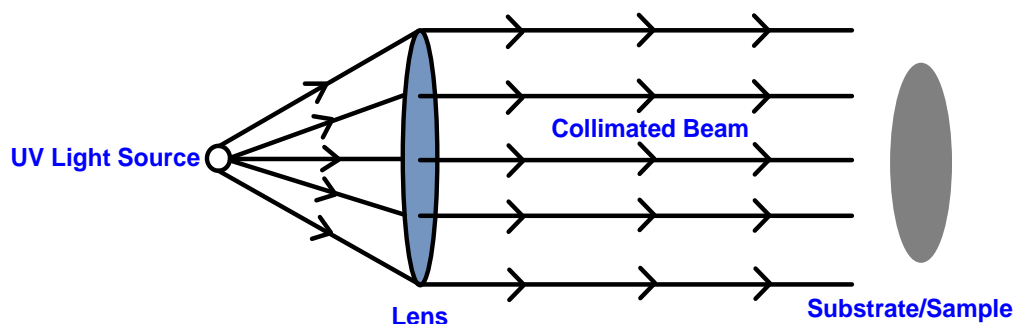


**Figure 3.13** Optical schematic used to collimate beam

Electrical characterization of these devices, presented in Chapter 5, resulted in unreliable device performance due to the unwanted distribution of the electric field within the device solid electrolyte layer. Due to this problem, an improvement in the process was investigated, as presented in Figure 3.5. Larger areas of the solid electrolyte film will result in larger distribution of the electric field, but the location where the electric field directly affects the device performance is situated within the vias. Therefore, it is desirable to confine the electric field within the via only. Since the filament growth is based on the movement of Ag ions under the influence of the applied electric field, it is necessary to control the electric field. In Gen. 2 devices, the formation of nano-columnar structure is limited to the device active area, which allowed the movement of Ag ions only through the vias and hence the effective area of the electric field was controlled. To validate the effectiveness of the Gen. 2 devices compared to the Gen. 1 devices, simulations were performed using COMSOL multi-physics software. This software uses

the Poisson equations to calculate the electrical voltage, electric fields, and electrical energy density at various locations in a given geometry.

### Improvement in Device Structure and COMSOL Simulation

Application of the Poisson equations require some user defined inputs, which are the device geometries, electric potential applied to the electrodes, and the permittivity of the material. Devices geometry and spacing of the electrodes determines the distribution of the electric fields and electrical energy density. These two variables can be used to manipulate the field distribution, which is crucial to ensure a consistent device performance. The geometries used for COMSOL simulations correspond to Gen. 1 and Gen. 2 devices process flow are presented in Figure 3.14. The geometry thicknesses are analogous to the films and the vias thickness used for the devices fabrication.

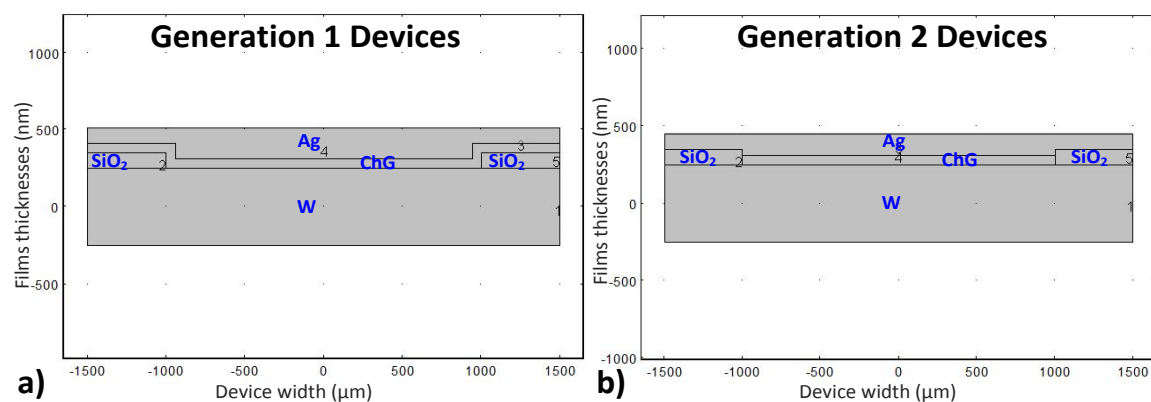


**Figure 3.14** Geometry used for COMSOL simulations corresponding to (a) Gen. 1 and (b) Gen. 2 devices process flow

Proper electrode biasing is extremely important for the conductive filament to grow. The geometries presented in Figure 3.14 are simulated by applying a +1V on the Ag electrode and grounding the W electrode. The simulations were performed with relative permittivity value of 6.98, which corresponds to  $\text{Ge}_{20}\text{Se}_{80}$  bulk glass composition

[135], providing a quantitative comparison of the ability to store charge in a material relative to air [136]. A number of studies have been performed enumerating the relative permittivity of bulk chalcogenide glasses [135]. Since the thin films are made from bulk glasses, an assumption of permittivity value correlating to the bulk glasses can be made, as using a different value of relative permittivity will only affect the quantitative values of the electric field, not the location [137]. So the slight alterations in the permittivity values can be tolerated.

Simulation outputs are plotted in Figure 3.15, which illustrate electric potential (Figure 3.15a-b), electric field (Figure 3.15c-d), and electric energy density (Figure 3.15 e-f) distributions within the device. Electric potential shows the distribution of the voltage across different layers within the device. The lateral distribution of the voltage near the interface of the via and adjacent interface (chalcogenide in Gen. 1 devices process flow and oxide in Gen. 2 devices process flow) is evident in Figure 3.15a as compared to Figure 3.15b, respectively. The electric field distributions and the energy density are highly concentrated in the vias and the adjacent interfaces. Figure 3.16 better illustrates a cutline analysis of electric field distribution through the via, Ag/chalcogenide/oxide and Ag/oxide interfaces.

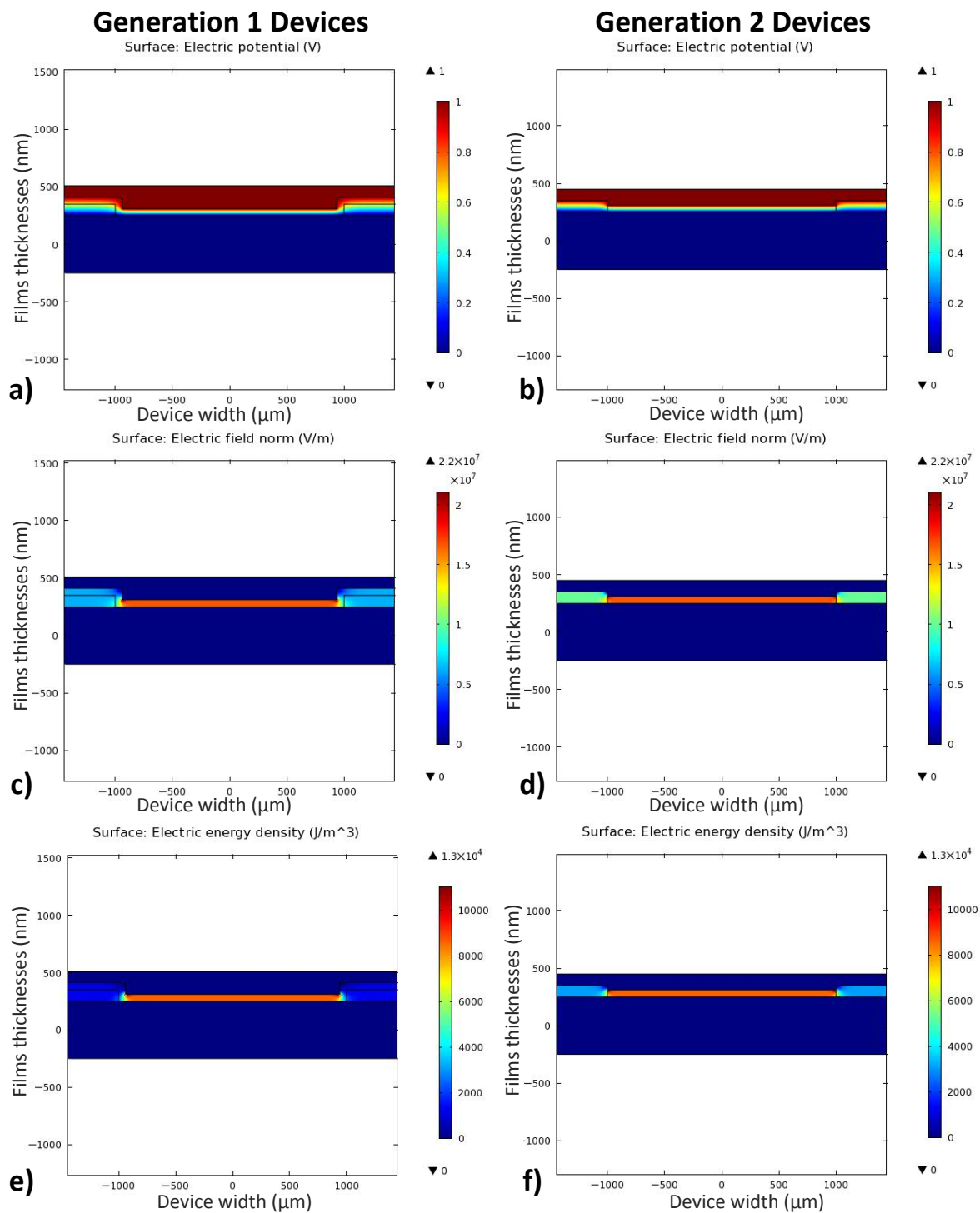


**Figure 3.15** COMSOL simulations for Gen. 1 and Gen. 2 devices representing (a & b) Electric potentials, (c & d) Electric field, and (e & f) Electric energy density

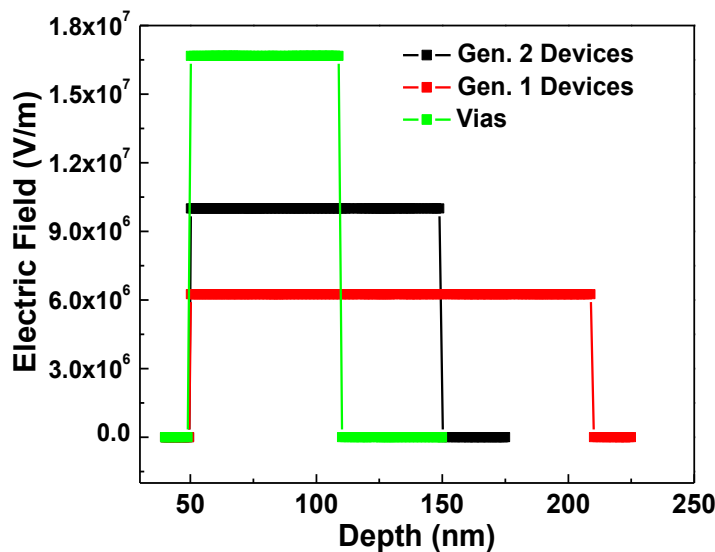


**Figure 3.16** Electric field distribution through via, Ag/chalcogenide/oxide (Gen. 1 devices) and Ag/oxide (Gen. 2 devices) interfaces

Applying a voltage bias will create an electric field and this electric field will drive the silver diffusion into the chalcogenide glass film. Researchers have shown that the application of an electric field of 125V/m (or greater) is the threshold to move silver in chalcogenide film [138]. It is evident from the simulations that the electric field in the Gen. 1 devices, Gen. 2 devices, and within the via is significantly higher than this threshold. In the Gen. 1 devices, the high affinity of Ag towards the chalcogenide matrix combined with the electric field at Ag/chalcogenide interface will result in majority of Ag atoms diffusing into the chalcogenide film, irrespective of whether this film is within the via or underneath of the contact pad. This will eventually result in depleting the Ag source. Once all the Ag is diffused into the chalcogenide film, the device cannot be appropriately biased for changing its state, which will result in an early device failure. On the other hand, in Gen. 2 devices process flow, even though the Ag ions can penetrate through the oxide layer, the diffusion rate through the oxide film is low. This will enhance the device endurance since a majority of the silver will remain at the contact pad.

### Columnar Structured Devices

The devices with nano-column structures were fabricated by using a 3-in-1 mask with an active-in-via concept by angular deposition of the active layer. An improvement in the device performance was observed by the formation of nano-columnar structures within the active film and by limiting the active layer deposition to only the vias. Since the chalcogenide glasses with columnar structure undergo either photo contraction or photo expansion due to the photo induced changes [139-142], the photo-diffusion step is not performed for these devices, fabricated with the Gen. 2 devices process flow in Figure 3.5.

For each device, a blanket film on the Si/SiO<sub>2</sub>/W stack was also created to analyze the material aspect of the films, thus dividing the examination of the devices into two main topics, its material characterization and its electrical, resistive switching, functionality.

## CHAPTER FOUR: MATERIALS RESEARCH RELATED TO ACTIVE FILMS

The chalcogenide deposition for the RCBM devices' active area using PECVD and thermal evaporation methods, in conjunction with the corresponding material characterization are discussed in this chapter. Energy dispersive X-ray Spectroscopy (EDS), Raman Spectroscopy, Atomic Force Microscopy (AFM), and Scanning Electron Microscope (SEM) are the methods used in this study to analyze the material perspectives enlightening its importance towards device performance. A brief explanation regarding each of these methods is presented in the following section, followed by the material characterization performed in this research.

### **Analytical Methods for Film Study**

#### Energy Dispersive X-ray Spectroscopy

The films were characterized using EDS, a method capable of detecting the presence of different elements in a film, and thus determining the exact film compositions. An accurate film composition helps in understanding the behavior of the device as the source (bulk) composition and the deposited film compositions may vary. EDS was performed using the LEO 1430VP Scanning Electron Microscope equipped with an Oxford X-ray Detector and a Hitachi S-3400N-II Scanning Electron Microscope with an Oxford Instruments Energy and EDS system. EDS analysis was performed by applying a voltage bias across a tungsten filament that generated a stream of electrons directed at the sample using a set of apertures and beam aligners [143, 144]. Interaction

of the electrons with the sample under observation results in generation of X-rays, which are collected and analyzed to evaluate the composition of the films. A characteristic X-ray originating from each atom with a specific energy is produced and hence the elements present within a specific film can be determined. In this study, the samples were analyzed using an electron accelerating voltage of 20kV with a working distance of 10mm and magnification of 2kX. On each sample, EDS was performed at five different locations so that multiple points were used to determine the uniformity and actual composition of the film for the samples.

The primary and secondary X-rays for all the elements used in this work were all between 0kV to 10kV. Since the electrons can scatter off the sides or other locations, they would arrive at the surface of the sample with different energies. Hence, setting the electrons accelerating voltage to twice the energy of the most energetic X-rays originating from the sample ensures that the majority of the generated electrons reach the sample. This enhances the signal from the sample, resulting in accurate compositional analysis of the material. Acquiring spectra from five locations provided sufficient statistics about the entire film so that an average composition and the standard deviation can be calculated.

A computer-aided program, developed by Oxford Company, compares the area under various peak locations and provides information about the composition of the sample by using a built-in library of the elements. Once a specific composition of the films is recorded, the composition is normalized to 100% to find the exact composition of the desired element. The beam intensity and the software were initially calibrated with a copper film, prior to measuring the composition of the samples.

## Raman Spectroscopy

Raman spectroscopy has developed into a powerful tool in the field of vibrational spectroscopy since its discovery by Raman and Krishan in 1928 [145]. Structural analysis of the various films is vital in understanding the initial film and the subsequent changes that arise either by changing the gas precursor ratio for the PECVD deposited films or by varying the deposition angle for the thermally evaporated films. The alteration in structures due to changing deposition conditions affects the device performance. Therefore, it is important to study these structural changes.

The basic working principle of Raman Scattering is illustrated in Figure 4.1. Here  $g_0$  depicts the zeroth vibrational level of the ground electronic state and  $g_E$  corresponds to an excited vibrational level of the ground electronic state. The solid lines represent the possible vibrational levels, whereas the dashed line represents virtually excited states,  $\nu_E$ .

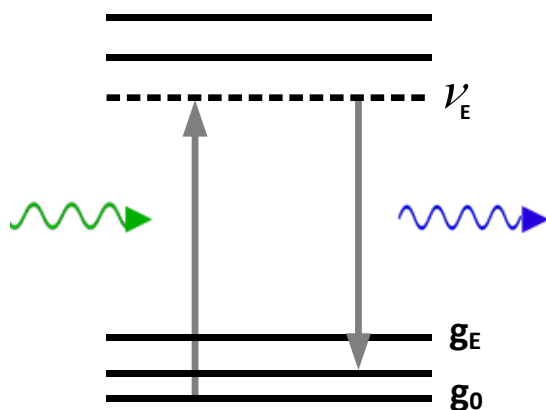


**Figure 4.1 Raman Scattering**

When a photon interacts with an isolated molecule, the photon energy is transferred to the molecule, thereby elevating it to an excited vibrational state. Since in Raman scattering higher photon energies are involved, the molecule is excited to a virtual

level, which then relaxes back down, emitting another photon in the process. Most of the time the excited molecule returns to the initial state by emitting a photon with the same energy and wavelength as that of the excited photon. This type of scattering is known as Rayleigh scattering. However, there is a possibility of the excited state photon relaxing to a vibrational state different than the initial state. In this case, the wavelength of the emitted photon would be different to that of the impinging photon, thus allowing the detection of the molecular structures that are present within the material. The resultant Raman spectra consist of Gaussian peaks corresponding to the scattering intensity of the specific structure. The intensity of each peak is proportional to the number of specific structures. To analyze the overall spectra with multiple peaks, such as the spectra for chalcogenide glasses, the baseline noise from all the spectra was removed followed by normalizing the spectra in order to compare different scans without extraneous variables.

The shift in frequency of the scattered light from that of the incident light is conventionally expressed in wavenumbers relative to the wavenumber of the laser, which is given by an expression expressed in equation 4.1:

$$\Delta \nu (cm^{-1}) = \frac{1}{\lambda_0} - \frac{1}{\lambda_n} \quad (4.1)$$

where  $\Delta \nu$  = Raman Shift

$\lambda_0$  = wavelength of excitation in cm

$\lambda_n$  = wavelength of scattered light in cm

The Raman analysis performed in this study involved a high precision laser that emits light having a wavelength of 442nm with minimal side lobes. The samples were analyzed with a laser intensity of 40mW and the laser beam size of ~1mm. The laser light

reflected off the sample is collected by a charge-coupled device (CCD). Raman spectra of the films were performed at room temperature in a vacuum chamber using a Horiba Jobin Yvon T64000 Raman spectroscopic system in back scattering mode.

### Atomic Force Microscopy (AFM)

AFM is a useful method of studying the roughness and the topography of the films surface. Since the performance of RCBM devices depends on the active layer morphology, it is also important to study the active film surfaces for surface smoothness. There are three modes of operation to measure the surface roughness: contact mode, non-contact mode, and tapping mode. In this work, samples roughness was measured by using the tapping mode, which applies the least amount of force onto the surface by periodically tapping the surface with a Si tip at the end of a flexible cantilever beam. The cantilever was excited by a resonance frequency causing the probe tip to traverse the surface of the film. The amplitude of the oscillation as well as the phase is modulated by the distance between the tip and the surface due to the interaction of both masses. Thereby, the tip slightly touches the surface and is shifted up and down by its drive to follow the profile of the sample with a constant distance. The feedback signal that controls the height of the tip is used to render the surface, which is scanned line-by-line to gather the information of a complete plane.

Since the quality of the AFM image is critically dependent on the scan area and the scan speed in  $\mu\text{m}\cdot\text{s}^{-1}$  [146], all of the AFM scans were performed at the scan rate of  $0.5\mu\text{m}\cdot\text{s}^{-1}$  with an oscillation frequency of 324 kHz for each  $25\mu\text{m}^2$  scan area with a Veeco Dimensions 3100 AFM system equipped with a NanoScope IV controller. The

measurements were performed in an ambient and dark environment. The recorded data was analyzed by using NanoScope software developed by the Bruker Corporation.

### Scanning Electron Microscopy

In SEM, an electron gun normally constructed as a field emission gun, which serves as the source of electrons that are accelerated by a field of 20 kV. Secondary electrons, which are generated by the interaction between the highly energetic electron beam and atoms in the surface region, are the origin of the image. The escaping secondary electrons have a kinetic energy of few eV and are registered by an in-lens detector or a detector beside the electron beam outlet. Due to their low energy, only electrons descending from surface atoms account for the signal, which thus creates an image of the topography. Electrons from areas deeper in the material do not reach the surface since they lose their energy through the scattering process on their way towards the surface. The intensity of the collected secondary electrons is then allied with the beam position to generate an image. A typical SEM schematic is illustrated in Figure 4.2.

The cross-sectional images of the obliquely grown films were captured and recorded by a Hitachi Scanning Electron Microscope capable of 5nm resolution with backscattering detector. Quartz imaging software was used to analyze and record the thin film growth morphology. The samples studied with the help of SEM consisted of an oxidized silicon substrate with sputtered tungsten and thermally evaporated obliquely deposited chalcogenide thin films. The oxides are highly insulating and not structured, which is why they create a high contrast to the metal structures during the examination of columnar structures within the chalcogenide films. A thin conductive gold coating was deposited on the top cross-sectional surface of the samples under examination to provide

SEM imaging under the most favorable resolution conditions. Sputtering of gold allowed the feature details below 15nm to be observable. Furthermore, to gain a better resolution, the electrons acceleration voltage was altered between 8kV to 25kV. Also the samples were turned towards the detector to achieve a higher intensity by the secondary electrons. Turning the sample towards the detector also helped to overcome problems like multiple shadings on the cross-sectional surface by nano-columnar structures and different contrast from the edges, which would reduce the image resolution. By these corrections, the resolution gained was sufficient for the examination of nano columnar structures within the chalcogenide films.

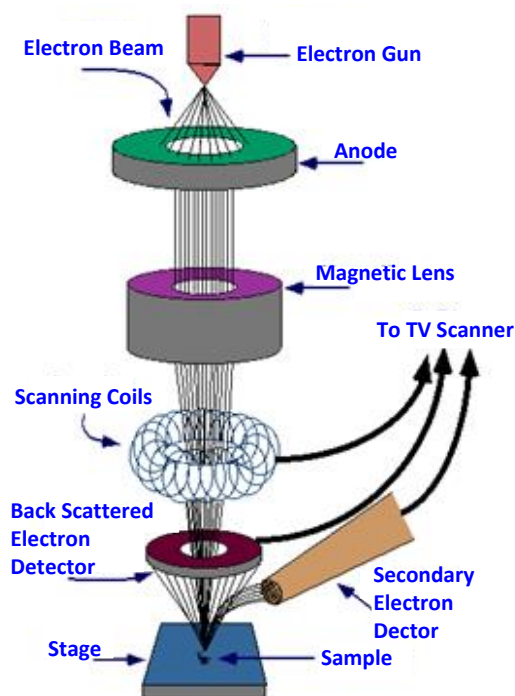


**Figure 4.2** Illustration of SEM Working [147]

The thicknesses of the deposited films as well as the dimensions and inter-columnar distances were determined by the SEM. The samples were cleaved in a standard way with extra precaution to have the cross-sectional area parallel to the incident vapor.

Since the samples were tilted towards the beam detector to get a good resolution, a correction must be applied to get the correct value of the thickness. The schematic for the sample tilted towards the beam and the correction required to measure the actual thickness of the film is illustrated in Figure 4.3, where the correction to get the actual thickness of the deposited layer is:

$$t_{actual\ thickness} = \frac{t_{image}}{\cos(1-\phi)} \quad (4.2)$$

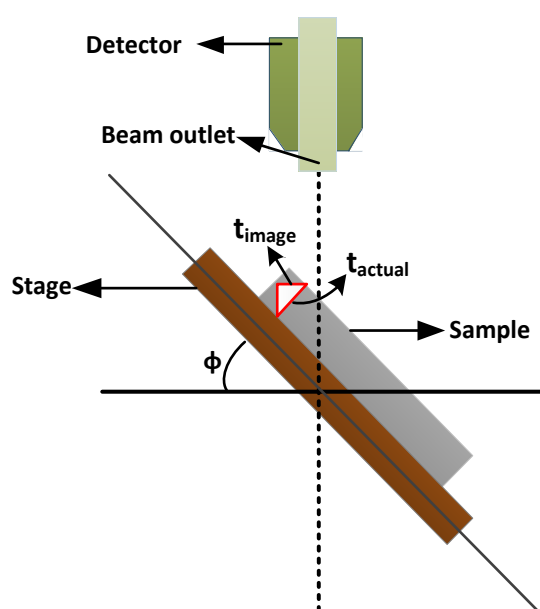


**Figure 4.3 Setup for thickness correction**

### **Thin Film Analysis/Characterization**

The bare film analysis of PECVD and obliquely deposited thermally evaporated active films was done on stacks comprised of a Si <100> substrate having a 200-300nm thermally grown oxide layer. Further, a 100nm layer of tungsten was sputtered on top of the grown oxide to have a good resolution for investigating the nano-columnar channels within the Ge-Se film. Figure 4.4 shows the stack used for bare film analysis for both

deposition methods. As mentioned previously, for PECVD deposited films the surface smoothness was imperative while for thermally evaporated films formation of nano-columnar channels was of prime importance.

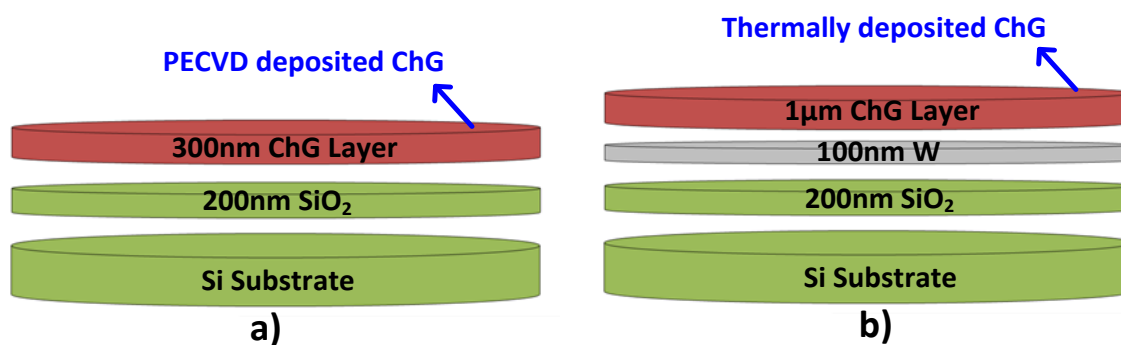


**Figure 4.4** Films stack for (a) PECVD deposited and (b) thermally evaporated chalcogenides (ChG)

#### PECVD Deposited Active Film

Sulfide glasses were preferred for the PECVD deposition technique since they show better temperature stability of up to 400°C, which is higher than the selenide-based glasses [148]. Ion movement is 10 times slower in sulfide glasses compared to selenium glasses [149]. While there is data about application of physical vapor deposition (PVD) methods like sputtering, evaporation, electron beam, etc. for deposition of chalcogenide active layer for RCBM devices, there is lack of information for fabricating RCBM devices using PECVD as the deposition technique for the active layer. Each of these methods has its own limitations; thermal evaporation does not allow dynamic compositional control whereas sputtering poses strict limitation on the composition due to the mechanical requirements of the sputtering targets. The best solution to overcome these shortcomings is the application of the PECVD method, which allows good control over the chalcogenide composition in a dynamic environment. The other advantages for

using the PECVD technique to deposit the active films are the ability to create relaxed films along with a good step coverage. These are all desirable features for creating nano-scaled devices. Also to achieve a high memory density, it is necessary to closely arrange the vias in an array stack. Therefore, a deposition method that is capable of conformal filling like chemical vapor deposition (CVD) or atomic layer deposition (ALD) will be indispensable. CVD application for thin films of Ge-Se were reported [150-153], however most of these attempts were focused on optical application and no data concerning the electrical performance of the devices were reported.

Because of the aforementioned motives, in this research work, application of PECVD deposited  $\text{Ge}_x\text{S}_{1-x}$  chalcogenide films were investigated for RCBM devices. Another advantage that comes with this deposition method is that it permits control over the chalcogenide glass composition in the research mode, which allows a wide range of material compositions to be evaluated for device optimization and in production allows one to readily compensate for any process drift.

#### PECVD Reactor

The experiments were conducted using a 3.5 inch by 10 inch vertically positioned PECVD reactor with a vapor drawn precursor delivery system and a RF plasma network. Small amounts of germanium and sulfur precursor vapors were injected into a continuously flowing argon (Ar) stream. The vapor streams were then transported into the reactor chamber plasma from the top of the reactor and then exited from the bottom. Precursors used for Ge and S were Germane ( $\text{GeH}_4$ ) and Di Isopropyl Sulfide ( $\text{C}_6\text{H}_{14}\text{S}$ ) respectively. Argon was added as a reactant gas to the precursor mixture, with a constant flow rate in the order of 500 SCCM (68% of the total gas flow). Delivery and control of

process gasses was through a customized gas frame equipped with MKS mass flow controllers and computer controlled pneumatic on/off valves. Gas sequencing and control are achieved through SMI process control software. The pressure in the reaction chamber was maintained constant at 35-40Pa, which was monitored via a capacitance manometer positioned on a T-Flange at the base of the reactor. The wafer was heated using a substrate heater whose temperature was varied from room temperature to 250°C. The temperature was maintained by monitoring the thermocouples embedded into the sample holder. Thin films of Ge-S were deposited for 30 minutes with growth rate varying from 5-10nm/minutes. The process was optimized for best conditions to have a smooth layer of the deposited Ge-S films. The typical process variables are summarized in Table 4.1.

<b>Table 4.1 Process tool variable</b>	
<b>Variable</b>	<b>Conditions</b>
Deposition Temperature	25°C to 350°C
Reactor Pressure	35Pa – 100Pa
Gas Precursors	GeH <sub>4</sub> , C <sub>6</sub> H <sub>14</sub> S, Elemental S (Ar used as carrier gas)
Growth Rate	5-10nm/minute

#### Material Characterization

The PECVD deposited film composition, chemical bonding structure and surface topography were studied by EDS, Raman Spectroscopy, and AFM, respectively.

EDS data for the deposited films under different conditions are summarized in Table 4.2. The deposited films were observed to be quite homogenous since EDS in different areas yielded a variation of ~1%. This is a key advantage of PECVD application for film deposition. It was observed that Ge composition decreased by decreasing the

temperature, while keeping the deposition temperature the same, an increase in the Ge:S gas precursor ratio resulted in an increase in Ge composition in the film.

<b>Sample ID</b>	<b>Growing Temp (°C)</b>	<b>Ge:S Precursor Ratio</b>	<b>Ge Atomic % by EDS</b>	<b>Thickness (nm)</b>
Sample 1	250	7.0	59.47	370
Sample 2	200	7.0	35.45	115
Sample 3	150	7.0	34.55	276
Sample 4	150	10.1	37.40	177
Sample 5	120	7.0	36.83	175
Sample 6	120	10.1	49.57	116
Sample 7	100	8.6	34.52	187

The Raman analysis of the deposited films showed the presence of particular structural units corresponding to relaxed films. The observed spectra resemble the bulk material with the same composition, thus showing a low number of wrong chemical bonds. Raman spectra for the PECVD deposited Ge-S films are shown in Figure 4.5. The results are consistent with already reported results with analogous compositions [154].

The major Raman peak for S rich glasses is located at  $340\text{cm}^{-1}$ , which represents the breathing mode of  $\text{Ge}(\text{S}_{0.5})_4$  corner sharing tetrahedra in which Ge is four-fold coordinated and S is twofold coordinated. Its dominance fades with increasing the relative amount of Ge over 37 at.% when the edge sharing (ES) tetrahedra, ethane-like structures and outrigger raft structure develop. The later Raman modes are specific characteristic for the most Ge rich film (Sample 1), which is partially crystallized. Samples 3, 5, and 6 have the highest concentration of S. In them, the presence of some S-S bonds at wavenumber  $475\text{cm}^{-1}$  and participation of corner sharing (CS) tetrahedral

structures manifested by the breathing mode at  $340\text{cm}^{-1}$  are specifically illustrated on the Raman spectra.

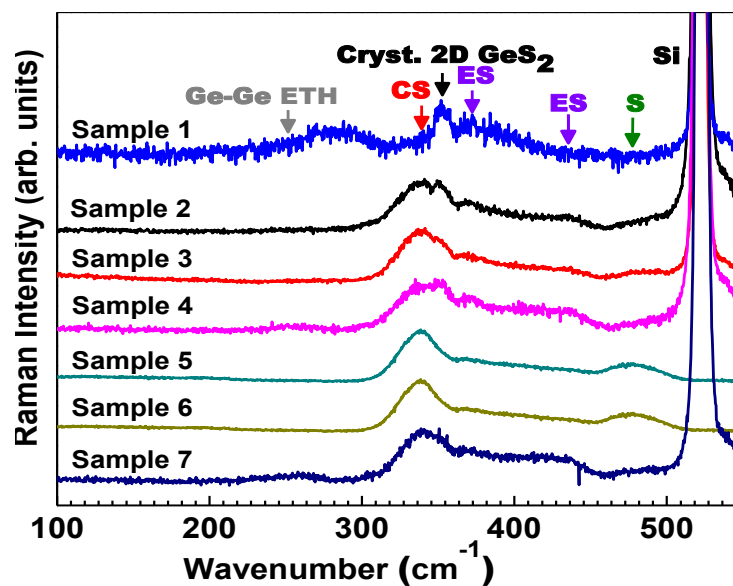


**Figure 4.5** Raman Analysis of PECVD deposited  $\text{Ge}_x\text{S}_{1-x}$  films

The AFM, topography study shown in Figure 4.6, revealed that low temperature deposited films with relatively low concentration of Ge had well relaxed structure, which could accommodate a high amount of Ag. With the deposition condition of sample 5, the structure appears to have relatively smooth surface with less frequency of hillocks, however in some cases hillock formations of up to 18nm were observed in the  $\text{Ge}_x\text{S}_{1-x}$  films, as presented in Figure 4.7. The smoothness of the deposited film was good, with low frequency of defects. The surface roughness in thin films is an important factor for the system reliability [155, 156]. In RCBM devices, the formation of the conductive bridge is dependent on the distance between the two electrodes. Thus, the conductive filament growth process will be determined not by free available adsorption sites at the

electrode surface but by the closest distance between the electrode and hillocks in the active layer [157].

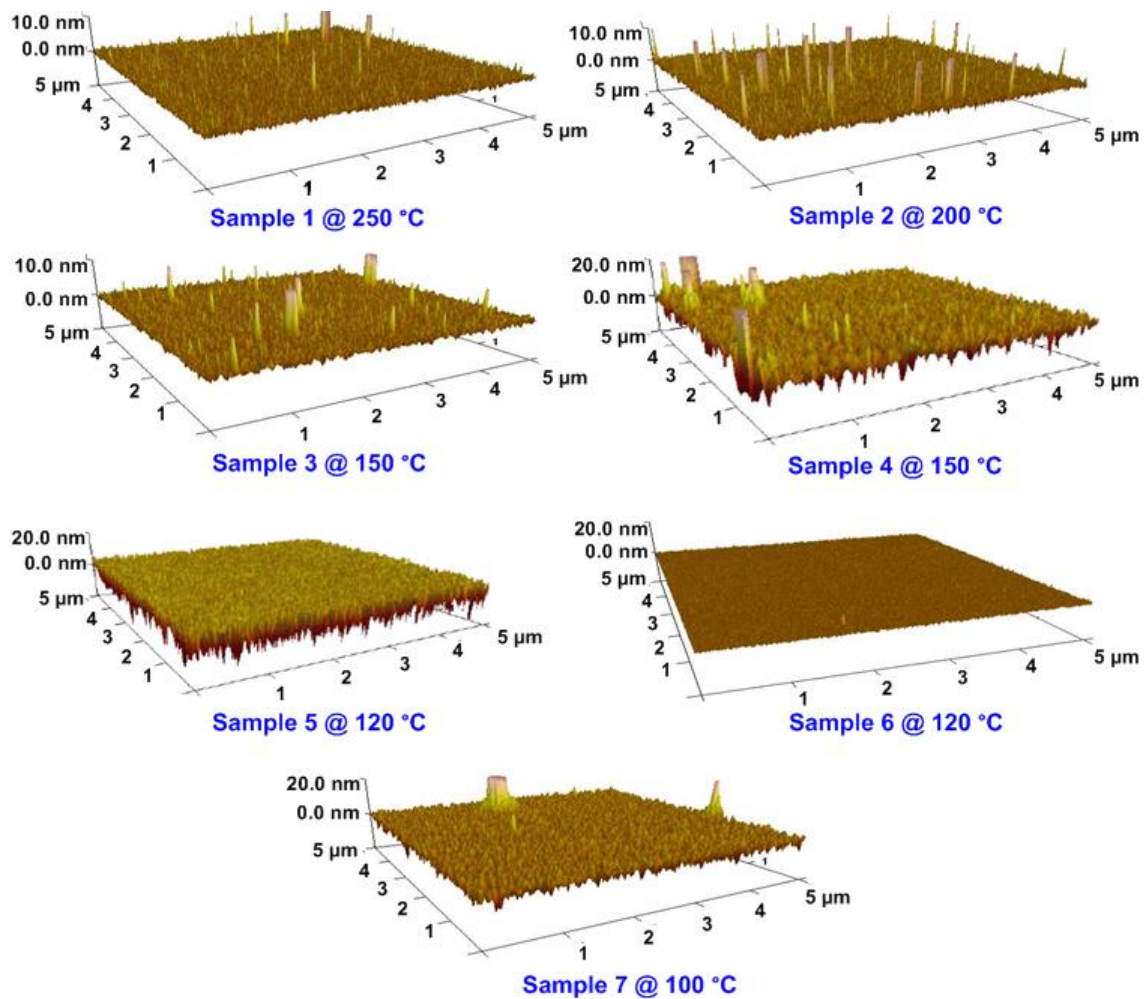
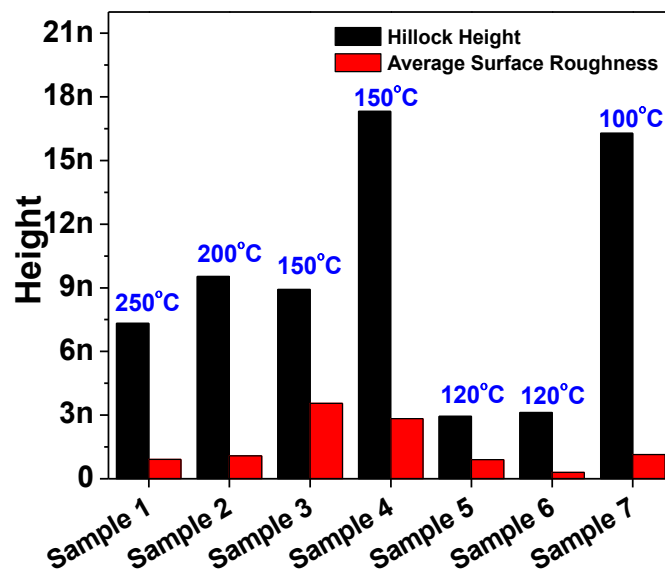
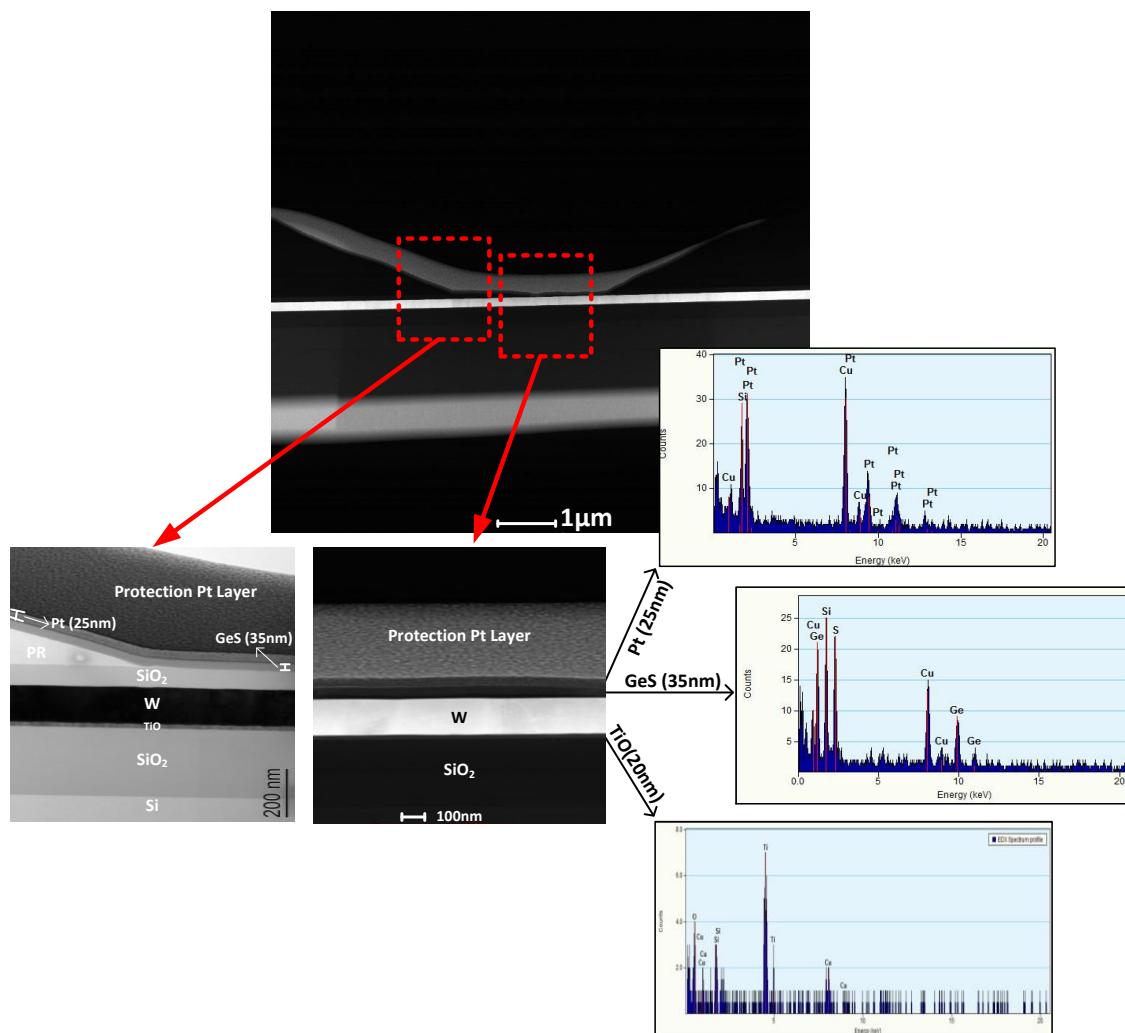


Figure 4.6 AFM result for  $\text{Ge}_x\text{S}_{1-x}$  film deposition at different temperatures



**Figure 4.7 Hillock formation and average surface roughness on the samples based on AFM scan of 5 $\mu$ m by 5 $\mu$ m area**

The active films thicknesses and smoothness was also examined by cross-sectional analysis of the deposited Ge-S film. SEM cross-sectional imaging was done on the smallest device via (2.1 $\mu$ m) to ensure that good step coverage was achieved with a smooth layer. The top cross-sectional area of the film was sputtered with Pt to protect the underlying films from Ga-ions during focused ion beam (FIB) cleaving. Figure 4.8 illustrates a higher magnification of the middle and left-middle area of the film with corresponding EDS spectrums of each layer. The Cu peaks in the spectra are from the Cu grid, which was used for supporting the SEM sample. The layer with brightest contrast at the middle of the image is W having a thickness of 100nm, while the phase in dark contrast below the W layer is SiO<sub>2</sub> films having a thickness of 280nm.



**Figure 4.8 SEM Images of 2 $\mu$ m device cross-section illustrating the smoothness of the PECVD Ge-S film with the corresponding layers composition determined through EDS**

The analysis of the PECVD deposited films illustrates that high quality films, for reliable and stable performance of the RCBM devices, are possible with this deposition method. AFM results suggest that some compromises should be made in terms of the application of relatively lower deposition temperatures, which result in a rougher surface, but at the same time, it could be very advantageous for the photolithographic process.

### Silver Diffusion Kinetics

Since the formation of a solid electrolyte, achieved through photo-diffusion, plays an important role in the device performance, it is imperative to study the silver photo-diffusion dynamics. In this work, the kinetics of Ag in  $\text{Ge}_x\text{S}_{1-x}$  ( $x=0.2, 0.4$ ) were studied by Neutron Reflectometry. Silver is believed to have a step-like silver concentration changes by photo-diffusion. Based on this, diffusion models have been suggested from numerous previous studies mainly using two methods: the time evolutionary changes using methods such as electrical resistivity [158] and optical reflectivity [159]; and determination of detailed concentration profiles using Rutherford Backscattering (RBS) [160, 161]. Rennie et al. [161] have shown in situ silver diffusion by light illumination and a step like silver depth profile using RBS spectra. However, the detailed Ag concentration profile is not reported as they remarked that the samples were sensitive to  $^4\text{He}^+$ , which limited the statistics about the Ag profile. RBS spectra time dependent variation of Ag concentration is reported by Wagner et al. [160]. This approach assumed that the progress of diffusion is halted when the exposure of the sample to visible light is stopped, which in fact is not the case.

Therefore, it is desirable to bypass the intrinsic limitation and assumptions of these techniques and measure the in-situ depth profile while the sample is being exposed with light. These transients in Ag profile can be achieved through X-Ray and Neutron reflectivity. However, X-Rays can induce silver diffusion in chalcogenides [162]. Neutrons on the other hand offer a safer approach by excluding the possibility of the beam-induced changes and the use of an intense pulsed neutron source is well suited to realize time resolved measurements. It is a popular technique for gaining valuable

information on the structure of thin films, where a highly collimated beam of neutrons is made incident onto the sample and the intensity of the reflected radiation is measured as a function of angle or neutron wavelength.

The neutron reflectivity measurement on the  $\text{Ge}_x\text{S}_{1-x}$  ( $x=0.2, 0.4$ ) films was carried out on a BL17-SHARAKU system, in which intense pulsed neutrons are generated through nuclear spallation reactions between a high-energy proton beam and the liquid-Hg neutron source target. In BL17 system, the neutron flux is proportional to the power of the incident proton beam, which was 200kW and 300kW for the measurement of the  $\text{Ag}/\text{Ge}_{40}\text{S}_{60}$  and  $\text{Ag}/\text{Ge}_{20}\text{S}_{80}$  films, respectively. The samples were illuminated by white light with a 300W Xenon lamp.

Neutron Reflectivity,  $R$ , was obtained by  $R = I/I_o$  where  $I$  is the intensity of the reflected beam and  $I_o$  is the intensity of the incident beam as a function of the neutron time of flight (TOF),  $t$ .  $I$  was obtained by measuring the intensity of the direct beam without holding the sample in the holder. The TOF was converted to the modulus of the wave vector transfer,  $Q$ , using the relationship:  $Q = 4\pi \sin \theta / \lambda$ , where  $\lambda = h t / mL$ .  $\lambda$  is the wavelength of the neutrons,  $h$  is the Planck constant,  $m$  is the mass of neutron, and  $L$  is the length between the neutron source and the detector,  $\theta = \theta_i$  is the incident angle, and  $\theta = \theta_f$  is the scattering angle [163]. The schematic for performing the experiment is presented in Figure 4.9.

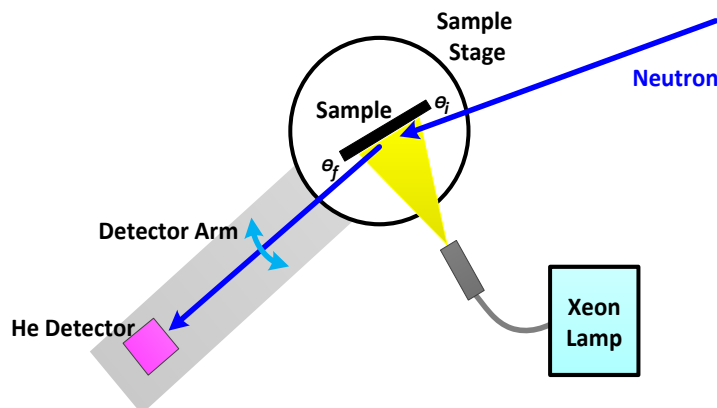


**Figure 4.9 Schematic for measuring Neutron Reflectivity**

Two types of measurements were performed in this work: static and transient. For static measurements, TOF spectra at two different angles were measured and combined to give wide  $Q$  range. In the transient measurements, the sample was fixed at one angle and the time evolution of TOF spectrum was measured while exposing the sample with a Xenon lamp. The neutron bombarded samples were prepared on a stack of Ag/GeS/Si. Thin films of Ag (50nm) and Ge-S (150nm) were thermally evaporated using a Cressington 308R Vacuum System.

The static neutron reflectivity profiles for both the samples, before and after the light illumination are presented in Figure 4.10. The  $\text{Ge}_{40}\text{S}_{60}$  was illuminated for 117 minutes whereas  $\text{Ge}_{20}\text{S}_{80}$  was illuminated for 71 minutes. According to the fitting results in Figure 4.10a, the Ag/ $\text{Ge}_{40}\text{S}_{60}$  structure is preserved with no silver diffusion before exposure to the xenon lamp. However, in the case of  $\text{Ge}_{20}\text{S}_{80}$ , silver has already diffused into the layer without any exposure to the light, which may have occurred during the thermal evaporation process.

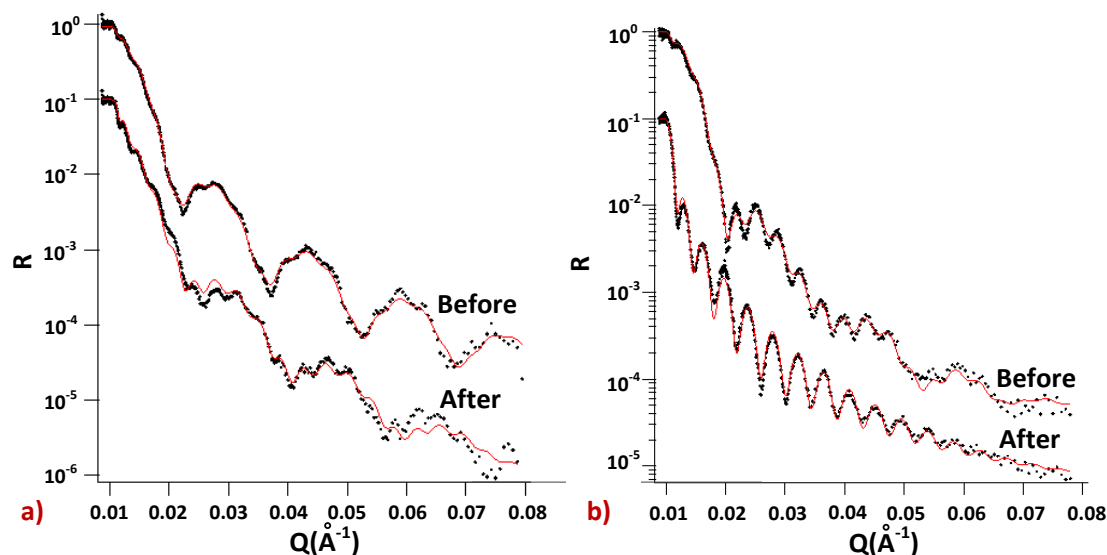


**Figure 4.10** Neutron reflectivity profiles before and after light exposure (a) Ag/Ge<sub>40</sub>S<sub>60</sub> and (b) Ag/Ge<sub>20</sub>S<sub>80</sub> films

Figure 4.11 presents the Fourier Transform of the neutron reflectivity profile. The peaks in Figure 4.11a, correspond to 400Å (Ag), 1200Å (a-Ge<sub>40</sub>S<sub>60</sub>), and 1600Å (total thickness) and confirms a two layer structure. After illuminating the sample with the lamp, the reflectivity profile has changed, indicating some degree of silver diffusion into the Ge<sub>40</sub>S<sub>60</sub> film. However, the Fourier Transform indicates that the two layer structure is preserved. Figure 4.11b shows a peak around 100Å that corresponds to the reaction layer. After light illumination, only one sharp peak around 1500Å is observed in Figure 4.11b, which supports the conclusion that the film is composed of one layer. The time evolution of neutron reflectivity is shown in Figure 4.12. Although the reflectivity changes with time, it is difficult to ascribe a physical meaning based on this observation alone. However, in the case of Ge<sub>20</sub>S<sub>80</sub>, Figure 4.12b, the neutron reflectivity changes significantly in the first 10 minutes after the illumination starts.

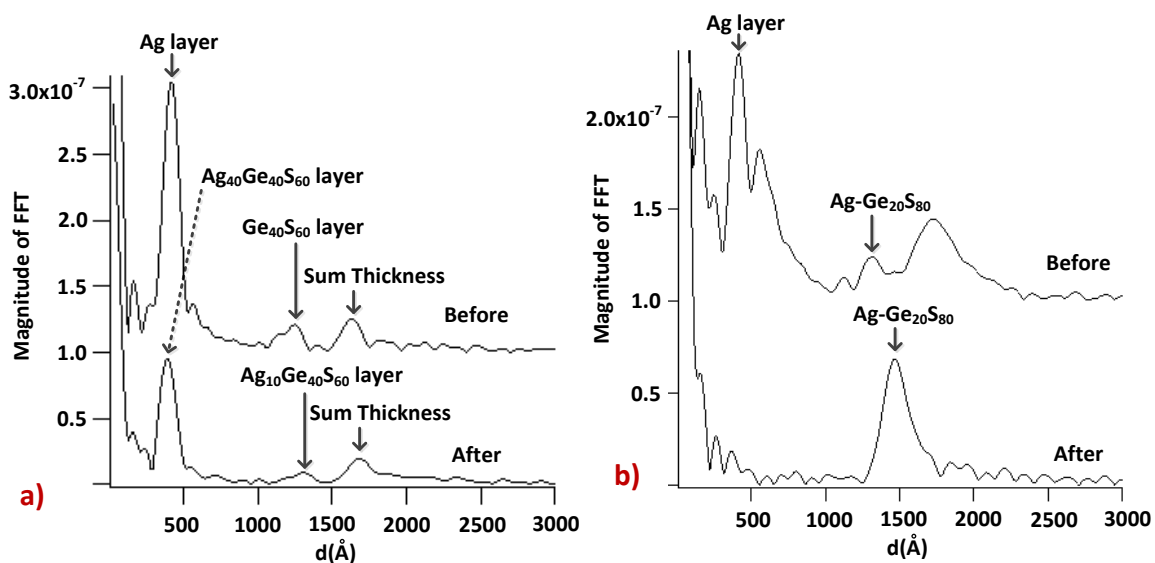


Figure 4.11 Fourier Transform of the reflectivity data (a)  $\text{Ag}/\text{Ge}_{40}\text{S}_{60}$  and (b)  $\text{Ag}/\text{Ge}_{20}\text{S}_{80}$  films presented in Figure 4.10

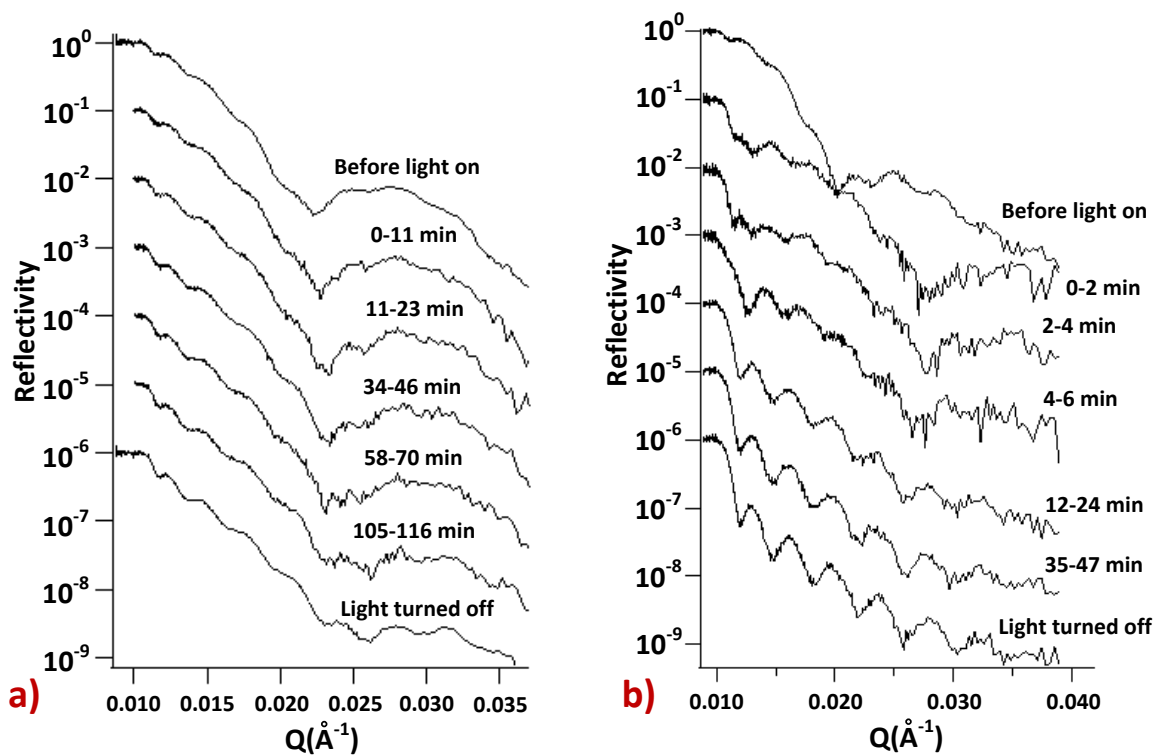
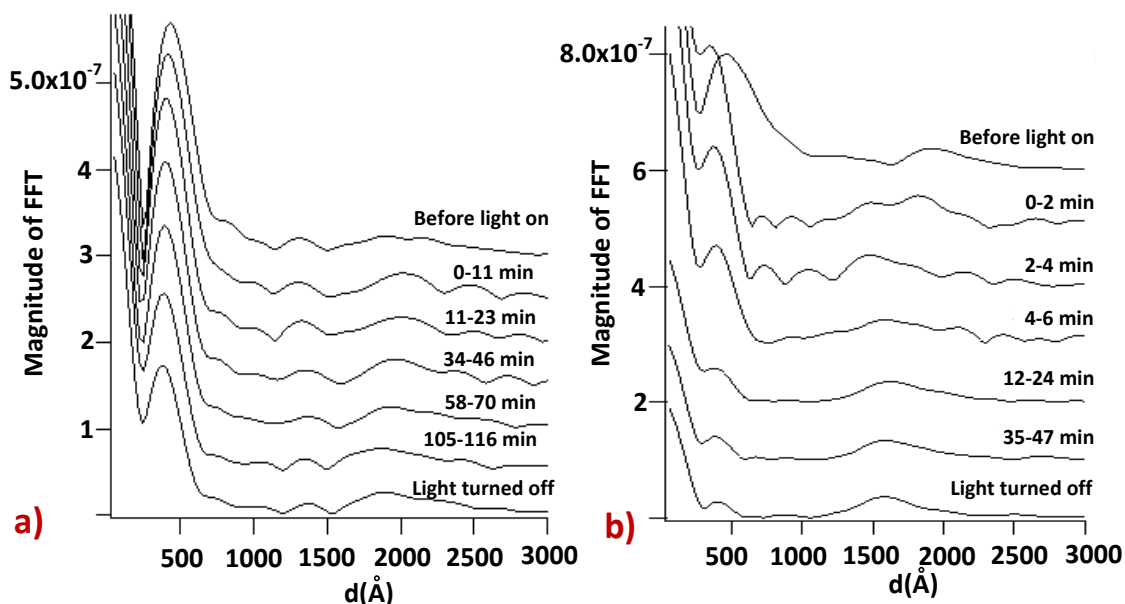


Figure 4.12 Time evolution of neutron reflectivity of (a)  $\text{Ag}/\text{Ge}_{40}\text{S}_{60}$  and (b)  $\text{Ag}/\text{Ge}_{20}\text{S}_{80}$  films substrate film under light illumination.

Fourier Transform of the reflectivity data for Figure 4.12 is presented in Figure 4.13 with rapid change also being observed to occur in  $\text{Ge}_{20}\text{S}_{80}$ .



**Figure 4.13** Fourier Transform of the time evolutionary reflectivity data of (a)  $\text{Ag}/\text{Ge}_{40}\text{S}_{60}$  and (b)  $\text{Ag}/\text{Ge}_{20}\text{S}_{80}$

The position and height of the first peak are plotted as a function of time in Figure 4.14a. Two types of diffusion process can be observed, a fast change observed in the first 10 minutes after the exposure starts while a second, slow, change can be observed after 107 minutes. Even after stopping the light illumination, the change seems to continue. Similarly, Figure 4.14b illustrates the peak position of the first and second peaks and height of the first peak is plotted as a function of time. Again, two diffusion processes can be distinguished: a fast change occurring after 2 minutes since the start the illumination, while a slower change is observed after 20 minutes. The silver diffusion has essentially finished after 20 minutes and the sample becomes a uniform homogeneous layer.

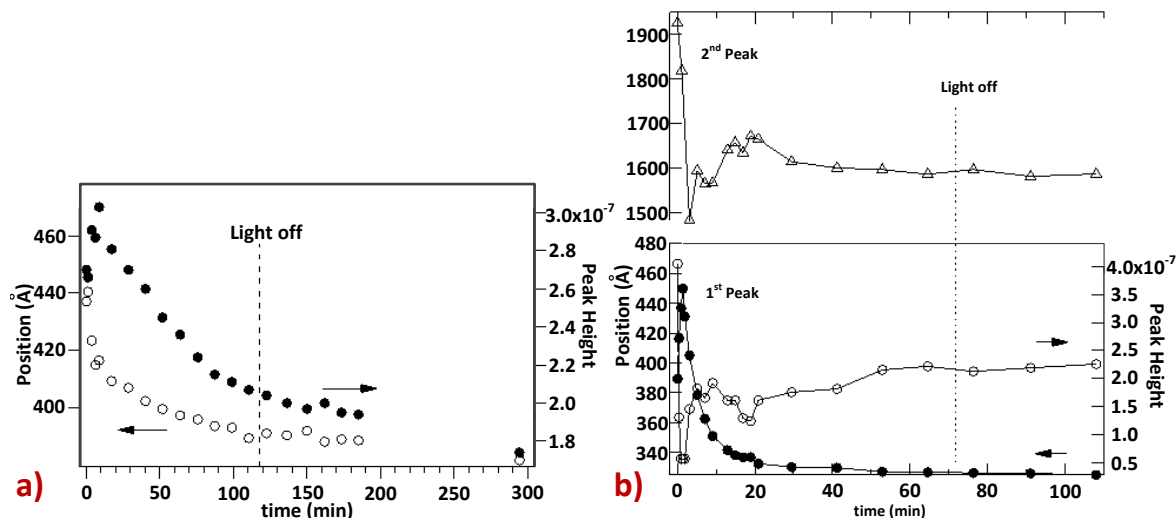


**Figure 4.14** Fourier Transform of the time variation plots: (a) the position (○) and the height (●) of the first peak in Ag/Ge<sub>40</sub>S<sub>60</sub> film and (b) the positions of the first (○) and the second peaks (△) and the height of the first peak (●) in Ag/Ge<sub>20</sub>S<sub>80</sub> film

A difference in the reaction rate is observed in both the systems. The reaction rate in Ag/Ge<sub>20</sub>S<sub>80</sub> film is faster than in Ag/Ge<sub>40</sub>S<sub>60</sub> film. This compositional dependence is consistent with the structural flexibility of the Ge-S system, which is often explained by a floppy-rigid transition model [164]. Another reason is the high availability of S in this composition, which has a high affinity towards Ag. The faster reaction rate in Ag/Ge<sub>20</sub>S<sub>80</sub> is attributed to the structural flexibility of Ge<sub>20</sub>S<sub>80</sub>. However, two silver diffusion processes, a faster and a slower one, is observed in both systems. This result is consistent with the reported Ge-Se result that showed the presence of slow and fast moving Ag ions [165]. The two diffusion processes imply the presence of a comparatively stable (metastable) state in the Ag-doped Ge<sub>x</sub>S<sub>1-x</sub> layer. In the first diffusion stage, a Ag-rich reaction layer is formed and the Ag layer is exhausted. Considering that the two layer structure is preserved and that the position of the interface is fixed by the completion of the diffusion, the next silver diffusion step takes place from the Ag-rich reaction layer to the Ag-poor reaction layer by getting over the potential barrier between the two layers. In

this way, both of the layers can keep their homogeneity and this could be the reason why fringes in the reflectivity are clearly observed even after the silver diffusion.

### Columnar Structure within Device Active Film

Apart from having a smooth active layer, another novel approach for improving the RCBM device performance was through the formation of nano-columnar structures in the active layer of the device. In this work, formation of nano-columnar structures in the Ge-Se and Ge-Te active films were investigated. The improvement achieved in the device performance was demonstrated through rigorous electrical testing. These suggested nano columnar structures are extendable to other chalcogenides compositions as well as the oxides family.

Typically, the active layer of RCBM devices are deposited at an angle normal to the incident vapor flux, i.e.  $\alpha = 90$ , which results in an amorphous structure of the films. This type of structure reduces the reliability of the devices as the pathways for formation of the contact bridge within the chalcogenide film could be different at each switching event. Multi-branching within the Ag filament results in a non-uniform switching at a different rate, hence fluctuating the performance of the devices. An illustration of electrochemically formed multi-branched filament through a 50nm Ag-Ge-Se film is presented in Figure 4.15.



**Figure 4.15** Electrochemical growth of the Ag dendrite in the Ag-Ge-Se electrolyte [166]

An ideal structure to avoid these shortcomings could be an amorphous disordered medium, which ensures high resistive state during the off state of the device, having nano-channels or nano-tunnels in the active layer of the device for the filament to grow, as presented in Figure 4.16. If the size of the channel is comparable to filament size, multi-branching within the conductive path will not occur. Moreover, the conductive filament, for each switching cycle, will grow through the provided channels, resulting in uniform switching of the devices. In fact, if these channels are properly addressed, the filaments growing through the channels can act as an individual devices. Therefore, an array of RCBM devices can be arranged in this manner.

Such structures are achievable for the RCBM active layer if the ChG film is deposited obliquely at an angle  $\alpha < 90^\circ$ . Obliquely deposited films form column structures become porous and display unusual functionalities [167-173]. The research related to formation of obliquely deposited chalcogenide films started in the late 1970s when in a series of reports Chopra and co-workers described formation of column structures in these materials [174-176].

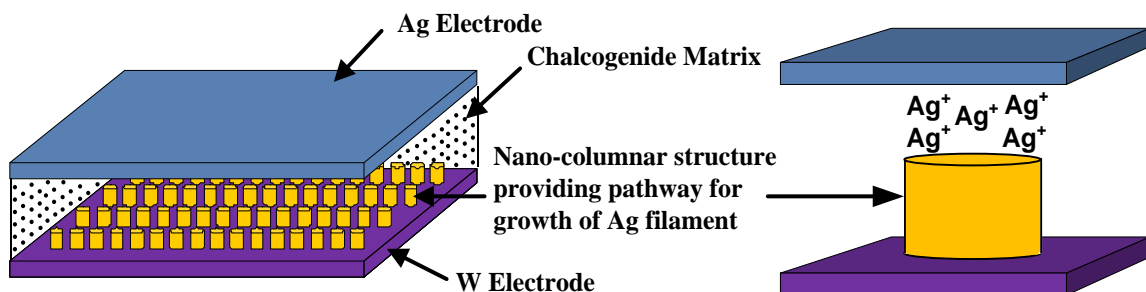


**Figure 4.16** Ideal RCBM device structure

## Experimental Results

Prior to the film preparation for nano-structures using the oblique angle method, it is important to mention that the bulk glasses used in this work were prepared from 99.99% pure elements. The glasses were prepared with a widely known method of the melt quench technique, where pure elements of germanium and a specific chalcogen element, for example selenium, were measured to correspond to a specific glass composition. For example, when creating GeSe<sub>2</sub> for a specific weight, the amount of selenium placed into a sealed and evacuated ampoule was twice than that of germanium. The sealed ampoule was then placed into a specialized furnace, which raised the temperature until all the materials in the ampoule were in molten liquid form. At this point, the furnace was rocked to ensure complete mixture of all the elements. This step was followed by a quick quench to solidify the mixture and maintain the amorphous nature of the glasses by freezing the equilibrium characteristic of the liquid mixture. When the molten alloy was quenched at a fast rate, the resultant material was in a glass form having a higher viscosity than the liquid from which it had originated. The characteristic temperature for the transition from liquid to solid state is called the glass transition temperature ( $T_G$ ).

Thin films of chalcogenides were evaporated on Si <100> substrate using the Cressington 308R Desktop coating system. A crucible shaped in the form of a Semi-Knudsen cell, shown in Figure 4.17, was used to thermally evaporate the Ge-Se and Ge-Te chalcogenide films. This Semi-Knudsen cell allowed to achieve equilibrated pressure to all the components of the glassy mixture. It is important to maintain a uniform pressure for the material being evaporated since thermal evaporation works on the properties of

partial pressure of the material being deposited. The atoms with the material having the same partial pressure will evaporate at similar rates and maintain the composition of the source material, but this is not always guaranteed, which is the case for the chalcogenide glasses. For example, in  $\text{GeSe}_2$ , selenium has a higher partial pressure, so when the source material is  $\text{GeSe}_2$ , the selenium will evaporate significantly earlier and faster than the germanium, creating selenium rich films rather than the original composition. Therefore, a special crucible, capable of maintaining constant pressure inside the crucible, was required to ensure that the composition of the source material is transferred to the evaporated film. This crucible was covered with a rectangular tungsten frame with small orifices, which at the same time were large enough to achieve a reasonable deposition rate. Once the chalcogen (Se) vapor strikes the cover, part of it will go through after losing substantial energy while the rest fills the close volume of the crucible. After the volume inside the crucible is filled with Se vapor, the vapor exerts pressure over the source and prevents it from further evaporating. However, at this point, the second element (Ge) starts to evaporate when the pressure inside the cell reaches its partial pressure. Hence, once an equilibrium state is reached between the vapor and the source inside the cell, the composition of the material being evaporated will be the same as the source.

The thickness of the deposited films was monitored by a 6MHz quartz crystal resonator (QCR). The films were deposited with a base deposition pressure of  $10^{-6}$  barr and deposition rate of  $2\text{nm}\cdot\text{s}^{-1}$ . Deposition rate is an important aspect towards forming the columnar structure. The incident vapor flux angle ( $\alpha$ ) and hence the columnar growth angle ( $\beta$ ) was altered by tilting the stage at the desired obliqueness value. It should be

noted that the vapor incidence angle and columnar growth angle were measured with respect to the arriving vapor flux and the substrate/stage axis, as represented in Figure 4.17. Bare films of Ge-Se and Ge-Te chalcogenides with thicknesses ranging from  $0.5\mu\text{m}$  to  $1\mu\text{m}$  were deposited under various deposition angles ( $\alpha = 90^\circ, 80^\circ, 70^\circ, 60^\circ, 45^\circ, 30^\circ$ ) to study the influence of the column structures inclination on the deposited material as well as electrical properties of the devices.

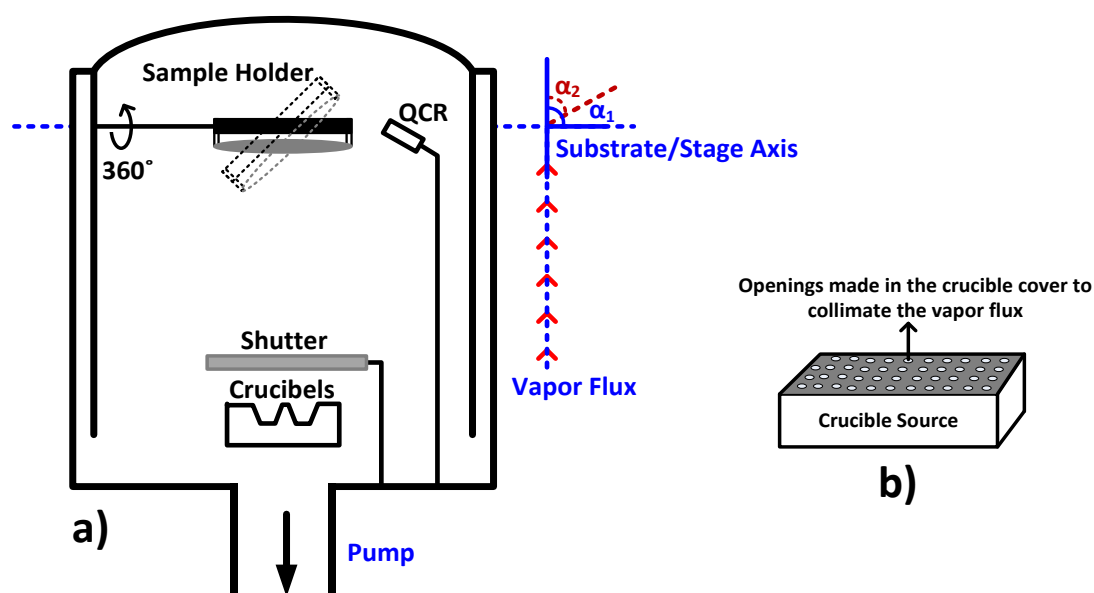


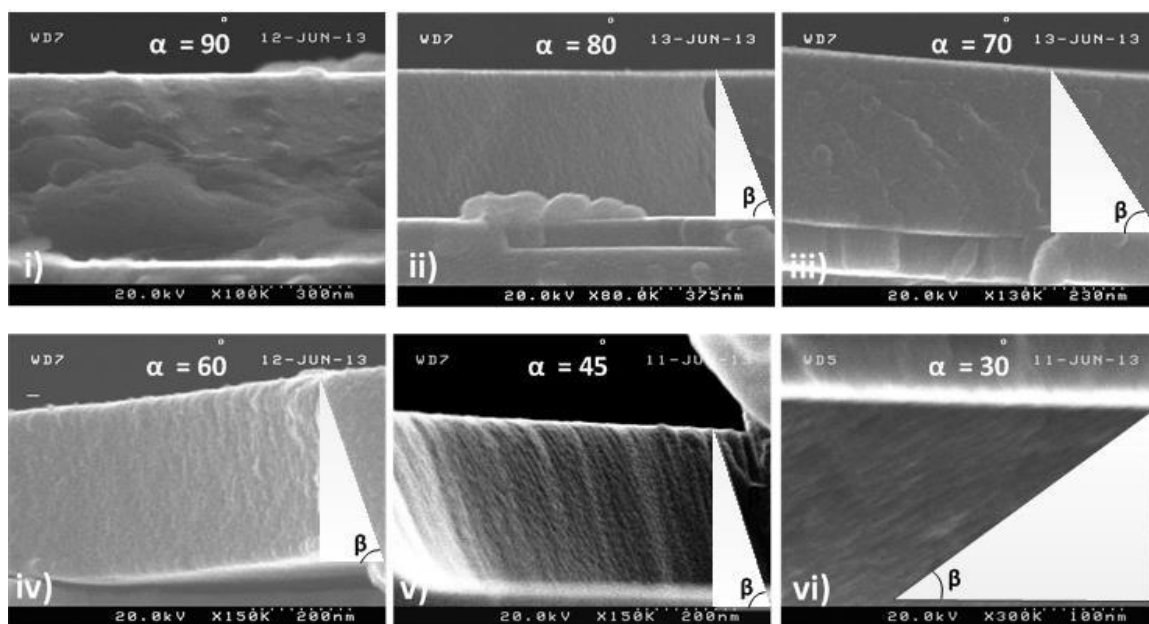
**Figure 4.17** (a) Schematic of thermal evaporation chamber illustrating incident vapor measuring method where  $\alpha_1$  is the normally deposited film ( $\alpha_1 = 90^\circ$ ) and  $\alpha_2$  is some angle less than  $90^\circ$  ( $\alpha_1 < 90^\circ$ ) and (b) Semi-Knudsen Cell structure used for thermally evaporated films

### Analysis of Columnar Structure

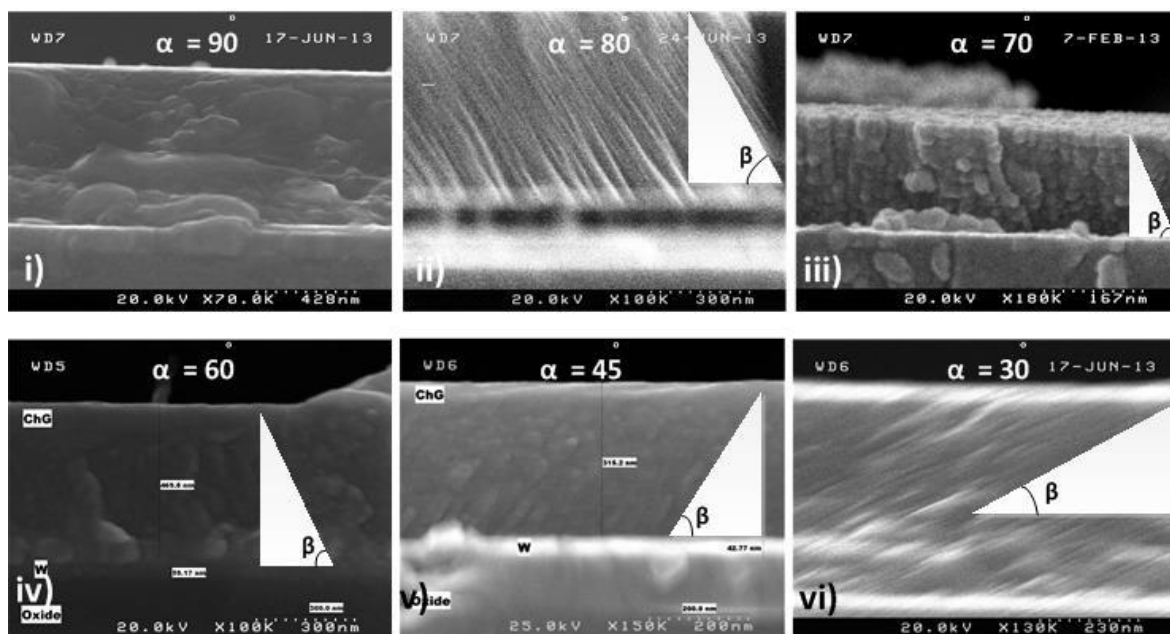
#### Cross-Sectional Study of Obliquely Deposited ChG Films

The cross-sectional SEM images of  $\text{Ge}_x\text{Se}_{1-x}$  ( $x = 0.2, 0.3, 0.4$ ) and  $\text{Ge}_x\text{Te}_{1-x}$  ( $x = 0.2, 0.5$ ) films deposited at vapor incident angles of  $90^\circ, 80^\circ, 70^\circ, 60^\circ, 45^\circ$ , and  $30^\circ$  are shown in Figure 4.18 and Figure 4.19, respectively. Inspection of these images illustrate

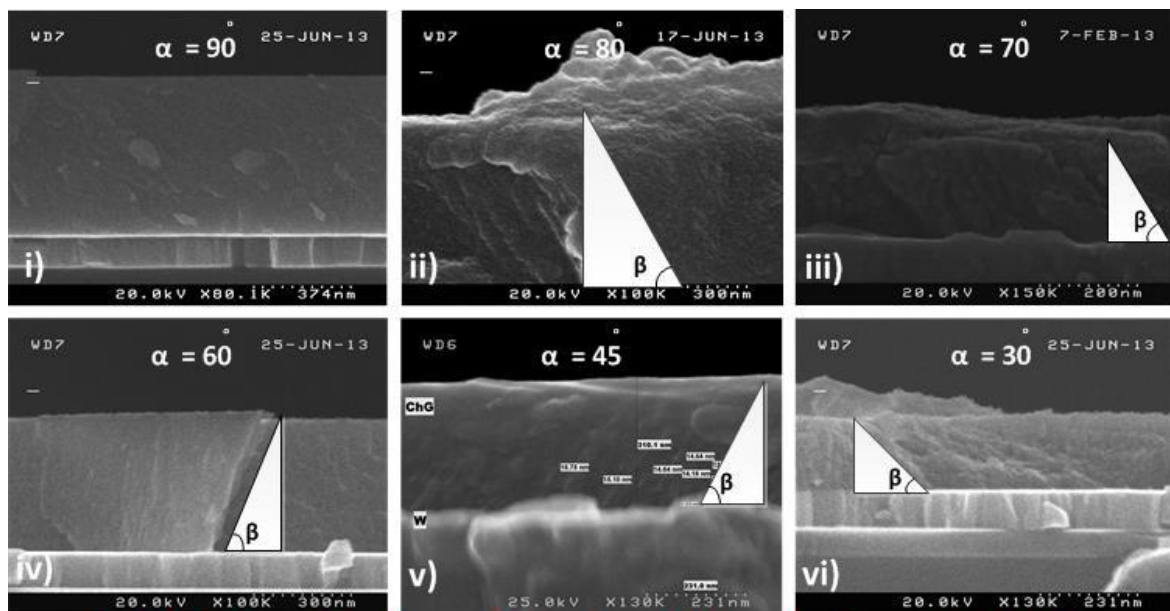
that films deposited under oblique angles are composed of columns and inter-columnar voids. These voids provided the pathways for the silver filament to grow. The obliquely deposited films are inclined towards the direction of the incoming vapor flux. As the deposition angle decreased, the column angle also decreased due to limited adatom diffusion during deposition process [83]. The average column width, in case of Ge-Se films, was found to be  $\sim 19.13\text{nm}$  with an average spacing of  $\sim 15.64\text{nm}$  between the columns. This highly oriented nano columnar structure fabricated by obliquely deposited films is anisotropic in nature. Such structure introduces the anisotropic dependence into the thermal, electrical, and optical properties of the thin films [177].



**a) SEM Cross Section of  $\text{Ge}_{20}\text{Se}_{80}$  Obliquely Deposited Films**

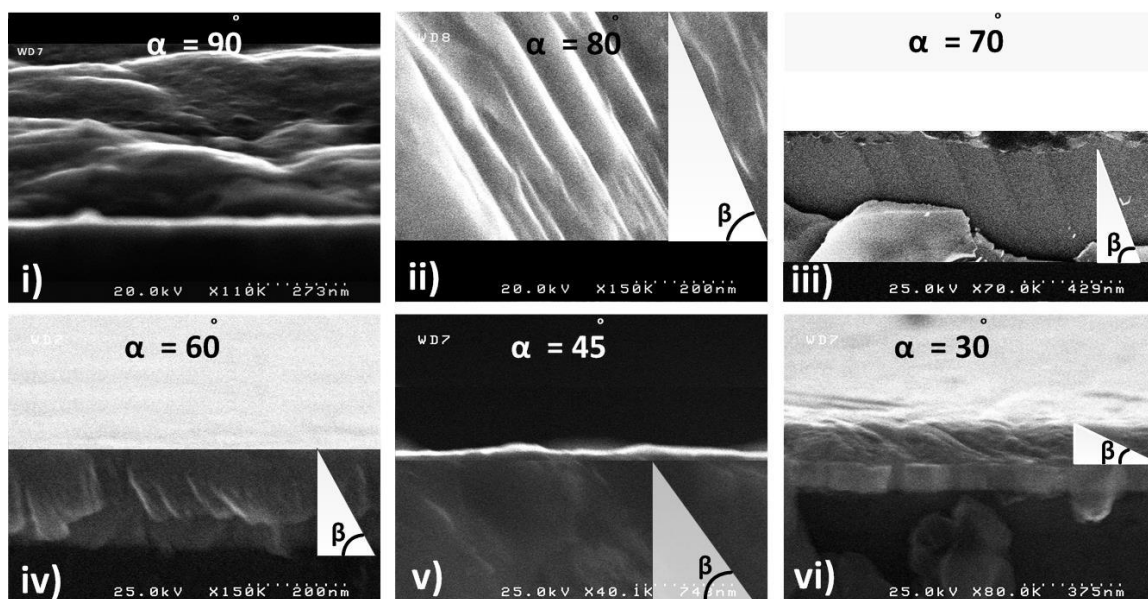


**b) SEM Cross Section of  $\text{Ge}_{30}\text{Se}_{70}$  Obliquely Deposited Films**

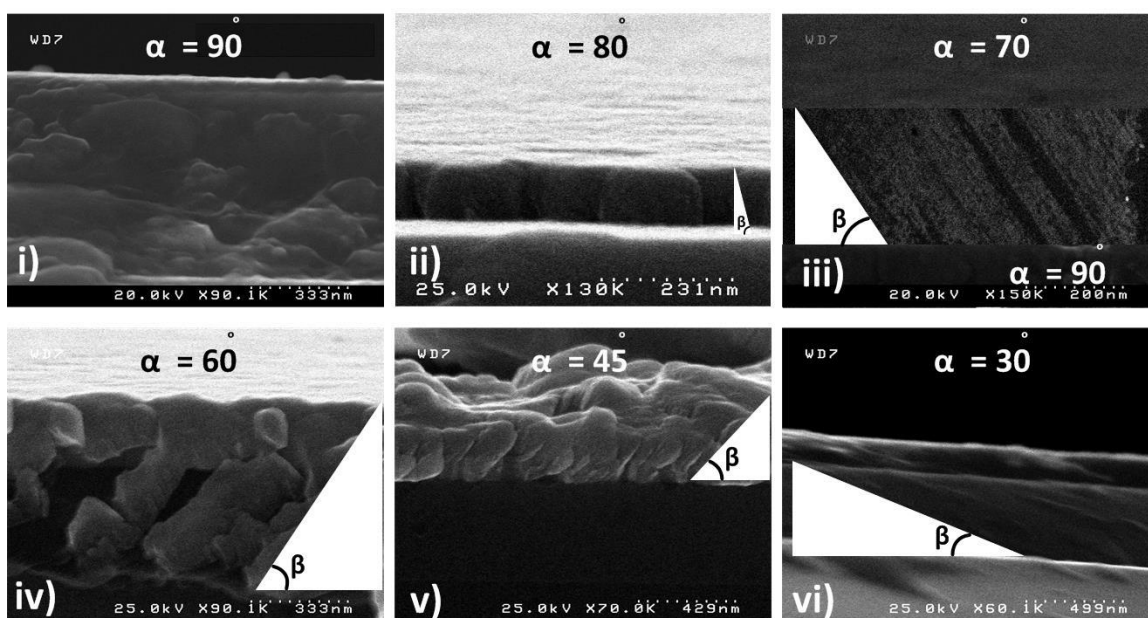


**c) SEM Cross Section of  $\text{Ge}_{40}\text{Se}_{60}$  Obliquely Deposited Films**

**Figure 4.18** SEM cross-sectional images of (a)  $\text{Ge}_{20}\text{Se}_{80}$ , (b)  $\text{Ge}_{30}\text{Se}_{70}$ , and (c)  $\text{Ge}_{40}\text{Se}_{60}$  under various incident vapor angles: (i)  $\alpha = 90^\circ$ , (ii)  $\alpha = 80^\circ$ , (iii)  $\alpha = 70^\circ$ , (iv)  $\alpha = 60^\circ$ , (v)  $\alpha = 45^\circ$ , (vi)  $\alpha = 30^\circ$



**a) SEM Cross Section of  $\text{Ge}_{20}\text{Te}_{80}$  Obliquely Deposited Films**



**b) SEM Cross Section of  $\text{Ge}_{50}\text{Te}_{50}$  Obliquely Deposited Films**

**Figure 4.19** SEM cross-sectional images of (a)  $\text{Ge}_{20}\text{Te}_{80}$  and (b)  $\text{Ge}_{50}\text{Te}_{50}$  under various incident vapor angles: (i)  $\alpha = 90^\circ$ , (ii)  $\alpha = 80^\circ$ , (iii)  $\alpha = 70^\circ$ , (iv)  $\alpha = 60^\circ$ , (v)  $\alpha = 45^\circ$ , (vi)  $\alpha = 30^\circ$

The measurement of the columnar structure inclination angles towards the incident vapor flux, deposited under different deposition angles, for Ge-Se and Ge-Te

films are presented in Table 4.3 and Table 4.4, respectively. The best approximation for predicting the inclination of the column growth under different angles is by the Tangent Rule (equation 2.1) [104]. The inclination angle of the experimentally grown columnar structure deviated quite a bit from the angle predicted by the Tangent Rule, which is shown in the tables. Therefore, a modified empirical formula is suggested to overcome this deviation in the Ge-Se and Ge-Te films, as:

$$\tan \alpha = 2/A \tan(\beta) \quad (4.3)$$

where A is a parameter that depends on materials and deposition rate. The parameter A for the chalcogenide glasses studied in this work is found to be 0.625.

<b>Table 4.3 Deposition and column angle growth for Ge-Se films (all units are in degrees)</b>					
Incident Vapor Flux ( $\alpha$ )	Columnar Angle ( $\beta$ ) Calculated by Tangent Rule	Ge <sub>20</sub> Se <sub>80</sub>	Ge <sub>30</sub> Se <sub>70</sub>	Ge <sub>40</sub> Se <sub>60</sub>	Columnar Angle ( $\beta$ ) Calculated by suggested correction
		Measured Columnar Angle ( $\beta$ )			
80	70.575	72	66	70	75.862
70	53.948	61	63	63	67.981
60	40.893	70	64	69	57.320
45	26.565	46	49	48	41.987
30	16.102	35	32	34	27.457

<b>Table 4.4 Deposition and column angle growth for Ge-Te films (all units are in degrees)</b>				
Incident Vapor Flux ( $\alpha$ )	Columnar Angle ( $\beta$ ) Calculated by Tangent Rule	Ge <sub>20</sub> Te <sub>80</sub>	Ge <sub>50</sub> Te <sub>50</sub>	Columnar Angle ( $\beta$ ) Calculated by suggested correction
		Measured Columnar Angle ( $\beta$ )		
80	70.575	66	75	75.862
70	53.948	69	57	67.981
60	40.893	62	56	57.320
45	26.565	53	46	41.987
30	16.102	28	22	27.457

A graphical comparison of the measured angles for the deposited Ge-Se and Ge-Te films, the Tangent Rule and the suggested correction to the Tangent Rule is presented in Figure 4.20. The suggested correction predicts the growth angle of these columns within  $\pm 10\%$  of the experimentally found angle.

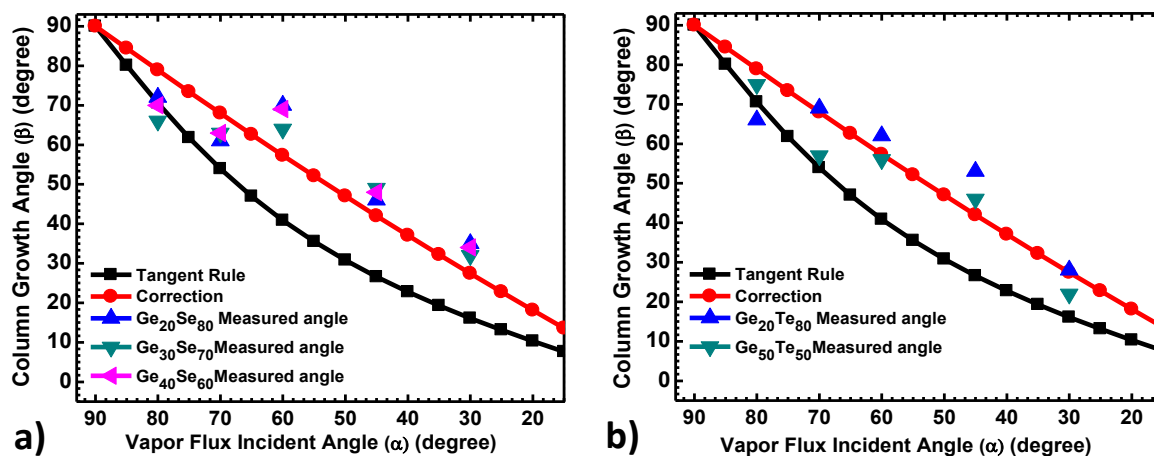


**Figure 4.20 Comparison of measured angles vs Tangent Rule and suggested correction for (a) Ge-Se system and (b) Ge-Te System**

The eventual goal of the oblique angle deposition technique, in this study, was to extend its application in the fabricated devices to form column structures. Therefore, SEM analysis was performed on the RCBM device, having a via size of  $2.1\ \mu\text{m}$  with  $\text{Ge}_{40}\text{Se}_{60}$  active film deposited at  $70^\circ$ , after completing all the processing steps. The SEM images, along with EDS results, are presented in Figure 4.21. Figure 4.21a illustrates the organization of the films at the base of the via. A careful examination of the Ge-Se film in Figure 4.21a confirms the presence of column structures. The columnar structures are very prominent in Figure 4.21b. These results provided evidence of the columnar structures existence inside the device's via. Hence, it can be concluded that with thermally evaporated obliquely deposited films, it is possible to form columnar structures within the device's vias, which will ensure dependable performance of the RCBM device.

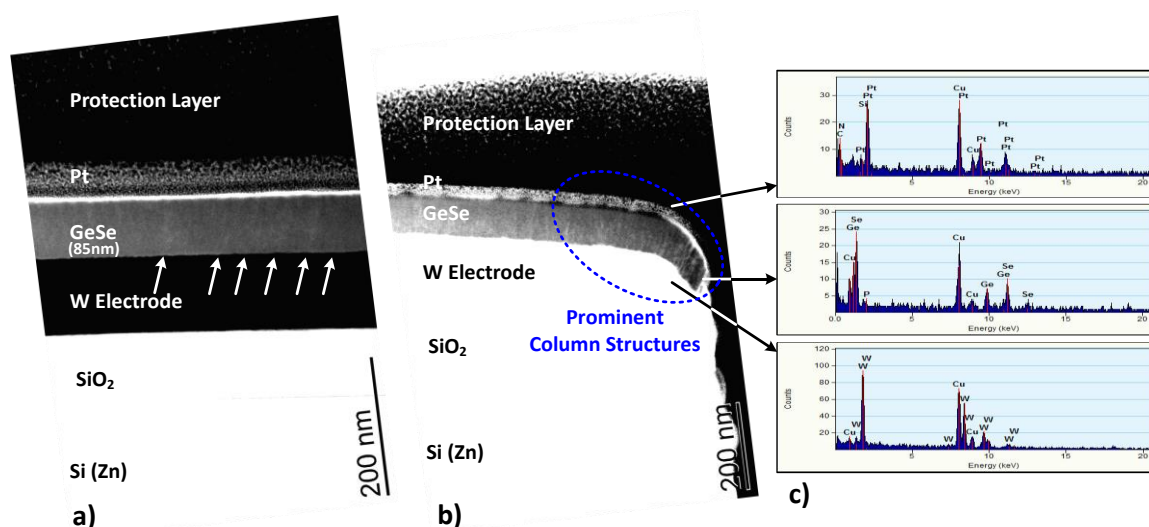


**Figure 4.21** SEM images (a & b) of the obliquely deposited  $\text{Ge}_{40}\text{Se}_{60}$  film and (c) EDS analysis performed on (a & b) to confirm the films under observation

#### Surface Morphology of Obliquely Deposited Films

Even though SEM is a good technique for characterizing the films, it has limitations in characterizing the chalcogenide films, which are sensitive towards the interaction with the electron beam that results in collapsing of the column structure. Because of this, surface morphologies of the obliquely deposited films were studied by AFM in tapping mode as explained earlier.

AFM surface scans, on a 500nm by 500nm area, for the obliquely deposited Ge-Se and Ge-Te films are presented in Figure 4.22 and Figure 4.23, which illustrate that the obliquely deposited films are predominantly porous in nature. It can be observed that the normally deposited films, for each case, have a relatively smooth surface. As the films are grown under some angle, voids are observed on the surface, which clearly indicate the porosity of the films. A close observation of the AFM height bar scale, z-axis, indicates that the voids start to get larger and larger as the deposition angle decreases, which leads to a conclusion that the inter-columnar spacing increases at steeper angles.

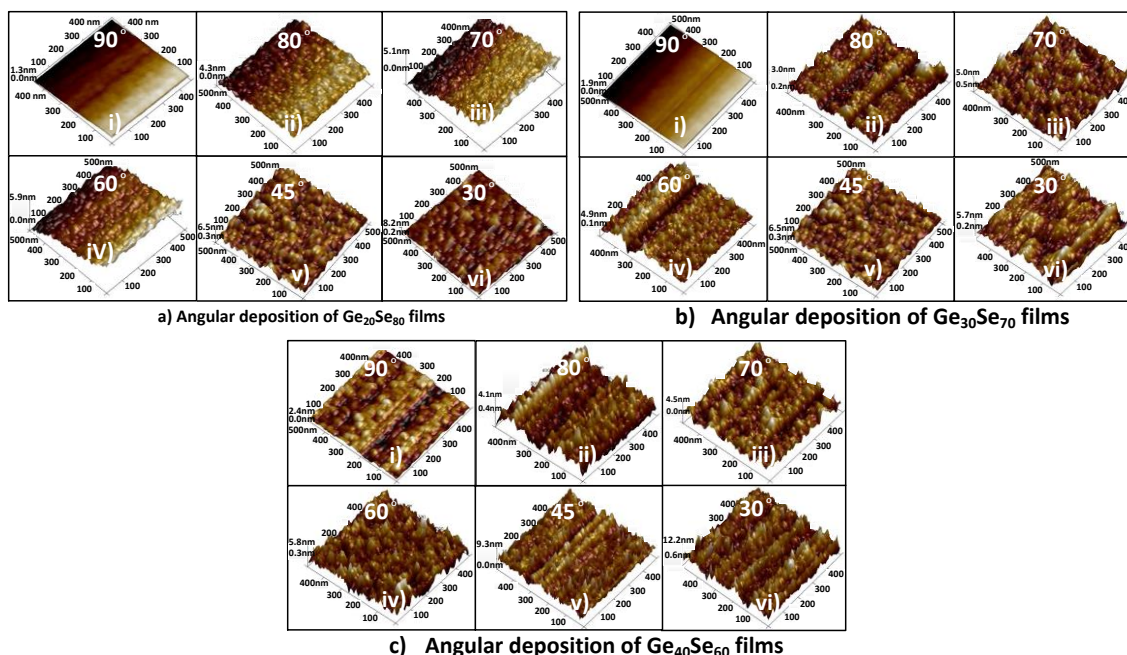


**Figure 4.22** AFM images for obliquely deposited (a)  $\text{Ge}_{20}\text{Se}_{80}$ , (b)  $\text{Ge}_{30}\text{Se}_{70}$ , and (c)  $\text{Ge}_{40}\text{Se}_{60}$  films under various angles: (i)  $\alpha = 90^\circ$ , (ii)  $\alpha = 80^\circ$ , (iii)  $\alpha = 70^\circ$ , (iv)  $\alpha = 60^\circ$ , (v)  $\alpha = 45^\circ$ , (vi)  $\alpha = 30^\circ$

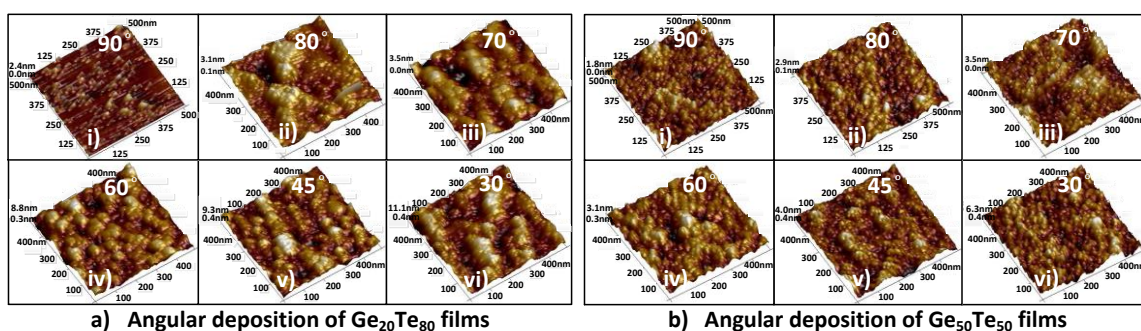


**Figure 4.23** AFM images for obliquely deposited (a)  $\text{Ge}_{20}\text{Te}_{80}$  and (b)  $\text{Ge}_{50}\text{Te}_{50}$  films under various angles: (i)  $\alpha = 90^\circ$ , (ii)  $\alpha = 80^\circ$ , (iii)  $\alpha = 70^\circ$ , (iv)  $\alpha = 60^\circ$ , (v)  $\alpha = 45^\circ$ , (vi)  $\alpha = 30^\circ$

In addition to studying the surface morphologies with AFM, the cross-sectional topography of the columnar structures were also studied. The SEM results for the columnar growth in the Ge-Se system with deposition angles of  $70^\circ$ ,  $45^\circ$ , and  $30^\circ$  and Ge-Te films with deposition angles of  $45^\circ$  were validated by AFM. The columnar structures, inclined towards the vapor flux in both the systems, are obvious in Figure 4.24 and

Figure 4.25. The details of the imaging method are explained in Chapter 5, along with electrical characterization of the devices, since this method was also used to verify the Ag growth filament through the columnar structure with no multi branching within the filament.

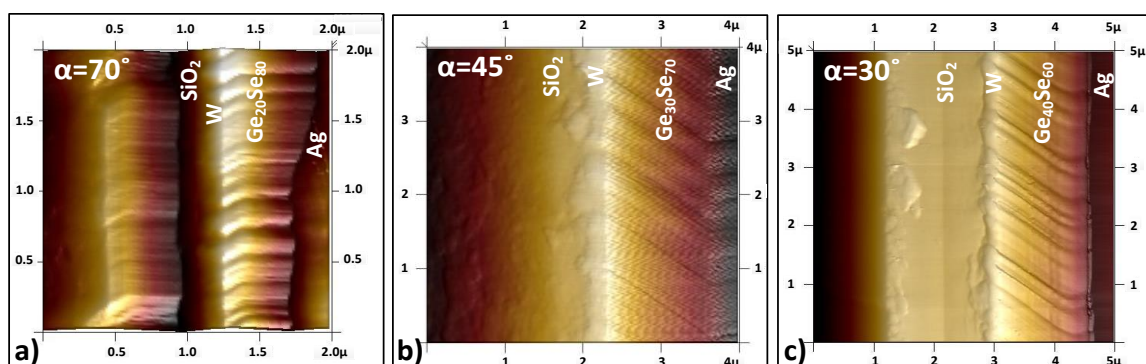


**Figure 4.24** AFM images of the columnar structure by scanning on the sample cross-section of (a)  $\text{Ge}_{20}\text{Se}_{80}$  at  $\alpha = 70^\circ$ , (b)  $\text{Ge}_{30}\text{Se}_{70}$  at  $\alpha = 45^\circ$ , and (c)  $\text{Ge}_{40}\text{Se}_{60}$  at  $\alpha = 30^\circ$

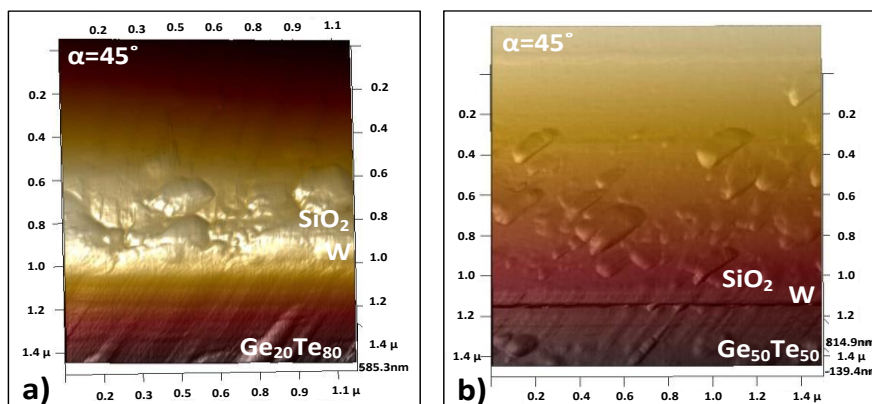


**Figure 4.25** AFM images of the columnar structure by scanning on the sample cross-section of (a)  $\text{Ge}_{20}\text{Te}_{80}$  at  $\alpha = 45^\circ$  and (b)  $\text{Ge}_{50}\text{Te}_{50}$  at  $\alpha = 45^\circ$

Since with decreasing the deposition angle the voids start to grow bigger, the surface roughness will be the smallest for the normally deposited films and will gradually increase as the deposition angle becomes smaller. The result was confirmed by analyzing the surface roughness of the obliquely deposited films over a  $5\mu\text{m} \times 5\mu\text{m}$  area on both the

Ge-Se and Ge-Te chalcogenide glasses and the results are presented in Figure 4.26 and Figure 4.27, respectively.

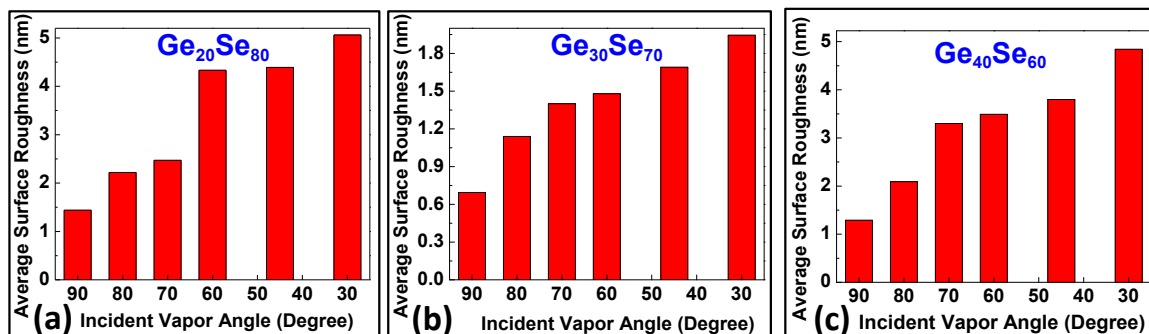


**Figure 4.26** Average surface roughness observed in (a)  $Ge_{20}Se_{80}$ , (b)  $Ge_{30}Se_{70}$ , and (c)  $Ge_{40}Se_{60}$  films under different depositions angles

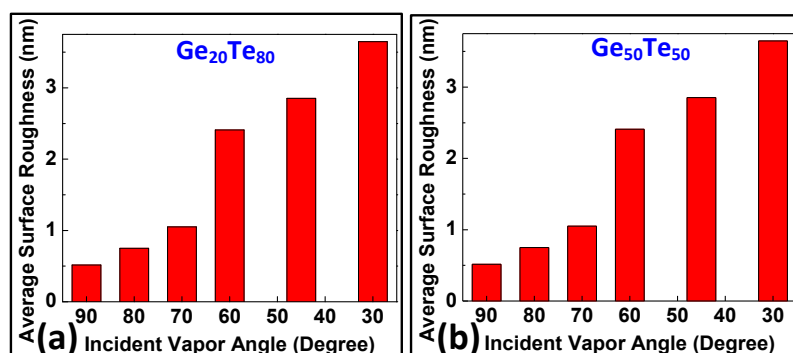


**Figure 4.27** Average surface roughness observed in (a)  $Ge_{20}Te_{80}$  and (b)  $Ge_{50}Te_{50}$  films under various deposition angles

However, it should be noted that the increased surface roughness with decreasing the deposition angle was to a great extent a relative effect related to the availability of pores, while the contact surface with the electrodes was not much affected by the deposition method.

#### Compositional Analysis of Obliquely Deposited Films

Since the device performance is dependent on the composition, it was important to study the compositional variations caused by altering the incident vapor angle.

Investigation of Ge-Se films compositions as a function of vapor incident angle is presented in Figure 4.28. The composition of the normally evaporated films ( $\alpha = 90^\circ$ ) is equal to the source composition for the  $\text{Ge}_{30}\text{Se}_{70}$  and  $\text{Ge}_{40}\text{Se}_{60}$  while the Se richest films with source composition  $\text{Ge}_{20}\text{Se}_{80}$  was Se depleted as the normally deposited films contained 75 at% Se. For  $\text{Ge}_{40}\text{Se}_{60}$  composition, the Se concentration decreased with the decrease in incident vapor flux angle, whereas for the other two compositions, an opposite trend was observed; that is, the Se concentration increased as the incident vapor flux arrived the substrate under lower angle. In the Ge-Te films, Figure 4.29, a decreasing trend is observed for  $\text{Ge}_{50}\text{Te}_{50}$  composition. However, no specific trend is observed in  $\text{Ge}_{20}\text{Te}_{80}$ .

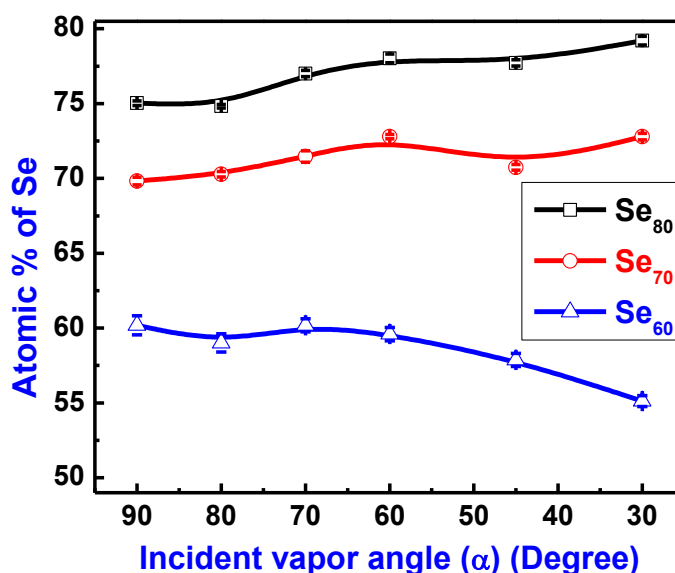


**Figure 4.28** Compositional analysis of  $\text{Ge}_x\text{Se}_{1-x}$  ( $x = 0.2, 0.3, 0.4$ ) films by altering the vapor flux angles

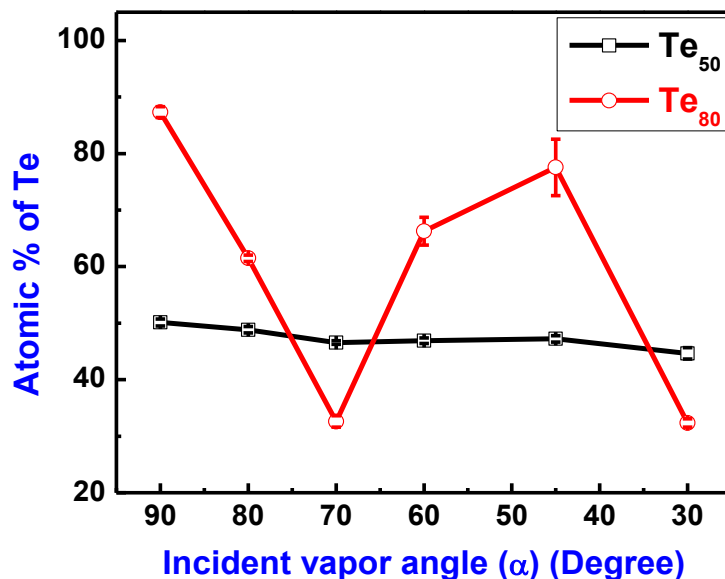


**Figure 4.29** Compositional analysis of  $\text{Ge}_x\text{Te}_{1-x}$  ( $x = 0.2, 0.5$ ) films by altering the vapor flux angles

The normally evaporated films ( $\alpha = 90^\circ$ ) are usually the standard for evaluating the evaporation technique. The results for  $\text{Ge}_{30}\text{Se}_{70}$  and  $\text{Ge}_{40}\text{Se}_{60}$  films in Figure 4.28 support the choice of the crucible and the evaporation rate since their compositions correspond to the source material. The Se rich samples resulted in Ge richer films, which is related to the high partial pressure of Se [178, 179] that contributes to repulsion of some Se atoms reaching the substrate with high energy. Evaporation of the Se rich compositions under oblique angles increased the Se content since, in these cases, the Se atoms reach the surface under a glancing angle, which reduces the energy of the interaction with the substrate and so reduces the repulsion of the Se atoms. The slight decrease of the Se content from the Ge rich films in the process of oblique deposition could be related to the full structural reorganization of these films, discussed in the Raman analysis section.

The deposition rate,  $D_d$ , for any system is dependent on the material to be evaporated, equilibrium vapor pressure and the geometry of the chamber [180]. The change in the compositions of the deposited material under oblique angles could also be related to partial pressure,  $P_e$  of the material being evaporated. Since, the partial pressure of Ge is much lower than Se [178, 179], in Se rich compositions ( $\text{Ge}_{20}\text{Se}_{80}$  &  $\text{Ge}_{30}\text{Se}_{70}$ ) the vapor flux will have more Se content at a given equilibrium vapor pressure ( $D_d \propto P_e$ ), thus increasing its concentration in the film. However, in  $\text{Ge}_{40}\text{Se}_{60}$  films, the Se concentration decreases as the source material becomes rich in Ge, resulting in a decrease of Se concentration as the vapor flux angle becomes small. The compositional results of  $\text{Ge}_{20}\text{Te}_{80}$  as a function of the deposition angle are inconclusive, which is related to the phase separation that occurs in this composition. It was determined through the experimental work that the evaporation rate for obliquely deposited films should be higher than for normally deposited films in order for the columnar structures to grow.

#### Raman Analysis of Obliquely Deposited Films

The Raman spectra of the obliquely deposited Ge-Se and Ge-Te films provided insight into the structural changes occurring in each film as a function of the vapor flux angle. The major result from these studies is that although the films had well expressed morphology, they were amorphous in their nature. Analysis of both systems is discussed separately as each system has its unique characteristics.

Raman spectra for  $\text{Ge}_{20}\text{Se}_{80}$ ,  $\text{Ge}_{30}\text{Se}_{70}$ , and  $\text{Ge}_{40}\text{Se}_{60}$  obliquely deposited films are depicted in Figure 4.30. In general, three regions in these spectra are distinguishable: (i) a relatively sharp high intensity band around  $197\text{cm}^{-1}$  along with a shoulder lobe around  $214\text{cm}^{-1}$ , (ii) a high intensity and broad spanning  $225$  to  $300\text{ cm}^{-1}$ , and (iii) a low intensity

band ranging from 305 to 330 $\text{cm}^{-1}$ . In the 1<sup>st</sup> region, the 197 $\text{cm}^{-1}$  band corresponds to symmetric stretching of Se atoms in Ge-Se-Ge linkages that are corner shared (CS) between  $\text{GeSe}_4$  tetrahedra while the 214 $\text{cm}^{-1}$  band corresponds to the breathing mode of a pair of Se atoms that are edge sharing (ES) two neighboring  $\text{GeSe}_4$  tetrahedra [181-185]. The frequency band in the 2<sup>nd</sup> region corresponds to the Raman characteristic spectrum of pure Se and is related to Se-Se stretching in Se chains and rings [186]. The last band is due to an asymmetric vibration in the  $\text{GeSe}_4$  edge shared tetrahedral [187]. In addition, the spectra of  $\text{Ge}_{30}\text{Se}_{70}$  and  $\text{Ge}_{40}\text{Se}_{60}$  reveal a sharp but low intensity band centered at  $\sim 178\text{ cm}^{-1}$ , which originates from Ge-Ge homopolar bond [188] related to the ethane-like structure (ETH). Also, in these two compositions, the band in 2<sup>nd</sup> region at 263 $\text{cm}^{-1}$  shifts to higher wavenumbers with increasing Ge content and, in the  $\text{Ge}_{40}\text{Se}_{60}$  film, both the initially resolved bands in the 3<sup>rd</sup> region ( $\sim 263$  and  $\sim 310\text{cm}^{-1}$ ) merge into a broad and intense band for films deposited under very low obliquely angle.

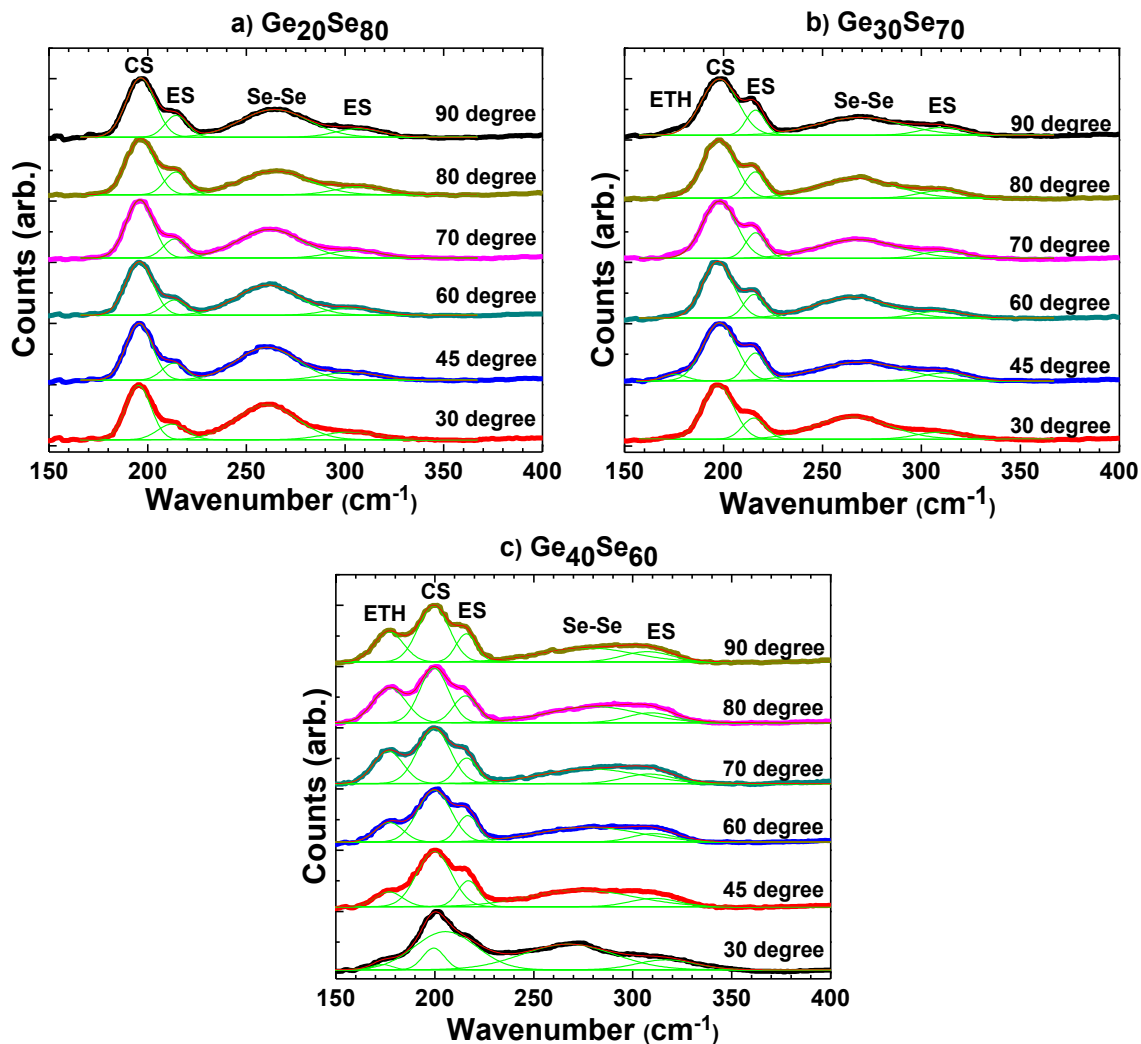


**Figure 4.30** Raman Spectra for obliquely deposited (a)  $\text{Ge}_{20}\text{Se}_{80}$ , (b)  $\text{Ge}_{30}\text{Se}_{70}$ , and (c)  $\text{Ge}_{40}\text{Se}_{60}$  films under different angles

The compositional results could be related to the structure of the films with the aid of Raman Spectroscopy studies. Raman spectra of  $\text{Ge}_{20}\text{Se}_{80}$  films show a clear red shift in CS frequency mode, characteristic for increased Se concentration [164] illustrated in the EDS data, with decreasing the deposition angle as shown in Figure 4.31a. This property is accompanied with an increase of the areal intensity of the Se-Se band vibration as shown in Figure 4.32a. The intensity of the vibrations for the CS mode increases in  $\text{Ge}_{20}\text{Se}_{80}$ , which suggests that the structure relaxes by enhancement of its

floppiness due to the formation of a three-dimensional network built predominantly by CS Ge-Se tetrahedra. This is indeed a structure that resembles the structure of the  $\text{Ge}_{20}\text{Se}_{80}$  bulk glass [164].

The structural data for the  $\text{Ge}_{30}\text{Se}_{70}$  films are ambiguous as the frequency mode of the CS undergoes variations, which are not in a clear dependence of the deposition angle. At the same time, the Se-Se areal intensity as well as the amount of Se in these films increases as a function of decreasing deposition angle, Figure 4.32a. There is not a clear dependence of these compositional changes related to changes of the areal intensity of the ES/CS structural units, Figure 4.32b. This suggest that, at this particular case, a phase separation occurs that keeps the equilibrium between the three dimensional Ge containing structural units with the Se-Se chains and rings. Similarly, phase separation has also been reported in [142].

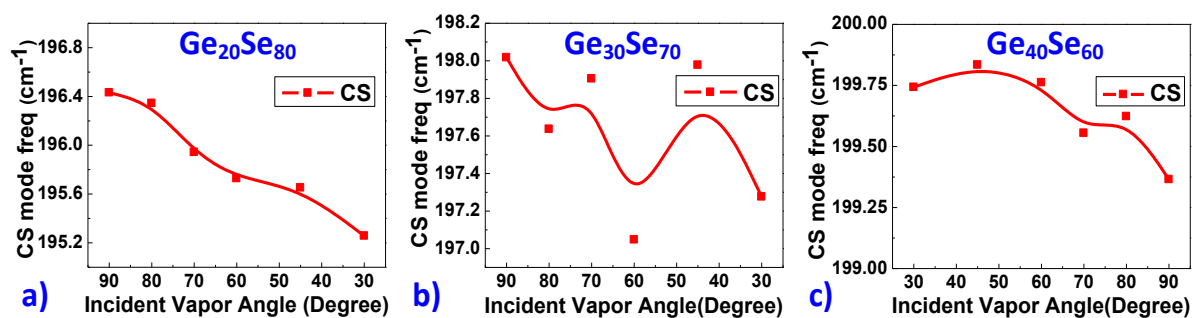


**Figure 4.31** Variations in CS-mode as a function of obliqueness angle in (a)  $\text{Ge}_{20}\text{Se}_{80}$ , (b)  $\text{Ge}_{30}\text{Se}_{70}$ , and (c)  $\text{Ge}_{40}\text{Se}_{60}$

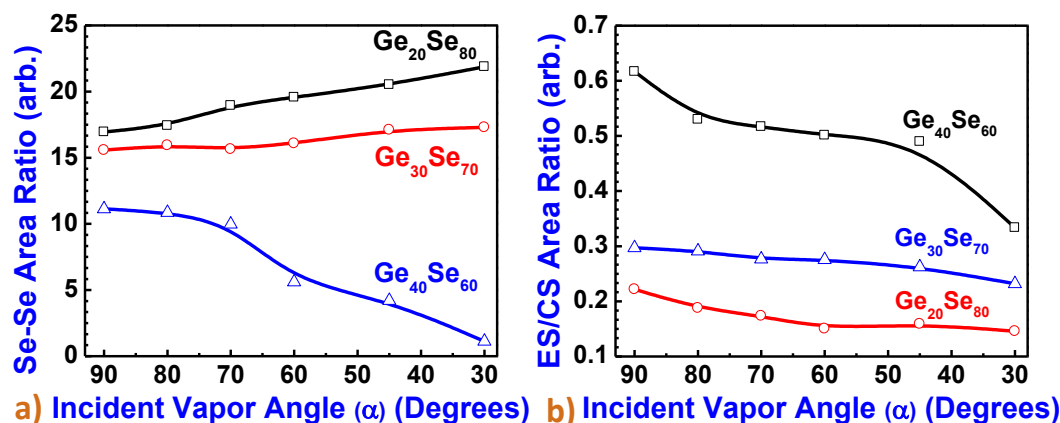


**Figure 4.32 Raman intensity area ratio of (a) Se-Se and (b) ES/CS bonding for Ge-Se system as a function of obliqueness angle**

The structural development for the Ge rich samples has an interesting development as a function of deposition angle. At normal angle deposition, it has a structure similar to the bulk material. However, after the deposition angle decreases, the structure degrades and cannot be fitted with the peaks characteristic for this stoichiometry. This composition is the representative of the Ge-Se glasses with the highest packing fraction [189], as presented in Figure 4.33. The packing stress is obviously released by destruction of the ETH structural units, which contributes to dense structural organization, which is relieved by formation of a tetrahedral structure with much bigger molecular volume. The stress release is the main reason for the structural reorganization as the angle decreases. A question may arise, what is building the column structures and how the structures are separated in the Ge-Se system? It is suggested that the columns are built by three-dimensional structural units containing Ge-Se tetrahedra connected in the inter-column space with Se-Se bonds.

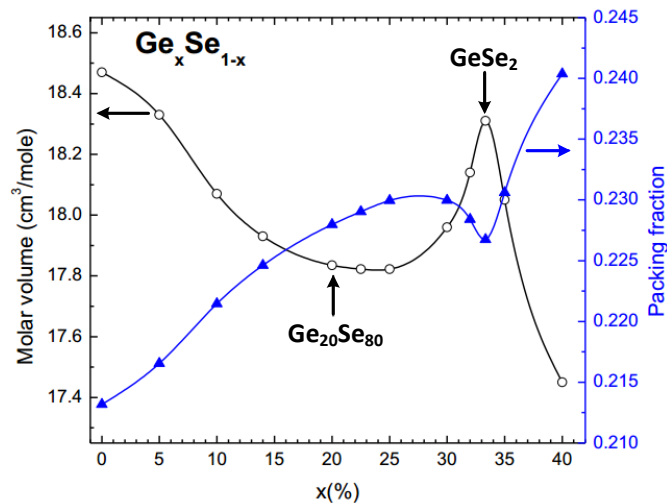


**Figure 4.33 Molar volume and packing fraction of Ge-Se glasses [189]**

The Raman spectra for  $\text{Ge}_{20}\text{Te}_{80}$  and  $\text{Ge}_{50}\text{Te}_{50}$  are presented in Figure 4.34. In both films compositions, there are three primary bands located at  $88\text{cm}^{-1}$ ,  $127\text{cm}^{-1}$ , and  $162\text{cm}^{-1}$  corresponding to rocksalt, corner-shared structure, and edge-shared structures, respectively. The other bands that are present at  $95\text{cm}^{-1}$  and  $118\text{cm}^{-1}$  correspond to the rocksalt and the corner shared structures. The aforementioned list of band locations, which have been ascribed in the fitted Raman results, are accepted as the primary bands for Ge-Te chalcogenide glass system. However, in  $\text{Ge}_{20}\text{Te}_{80}$ , films another peak arises at  $150\text{cm}^{-1}$ , which is attributed to the Te-Te bonding and is derived from the study of a-Te and c-Te material. The Raman spectra for a-Te reveals a peak at  $150\text{cm}^{-1}$ , while the crystalline phase produces a band at  $123\text{cm}^{-1}$ , therefore it can be concluded that  $\text{Ge}_{20}\text{Te}_{80}$  films are amorphous in nature due to the presence of this specific peak and shape without steep tops.

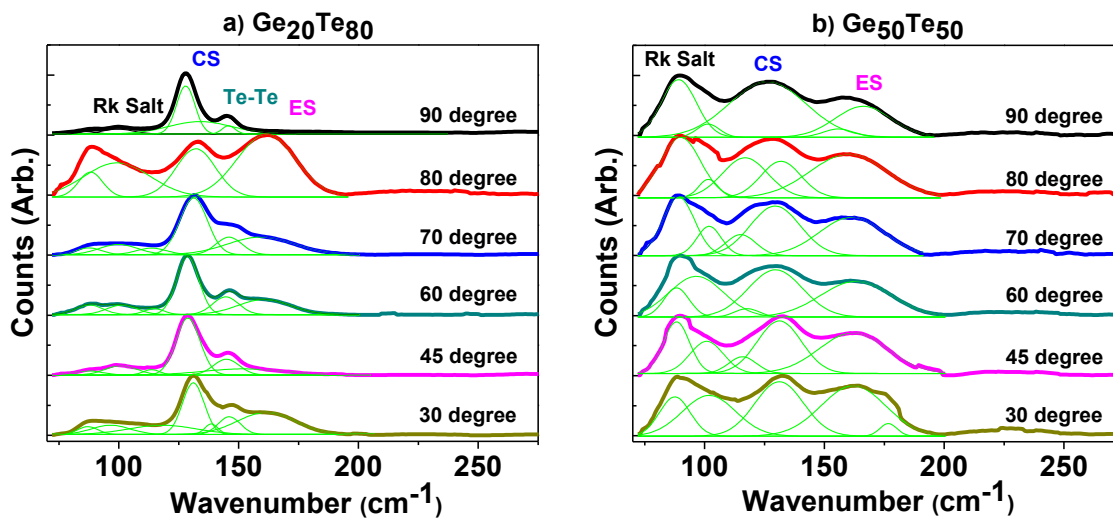


**Figure 4.34** Raman Spectra for obliquely deposited (a)  $\text{Ge}_{20}\text{Te}_{80}$  and (b)  $\text{Ge}_{50}\text{Te}_{50}$

In contrast to Ge-Se films, the deconvoluted Raman spectra in terms of the vibrational mode frequency, for the Te rich and Ge rich films, reveal structural changes occurring in the films as a function of altering deposition angle. A large shift is observed in CS mode (and of course others modes as well) as illustrated in Figure 4.35.

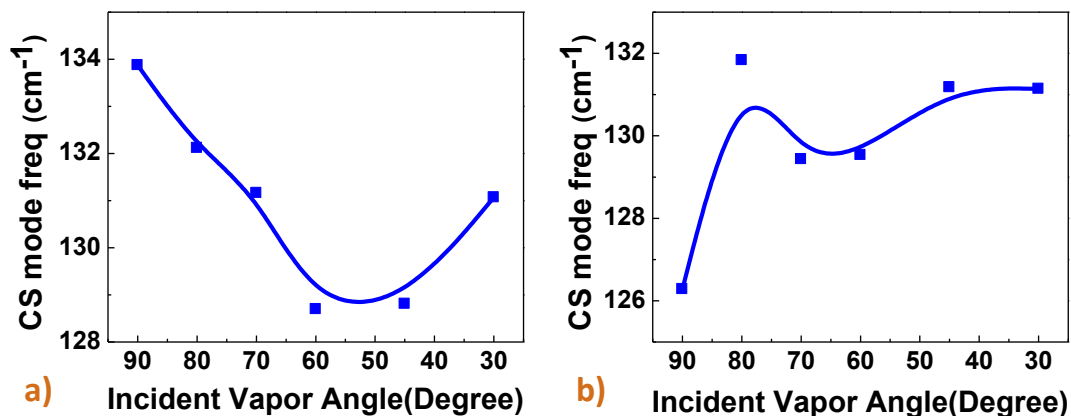


**Figure 4.35** Variations in CS-mode as a function of obliqueness angle in (a)  $\text{Ge}_{20}\text{Te}_{80}$  and (b)  $\text{Ge}_{50}\text{Te}_{50}$

The structural changes are better understood by plotting the area ratios of the corresponding modes, which are presented in Figure 4.36. Figure 4.36a illustrates a

decrease in the ES/CS structural units in Te rich samples with no significant changes in the Ge rich samples (Figure 4.36b). The Te rich films at  $\alpha = 90^\circ$  reveal no ES bonding, resulting in no data point for the ES/CS ratio in Figure 4.36a. The Te containing glasses offer a unique ability to analyze the rocksalt structure. In both Ge-Te compositions, a decrease in rocksalt bonding is observed by decreasing the deposition angle, with the Ge rich sample undergoing a larger change as illustrated in Figure 4.36b. Also, the homopolar bonding in Te rich films is observed to be less dominant in the normally deposited films. However, an increase in Te-Te bonding can be noticed in Figure 4.36a by decreasing the bonding angle. In the Ge rich films, no homopolar bonding is detected, as expected.

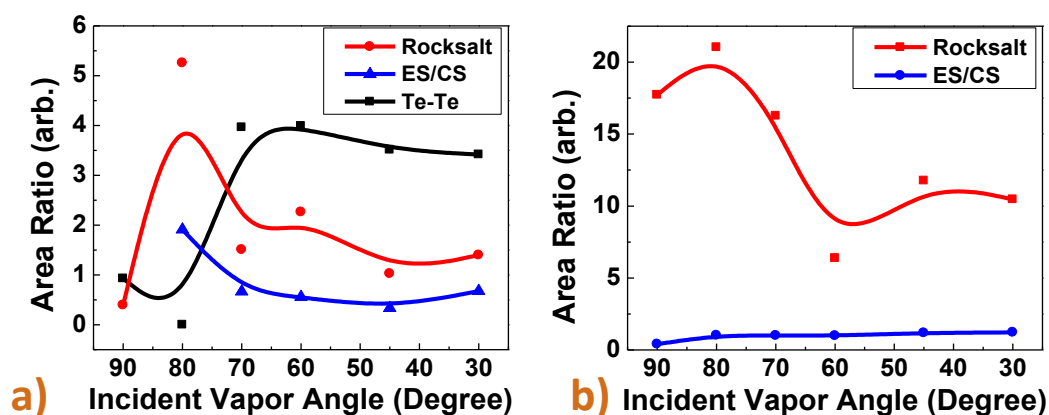


**Figure 4.36** Area ratio illustrating various bonds trends in (a)  $\text{Ge}_{20}\text{Te}_{80}$  and (b)  $\text{Ge}_{50}\text{Te}_{50}$  as a function of obliqueness angles

The observed changes in the rocksalt layered structure reveal that there is a structural transition after  $\alpha = 80^\circ$ , in both systems. Prior to this transition, the rise of the rocksalt is attributed to the local rearrangement of the structure and the beginning of the columnar formation. The columns that are formed at  $\alpha = 80^\circ$  can be due to the specific structure of the rocksalt units with a ternary coordinated Ge and Te. The further structural

reorganization with decreasing of the deposition angle suggests the occurrence of phase separation with similar composition specifics as in the system with Se, characterized by columns formed by tetrahedral structural units and inter-columnar space filled with Te chains.

### Summary

The surface morphologies, chemical compositions, and bonding structure of the PECVD deposited  $\text{Ge}_x\text{S}_{1-x}$  thin films and obliquely deposited thermally evaporated  $\text{Ge}_x\text{Se}_{1-x}$  ( $x = 0.2, 0.3, 0.4$ ) and  $\text{Ge}_x\text{Te}_{1-x}$  ( $x = 0.2, 0.5$ ) films were investigated in this chapter.

It was demonstrated that with the PECVD method for active layer deposition, the composition of the grown film could be controlled in a dynamic environment. The films obtained with this deposition method were relaxed and their structure resembled the bulk glasses with the same compositions. High quality films with smooth surfaces were possible using the PECVD method, which resulted in reliable and consistent device performance. Filling of the vias with a high aspect ratio was also demonstrated through this deposition method.

For the obliquely deposited Ge-Se and Ge-Te chalcogenide glasses, it was found that the deposition angle and deposition rate strongly influence the formation and inclination of columnar nano-structures. Examination of SEM images revealed that the nano-structures were composed of inclined column structures separated by voids between the adjacent structures. An increase in the surface porosity by decreasing the deposition angle was demonstrated through AFM. In the Ge-Se system, the Se rich films and the Ge rich films reacted differently to the obliquely deposited films. The composition of the

films deposited at normal incidence angle, changed by decrease of the deposition angle. The Raman results showed changes in the structure occurring in the obliquely deposited films due to formation of a phase separated material or the relief of the packaging stress in the particular composition. However, in Ge-Te chalcogenide matrix, structural reorganizations are recorded for  $\alpha \leq 70^\circ$ .

The materials characterization of the column structure films indicate that oblique angle deposition method is an effective technique for controlling the growth of the nano-columnar structures in thin films. Since the nano-columnar structure within the thin film strongly influences its electrical, optical, and mechanical properties, having control over the growth of these structures allows one to have a functional layer to control such properties for a wide practical applications without involving any additional cost in the fabrication line.

## CHAPTER FIVE: ELECTRICAL TESTING OF FABRICATED DEVICES

Aside from the process technology, the backbone of this work is to reflect the improvement achieved in the fabricated devices, by the suggested methods, with the electrical characterization of the devices.

### Quasi-Static Electrical Measurements

Quasi-static electrical measurements are used to characterize the basic electrical parameters of devices such as the resistance performance of the devices or their long-term voltage characteristics under a certain current load. The generated signal can also be employed as a control signal with a constant or time dependent voltage or current function to get insight into the device characteristics. Hence, the signal is an incremental step function and not continuous. Each step is divided into the delay time and integration time as illustrated in Figure 5.1. The former should be large enough to bring the sample into a static state after the preceding voltage step. The integration time is used to obtain several measurement values, which are averaged to suppress noise. The voltage signal starts at zero volts and increases with a predefined voltage step,  $V_{\text{Step}}$ , until it reaches the set maximum voltage level,  $V_{\text{max}}$ . Additional parameters that can be controlled during the measurements are the delay time,  $t_{\text{delay}}$ , which affects the integration time of the signal and the hold time,  $t_{\text{hold}}$ , which is set to have a wait time between subsequent measurements. Another important consideration for the test setup is to limit the current that flows through the device when the device is in low resistive state. This requirement is to protect

the devices from getting damage by overheating through excessive current and is achieved by limiting the current through the compliance current,  $I_{\text{compliance}}$  value.

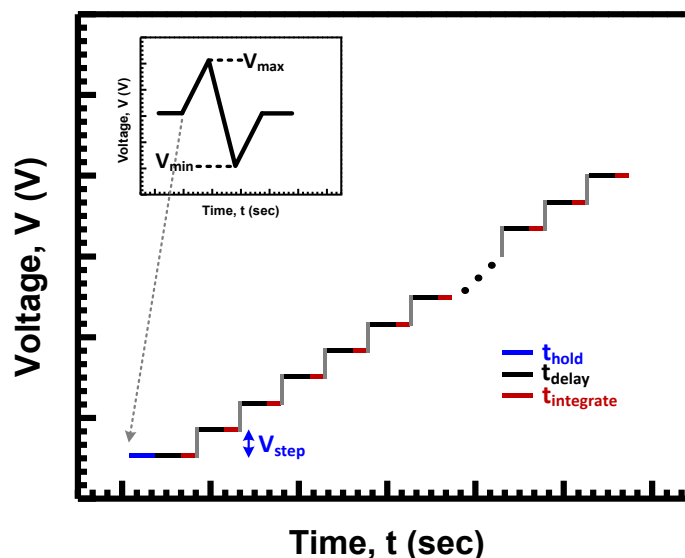


**Figure 5.1** Step increase in the voltage with voltage sweep from  $V_{\text{min}}$  to  $V_{\text{max}}$

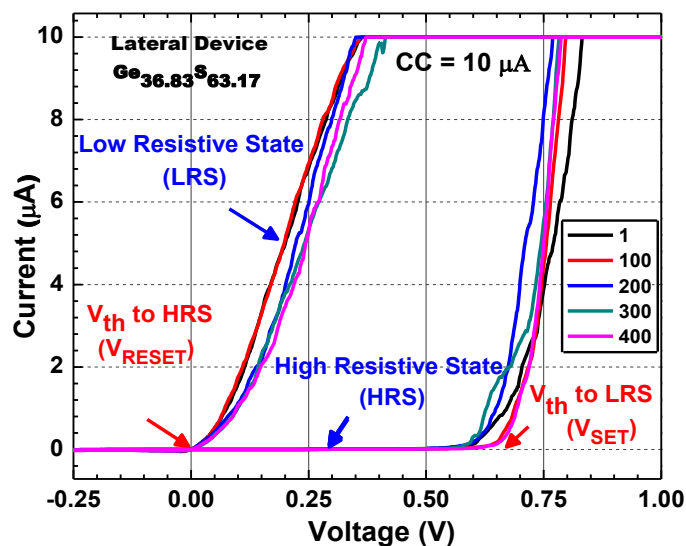
The current-voltage (IV) and the resistance-voltage (RV) measurements of the fabricated devices were carried out using the Agilent 4155B Semiconductors Parameter Analyzer equipped with triax cables to avoid residual charge buildup. The testing equipment (sample stage holder, triax cables, and probes) was placed inside a Faraday cage sharing a common ground to avoid static charge build up.

The devices were tested in dual sweep mode with various voltage step sizes ranging from of 2mV to 10mV and with different compliance current settings. Typically the integration time was set to MEDIUM with a hold time of 3 seconds between subsequent measurements. The double sweep voltage covers the entire device operation characteristics from write operation to erase operation. The IV measurements were carried out at room temperature, as well as higher temperatures (130°C) to test the device stability.

### Electrical Testing of PECVD Devices

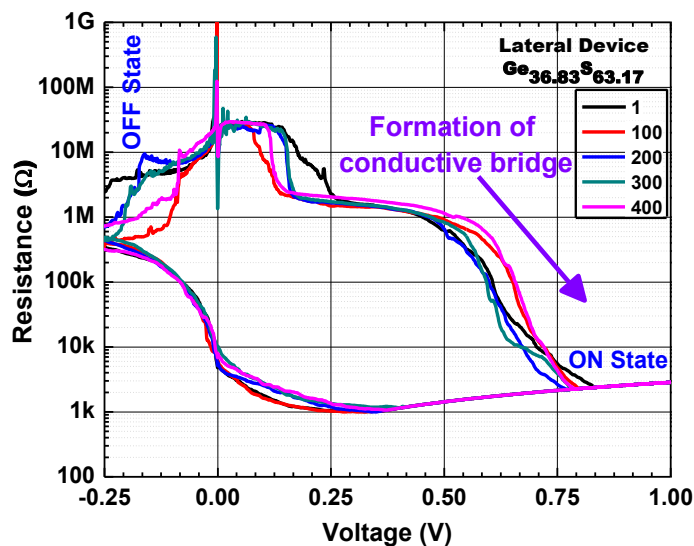
The IV sweeps of the electrical measurements conducted on the laterally fabricated devices with composition corresponding to sample 5 ( $\text{Ge}_{36.83}\text{S}_{63.17}$ ) are presented in Figure 5.2. This composition was selected as it offered the smoothest surface. Since the RCBM device operation is based on an oxidation and reduction principle, correct biasing of the device is vital to achieve the switching. Initially the devices are in the OFF state. During the dual sweep mode, in the forward sweep, the devices are written (SET State) by applying a positive potential to the Ag electrode and by grounding the Al electrode. Then in the backward sweep, the voltage on corresponding electrodes is reversed, which resulted in the erasing (RESET State) of the device state. 400 sweeps of the current-voltage (IV) characteristics of the PECVD devices are presented in Figure 5.2. Each cycle starts at  $-0.25\text{V}$ , the voltage first sweeps forward to  $+1\text{V}$ , and then sweeps back to  $-0.25\text{V}$ . The IV curves show a very uniform distribution of  $V_{\text{SET}}$  and  $V_{\text{RESET}}$  for the selected device.

Initially, when the device is in the OFF state, the cell is in a high resistive state. The resistance switches to a low resistance state when the threshold potential of approximately  $0.65\text{ V}$  is exceeded. At that moment, a conductive connection is formed between the top electrode and the bottom electrode, causing a steep increase in the current, until it reaches the compliance current limited to  $10\mu\text{A}$  (cell resistance: low).



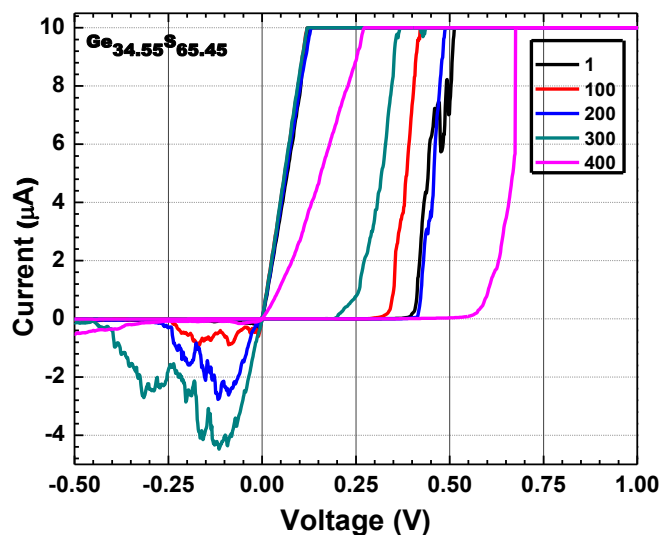
**Figure 5.2** IV curve of PECVD deposited lateral devices ( $\text{Ge}_{36.83}\text{S}_{63.17}$ )

Figure 5.3 illustrates the resistance voltage (RV) plot of the lateral device with dual sweep voltage. The plot shows four orders of magnitude difference between the ON and OFF state of the device. The resistance of the device varies from tens of mega-ohms in the OFF state to few kilo-ohms in the ON state, ensuring good retention of the device [190]. The fact of the formation of a second plateau on the RV characteristic suggests dual growth of a conductive filament in the active film. Lateral devices fabricated by the PECVD method showed relatively higher threshold voltage. The main reason for this is the larger distance between the two metal electrodes.



**Figure 5.3 Resistance vs Voltage Plot for lateral devices**

The largest surface roughness, in case of the PECVD technique, is observed in sample 3, having a composition of  $\text{Ge}_{34.55}\text{S}_{65.45}$ . The electrical performance of the device is presented in Figure 5.4. Even though the  $V_{\text{RESET}}$  of the device is consistent, the  $V_{\text{SET}}$  of the device fluctuates from 0.3V to 0.65V, emphasizing the importance of having a smooth surface at the chalcogenide/Ag interface.



**Figure 5.4 IV curve of PECVD deposited lateral devices ( $\text{Ge}_{34.55}\text{S}_{65.45}$ )**

The non-uniform switching can be explained by a rough surface at the chalcogenide/Ag surface, which results in switching voltage variations in the device. These rough areas consist of hillocks or pinholes at the surface, thus making those regions a preferential site for the conductive filament to grow. Having a lot of hillocks will result in a new nucleation site for each switching event, which will result in non-uniform switching. A schematic representation of this is presented in Figure 5.5, where a filament is formed at two different locations during the switching events. The preferential site for the filament to grow is where the distance is shortest between the two electrodes. The smooth film is also important as it will ensure good adhesion of Ag to the chalcogenide layer. Therefore, having a uniform Ge-S surface will help to improve the device performance considerably.

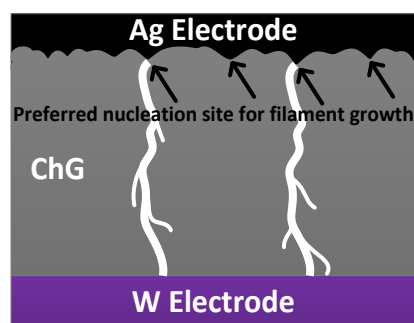
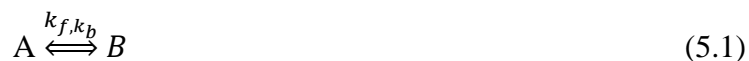


**Figure 5.5** Non-uniform switching due to surface roughness at Chalcogenide/Ag interface

The variation in the switching voltage can also be explained by an insight into the parameters affecting the formation of the conductive filament. The kinetics of the oxidation-reduction reaction between two substances A and B reacting with rate constants  $k$  can be expressed by equation 5.1, where  $k_f$  corresponds to a reaction rate in

forward direction (Oxidation) and  $k_b$  represents the reaction rate in the backward direction (Reduction):



The rate constants  $k$  can be expressed in Arrhenius form as:

$$k = A \cdot e^{-E_A/RT} \quad (5.2)$$

where  $E_A$  is activation energy,  $A$  is a constant,  $T$  is the temperature and  $R$  is the gas constant. The reaction rate kinetics can be explained with the help of Figure 5.6, which represents the standard free energy change of the reacting species in going from the metal electrode to solid electrolyte. The reaction coordinates express the progress of the reaction along a forward path, e.g. the position of the species with respect to the interface. The inclined barrier energies correspond to the respective activation energies of the oxidation  $E_{AO}$  and the reduction  $E_{AR}$ . Varying the electrode potential can vary the energy deviation and therefore the activation energy for the respective reaction, as indicated in Figure 5.6. Due to voltage dependence, current density can be associated with this interface as described in the Butler-Volmer equation [53, 54].

$$j = j_o \exp \left[ \frac{\alpha n F \eta}{RT} \right] - j_o \exp \left[ -\frac{(1-\alpha) n F \eta}{RT} \right] \quad (5.3)$$

where  $j_o$  is the exchange current density flowing in both the anodic and cathodic direction for equilibrium condition,  $n$  is the number of electrons involved in the reaction,  $F$  is the Faraday constant,  $R$  is the gas constant,  $T$  is the temperature,  $\eta$  is the potential deviation from the equilibrium voltage conditions and  $\alpha$  is the transfer coefficient, which depends on the shape of the intersection region of the energy curve in Figure 5.6. The exponential behavior of the rate constants  $k$  in equation 5.2 is reflected in the exponential behavior of the anodic and cathodic currents.

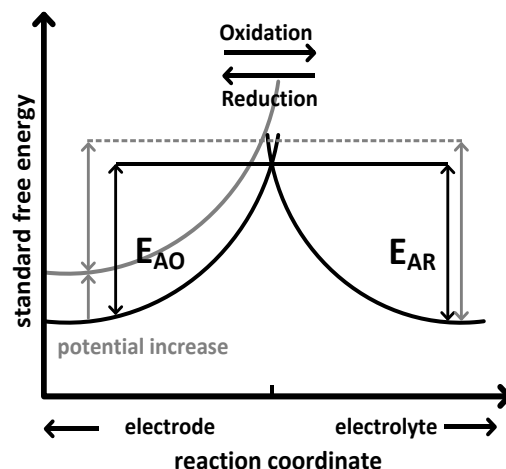


**Figure 5.6** Standard free energy changes during an electrode reaction [53]

To switch the RCBM device in the SET state, a certain amount of Ag is required to form the conductive bridge. This amount of Ag is proportional to the charge  $Q_0$  flowing through the device during a program (SET) operation. The quantity of silver ions generated at the metal electrode/electrolyte interface is determined by the over potential  $\eta$  and equation 5.3. To determine the ion current, one has to take into account the effective area that is involved in the ion generation process, which can be expressed as:

$$I = jA_{eff} \quad (5.4)$$

In equation 5.4,  $j$  is the net current density and  $A_{eff}$  is the effective area at the metal electrode/electrolyte interface taking part in the reaction. Since the entire electrode/electrolyte interface is not involved in the ion generation process, inhomogeneity of current density will occur. With a rough surface, each time the effective area participating in the ion generation process will vary, which will give rise to a different switching voltage, resulting in inconsistent switching during the SET process. However, with a smoother interface between the metal electrode and the solid electrolyte, it is expected that the effective area participating in the ion generation process will be the

same during each switching occurrence. This will result in uniform switching, even though the nucleation site may vary at each switching cycle.

### Thermally Evaporated Devices

Initially, Gen. 1 devices were fabricated with the standard process flow to optimize the process variations for device fabrication. These devices were fabricated by the process flow presented in Appendix A. The electrical characterization of the Gen. 1 devices is discussed in the following section.

#### Normally Deposited Film

The IV characteristics of the fabricated devices with normally deposited active layer and solid electrolyte formation is presented in Figure 5.7. The device enters the low resistive state at a threshold voltage of approximately 0.42V, indicating a conductive connection between the top and bottom electrodes, resulting in a steep increase in the current until it reaches the compliance current limited to 50nA.

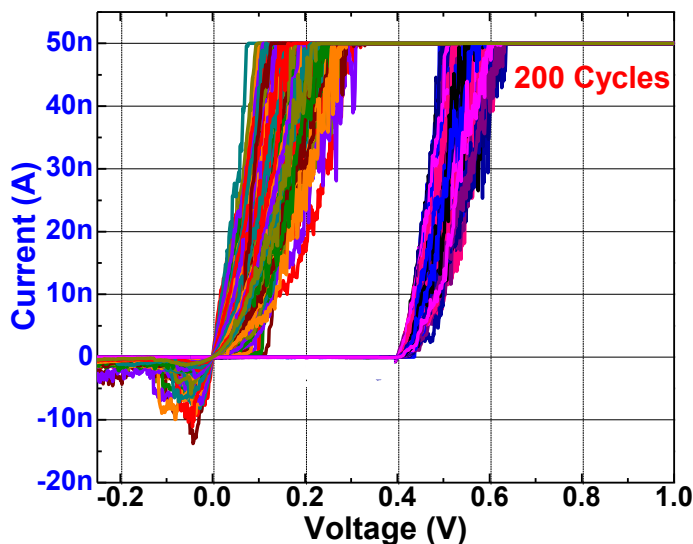


**Figure 5.7** IV Characteristics of RCBM devices with planar deposition and solid electrolyte formation

On the reverse voltage sweep, the bridge is partially dissolved, but during the next forward sweep, the bridge does not continue formation from the same location from which the previous filament was grown. This unpredictable filament growth through the solid electrolyte is the cause of unreliability in device performance. The operation of Gen. 1 devices with  $\text{Ge}_{40}\text{Se}_{60}$  film as the active layer lasted for approximately 1200 cycles. The devices did not switch to LRS even by increasing the forward voltage sweep to 5V after 1200 cycles, as shown in Figure 5.8. Since with the solid electrolyte area underneath the entire Ag pad, a time will be reached when all the Ag is diffused into the underlying film, which explains the shortcoming in the Gen. 1 devices process flow.

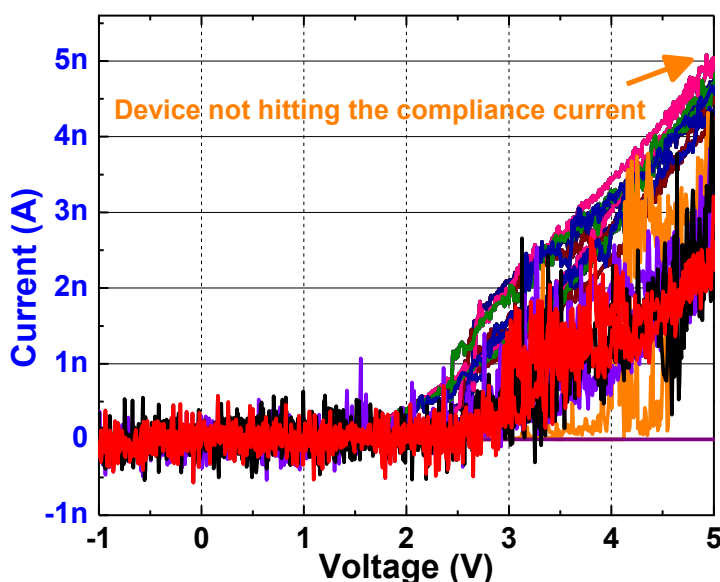


**Figure 5.8** IV characteristic for the device not turning on after 1200 cycles

The failure of the Gen. 1 devices can be attributed to the significant amount of free volume available in the chalcogenide glass film. Chalcogenide glasses are amorphous material with varied regions of high and low density of material in addition to voids within the structure. The amount of free volume space available in Ge-Se system is

around 10-15% [191] with  $\text{Ge}_{33}\text{Se}_{67}$  offering the most free volume space [192]. This free volume within the glass structure provides ideal locations for silver ions to move and reside, which contributes to the ionic conduction. Numerous models have been proposed to suggest the preferential path for ionic conduction [193, 194]. A generalized schematic representation the free volume concept in amorphous chalcogenide system is presented in Figure 5.9. The size of the silver ion is significantly small when compared to the size of the channels and voids, therefore the silver atoms have the ability to diffuse through these regions. Figure 5.9 illustrates two characteristic regions where silver can reside, labeled as A and B. The pathway, represented as region A in Figure 5.9, provides the preferential path for the filament growth. While region B represents isolated Ag islands, where the silver atoms within these regions are isolated from nearby pathways and cannot contribute to filament formation.

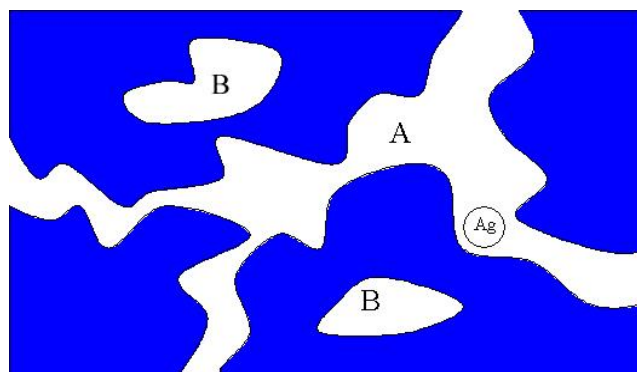


**Figure 5.9** Schematic illustration of free volume in silver doped chalcogenides [195]

Since there are multiple pathways within the chalcogenide structure for the silver filament to grow, during each switching event, the growth of silver filament will occur through an alternate path, which will result in non-uniform switching of the device.

Increasing the number of switching events will increase the probability for the formation of silver islands, which eventually lead to the failure of the device switching behavior.

In this research, this problem is dealt with by the formation of columnar structures within the active materials, which offered definite alleyways for the silver ions to follow, therefore improving the device performance.

### Columnar Structured Devices

The electrical characterization of the developed nano-structured columnar configuration application to the RCBM technology, Gen. 2 devices, with active layers of Ge-Se and Ge-Te films, deposited under different incident vapor flux angles are discussed in the following section. Gen. 2 devices were characterized mainly by the IV curves to ensure the endurance, data retention, multilevel switching, scalability, and speed of the devices. Controlling the devices threshold voltage based on the columnar structure inclination is also presented in this section, with temperature ramp measurements to check for the device stability at higher temperature.

### Endurance Measurements

The emerging resistive memories are targeting Flash applications, which require these devices to have an endurance of well over  $10^4$  switching cycles. The endurance measurements, for the fabricated RCBM devices, were carried out with the previously mentioned HP parametric analyzer setup (page 122). However, in order to achieve  $10^6$  switching cycles, a pulse generator having a time period of 50msec, in conjunction with the parameter analyzer, was used. The IV characteristics of  $\text{Ge}_x\text{Se}_{1-x}$  and  $\text{Ge}_x\text{Te}_{1-x}$  devices with nano-columnar structure are presented in Figure 5.10 and Figure 5.11, respectively.

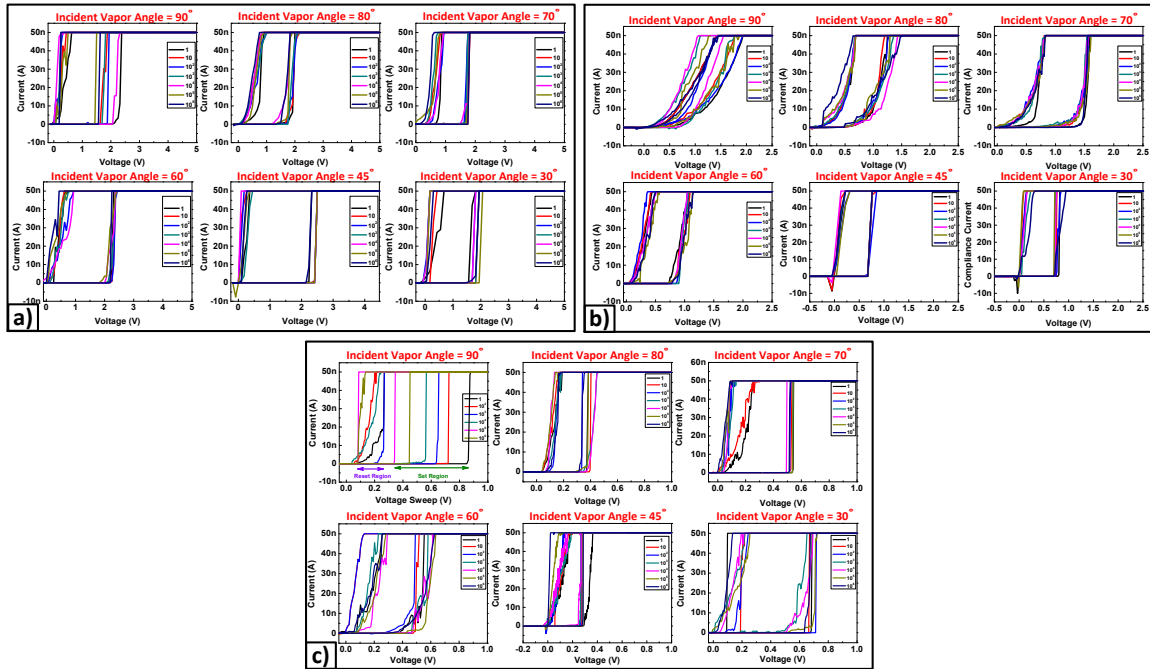


**Figure 5.10** IV curves for  $10^6$  cycles for (a)  $\text{Ge}_{20}\text{Se}_{80}$ , (b)  $\text{Ge}_{30}\text{Se}_{70}$ , and (c)  $\text{Ge}_{40}\text{Se}_{60}$  having nano-columnar structure in the active films under various incident angles: (i)  $\alpha = 90^\circ$ , (ii)  $\alpha = 80^\circ$ , (iii)  $\alpha = 70^\circ$ , (iv)  $\alpha = 60^\circ$ , (v)  $\alpha = 45^\circ$ , (vi)  $\alpha = 30^\circ$

In both the Ge-Se and Ge-Te active layers, a lot of variation is observed in the switching voltage of the normally deposited films. A significant improvement is observed in the devices' performance when fabricated with obliquely deposited active films. This improvement in the devices performance is achieved by steering the filament growth formation through the columnar structure. Close observations of the IV curves illustrate the write threshold voltage as a function of the deposition angle as well as the active layer compositions. It is important to reiterate that no photo diffusion step was performed for the angularly deposited films, thereby saving time, cost, and labor for an additional step.

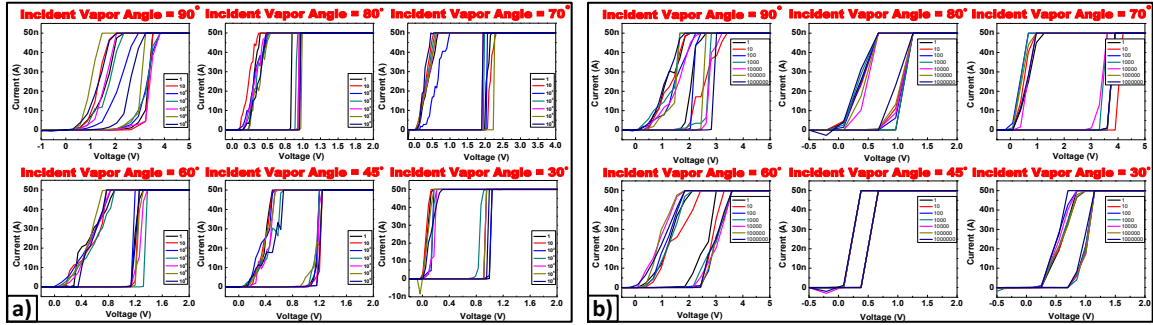


**Figure 5.11** IV curves for  $10^6$  cycles for (a)  $\text{Ge}_{20}\text{Te}_{80}$  and (b)  $\text{Ge}_{50}\text{Te}_{50}$  layers having nano-columnar structure in the active films under various incident angles: (i)  $\alpha = 90^\circ$ , (ii)  $\alpha = 80^\circ$ , (iii)  $\alpha = 70^\circ$ , (iv)  $\alpha = 60^\circ$ , (v)  $\alpha = 45^\circ$ , (vi)  $\alpha = 30^\circ$

Another improvement achieved with the nano-structured devices is the shift of programming threshold voltage to relatively higher voltages. In both systems, the devices switch to the ON state for a voltage higher than 0.6V. Hence, the probability of devices', embedded into the integrated circuit, falsely switching during an event of noise generation will be minimal. It can be inferred from the IV curves of both the chalcogenide systems that the obliquely deposited  $\text{Ge}_{20}\text{Se}_{80}$  devices are best suited for logic applications, since all the devices have a turn ON voltage of greater than 1V.

The devices with active column films show comparatively higher switching voltage, Figure 5.10 and Figure 5.11, compared to the photo-doped devices [44] with the same compositions. This can be attributed to the longer distance the ions have to travel for the formation of the filament and the reduction of the effective area taking part in the redox reaction. To accumulate the charge  $Q_o$ , the ion current expressed in equation 5.4 has to be effective for a certain programming time,  $t_{prog}$ . This relation can be expressed as

$$Q_o = A_{eff} j t_{prog} \quad (5.5)$$

Equation 5.5 can be written as:

$$t_{prog} = \frac{Q_o}{j A_{eff}} \quad (5.6)$$

Since with the formation of columnar structures in the devices active layer, the effective area,  $A_{eff}$ , participating in the silver ions generation is reduced, thus the time to program (write) of the RCBM devices increase, resulting in higher SET voltage of the device.

### Memory Window

Memory window, for RCBM devices, can be defined as the resistance difference between the ON and OFF states of the device. Mathematically, it can be expressed as:

$$Memory\ Window = R_{OFF} - R_{ON} \quad (5.7)$$

Having a good memory window will ensure a larger tolerance value for the read out bit stored in the RCBM cell, thus reducing the circuit complexity of the error correction bit. The reported resistive memory devices [21, 22] have shown two to four orders of magnitude difference between the two stable states.

In the column structured devices, no deterioration has been observed in the memory window. The devices, with both the Ge-Se and Ge-Te active layers, showed four to five orders of magnitude difference between the HRS and LRS as illustrated in the resistance-voltage (RV) plot in Figure 5.12 and Figure 5.13. The consistency in the switching voltage is also presented on the plot to highlight the improvement achieved in the devices by formation of such nano-structures.

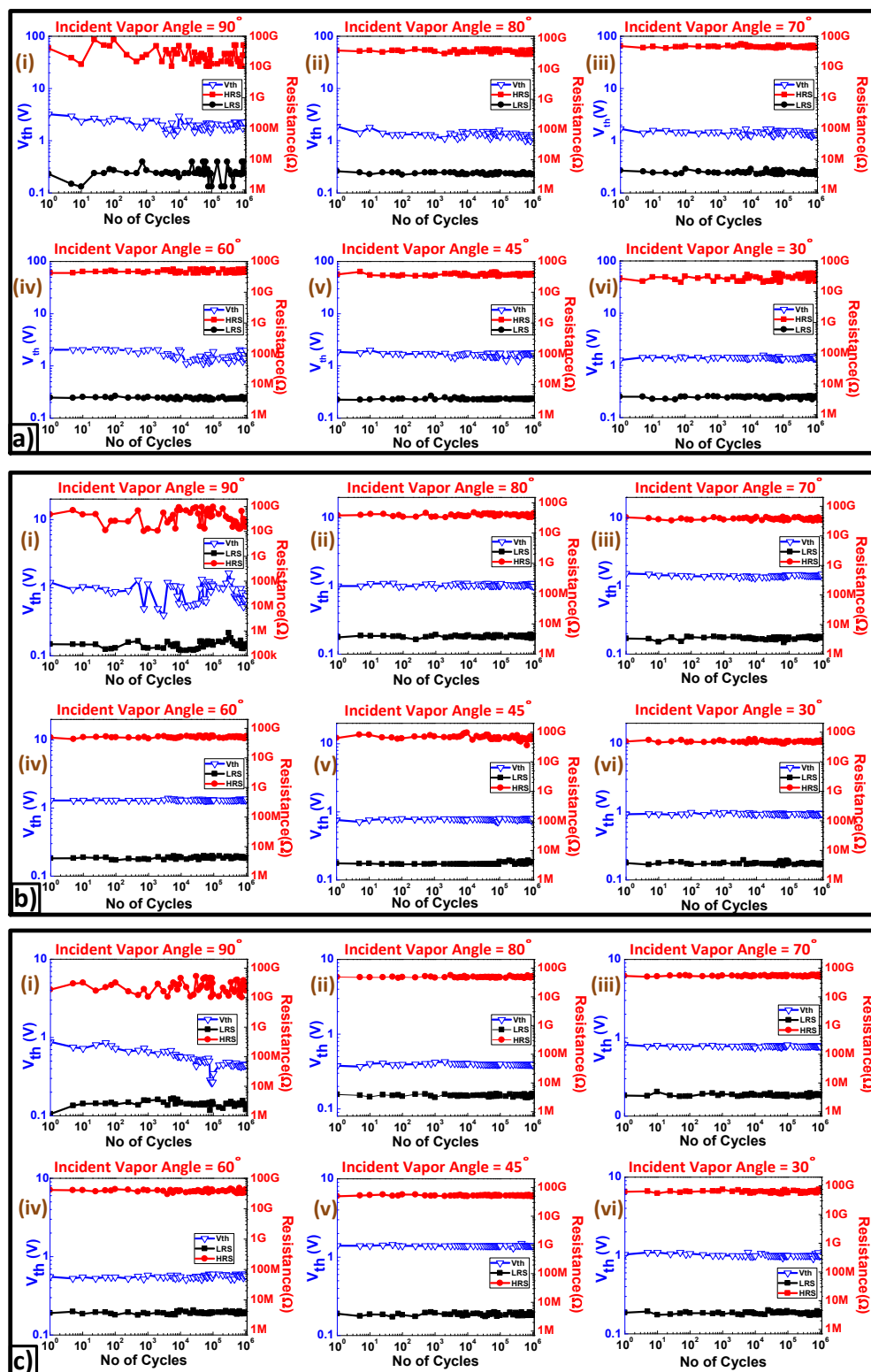
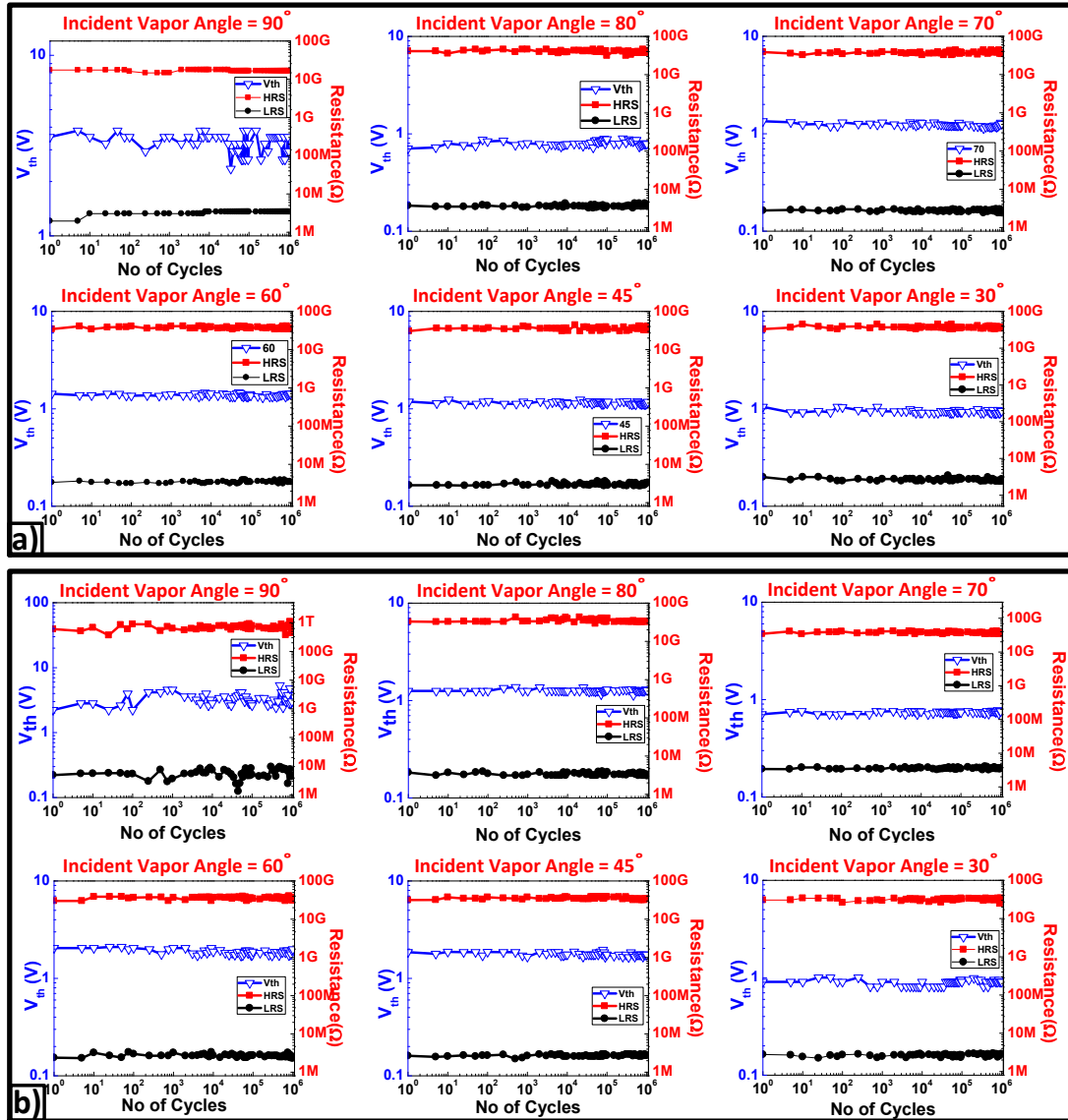


Figure 5.12 RV plot for  $10^6$  cycles for (a)  $\text{Ge}_{20}\text{Se}_{80}$ , (b)  $\text{Ge}_{30}\text{Se}_{70}$ , and (c)  $\text{Ge}_{40}\text{Se}_{60}$  films having nano-columnar structure in the active films under various incident angles: (i)  $\alpha = 90^\circ$ , (ii)  $\alpha = 80^\circ$ , (iii)  $\alpha = 70^\circ$ , (iv)  $\alpha = 60^\circ$ , (v)  $\alpha = 45^\circ$ , (vi)  $\alpha = 30^\circ$



**Figure 5.13** RV plot for  $10^6$  cycles for (a)  $\text{Ge}_{20}\text{Te}_{80}$  and (b)  $\text{Ge}_{50}\text{Te}_{50}$  films having nano-columnar structure in the active films under various incident angles: (i)  $\alpha = 90^\circ$ , (ii)  $\alpha = 80^\circ$ , (iii)  $\alpha = 70^\circ$ , (iv)  $\alpha = 60^\circ$ , (v)  $\alpha = 45^\circ$ , (vi)  $\alpha = 30^\circ$

#### Threshold Voltage Control with Oblique Angle

A unique advantage of the application of obliquely deposited active films in the RCBM cells is to have control over the turn ON voltage of the devices without involving any complex circuitry. Since the inclination of the growing structure is dependent on the incident vapor flux, altering the source vapor angle the column structure in the active

layer of the device also changes. The change in inclination of the columns provides different lengths for the growing filament, which affects the switching voltage. The switching voltage dependence of Ge-Se and Ge-Te system, on the obliqueness of the incident vapor flux, are presented in Figure 5.14 and Figure 5.15, respectively.

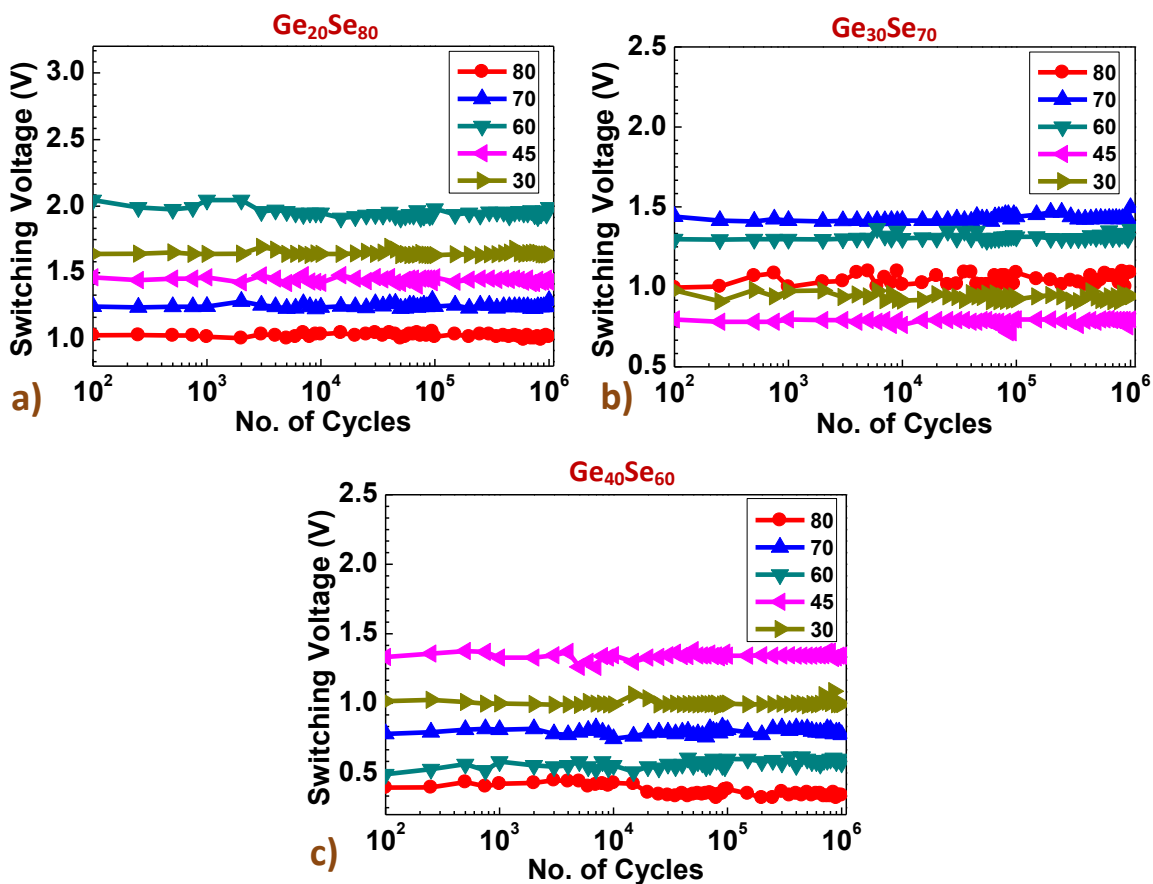
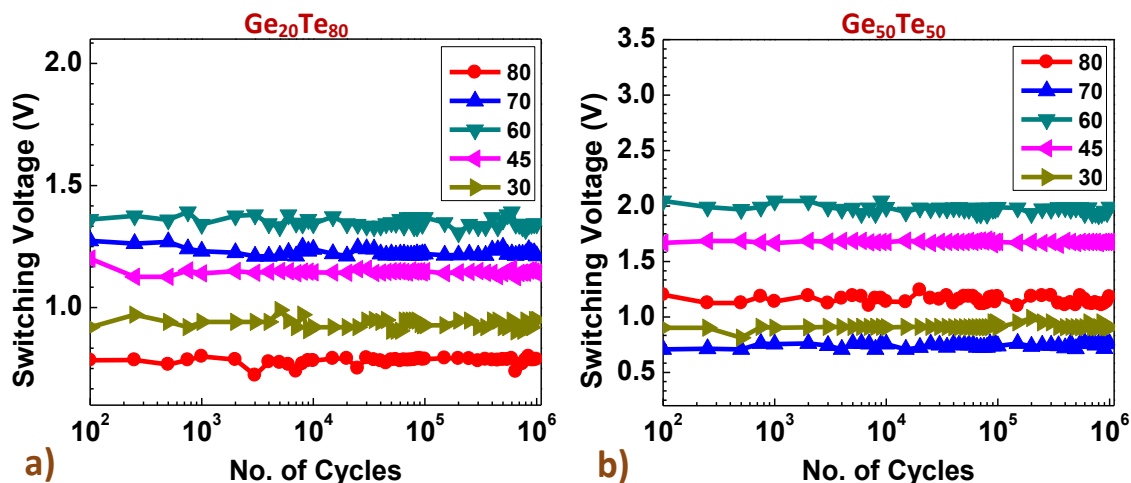


Figure 5.14 Switching voltage dependence on the incident vapor angle for (a)  $\text{Ge}_{20}\text{Se}_{80}$ , (b)  $\text{Ge}_{30}\text{Se}_{70}$ , and (c)  $\text{Ge}_{40}\text{Se}_{60}$  devices



**Figure 5.15** Switching voltage dependence on the incident vapor angle for (a)  $\text{Ge}_{20}\text{Te}_{80}$  and (b)  $\text{Ge}_{50}\text{Te}_{50}$  devices

Figures 5.14 and 5.15 demonstrate that there is a clear dependence of the threshold voltage upon the deposition angle. This gives an opportunity for prediction of the threshold voltage with the technological tools of films deposition. This dependence upon the angle does not go in the same way for all the compositions as it is related to their structural specifics compositional alterations influenced by the deposition angle as discussed in the Raman and EDS studies of the individual films. For example, the graphs demonstrate that the deposition angle affects the threshold voltage of the devices based on the Ge-Te system more compared to the Ge-Se based films. Indeed for the Ge-Te system, the structural transformations are much stronger, which affects the electrical performance of devices as well.

#### Switching Voltage Dependence on the Material

The benefit of depositing various active films compositions allows the flexibility to investigate the switching voltage dependence on different materials at the same deposition angles. Each composition under different incident vapor angle has a

characteristic turn ON voltage, allowing users the freedom of materials selection for different applications. Amongst the Ge-Se studied compositions, the  $\text{Ge}_{20}\text{Se}_{80}$  columnar devices deposited at  $\alpha = 60^\circ$  showed the highest ON switching voltage, whereas the smallest switching voltage was observed in  $\text{Ge}_{40}\text{Se}_{60}$  columnar devices deposited at  $\alpha = 80^\circ$ . The switching voltage dependence of Ge-Se and Ge-Te devices with nano-column structures are presented in Figure 5.16 and Figure 5.17, respectively. This dependence provides evidence about the stabilizing role of the ETH and rock salt structures in these materials since when such structure is available in the films, the fluctuations of the switching voltage with the deposition angle are the lowest.

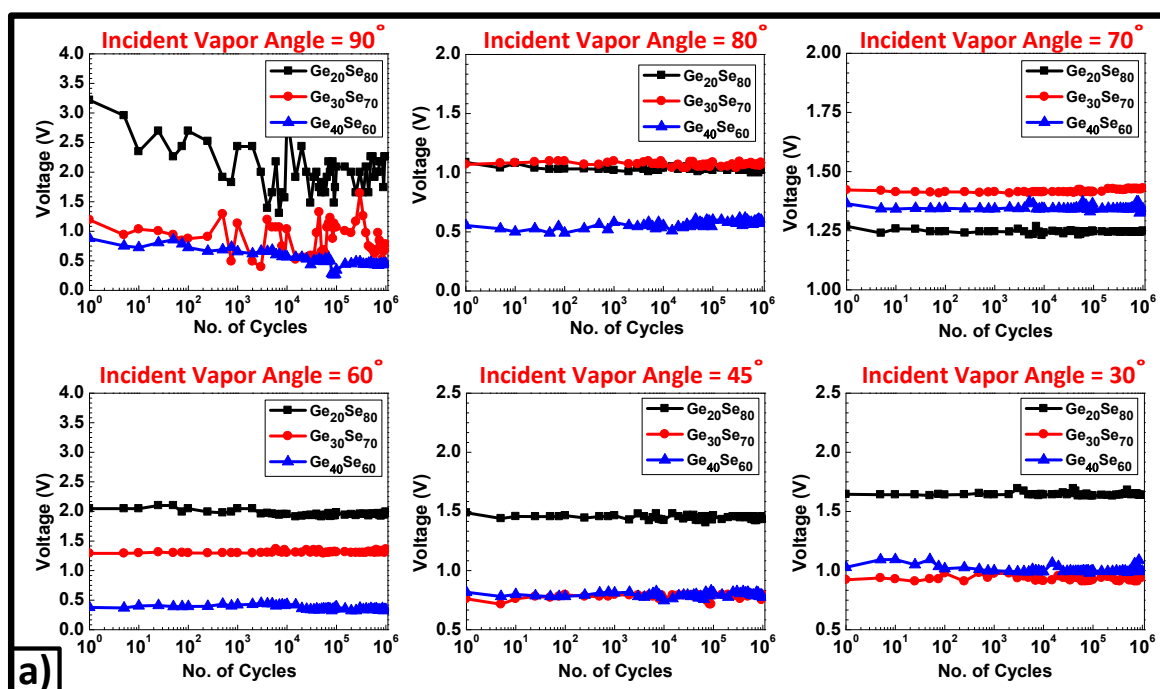


**Figure 5.16** Switching voltage dependence on the Ge-Se active layer materials and incident vapor flux angle

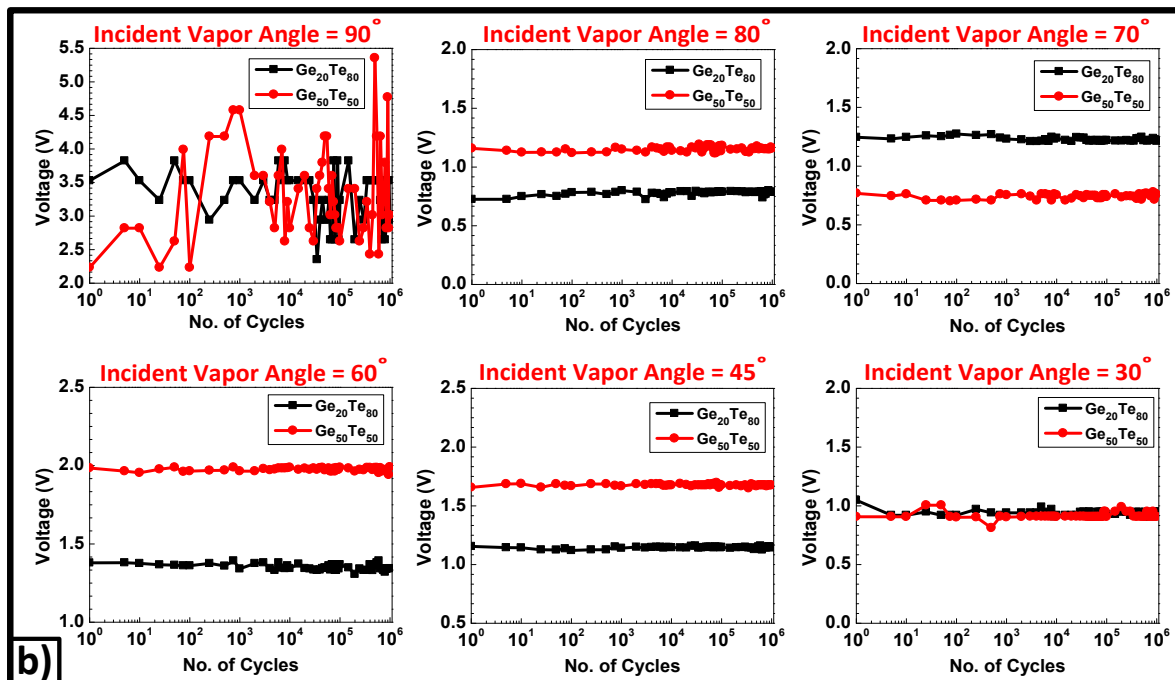


Figure 5.17 Switching voltage dependence on the Te-Se active layer materials and incident vapor flux angle

The dependence of the switching voltage on the incident vapor angle on the Ge-Se and Ge-Te compositions is presented in Figure 5.18.

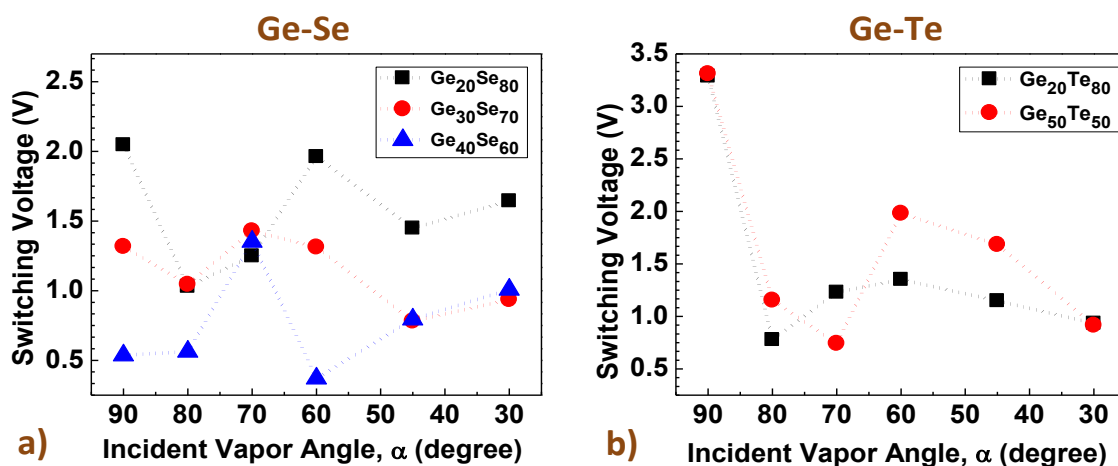


Figure 5.18 Switching voltage dependence on active layer incident angle for (a) Ge-Se and (b) Ge-Te system

In summary, quasi-static measurements of the devices with columnar structure active films showed an improved performance with uniform and stable switching voltages. The results demonstrate that a wide range of stable and reliable RCBM devices can be fabricated, by appropriate selection of material and incident vapor obliqueness angle, for specific applications.

### Higher Temperature Measurements

In addition to the reliable device performance, the operating temperature range specified for existing memory technologies have to be investigated for the devices to be commercially viable. The specified temperature range for guaranteed performance of Flash and DRAM commodities are  $-30^{\circ}\text{C}$  to  $80^{\circ}\text{C}$  and  $0^{\circ}\text{C}$  to  $95^{\circ}\text{C}$  [196-199], respectively. The fabricated RCBM devices were tested at  $130^{\circ}\text{C}$  only, which is well above the required specifications of the developed memory technologies. The low temperature testing was not accomplished due to the non-availability of the appropriate equipment. The higher temperature testing was achieved by holding the sample onto the stage, which was heated using a thermal resistance heater. The devices' memory window, for both the Ge-Se and Ge-Te columnar devices, did not show any significant degradation in performance. However, a slight change is observed in the switching threshold voltage at higher temperature compared to room temperature, which is attributed to thermal activation of the electrochemical process for filament formation. Also, heating the sample to higher temperatures results in higher silver ion movement during the conductive bridge formation due to which the filament does not grow in a usual directional manner; rather, the Ag filament does form by traversing through the voids between the columnar structures, resulting in some variation between consequent sweeps. The switching voltage

and memory window performance of the fabricated Ge-Se and Ge-Te nano-columnar structure devices for 500 cycles are presented in Figure 5.19 and Figure 5.20, respectively.

Except for  $\text{Ge}_{20}\text{Se}_{80}$  columnar device, Figure 5.19a, all the devices successfully completed the 500 cycles of testing at the elevated temperature. Amongst the studied compositions,  $\text{Ge}_{20}\text{Se}_{80}$  has the lowest glass transition temperature,  $T_g$  ( $\sim 160^\circ\text{C}$ ). Heating the  $\text{Ge}_{20}\text{Se}_{80}$  devices closer to  $T_g$  may have altered the active layer of the film, resulting in device failure as seen Figure 5.19a. EDS results showed that by reducing the deposition angle Se concentration increases in  $\text{Ge}_{20}\text{Se}_{80}$  films, which suggest an improvement in the performance of these devices, due to a possibility of netting the structure with Se chains. All other devices achieved the 500 testing cycles without failure. Close observation of the high resistive state reveals a slight decrease in its state, which is in accordance with the expected behavior, i.e. increasing the temperature multiplies the number of charge carriers in a p-type semiconductor, thus enhancing the Ge-Se and Ge-Te conductivity and therefore reducing the corresponding resistance.

Despite of this reduction in the high resistive value, still more than four orders of magnitude difference is observed in the ON and OFF state of the devices. Hence, no additional temperature sensing circuitry is required to reduce the read out error. On the basis of presented data, reliable performance of RCBM cells is expected in the temperature range that is standard for the memory applications.

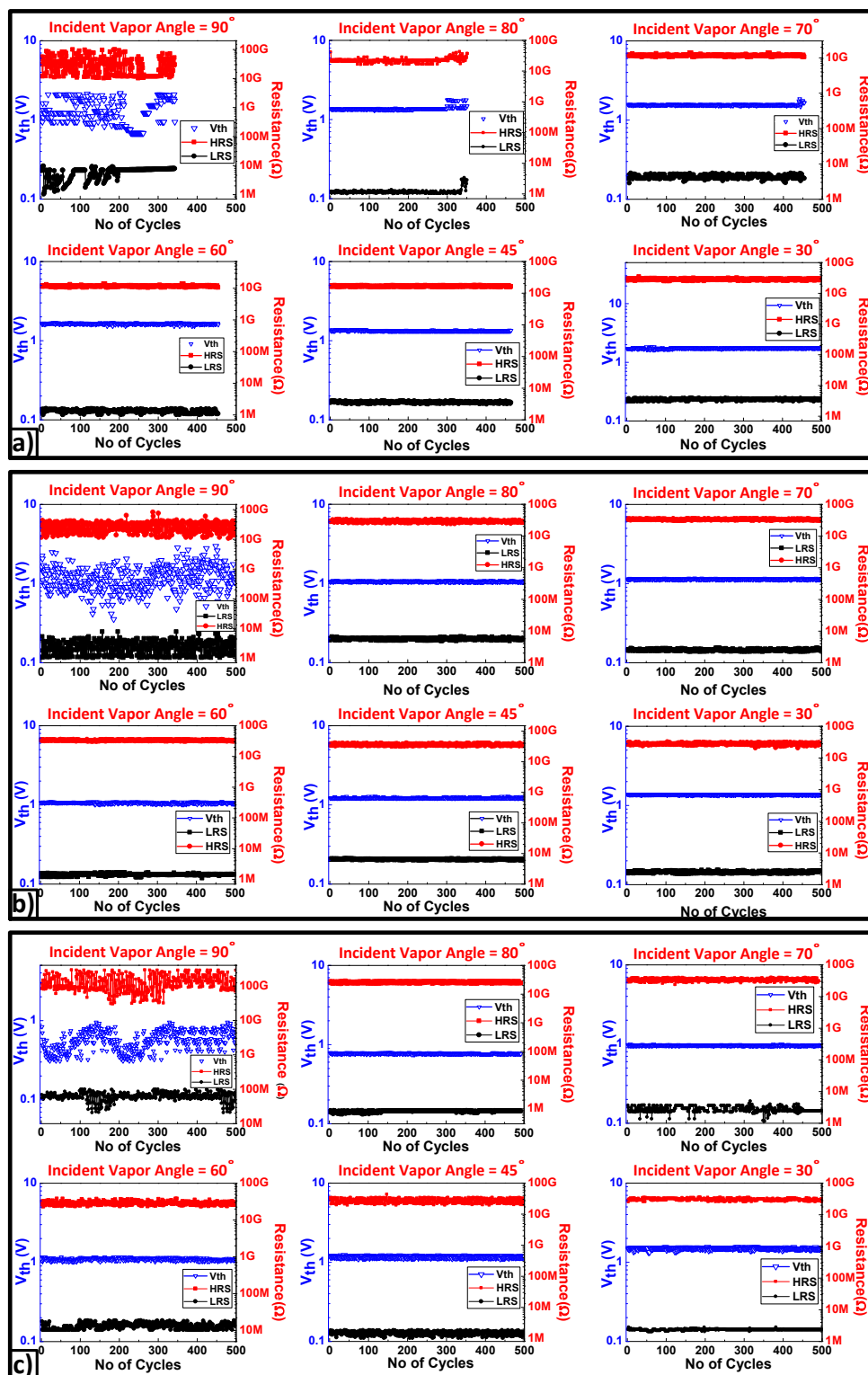
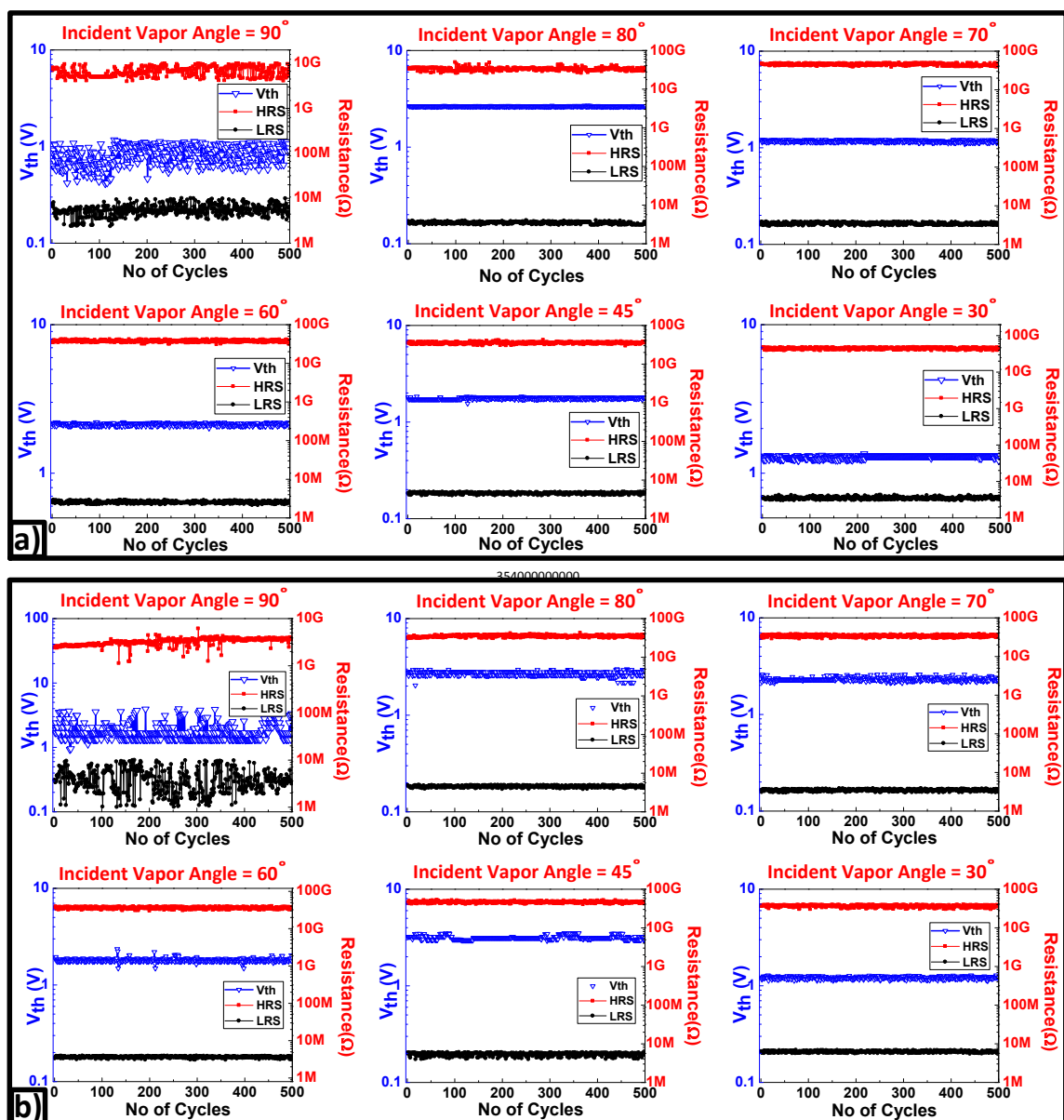


Figure 5.19 500 cycles of RV plots for (a)  $\text{Ge}_{20}\text{Se}_{80}$ , (b)  $\text{Ge}_{30}\text{Se}_{70}$ , and (c)  $\text{Ge}_{30}\text{Se}_{70}$  films having nano-columnar structure in the active films under various incident angles



**Figure 5.20** 500 cycles of RV plots for (a)  $\text{Ge}_{20}\text{Te}_{50}$  and (b)  $\text{Ge}_{50}\text{Te}_{50}$  films with nano-columnar structure in the active films under various incident angles

### Retention Testing

The stability of the memory states of the fabricated column structured devices were analyzed through retention measurements. The devices were programmed to the low resistive state by setting the compliance current to  $10\mu\text{A}$  with a step size of  $10\text{mV}$  in a single forward sweep direction. Once the devices were programmed, the change in state

of the device would occur only when the conductive filament deteriorates over time. The fabricated devices were tested for retention properties at 90°C and 130°C to predict the device's lifetime [22, 200]. The state of the programmed devices was detected by reading the state of the cell with the parameter analyzer at specific times with a read voltage ranging from 0.3V to 0.5V. The retention testing was performed on one column structured device from each composition and the results are presented in Figure 5.21. Since the high resistive state of the devices is above the resolution limit ( $10^{10}$  ohms), the devices were tested for their retention property in low resistive state only. The experimental results reveal the stability of the column structured devices in low resistive state to be more than 10 years [22].

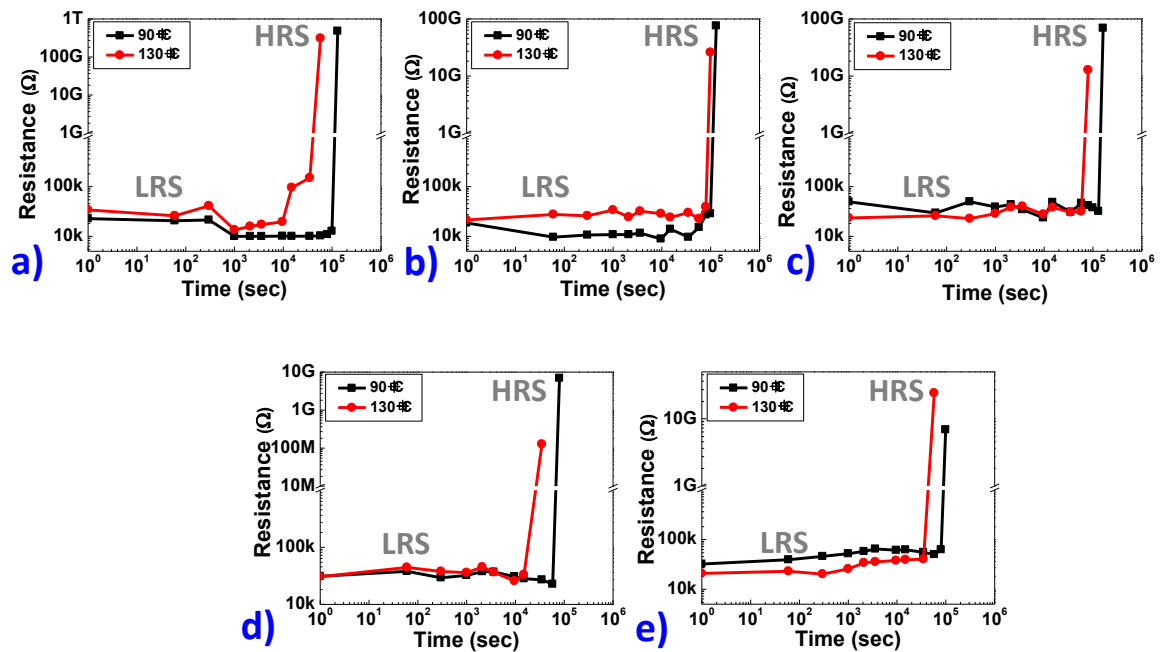


**Figure 5.21** Data retention of low resistive state of the devices written at a compliance current value of  $10\mu\text{A}$  for (a)  $\text{Ge}_{20}\text{Se}_{80}$  with  $\alpha = 80^\circ$ , (b)  $\text{Ge}_{30}\text{Se}_{70}$  with  $\alpha = 60^\circ$ , (c)  $\text{Ge}_{40}\text{Se}_{60}$  with  $\alpha = 45^\circ$ , (d)  $\text{Ge}_{20}\text{Te}_{80}$  with  $\alpha = 30^\circ$ , and (e)  $\text{Ge}_{50}\text{Te}_{50}$  with  $\alpha = 30^\circ$  devices. The data for the written bit is read at voltage ranging from 0.3V to 0.5V

The tested devices show that the low resistance state was preserved for  $\sim 10^5$  seconds at  $90^\circ\text{C}$  and  $130^\circ\text{C}$ . The failure of the devices over time can be associated with the silver diffusion mechanism.

A silver conductive bridge is formed by programming the RCBM cell to the Set state. Due to high silver concentration in the conductive path, a lateral diffusion of the silver atom may occur over time at higher temperature. This lateral diffusion of silver is due to diffusion coefficient dependence on silver concentration, which can vary by almost 10 orders of magnitude, with variation in silver concentration ranging from 0% to 25%. Since the silver electrode has the highest concentration of silver, it causes diffusion of silver from the top electrode to form the conductive path, which has a high silver concentration and corresponding higher diffusion coefficient. With the applied bias, while the lateral diffusion is weakening the conductive bridge, the silver diffusion from top electrode is strengthening it. During the retention testing, the devices were written only once and were being read continuously, thus the lateral diffusion outweighs the silver concentration in the filament, causing ruptures in it, which eventually results in device failure. However, in the columnar structure devices, the filament grows through inter-columnar voids, which helps to diminish the lateral diffusion effect, therefore enhancing the retention performance of the fabricated devices.

The accelerated tested devices for retention properties can be interpolated with Arrhenius theory to predict the actual lifetime of the devices.

$$AF = e^{-\frac{E_a}{k}\left(\frac{1}{T_2} - \frac{1}{T_1}\right)} \quad (5.8)$$

Where AF = Acceleration Factor

$E_a$  = Activation Energy

$k$  = Boltzmann's Constant

$T_1$  = Application junction temperature in Kelvin

$T_2$  = Accelerated stress junction temperature in Kelvin

Depending on AF, a back calculation using the Arrhenius equation for any desired temperature leads to fairly accurate data retention times. As stated earlier, the fabricated devices were tested for retention at 90°C and 130°C. Prior to testing, the samples were subjected to high temperature for 96 hours. The purpose of this was to determine data retention at higher temperatures and calculate expected data retention at 25°C.

$$AF = e^{-\frac{E_a}{k}\left(\frac{1}{T_2} - \frac{1}{T_1}\right)} = e^{-\frac{0.67}{8.623 \times 10^{-5}}\left(\frac{1}{(130+273)} - \frac{1}{(25+273)}\right)} \approx 892 \quad (5.9)$$

Using this AF information, back substitution gives the data retention in years at 25°C.

$$Data\ Retention_{@25^\circ C} = \frac{96 \times 892}{24 \times 365} \approx 11\ years \quad (5.10)$$

The stable states achieved with the test results interpolates to over 10 years of data retention. Thus, the devices having the nano-columnar structure are well placed for being used in non-volatile applications.

### Multilevel Switching Capability

A memory cell that can be programmed to more than one state can store multiple bits, which will increase the storage density of the memory architecture. In RCBM technology, the ON state resistance (LRS) of the device can be programmed to multiple resistance levels. This can be achieved by controlling the write current (compliance

current) through the cell being programmed. The ON resistance,  $R_{ON}$ , of RCBM devices decreases monotonically with increasing the write current ( $I_{Set}$  or  $I_{CC}$ ) [51]. The dependence of  $R_{ON}$  on  $I_{Set}$  often follows the power law  $R_{ON} = A/I_{Set}^n$  where A is a constant with units of voltage and n is a dimensionless number typically quite close to one. The power law equation is generally valid for currents less than  $80\mu\text{A}$  [201]. This relation is reported for a variety of device sizes and materials including Ag/Ge-S/W [202, 203], Ag/Ge-Se/Pt [204], and Cu/SiO<sub>2</sub>/W [205]. The same dependence has been reported for bilayer ECM devices, e.g. Cu/Ge-Se/Ta<sub>2</sub>O<sub>5</sub>/W [206], which suggests the power law to be material independent. Similar behavior has been observed with columnar structure devices. The  $R_{ON} \propto 1/I_{Set}$  can be thought of as being a natural consequence of having a resistor in series with a RCBM cell during the Set state. With RCBM cell in OFF state, it can be presumed to have resistance  $R_{OFF}$  much larger than the series resistance,  $R_s$  and the applied voltage is dropped primarily across the RCBM cell at the beginning of SET operation. As the cell starts to go in SET state, its resistance drops to a value comparable to  $R_s$  and a large fraction of the applied voltage begins to fall across the series resistor.

To achieve multilevel switching in the fabricated nano-columnar structured devices, the RCBM cells were programmed with different write current levels controlled by the HP parametric analyzer. Since the voltage switching is achieved in all the studied Ge-Se and Ge-Te compositions under all the incident vapor angles, the same is achieved by setting multiple compliance current values to demonstrate multilevel switching. All the fabricated devices were tested with compliance current values separated by five orders of magnitude difference. The multilevel switching performance of Ge<sub>30</sub>Se<sub>70</sub> nano-structured devices under vapor incident angle of 60° is demonstrated in Figure 5.22.

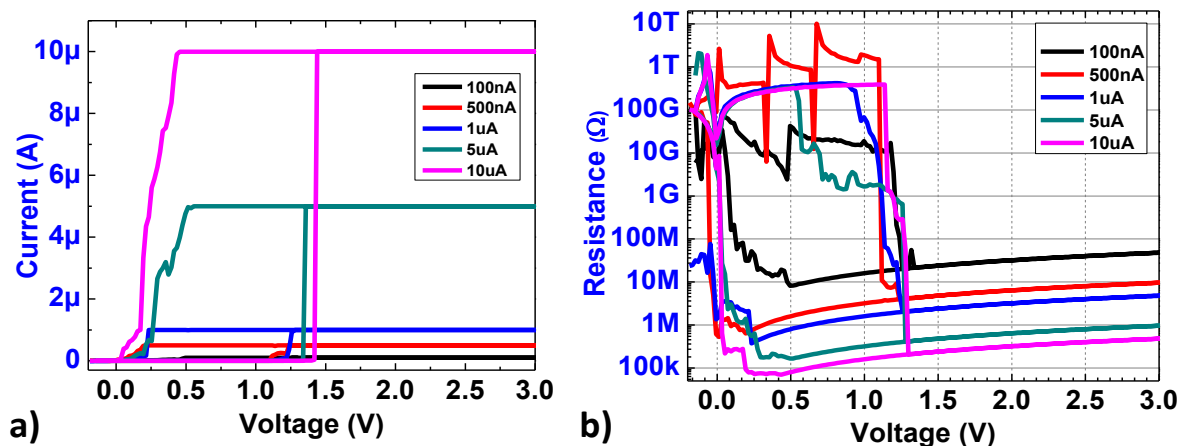


**Figure 5.22** (a) Current-Voltage and (b) Resistance-Voltage curves with varying compliance current values for  $\text{Ge}_{30}\text{Se}_{70}$  column-structured devices with deposition angle,  $\alpha = 60^\circ$

The measured relation between the compliance current and the respective low resistant values is illustrated in Figure 5.23. A decrease in the low resistance value with increasing the compliance current can be observed. A change in the low resistance value from 5M to 500K is achievable by varying the compliance current from 100nA to 10 $\mu\text{m}$ . The presented data illustrate that the low resistance state of the RCBM cell can be programmed to different states by employing a defined compliance current level. This is the key advantage of resistive memory for competitiveness in the emerging memory technology.

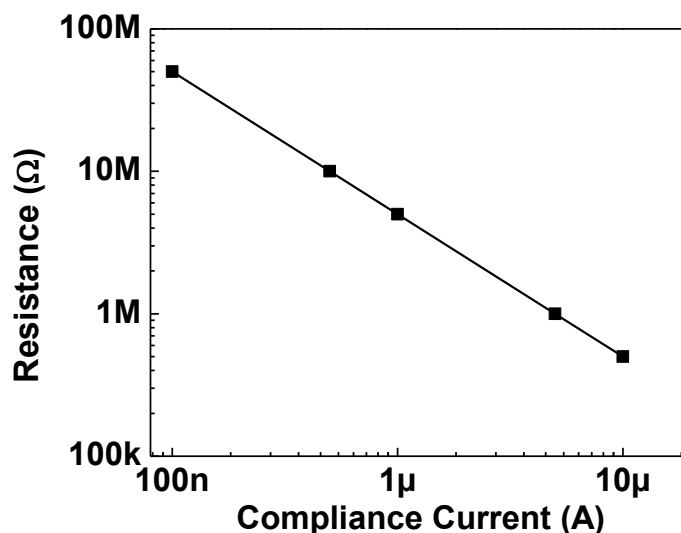


**Figure 5.23** Dependence of low resistive state on the compliance current value at room temperature

#### Filament Growth through Columnar Structure - Atomic Level Switching

In the modern era where consumer electronics are an essential commodity for everyday life, cost benefits that are achievable with shrinking the memory technology requires the new memory technology to be feasible beyond the projected dimensions for future applications. Nano-scaled electrical characterization of the fabricated column structured devices was performed to demonstrate the possibility of building a RCBM ultra-high dense non-volatile memory with superior scalability potential [207, 208].

To achieve nano-scale characterization of the devices and to attain a better understanding of Ag diffusion through the columnar structures, it was important to develop a method and an environment that does not affect the filament formation. The environment within the SEM consists of high energy electron, which interacts with the filament. The random growth of the filament in normally deposited films and the interaction of the electrons in SEM will rupture the Ag filament as illustrated in Figure

5.24. This is a dynamic process that hinders the recording of the Ag filament, thus making SEM an unfavorable choice.

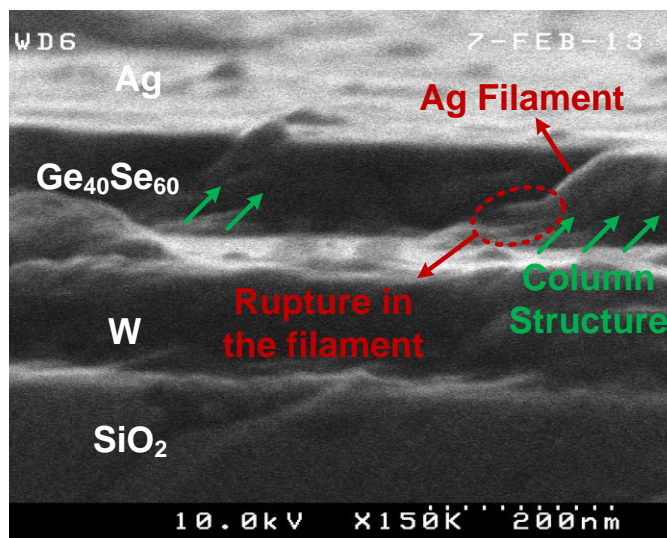


**Figure 5.24** SEM image of the filament rupture caused by electron beam

To overcome this, and to illustrate the Ag diffusion and filament formation with no multi-branching through the pathways provided by columnar structure, a novel experimental setup for imaging the cross-sectional areas of the samples using Atomic Force Microscopy was engineered. Conventional AFM conductivity mapping is based on a contact mode that involves lateral forces leading to sample damage and tip contamination, which may result in artifacts that may disguise the desired information. So to overcome these concerns, AFM was used in two special modes: Peak Force Tunneling AFM (PF-TUNA) and Peak Force Kelvin Probe AFM (PF-KPFM). Both of these methods provided an insight into the filament growth through the column structure by analyzing the nano-scaled electrical characterization of the fabricated devices. PF-TUNA was used to record the Ag dendrites growth through the columnar structure while PF-KPFM enabled imaging of the surface potential of the topological layers allowing the

flexibility to see Ag distribution within the columnar structure. These nano-electrical characterization techniques provided near atomic scale information on the fabricated devices, suggesting that these devices are scalable to atomic level.

#### PF-TUNA Measurements

PF-TUNA was used to develop a cross-sectional conductivity map of the fabricated column structured active layered devices. PF-TUNA measurements were based on a peak force tapping method that is capable of acquiring nano electrical/mechanical measurements. The probe interacts with the sample intermittently, thereby avoiding lateral forces during measurements and imaging. The feedback loop controls the maximum force on the tip for each cycle. The sequence of the periodically modulated probe interacting with the sample surface is illustrated in Figure 5.25. Z position, in Figure 5.25, shows the cantilever position during one PF cycle, as a function of time. The force measured by the probe when approaching the sample surface and the withdrawal phase is represented in the middle figure while the current passing through the sample, by application of proper voltage bias, is represented in the bottom of Figure 5.25.

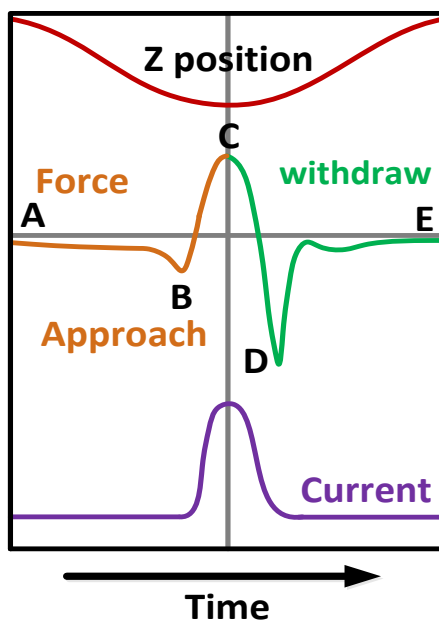


**Figure 5.25** Plots of Probe (Z position), Force and Current as a function of time during one PF-TUNA Cycle [209]

As the tip comes close to the surface, the cantilever is pulled down towards the surface by attractive forces, which are usually van der Waals and electrostatic forces and is represented as a negative force (middle line in Figure 5.25). At point B, the attractive forces overcome the cantilever stiffness and the tip comes in contact with the surface. Tip remains in contact with the surface, until Z position reaches the bottom most position (point C in the Figure). At this point, maximum force is exerted onto the surface, which is kept constant during this period by a feedback system. The probe then starts to withdraw and the force starts to decrease until it reaches point D. At this point, the tip experiences minimum force, which is also known as the pull-off point. Once the tip comes off the surface, only long range forces affect the tip and the force curve goes to zero (point E in the Figure). The current time plot achieved during one cycle can be extracted into three measurements: (i) Peak current (point C), (ii) Contact averaged current (point B to D), (iii) TUNA Current (averaged from point A to E).

The growth of the silver filament and intercalation of silver through the devices column structure active layers, as a function of the applied voltage, was monitored and imaged using a Bruker Dimension Icon AFM operating in Bruker's proprietary PF-TUNA mode. Concurrent PF tapping and imaging, enabled identification of all the underlying films ( $\text{SiO}_2/\text{W}/\text{ChG}$  with nano-columnar structures/ $\text{Ag}$ ) due to variations in topography and/or nano-mechanical properties of each film such as deformation, dissipation and adhesion, thus allowing to completely map the device structure using cross-sectional PF-TUNA imaging method.

PF tapping was chosen for two reasons. First, it enabled extremely fine control over the AFM tip-sample interaction force, which was important given the fragility of the chalcogenide pillars. In addition, it allowed the simultaneous acquisition of point by point nano-mechanical data (e.g., deformation, dissipation, adhesion, and Young's modulus) via real-time force curve analysis. These nano-mechanical channels were found to be useful in differentiating among the various layers within the device structure.

The samples were cleaved, prior to imaging, using the standing cleaving method with extra precaution to have the surface as smooth as possible. The Icon's integrated high resolution optical camera was used to identify areas exhibiting the least damaged from cleavage, which was used for imaging and positioning the AFM tip within a few microns of the sample's cross-sectional edge prior to engaging the surface, as illustrated in Figure 5.26. Bruker PF-TUNA probes having a 25nm radius of curvature and SiN cantilever with a conductive Pt/Ir over-coating was chosen to provide a combination of low force, high conductivity, and optimal spatial resolution during the PF-TUNA measurements. The low force constant arising from the SiN cantilever enabled the use of

extremely low (nN) forces to preserve the integrity of the fragile chalcogenide columns (pillars), while the ultrathin Pt/Ir coating enabled high conductivity and current sensitivity without significantly reducing the spatial resolution. All PF-TUNA measurements were performed at room temperature (21 °C) and ambient humidity (~20-30%).

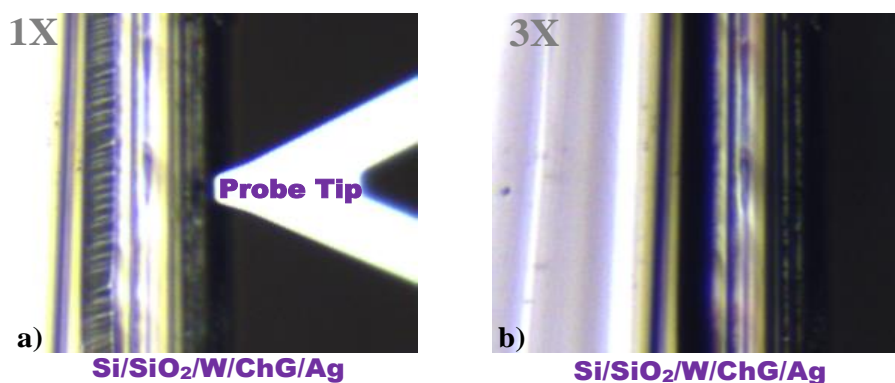


**Figure 5.26** Optical image (a) 1X zoomed and (b) 3X zoomed image of the cleaved sample for imaging using PF-TUNA

Concurrent with the topographical and nano-mechanical measurements, the sample conductivity was monitored as a function of applied sample bias (0 to -2V in 100mV increments). Biasing of the sample was accomplished by establishing a direct electrical connection between the sample chuck and the tungsten electrode using silver paste. Silver paste was used to ensure a good connection between the chuck and the tungsten layer. To image the silver filament growth through the column structures, the chuck was biased to a lower potential relative to the tip. The experimental setup for imaging the cross-sectional area of the active layer filament is illustrated in Figure 5.27.

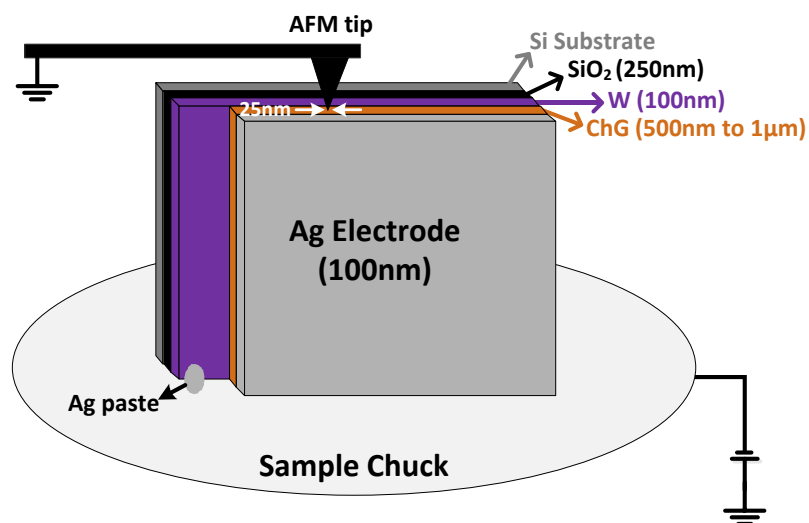


**Figure 5.27** Experimental setup for imaging the growth of conductive path through the columnar structure in the active layer of the devices

With the electrically conductive AFM probe held at ground, the voltage bias was only effective during the portion of the force curve where the tip was in contact with the sample, for  $\sim 250\text{-}500\mu\text{s}$  out of each 1ms force curve cycle, depending upon the peak force set point. Thus, the growth of the silver filaments could be controlled by a combination of sample bias voltage and contact time.

Initially, the cross-sectional imaging of the samples was performed under no biased condition to validate the SEM results for the column structures. For each measurement, the Peak, Contact, and Tuna currents were recorded. Under no biasing conditions, less current was detected, as expected. Figure 5.28 presents the results of PF-TUNA scanning on the cross-sectional area of the  $\text{Ge}_{20}\text{Se}_{80}$ ,  $\text{Ge}_{30}\text{Se}_{70}$ , and  $\text{Ge}_{40}\text{Se}_{60}$  devices with active layer being deposited at incident angle of  $30^\circ$ ,  $45^\circ$ , and  $70^\circ$ , respectively.

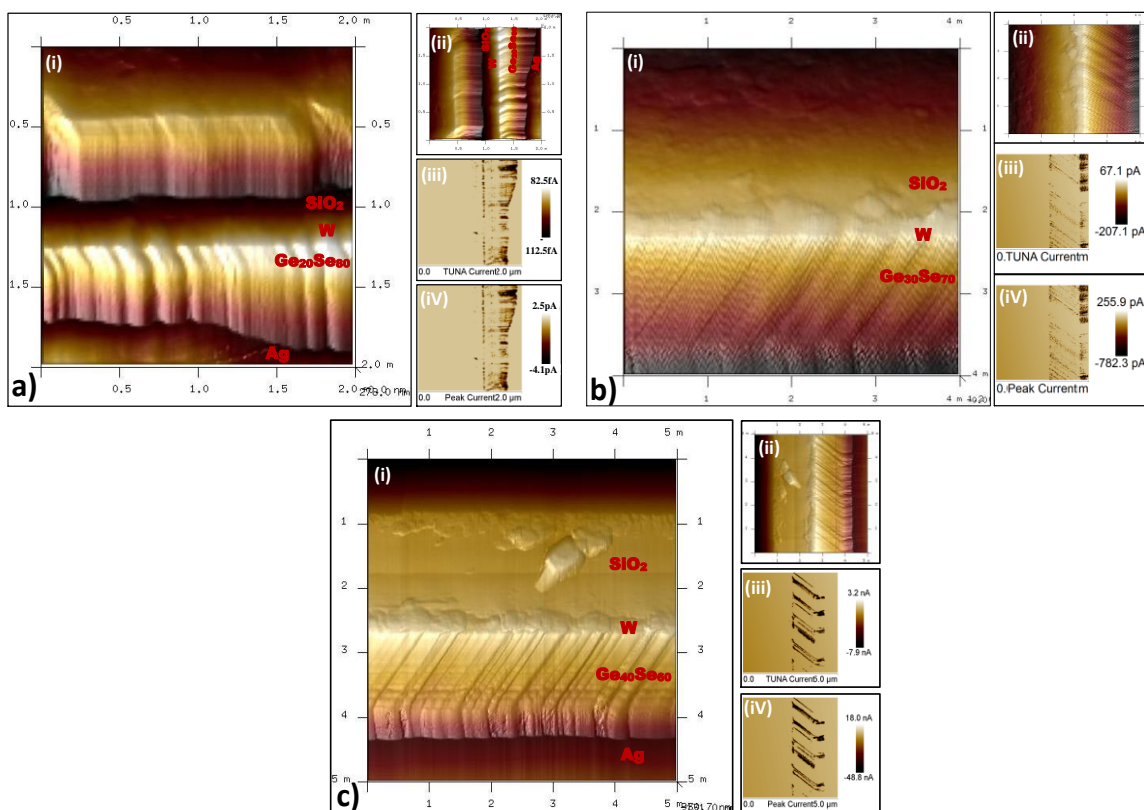


**Figure 5.28** PF-TUNA scans with No biasing and peak force set 10nN for (a)  $\text{Ge}_{20}\text{Se}_{80}$  with  $\alpha = 70^\circ$ , (b)  $\text{Ge}_{30}\text{Se}_{70}$  with  $\alpha = 45^\circ$ , and (c)  $\text{Ge}_{40}\text{Se}_{60}$  with  $\alpha = 30^\circ$  where (i) the top view image of the cross-sectional area (ii) the side view of the cross-sectional area (iii) Tuna current measurement (iv) Peak Current measurement for each case

The growth of the columnar pillars is very obvious in the Ge-Se compositions under all incident vapor angles. Since no biasing was applied, the TUNA and Peak current measured were very small. However, in the case of  $\text{Ge}_{40}\text{Se}_{60}$  (Figure 5.28 c-iii & iv), a significantly higher current is observed, which may be due to the encroachment of Ag from the Ag layer during the scan. The encroached Ag gets into the voids while the tip is in contact with the surface, resulting in a relatively higher current.

The confirmation the Ag filament growth through the inter-columnar spacing between the pillars is achieved by appropriately biasing the tip and stage. Since the tip was in contact with Ag at the start of the scan, in order for the redox reaction to start, the

tip was positively biased with respect to the stage. Figure 5.29 represents the growth of the Ag filament (dark brown color) through the voids between the columns for the studied  $\text{Ge}_{20}\text{Se}_{80}$ ,  $\text{Ge}_{30}\text{Se}_{70}$ , and  $\text{Ge}_{40}\text{Se}_{60}$  devices with obliquely deposited active films. A close observation of the films reveals the formation of the filament with no multi-branching within the filament. A significant increase in the current can be observed in Figure 5.29a-c (vi-vii) due to the conduction path available between the W and Ag electrode. A relatively large number of filaments are observed in the cross-sectional image, for all the cases in Figure 5.29, as the films were fabricated using continuous planar layers of W, obliquely deposited Ge-Se active films and Ag due to the limitation of the equipment.

Since peak current is recorded when the tip is in contact with surface, it measured the highest current flowing through the devices, as shown in Figure 5.29a-c (viii). As the TUNA current measures the average current during one complete force curve cycle, including the idle period when the tip is not in contact with the surface, it displays the least current reading as indicated on the current scale in Figure 5.29a-c (vi).

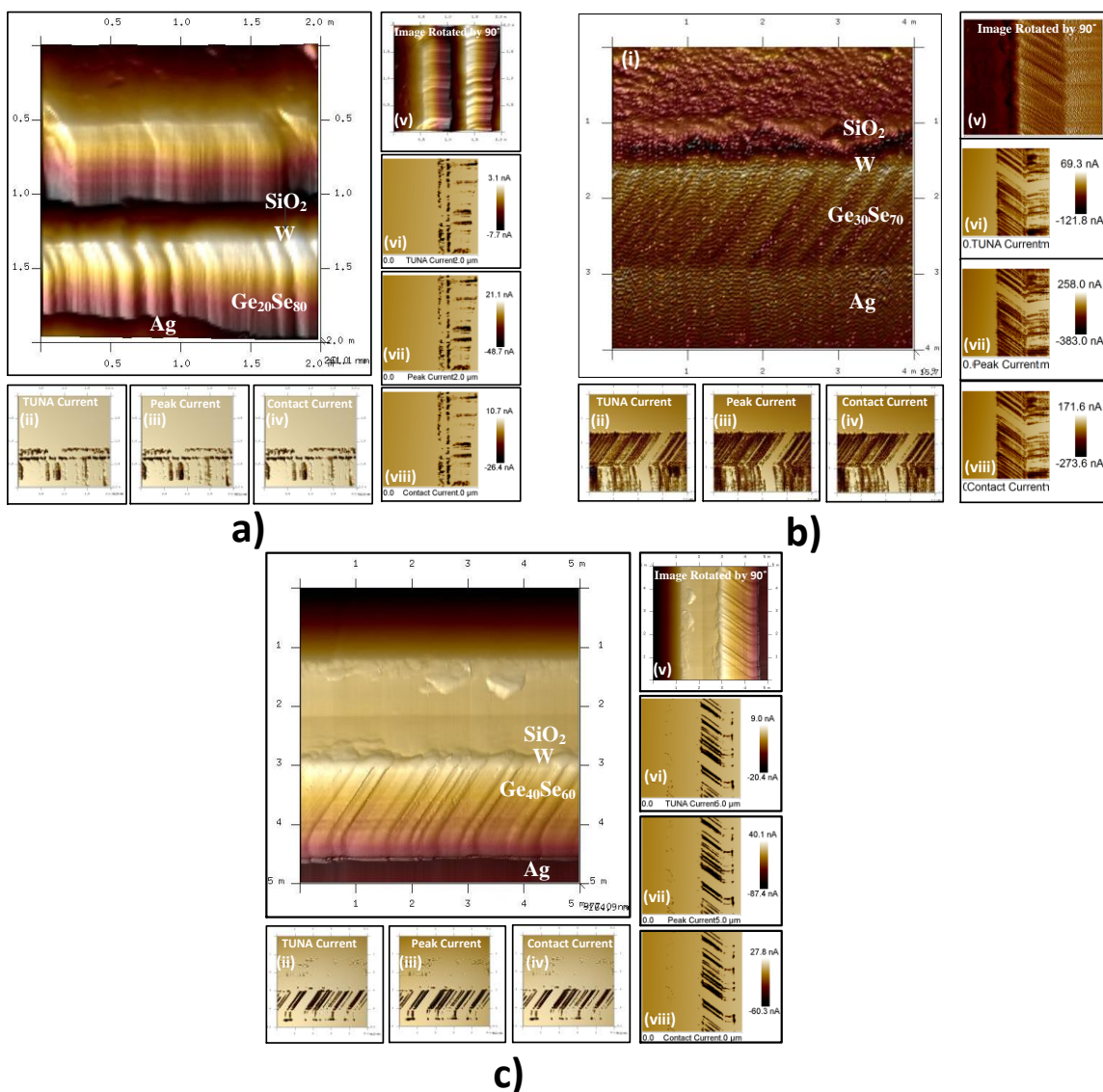


**Figure 5.29** PF-TUNA scans with stage biased at  $-0.5\text{V}$  and peak force set  $10\text{nN}$  for (a)  $\text{Ge}_{20}\text{Se}_{80}$  with  $\alpha = 70^\circ$ , (b)  $\text{Ge}_{30}\text{Se}_{70}$  with  $\alpha = 45^\circ$ , and (c)  $\text{Ge}_{40}\text{Se}_{60}$  with  $\alpha = 30^\circ$  where (i-iv) the top scan view and the filament growth through the voids in the columnar structure (v) the top view image rotated by  $90^\circ$  (vi-viii) the side scan view of the cross-sectional area and the filament growth through the voids in the columnar structure with corresponding current scale

Following the formation of the intercalated silver in the voids, reversal of the biasing would lead to dissolution of the grown filament. To validate this, a potential of  $+5\text{V}$  was applied to the stage. The result of inverting the polarity on the conductivity is presented in Figure 5.30 for  $\text{Ge}_{30}\text{Se}_{70}$  with the deposition angle of  $45^\circ$ . A close

comparison of Figure 5.29b (vii) and Figure 5.30 reveals that some silver is extracted back towards the Ag electrode. Even though the voltage bias is reversed, the current scale in Figure 5.30 (vi-viii) shows a significant current flowing through the device. However, the measured current when the device is reversed biased is comparatively less as compared to the current measured when the devices is forward biased. The applied bias is effective only when the probe comes in contact with the Ag surface, with a maximum contact time of  $500\mu\text{s}$ . This could be the reason for incomplete dissolution of the filament. The sample would no longer be reversed biased once the silver layer is scanned. Furthermore, when the probe is lifted off the sample, it is actually floating. Because of these reasons, the grown Ag filament is not completely dissolved. However, a decrease in the current by reverse biasing the sample, as illustrated in Figure 5.30, suggest a reduction in the filament number or weakening of the conduction path by extracting Ag back towards the Ag source.

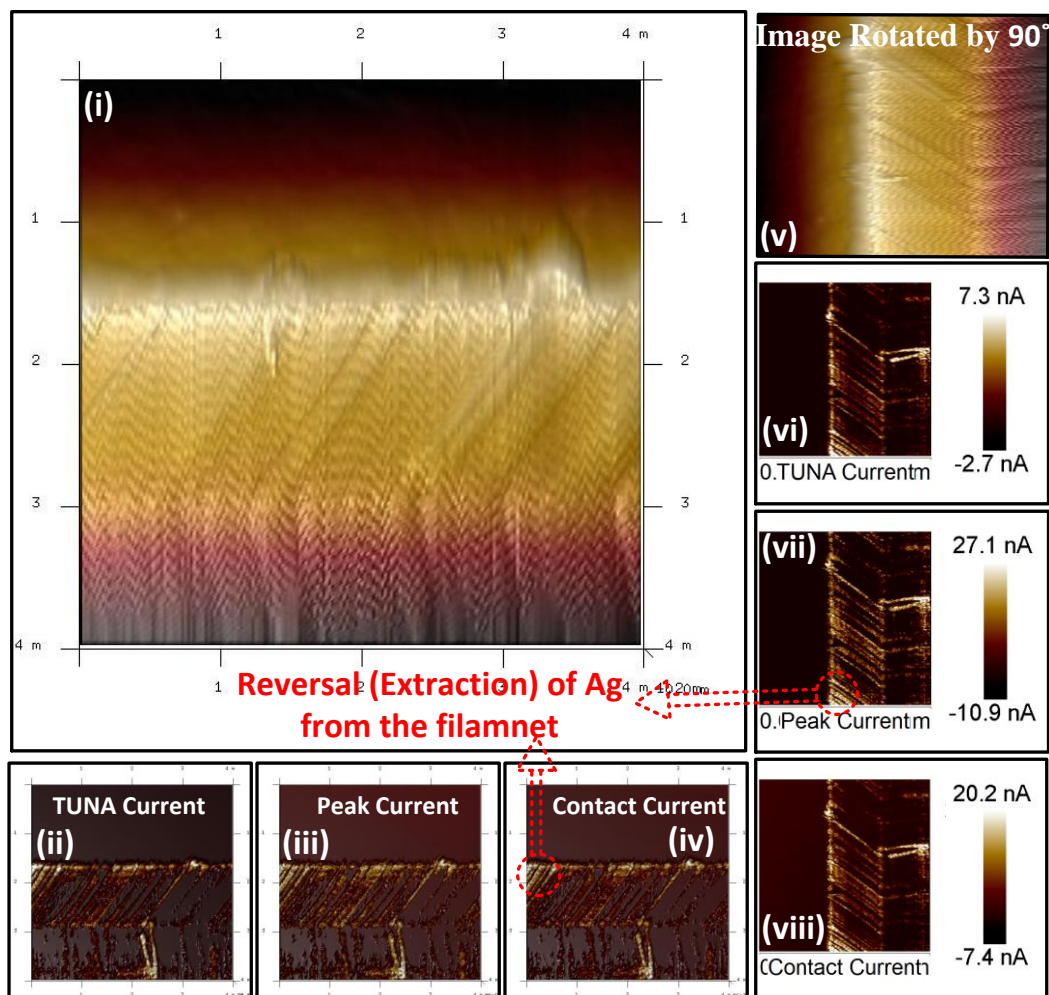


**Figure 5.30** PF-TUNA scans with stage biased at +5V and peak force set 10nN for  $\text{Ge}_{30}\text{Se}_{70}$  with  $\alpha = 45^\circ$  where (i-iv) is the top scan view and the filament growth through the voids in the columnar structure (v) is the top view image rotated by  $90^\circ$  (vi-viii) is the side scan view of the cross-sectional area and the filament growth through the voids in the columnar structure with corresponding current scales.

Since forward biasing the sample resulted in immediate growth of the silver dendrite, an incremental increase of 10mV in the voltage from no bias condition was also performed for the  $\text{Ge}_{30}\text{Se}_{70}$  sample, with an anticipation to grow fewer filaments as illustrated in Figure 5.31.

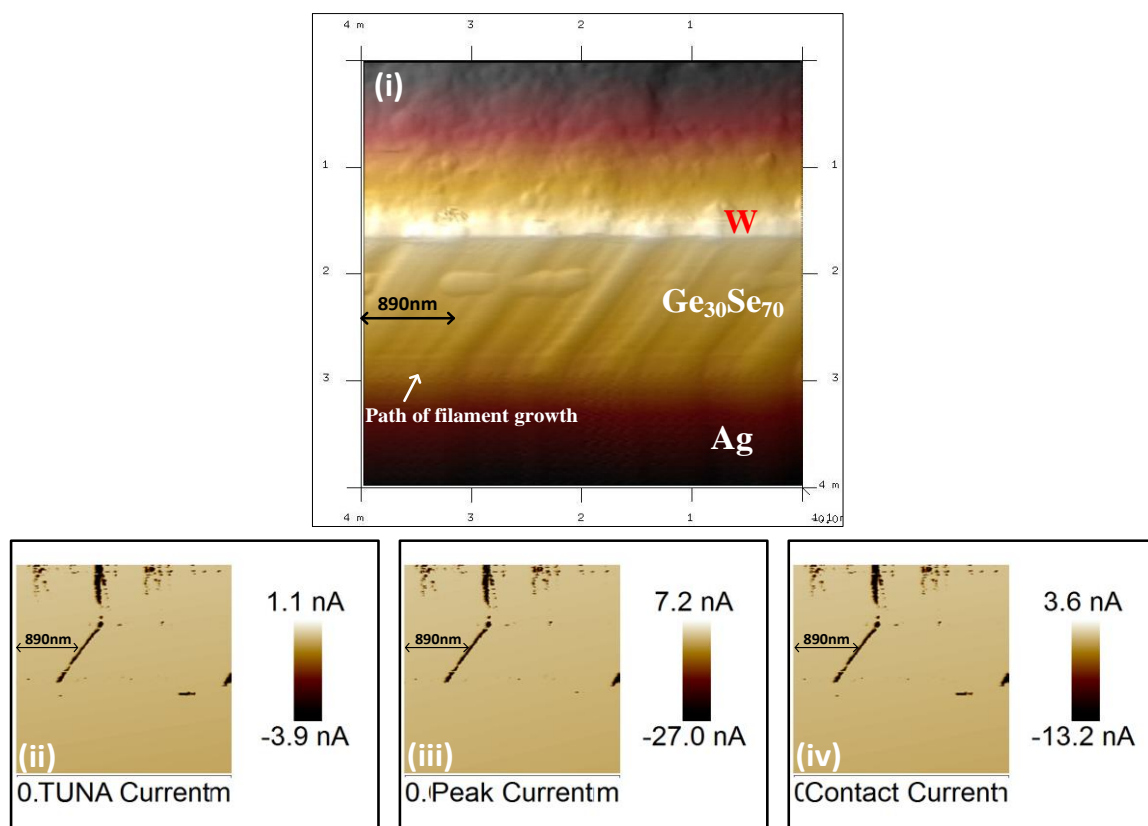


**Figure 5.31** Filament growth by applying a voltage bias of 25mV on Ge<sub>30</sub>Se<sub>70</sub> sample with  $\alpha = 45^\circ$

Since for the changing the state of the device from high resistive state to low resistive only one filament is required, so each individual filament may be regarded as a separate device. This may lead to a conclusion that an array of devices can be fabricated in such a manner, however, addressing each individual device (filament) for programming and erasing will be challenging. The average width of the filaments growing through the inter-columnar voids was found to be  $\sim 15\text{nm}$  and considering width of the tip of the probe (25nm), atomic level switching is possible with RCBM devices. Therefore, a highly compact and dense memory is possible with underlying nano-columnar structures in the active films; however, an architecture that can address an individual filament for storing the bits will be required.

### PF-KPFM Measurements

PF-KPFM is a tool that demonstrates unique usefulness in characterizing the properties of various electronic devices by correlating the potential distribution within the device structure. It measures the potential difference between a conducting AFM tip and the sample, thereby mapping the surface potential or work function of the sample with high spatial resolution. Since PF-KPFM measurements provide near atomic scale high resolution potential profiles, this technique was used to further demonstrate the filament growth through the columnar structures.

PF-KPFM records data by the interaction of the periodically modulate probe with the samples, as illustrated in PF-TUNA measurements, Figure 5.25. PFQNE-Al tip (Peak Force Quantitative Nano-electrical - Aluminum) having a thickness of 5nm and coated with aluminum on the backside of the cantilever was used to perform KPFM imaging. The recorded KPFM data on  $\text{Ge}_{30}\text{Se}_{70}$  films deposited at  $\alpha = 45^\circ$  under unbiased and biased conditions is presented in Figure 5.32. A clear difference in the potential of the  $\text{Ge}_{30}\text{Se}_{70}$  film can be observed under the two conditions. A close observation shows the formation of Ag filament, after the bias was applied, through the columnar structure.

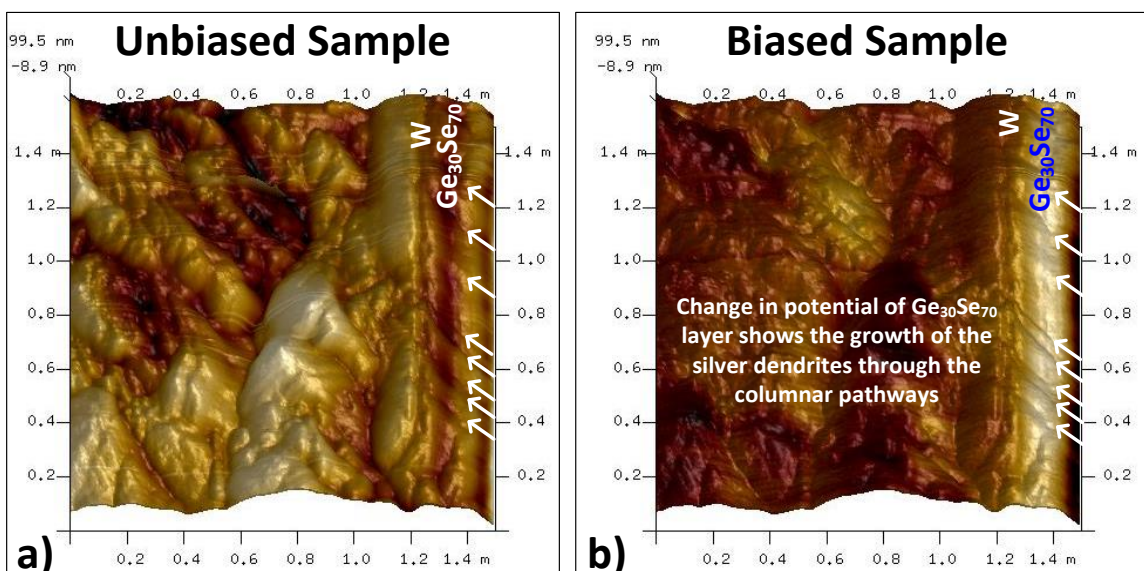


**Figure 5.32** PF-KPFM scan (a) under unbiased and (b) biased condition with peak force set to 10nN for  $\text{Ge}_{30}\text{Se}_{70}$  film at  $\alpha = 45^\circ$

### Summary

The electrical characterization of the devices prepared by PECVD deposited active films and with nano-columnar structure were demonstrated. The PECVD devices showed excellent endurance. The importance of having a smooth surface for reliable device performance was demonstrated. Another improvement of the devices was demonstrated by nano-engineering the columnar structures with the device active layer. It was shown that very reliable and uniform switching devices are possible with obliquely deposited films. Electrical testing of the fabricated devices having nano-columnar structures showed excellent endurance and improved retention characteristics. The switching voltage dependence on the obliqueness angle of the arrival vapor flux and various compositions of Ge-Se and Ge-Te is established. Also, the device's capability for multilevel switching, to achieve high dense memory, is demonstrated. The hypothesis of the filament growth through the columnar structure is validated by performing AFM studies in PF-TUNA and KPFM mode. The results illustrate that the filament grows

through the voids between the inter-columnar spacing with no side branches within the filament. A significant improvement in the devices performance can be observed by the innovative approach of fabricating nano-structured pillars in the active region of the devices. Time resolved neutron reflectivity measurements of Ag/Ge<sub>x</sub>S<sub>1-x</sub> (x = 0.2, 0.4) films under light illumination revealed a difference in the reaction rate of the two systems, which is attributed to the difference in energy of the two potential barriers at the Ag/Ag rich reaction layer and Ag rich reaction layer/Ag poor reaction layer interfaces.

## CHAPTER SIX: FORMATION OF THE MEMRISTIVE ARRAY

The nano-scaling attribute of memristive devices created a broad range of opportunities for innovative memory architectures. Success achieved at the single cell level suggests that RCBM is well positioned for ultra-high performance memory and logic applications. By incorporating the RCBM cells into a system, these devices can fulfill the essential role of memory in various applications. RCBM cells in an array possess significant advantages for memory, including massive storage capacity with high storage density, precision, and access speed [210].

An array of these devices can be created by laying a nano-wire (electrode) over the vias filled with Ag and the inert electrode, with chalcogenide film acting as a dielectric medium between the two electrodes, as illustrated in Figure 6.1. Therefore, the formation of such an array relies on the high resistivity of the chalcogenide film, which expands in the range of hundreds of giga-ohms. This structure offers a high device density with the simplest of configuration and allows access to each nano device, enabling devices to be individually addressed.

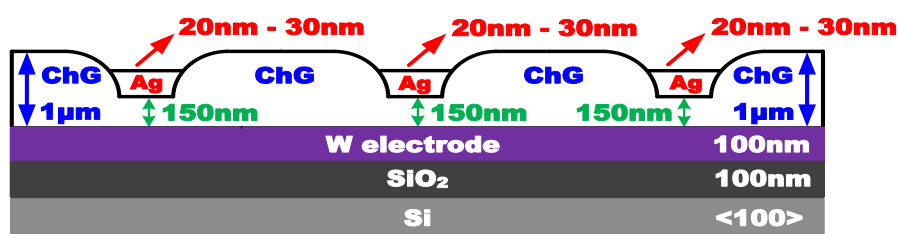


**Figure 6.1** Schematic Illustration of RCBM Array

A scheme for fabricating  $\text{Ge}_x\text{Se}_{1-x}$  ( $x = 0.25, 0.3$  and  $0.4$ ) chalcogenide-based RCBM arrays using ion bombardment through a mask is demonstrated in this chapter. This method provides a unique alternative to the conventional lithography technique for prototyping such devices without any wet chemistry. The openings in the mask thus defined the devices size and the non-sputtered regions act as isolation between the adjacent cells in the array. The arrival of the energetic ions causes the surface atoms to be removed from the material. As a consequence, vias are created in the Ge-Se layer, forming the devices. The high energy particles cause surface roughness, compositional variations, and structural alterations in the irradiated layer [211], which are studied with the previously described techniques (AFM, EDS, and Raman Spectroscopy). The viability of the ion bombardment method for array fabrication is demonstrated by electrical testing of the cells in the array.

### **Lithography Free Formation of RCBM Array**

The ChG films were deposited on stacks of  $\text{Ge}_x\text{Se}_{1-x}/\text{W}/\text{SiO}_2/\text{Si}$  (where  $x=0.25, 0.3, 0.4$ ). The thickness of the films comprising the device structure was as follows: Si  $\langle 100 \rangle$  substrate was covered with 100nm of thermally grown  $\text{SiO}_2$ ; followed by sputtering of 100nm of W layer and  $1\mu\text{m}$  of thermally evaporated Ge-Se ChG films. The device array was created by bombarding the Ge-Se layer with  $\text{Ar}^+$  ions using an INA-X (SPECS, Berlin) Secondary Neutral Mass Spectrometer (SNMS) [212] by placing a  $40\mu\text{m} \times 40\mu\text{m}$  nickel mesh over the sample. In contrast to most ion beam tools where ion energy has a Gaussian distribution, the current is highly uniform within the SNMS machine over the entire bombarded region. This resulted in uniform depth profiles in the Ge-Se layer for all the cells in an array. A copper holder was placed on top of the nickel

mesh to hold it in place and protect part of the sample from ion bombardment for analysis of ion-induced effects. Surface bombardment was performed with low pressure Electron Cyclotron Wave Resonance (ECWR)  $\text{Ar}^+$  plasma. The resulting configuration for the sample is shown in Figure 6.2. SNMS depth profile data was used to calculate the sputtering rate. A 350V sputtering potential at 100 kHz frequency with 80% duty cycle was applied on the sample. A 20nm silver (Ag) layer was deposited by DC magnetron sputtering with a deposition pressure of  $5 \times 10^{-3}$  mbar.

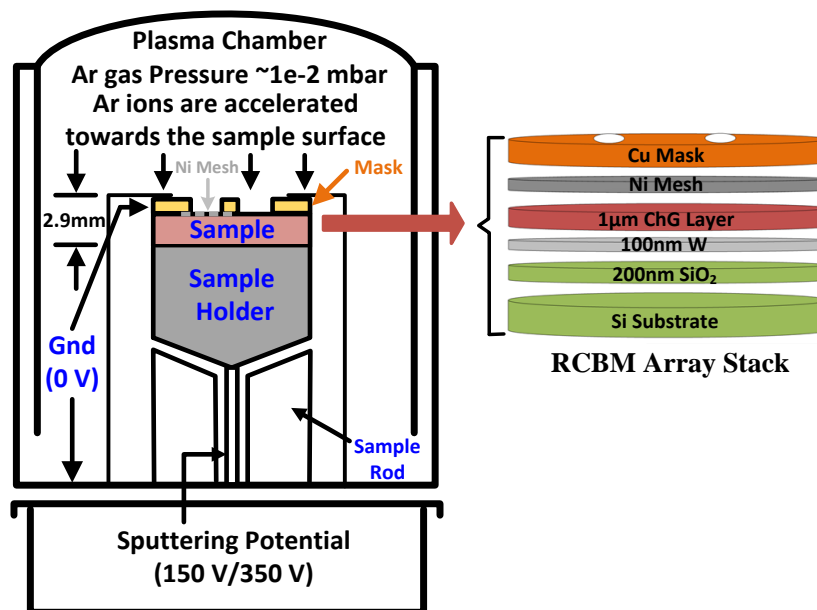


**Figure 6.2** SNMS System configurations with sample stack

### Material Characterization of the Ion Bombarded Regions

An SEM image of the fabricated array is shown in Figure 6.3 with Ge-Se film isolating individual cells. EDS was performed in five different cells at five different locations on each sample, so that 25 points were used to determine the uniformity of the film within each composition. The film compositions were measured in the cell vias

created by ion bombardment as well as in the planar regions shadowed by the mask and the results are presented in Table 6.1.

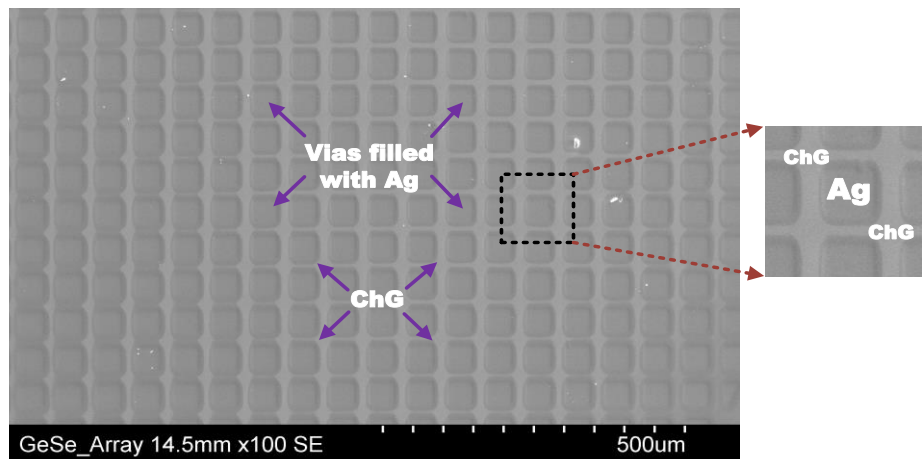


**Figure 6.3 SEM image of the array formed by ion bombardment**

Sr. No.	Source Composition	Planar Region		Ion Bombarded Region		% Change
		%Ge	%Se	%Ge	%Se	$\Delta$
1	$\text{Ge}_{25}\text{Se}_{75}$	$25.6 \pm 0.061$	$74.4 \pm 0.061$	$24.8 \pm 0.51$	$75.2 \pm 0.51$	$\pm 0.8$
2	$\text{Ge}_{30}\text{Se}_{70}$	$31.2 \pm 0.037$	$68.8 \pm 0.037$	$30.7 \pm 0.15$	$69.3 \pm 0.15$	$\pm 0.5$
3	$\text{Ge}_{40}\text{Se}_{60}$	$39.9 \pm 0.19$	$60.1 \pm 0.19$	$38.8 \pm 0.14$	$61.2 \pm 0.14$	$\pm 1.1$

The alteration in the concentration of Ge and Se composition, determined through EDS elemental mapping are presented in Figure 6.4. The change in color corresponds to thicker Ge-Se film outside the via.

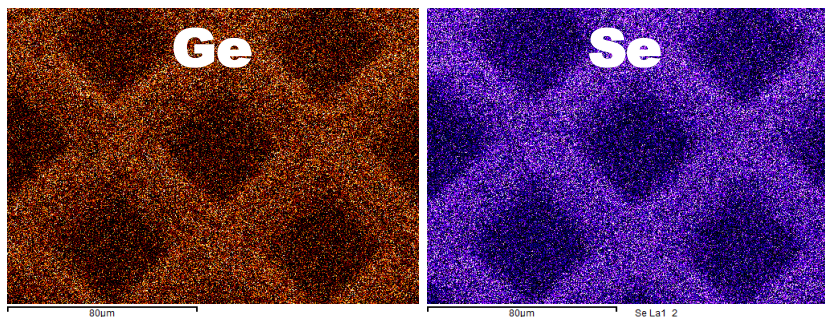


**Figure 6.4** EDS elemental mapping distribution of Ge-Se before and after ion bombardment

Raman spectra of the as deposited films, ion bombardment areas (vias), mode assignments, and corresponding structural units characteristic for the studies  $\text{Ge}_x\text{Se}_{1-x}$  film compositions are presented in Figure 6.5a. The as deposited films are well relaxed since their structure resembles the one of the bulk material with the corresponding compositions. The spectra show peaks located at  $178\text{cm}^{-1}$ ,  $195\text{cm}^{-1}$ , and  $219\text{cm}^{-1}$ , corresponding to ethane-like (ETH), corner-sharing (CS), and edge-shared (ES) structural units, respectively [213]. Development of the spectra as a function of increasing Ge concentration shows an increase in the intensity of the peaks relating to the ES and ETH modes. A close observation of ES to CS area ratio demonstrates a change in the area ratio for Ge rich compositions for the ion bombarded regions, as shown in Figure 6.5b, with the largest change being observed in  $\text{Ge}_{40}\text{Se}_{60}$ , as illustrated in Figure 6.5c.

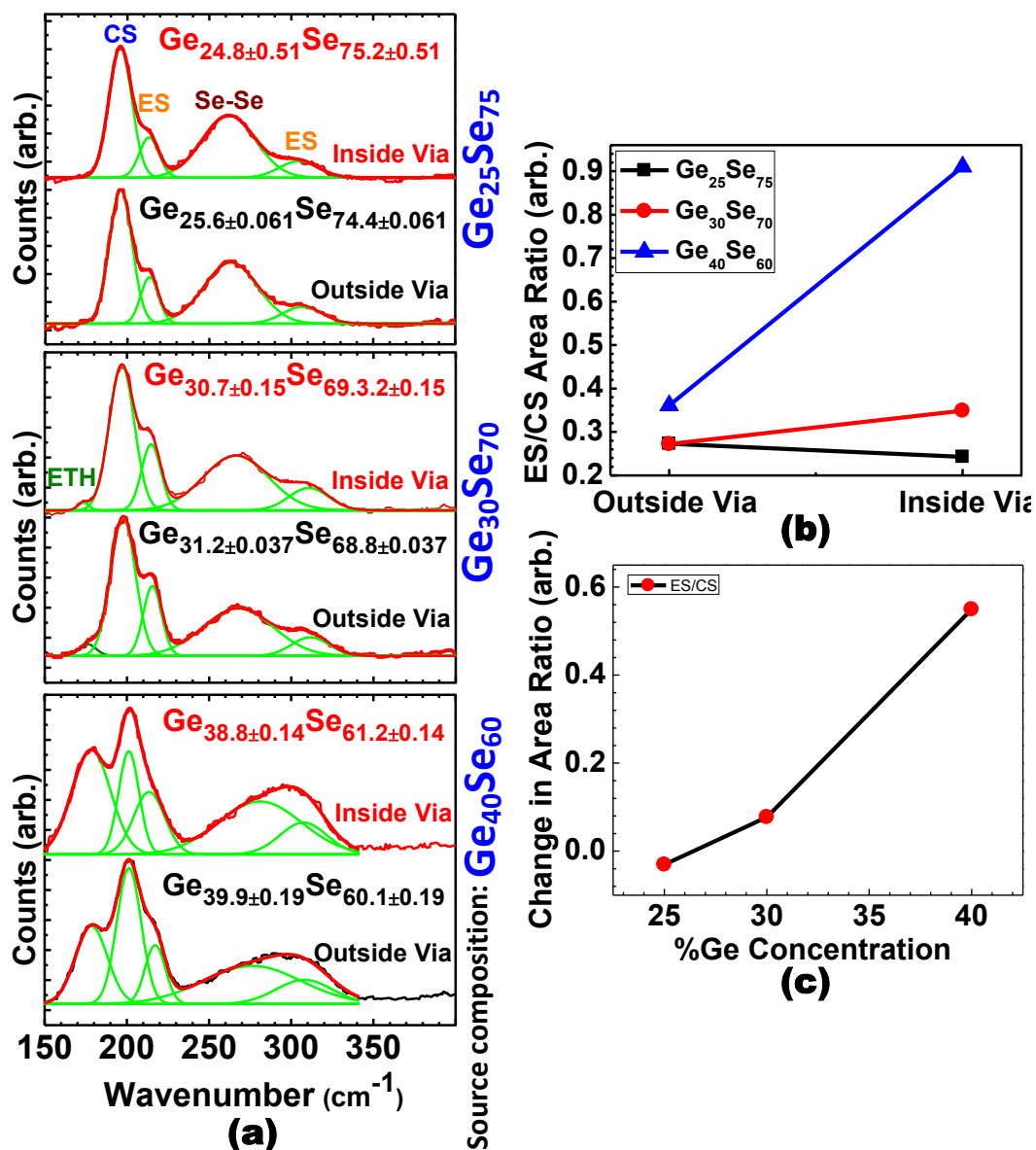


**Figure 6.5** (a) Raman data and the corresponding mode assignment, (b) Area Ratios b/w ES and CS modes, and (c) Change in area ratio with different Ge concentrations

The surface morphology within the cell vias of the  $\text{Ge}_x\text{Se}_{1-x}$  layer created by Ar<sup>+</sup> ion bombardment were studied by AFM. The result of AFM scans on the entire via in the 10<sup>th</sup> cell of the 20<sup>th</sup> row, for each composition, is presented in Figure 6.6, which confirms the formation of vias. To study the surface roughness, AFM scans were also performed on the virgin (non-bombarded area), cell 1, cell 10, and cell 20 in the 20<sup>th</sup> row of the array

structure on a  $25\mu\text{m}^2$  area within the device vias and the results are presented in Figure 6.7. A clear tendency for improvement in the surface smoothness can be observed with increase in Ge concentration.

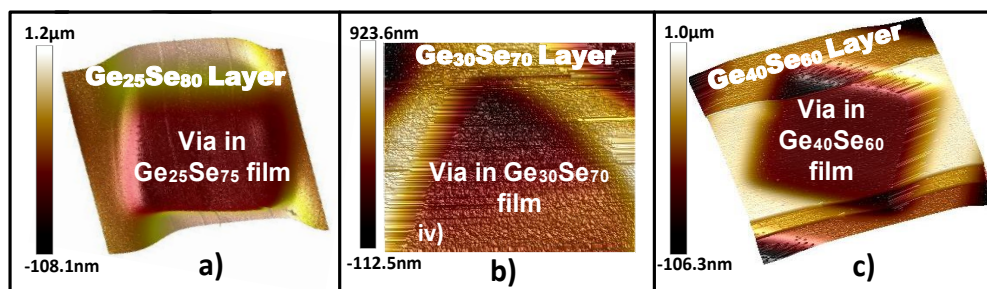


Figure 6.6 Formation of via in (a)  $\text{Ge}_{25}\text{Se}_{75}$ , (b)  $\text{Ge}_{30}\text{Se}_{70}$ , and (c)  $\text{Ge}_{40}\text{Se}_{60}$  films by  $\text{Ar}^+$  ion bombardment

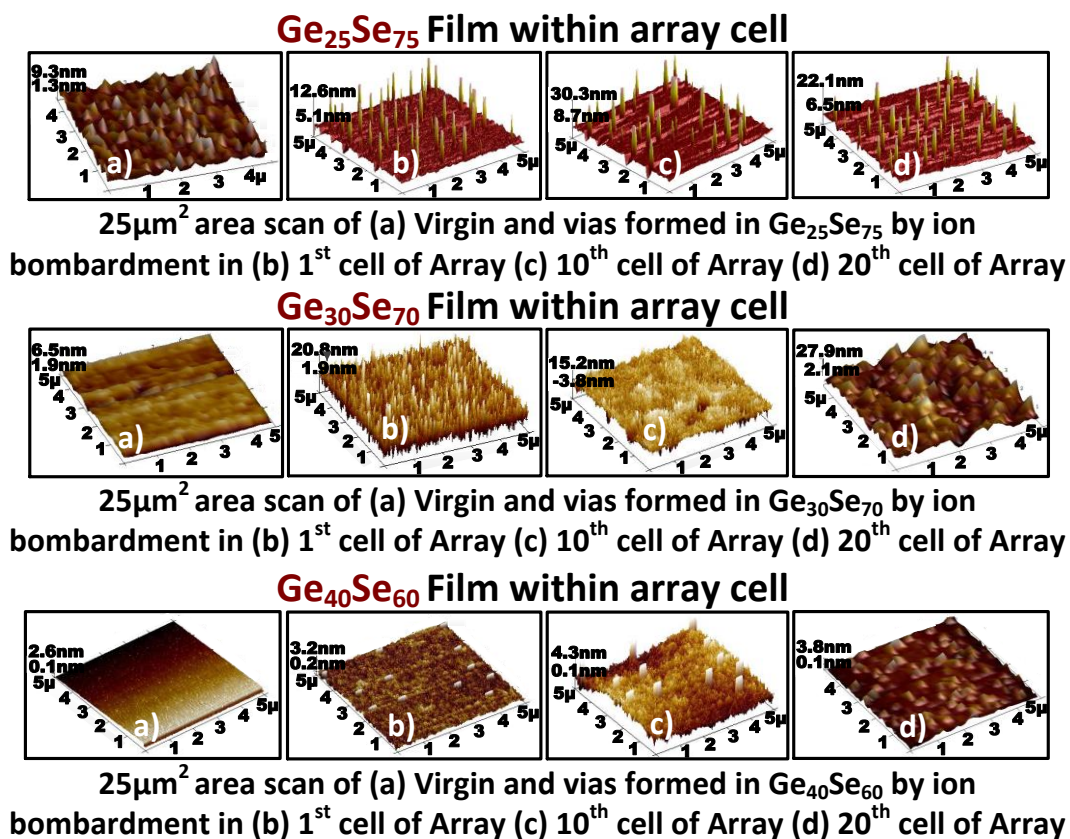


Figure 6.7 Surface morphology of  $\text{Ge}_x\text{Se}_{1-x}$  on a  $25\mu\text{m}^2$  area

### Explanation

The accelerated  $\text{Ar}^+$  ions used to form the vias in the  $\text{Ge}_x\text{Se}_{1-x}$  films alter the film composition, which causes structural changes and eventually affects the device performance. The two processes of compositional and structural changes taking place by ion bombardment are imperative for understanding thin films stability and hence device performance [155, 156].

EDS data suggests that Ge atoms having lower atomic mass sputter out faster than Se atoms. The lowest amount of Ge lost is observed in  $\text{Ge}_{30}\text{Se}_{70}$ , which is attributed to its closeness to the stoichiometric composition where the structure has the lowest number of wrong chemical bonds. Since the bond binding energy of Ge-Se is higher (2.38eV) compared to Ge-Ge (1.92eV) or Se-Se (2.33eV), more loss of Ge is observed in the  $\text{Ge}_{40}\text{Se}_{60}$  composition where a high number of ETH units are populated.

Analysis of the Raman spectra using the area ratio between the ES structural units corresponding to the peak located at  $218\text{cm}^{-1}$  and CS structural units corresponding to the peak at  $202\text{cm}^{-1}$  demonstrates compositional dependence of the ion beam induced structural changes in the sputtered material. This suggests that the  $\text{Ar}^+$  ions mainly affect the bonding sites between Ge-Se atoms. In essence, the loss of Ge atoms should result in increased amount of CS structural units, which is the case in the  $\text{Ge}_{25}\text{Se}_{75}$  samples. The increased areal intensity of the ES structural units could be related to the lower steric energy related to the formation of this structure, which keeps its appearance even at reduced amounts of Ge. In the Ge rich samples, the availability of ETH structural units includes one more variation for Ge loss. Since the Ge-Ge bond is the weakest, the probability of detaching Ge from this bond is the highest. So the charge distribution and

atoms position prefers the formation of ES structural units. At this composition, the loss of Ge is the biggest, which we relate to the lower energy that is necessary to expel Ge and therefore form this type of structure. However, the relative intensity of the ETH structural units remains dominant and even remarkably increases after ion bombardment, which suggests that the energy introduced to the films by the bombarding  $\text{Ar}^+$  ions contributes to their self-organization and formation of a compact structure. It is realized through clusters formation in which different fractions of ES and ETH units are engaged. The increase of the cluster size leads to formation of ring structures that contain more than the four atoms of the simple ES tetrahedra [214], which relaxes the structure. It is for this reason that the surface roughness, after ion bombardment, is much reduced in  $\text{Ge}_{40}\text{Se}_{60}$  films as illustrated in Figure 6.8.

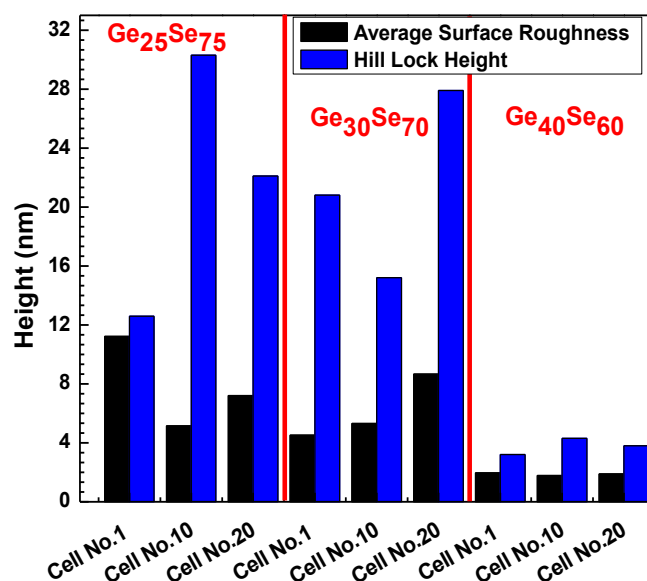


**Figure 6.8** Surface roughness RMS and peak hillocks in the vias of the cell

Interestingly, the results show that the optimal coordination of 2.4 for the  $\text{Ge}_{20}\text{Se}_{80}$  films, leading to high stability of the glass formation of the system according to

the Constrain Counting Theory [215], is not the leading factor for the strength of the structure. It is the higher coordination of 2.6 and especially 2.8 that results in more stable reaction of the films to the mechanical stress. Indeed, in the studied case, the stability of the network is related to how amenable it is to continuous deformation. The covalent forces that also affect the bond length, bond angles, and the increased rigidity are important factors, which in fact keep the structure intact [216]. The floppy modes related to the Se-Se bonding within the system require much lower energy to be destroyed and they quantify the instability of the films in the studied case.

### **Electrical Testing of the Fabricated Devices**

The electrical measurements conducted on the fabricated array for the studied compositions of  $\text{Ge}_x\text{Se}_{1-x}$  for cell # 20 are presented in Figure 6.9. Each cycle starts at -0.1V. Then, the voltage sweeps to +1.5V and sweeps back to -0.1V. At first, the current is very low until a threshold voltage of approximately 0.6 V is exceeded. At that moment, a conductive connection is formed between the top and bottom electrodes, causing a steep increase in the current until it reaches the compliance current. Multiple IV sweeps under the same conditions are presented in Figure 6.9. Analysis of these results shows a relatively small variation in switching voltage of the Ge rich devices when compared to  $\text{Ge}_{30}\text{Se}_{70}$  and  $\text{Ge}_{25}\text{Se}_{75}$  devices.

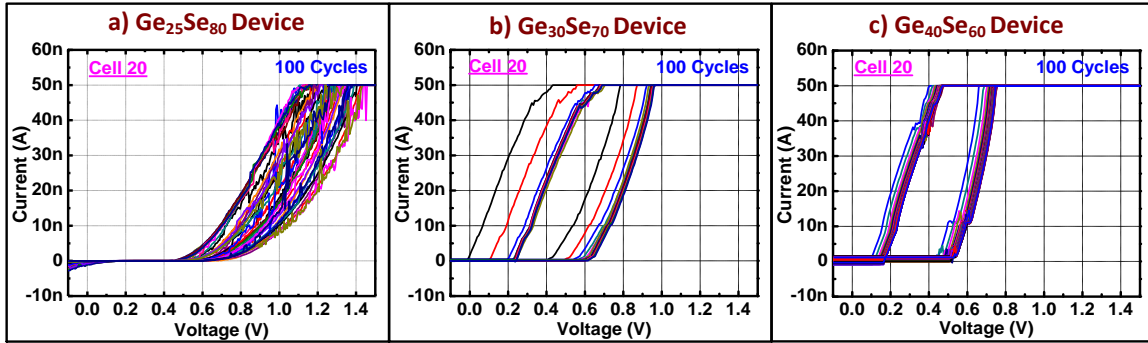


**Figure 6.9** IV Curves of the single bit device

The resistance and  $V_{th}$  plots in various cells, for all three compositions are in good agreement with Raman and AFM results, and are presented in Figure 6.10. All cells show four orders of magnitude difference between the ON and OFF states of the device. The resistance of the device varies from tens of giga ohms in the OFF state to a mega in the ON state, ensuring a good memory window of the devices [217]. However, the  $V_{th}$  of  $\text{Ge}_{20}\text{Se}_{80}$  illustrates variations within the cells and also in different cells of the array structure. On the other hand,  $\text{Ge}_{30}\text{Se}_{70}$  and  $\text{Ge}_{40}\text{Se}_{60}$  devices offer excellent repeatability within a cell and the array.

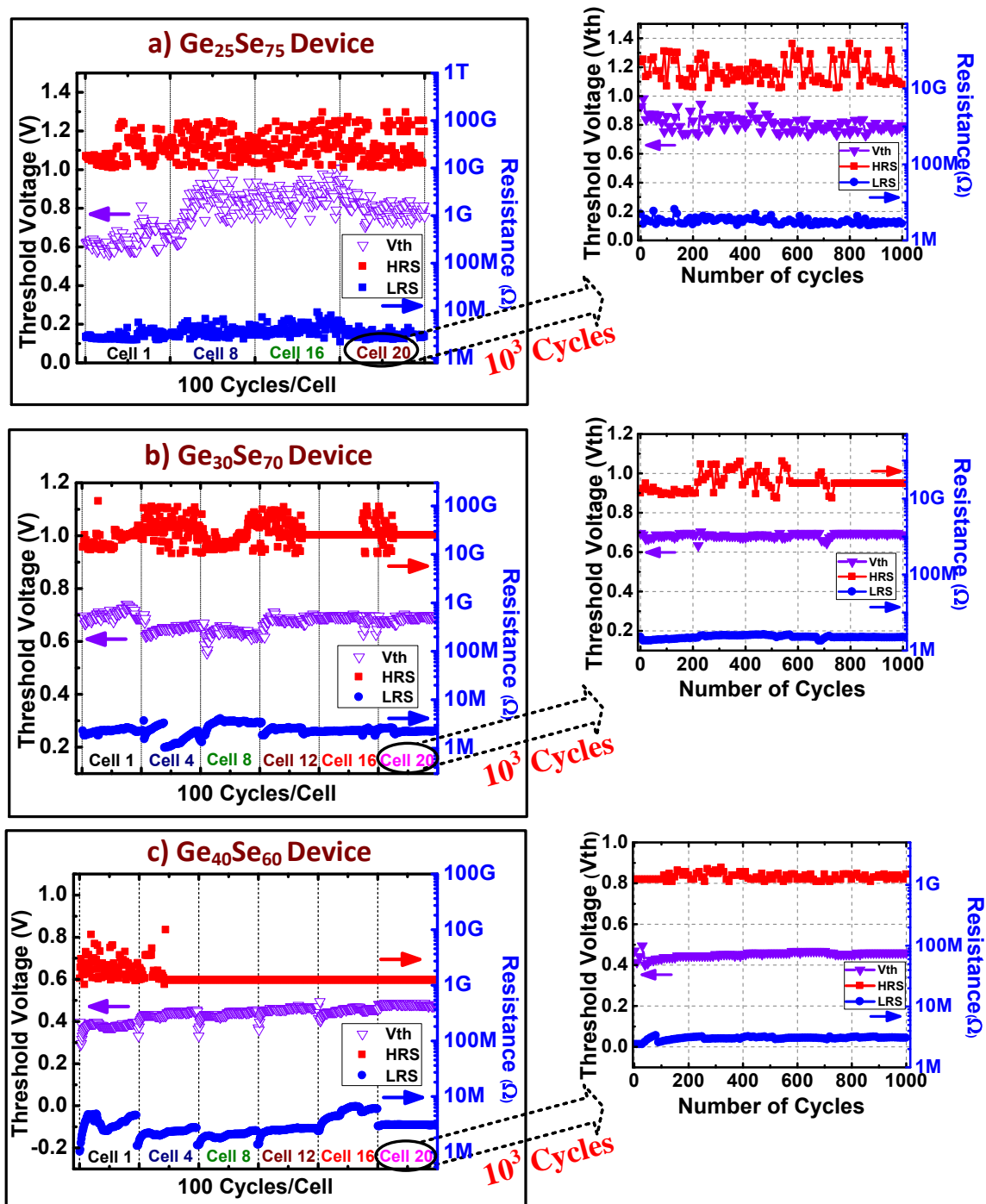


**Figure 6.10** Resistance and threshold voltage plot of (a)  $\text{Ge}_{25}\text{Se}_{75}$ , (b)  $\text{Ge}_{30}\text{Se}_{70}$ , and (c)  $\text{Ge}_{40}\text{Se}_{60}$  in different cells of the array where  $10^3$  cycles for cell 20 for each composition

Relating the films characterization data to devices performance, it is suggested that there are two main reasons for the poor performance of the  $\text{Ge}_{25}\text{Se}_{75}$  devices: higher surface roughness, which is the reason for uncontrolled growth of the conductive bridge and the fact that, after ion bombardment the composition keeps a structure characteristic for Se rich films, which results in the development of heterogeneous structure [218] when Ag is introduced in them, due to the formation of Ag clusters, causing variable distribution within the chalcogenide matrix. However, in the case of Ge rich binary glasses, due to the better surface smoothness the bridge formation is stable over the entire ChG and electrodes interface. The presence of ETH units despite the Ge loss categorizes these films as Ge rich. Therefore, they form homogeneous material with Ag introduction [218], which stabilizes the switching characteristics of the devices. Also, the fact that the devices with a higher Ge concentration perform better means that the damage caused by the  $\text{Ar}^+$  ions does not penetrate throughout the entire film and is distributed closely to the surface of the films. However, in the case of Ge deficient films, a high number of defects penetrate deep into the film and are also distributed unevenly on the surface, resulting in poor device performance.

### **Summary**

A scheme for a RCBM array with no lithography step is successfully demonstrated. Ion bombardment results indicate that it causes compositional changes by which the element with the smallest mass is sputtered faster, resulting in structural transformations occurring in the films. The structural transformation is also related to direct interaction of  $\text{Ar}^+$  ions with Ge-Se films. The fabricated non-lithography array structure allowed individual cell addressing. The individual cells built by thin Ge-Se

films showed excellent yield with good endurance at over  $10^3$  cycles. It was found that the Ge rich film offered the least surface roughness and homogenous distribution of Ag, which contribute to a more stable and repeatable device performance.

## CHAPTER SEVEN: SUMMARY AND CONCLUSION

Even though a number of materials have successfully demonstrated resistive switching behavior, a significant research work is currently being undertaken to investigate new materials that exhibit improved resistive switching mechanism and device behavior. Therefore, it is important to narrow down the list of materials to include only those that provide excellent device characteristics and can make significant progress in improving all aspects of non-volatile memory.

With the abundance of available literature and research regarding Ge containing chalcogenide glasses for RCBM devices, the PECVD method for deposition of Ge-S active film was never studied. In addition to novel deposition techniques, significant studies in material engineering were made as a result of this research by creating nanostructure columnar rods in the active film. These advancements allowed the formation of filament growth within the nanostructure columnar rods, which considerably improved the device performance by solving the fundamental problem of multi-branching during the filament growth. No such work has been reported previously with such structures in the active layer and the data collected have no counterparts in literature. These techniques were patented due to the unique nature of this discovery. In addition, a lithography free scheme for RCBM array fabrication was demonstrated without involving any wet chemistry. The particular findings of this dissertation are highlighted below:

### PECVD Devices

- The PECVD deposited films permitted the dynamic control of the composition by controlling the gas precursor ratios. Sulfide glasses were preferred for the PECVD deposition technique since they present a better temperature stability of up to 400°C.
  - Raman analysis revealed the presence of specific structural units corresponding to films with reduced structural stress.
  - EDS analysis of the films revealed a ~1% compositional variation, which confirmed homogeneous deposition of the film using this depositional technique.
  - Films deposited at low temperature (120°C) with relatively less Ge concentration had a smooth surface with less frequency of hillocks.

### Column Structured Devices

- Nano-columnar structures in thin films were created and studied by having a strict control over the deposition current, deposition rate, and uniform temperature within the chamber.
  - SEM and AFM tools were used to study the nano-columnar structures in thin films, which validated the presence of columnar structures in the  $\text{Ge}_x\text{Se}_{1-x}$  ( $x = 0.2, 0.3, 0.4$ ) and  $\text{Ge}_x\text{Te}_{1-x}$  ( $x = 0.2, 0.5$ ) chalcogenide glasses.
  - A correction was suggested to the Tangent Rule for the studied glass compositions to better predict the inclination of the column structures.

- Raman results illustrated changes occurring in Ge-Se structure as a function of oblique angle deposition due to formation of a phase separated material or the relief of the packaging stress in the particular composition. Small alterations in chemical structure of the Ge-Te films were also detected due the presence of the rocksalt structure.
- An increase in the surface roughness of the films was observed by decreasing the vapor flux angle, which suggested an increase in the inter-column voids.
- An innovative 3-in-1 mask was designed and applied for fabricating RCBM devices.
- A strategic improvement in the process flow for fabricating the RCBM devices was implemented by modeling the electric field distribution in the active layer using COMSOL multi-physics software. Additionally, the photo-diffusion setup was eliminated for the column structure devices.
- The electrical testing of the devices revealed Write/Read voltages were dependent on deposition angle. Due to this unique relationship of the devices, switching voltage can be engineered by varying the deposition angle.
- Formation of columnar structures enhanced the performance of devices fabricated with active films from both Ge-Se and Ge-Te systems. These device exhibited excellent uniformity in switching voltage with endurance of well over  $10^6$  cycles, retention of over  $10^4$  seconds @  $130^\circ\text{C}$ , and a good memory window.

- Nano-scaled electrical characterization of the devices through PF-TUNA and PF-KPFM illustrated the directional growth of the nano-ionic metallic filament through the nano-engineered columnar structures, with no multi-branching, which is the basis for the improved device performance.

#### Lithography-Free Array Formation

- A lithography free method for prototyping RCBM arrays, without the application of wet chemistry, was suggested and presented with individual cell addressing.
  - Ion bombardment causes compositional changes by which the element with smallest mass was sputtered faster, resulting in structural transformations within the films. The structural transformation was also related to the direct interaction of Ar<sup>+</sup> ions with Ge-Se films that caused significant structural changes in the Ge rich films.
  - The Ge rich films incurred the least surface roughness, which correlated to the best device performance, and is attributed to the formation of rigid structure and the availability of Ge-Ge bonds.
  - Excellent endurance and retention performance was achieved for the cells within the array fabricated by the lithography free method.

The goal of this research work was to improve the RCBM device performance by providing new and innovative solutions for the active films. This was successfully achieved by studying novel film deposition techniques (PECVD), the formation of columnar structures that ensured single filament growth process, and the device fabrication using lithography free method. The processes, methodologies, and machines utilized in this dissertation are currently available and being used by the major

semiconductor companies, therefore these improved device performance can be replicated for mass device fabrication.

## REFERENCES

- [1] G. E. Moore, "Cramming more components onto integrated circuits, Reprinted from Electronics, volume 38, number 8, April 19, 1965, pp.114 ff," *Solid-State Circuits Newsletter, IEEE*, vol. 11, pp. 33-35, 2006.
- [2] G. E. Moore, "Progress in digital integrated electronics," in *Electron Devices Meeting, 1975 International*, 1975, pp. 11-13.
- [3] M. T. Bohr, "Nanotechnology goals and challenges for electronic applications," *Nanotechnology, IEEE Transactions on*, vol. 1, pp. 56-62, 2002.
- [4] M. A. W. Erm, J. Hutchby & M. Garner "Assessment of the Potential & Maturity of Selected Emerging Research Memory Technologies Workshop," *New directions for youth development*, vol. 2011, pp. 7-11, 2011.
- [5] S. E. Ahn, M. J. Lee, Y. Park, B. S. Kang, C. B. Lee, K. H. Kim, *et al.*, "Write current reduction in transition metal oxide based resistance change memory," *Advanced Materials*, vol. 20, pp. 924-928, 2008.
- [6] D. Ielmini, A. S. Spinelli, and A. L. Lacaita, "Recent developments on Flash memory reliability," *Microelectronic Engineering*, vol. 80, pp. 321-328, 6/17/ 2005.
- [7] Y. S. Kim, D. J. Lee, C. K. Lee, H. K. Choi, S. S. Kim, J. H. Song, *et al.*, "New scaling limitation of the floating gate cell in NAND Flash Memory," in *Reliability Physics Symposium (IRPS), 2010 IEEE International*, 2010, pp. 599-603.
- [8] B. Govoreanu, D. Brunco, and J. Van Houdt, "Scaling down the interpoly dielectric for next generation flash memory: Challenges and opportunities," *Solid-state electronics*, vol. 49, pp. 1841-1848, 2005.

- [9] Y. Koh, "NAND Flash scaling beyond 20nm," in *Memory Workshop, 2009. IMW'09. IEEE International*, 2009, pp. 1-3.
- [10] S. Tehrani, J. Slaughter, E. Chen, M. Durlam, J. Shi, and M. DeHerren, "Progress and outlook for MRAM technology," *Magnetics, IEEE Transactions on*, vol. 35, pp. 2814-2819, 1999.
- [11] H. Duiker, P. Beale, J. Scott, C. Paz de Araujo, B. Melnick, J. Cuchiario, *et al.*, "Fatigue and switching in ferroelectric memories: Theory and experiment," *Journal of applied physics*, vol. 68, pp. 5783-5791, 1990.
- [12] Y. Fujisaki, "Overview of emerging semiconductor non-volatile memories," *IEICE Electronics Express*, vol. 9, pp. 908-925, 2012 2012.
- [13] W. Y. Cho, B. H. Cho, B. G. Choi, H. R. Oh, S. Kang, K.-S. Kim, *et al.*, "A 0.18- $\mu\text{m}$  3.0-V 64-Mb nonvolatile phase-transition random access memory (PRAM)," *Solid-State Circuits, IEEE Journal of*, vol. 40, pp. 293-300, 2005.
- [14] L. Chua, "Memristor-the missing circuit element," *Circuit Theory, IEEE Transactions on*, vol. 18, pp. 507-519, 1971.
- [15] L. O. Chua and S. M. Kang, "Memristive devices and systems," *Proceedings of the IEEE*, vol. 64, pp. 209-223, 1976.
- [16] S. Seo, M. J. Lee, D. H. Seo, E. J. Jeoung, D. S. Suh, Y. S. Joung, *et al.*, "Reproducible resistance switching in polycrystalline NiO films," *Applied Physics Letters*, vol. 85, pp. 5655-5657, 2004.
- [17] J. F. Gibbons and W. E. Beadle, "Switching properties of thin NiO films," *Solid-State Electronics*, vol. 7, pp. 785-790, 11/ 1964.
- [18] O. Kavehei, C. Kyoungrok, L. Sangjin, K. Sung Jin, S. Al-Sarawi, D. Abbott, *et al.*, "Fabrication and modeling of Ag/TiO<sub>2</sub>/ITO memristor," in *Circuits and Systems (MWSCAS), 2011 IEEE 54th International Midwest Symposium on*, 2011, pp. 1-4.

- [19] B. J. Choi, D. S. Jeong, S. K. Kim, C. Rohde, S. Choi, J. H. Oh, *et al.*, "Resistive switching mechanism of TiO<sub>2</sub> thin films grown by atomic-layer deposition," *Journal of Applied Physics*, vol. 98, pp. 033710-033715, 2005.
- [20] Z. Fang, H. Yu, W. Liu, Z. Wang, X. Tran, B. Gao, *et al.*, "Temperature Instability of Resistive Switching on HfO<sub>x</sub>-Based RRAM Devices," *IEEE Electron Device Letters*, vol. 31, pp. 476-478, 2010.
- [21] H. Lee, P. Chen, T. Wu, Y. Chen, C. Wang, P. Tzeng, *et al.*, "Low power and high speed bipolar switching with a thin reactive Ti buffer layer in robust HfO<sub>2</sub> based RRAM," in *Electron Devices Meeting, 2008. IEDM 2008. IEEE International*, 2008, pp. 1-4.
- [22] Y. S. Chen, T. Y. Wu, P. J. Tzeng, P. S. Chen, H. Y. Lee, C. H. Lin, *et al.*, "Forming-free HfO<sub>2</sub> bipolar RRAM device with improved endurance and high speed operation," in *VLSI Technology, Systems, and Applications, 2009. VLSI-TSA'09. International Symposium on*, 2009, pp. 37-38.
- [23] M. Janousch, G. I. Meijer, U. Staub, B. Delley, S. F. Karg, and B. P. Andreasson, "Role of Oxygen Vacancies in Cr-Doped SrTiO<sub>3</sub> for Resistance-Change Memory," *Advanced Materials*, vol. 19, pp. 2232-2235, 2007.
- [24] D. S. Shang, Q. Wang, L. D. Chen, R. Dong, X. M. Li, and W. Q. Zhang, "Effect of carrier trapping on the hysteretic current-voltage characteristics in Ag/La<sub>0.7</sub>Ca<sub>0.3</sub>MnO<sub>3</sub>/Pt heterostructures," *Physical Review B*, vol. 73, p. 245427, 06/22/ 2006.
- [25] L. Huang, B. Qu, L. Liu, and L. Zhang, "Study on the resistive switching properties of epitaxial La<sub>0.67</sub>Sr<sub>0.33</sub>MnO<sub>3</sub> films," *Solid State Communications*, vol. 143, pp. 382-385, 8/ 2007.
- [26] S. Q. Liu, N. J. Wu, and A. Ignatiev, "Electric-pulse-induced reversible resistance change effect in magnetoresistive films," *Applied Physics Letters*, vol. 76, pp. 2749-2751, 2000.

- [27] B. C. Lee, E. Ipek, O. Mutlu, and D. Burger, "Phase change memory architecture and the quest for scalability," *Communications of the ACM*, vol. 53, pp. 99-106, 2010.
- [28] G. W. Burr, M. J. Breitwisch, M. Franceschini, D. Garetto, K. Gopalakrishnan, B. Jackson, *et al.*, "Phase change memory technology," *Journal of Vacuum Science & Technology B: Microelectronics and Nanometer Structures*, vol. 28, pp. 223-262, 2010.
- [29] M. Mitkova and Y. Sakaguchi, "Nano-ionic nonvolatile memory devices—basic ideas and structural model of rigid Ge-S glasses as medium for them," 2009.
- [30] M. Mitkova, Y. Sakaguchi, D. Tenne, S. K. Bhagat, and T. L. Alford, "Structural details of Ge-rich and silver-doped chalcogenide glasses for nanoionic nonvolatile memory," *physica status solidi (a)*, vol. 207, pp. 621-626, 2010.
- [31] M. N. Kozicki, M. Park, and M. Mitkova, "Nanoscale memory elements based on solid-state electrolytes," *Nanotechnology, IEEE Transactions on*, vol. 4, pp. 331-338, 2005.
- [32] F. Argall, "Switching phenomena in titanium oxide thin films," *Solid-State Electronics*, vol. 11, pp. 535-541, 1968.
- [33] D. S. Jeong, H. Schroeder, and R. Waser, "Impedance spectroscopy of TiO thin films showing resistive switching," *Applied physics letters*, vol. 89, p. 082909, 2006.
- [34] C. Lee, B. Kang, M. Lee, S. Ahn, G. Stefanovich, W. Xianyu, *et al.*, "Electromigration effect of Ni electrodes on the resistive switching characteristics of NiO thin films," *Applied Physics Letters*, vol. 91, pp. 082104-082104-3, 2007.
- [35] R. Waser and M. Aono, "Nanoionics-based resistive switching memories," *Nat Mater Nature Materials*, vol. 6, pp. 833-840, 2007.

- [36] M. Wuttig, "Phase-change materials: towards a universal memory?," *Nature materials*, vol. 4, pp. 265-266, 2005.
- [37] A. Pirovano, A. Lacaita, A. Benvenuti, F. Pellizzer, S. Hudgens, and R. Bez, "Scaling analysis of phase-change memory technology," in *Electron Devices Meeting, 2003. IEDM'03 Technical Digest. IEEE International*, 2003, pp. 29.6. 1-29.6. 4.
- [38] D. C. Kim, S. Seo, S. E. Ahn, D. S. Suh, M. J. Lee, B. H. Park, *et al.*, "Electrical observations of filamentary conduction for the resistive memory switching in NiO films," *Applied Physics Letters*, vol. 88, 2006.
- [39] J. J. Yang, F. Miao, M. D. Pickett, D. A. Ohlberg, D. R. Stewart, C. N. Lau, *et al.*, "The mechanism of electroforming of metal oxide memristive switches," *Nanotechnology*, vol. 20, p. 215201, 2009.
- [40] D. S. Jeong, H. Schroeder, U. Breuer, and R. Waser, "Characteristic electroforming behavior in Pt/TiO/Pt resistive switching cells depending on atmosphere," *Journal of Applied Physics*, vol. 104, p. 123716, 2008.
- [41] V. V. Zhirnov and R. K. Cavin, "Nanodevices: Charge of the heavy brigade," *Nature nanotechnology*, vol. 3, pp. 377-378, 2008.
- [42] J. J. Yang, M. D. Pickett, X. Li, D. A. Ohlberg, D. R. Stewart, and R. S. Williams, "Memristive switching mechanism for metal/oxide/metal nanodevices," *Nature nanotechnology*, vol. 3, pp. 429-433, 2008.
- [43] D. B. Strukov, G. S. Snider, D. R. Stewart, and R. S. Williams, "The missing memristor found," *Nature*, vol. 453, pp. 80-83, 2008.
- [44] X. Guo, C. Schindler, S. Menzel, and R. Waser, "Understanding the switching-off mechanism in Ag<sup>+</sup> migration based resistively switching model systems," *Applied Physics Letters*, vol. 91, p. 133513, 2007.

- [45] C. Schindler, S. C. P. Thermadam, R. Waser, and M. N. Kozicki, "Bipolar and Unipolar Resistive Switching in Cu-Doped SiO<sub>2</sub>," *Electron Devices, IEEE Transactions on*, vol. 54, pp. 2762-2768, 2007.
- [46] A. Sawa, T. Fujii, M. Kawasaki, and Y. Tokura, "Interface resistance switching at a few nanometer thick perovskite manganite active layers," *Applied physics letters*., vol. 88, p. 232112, 2006.
- [47] I. Valov, R. Waser, J. R. Jameson, and M. N. Kozicki, "Electrochemical metallization memories - fundamentals, applications, prospects," *Nanotechnology*, vol. 22, p. 254003, 2011.
- [48] S. Kaeriyama, T. Sakamoto, H. Sunamura, M. Mizuno, H. Kawaura, T. Hasegawa, *et al.*, "A nonvolatile programmable solid-electrolyte nanometer switch," *Solid-State Circuits, IEEE Journal of*, vol. 40, pp. 168-176, 2005.
- [49] K. Terabe, T. Hasegawa, T. Nakayama, and M. Aono, "Quantized conductance atomic switch," *Nature*, vol. 433, pp. 47-50, 2005.
- [50] K. Aratani, K. Ohba, T. Mizuguchi, S. Yasuda, T. Shiimoto, T. Tsushima, *et al.*, "A novel resistance memory with high scalability and nanosecond switching," in *Electron Devices Meeting, 2007. IEDM 2007. IEEE International*, 2007, pp. 783-786.
- [51] M. Kund, G. Beitel, C.-U. Pinnow, T. Rohr, J. Schumann, R. Symanczyk, *et al.*, "Conductive bridging RAM (CBRAM): An emerging non-volatile memory technology scalable to sub 20nm," in *Electron Devices Meeting, 2005. IEDM Technical Digest. IEEE International*, 2005, pp. 754-757.
- [52] R. Waser, R. Dittmann, G. Staikov, and K. Szot, "Redox-Based Resistive Switching Memories - Nanoionic Mechanisms, Prospects, and Challenges," *Advanced Materials*, vol. 21, pp. 2632-2663, Jul 2009.

- [53] J. B. Allen and R. F. Larry, "Electrochemical methods: fundamentals and applications," *Department of Chemistry and Biochemistry University of Texas at Austin, John Wiley & Sons, Inc*, 2001.
- [54] C. H. Hamann, A. Hamnett, and W. Vielstich, "Electrochemistry. 1998," ed: Wiley-VCH, 1998.
- [55] C. Schindler, I. Valov, and R. Waser, "Faradaic currents during electroforming of resistively switching Ag–Ge–Se type electrochemical metallization memory cells," *Physical Chemistry Chemical Physics*, vol. 11, pp. 5974-5979, 2009.
- [56] C. M. Compagnoni, D. Ielmini, A. Spinelli, A. Lacaita, C. Previtali, and C. Gerardi, "Study of data retention for nanocrystal Flash memories," in *Reliability Physics Symposium Proceedings, 2003. 41st Annual. 2003 IEEE International*, 2003, pp. 506-512.
- [57] R. Symanczyk, M. Balakrishnan, C. Gopalan, T. Happ, M. Kozicki, M. Kund, *et al.*, "Electrical Characterization of Solid State Ionic Memory Elements," 2003.
- [58] S. Tappertzhofen, I. Valov, and R. Waser, "Quantum conductance and switching kinetics of AgI-based microcrossbar cells," *Nanotechnology*, vol. 23, p. 145703, 2012.
- [59] Y. Hosoi, Y. Tamai, T. Ohnishi, K. Ishihara, T. Shibuya, Y. Inoue, *et al.*, "High Speed Unipolar Switching Resistance RAM (RRAM) Technology," in *Electron Devices Meeting, 2006. IEDM '06. International*, 2006, pp. 1-4.
- [60] Y. C. Yang, F. Pan, Q. Liu, M. Liu, and F. Zeng, "Fully room-temperature-fabricated nonvolatile resistive memory for ultrafast and high-density memory application," *Nano Lett*, vol. 9, pp. 1636-1643, 2009.
- [61] J. J. Yang, D. B. Strukov, and D. R. Stewart, "Memristive devices for computing," *Nature nanotechnology*, vol. 8, pp. 13-24, 2012.

- [62] D. S. Jeong, R. Thomas, R. Katiyar, J. Scott, H. Kohlstedt, A. Petraru, *et al.*, "Emerging memories: resistive switching mechanisms and current status," *Reports on Progress in Physics*, vol. 75, p. 076502, 2012.
- [63] P. Calka, E. Martinez, D. Lafond, S. Minoret, S. Tirano, B. Detlefs, *et al.*, "Origin of resistivity change in NiO thin films studied by hard x-ray photoelectron spectroscopy," *Journal of Applied Physics*, vol. 109, pp. 124507-124507-6, 2011.
- [64] L. Ying Tao, L. Shi Bing, L. Hang Bing, L. Qi, W. Qin, W. Yan, *et al.*, "Investigation of resistive switching behaviours in WO<sub>3</sub> based RRAM devices," *Chinese Physics B*, vol. 20, p. 017305, 2011.
- [65] F. Pan, S. Yin, and V. Subramanian, "A Comprehensive Simulation Study on Metal Conducting Filament Formation in Resistive Switching Memories," in *Memory Workshop (IMW), 2011 3rd IEEE International*, 2011, pp. 1-4.
- [66] Y. Hirose and H. Hirose, "Polarity-dependent memory switching and behavior of Ag dendrite in Ag-photodoped amorphous As<sub>2</sub>S<sub>3</sub> films," *Journal of Applied Physics*, vol. 47, pp. 2767-2772, 1976.
- [67] R. F. Bunshah, *Handbook of deposition technologies for films and coatings: science, technology, and applications*: Access Online via Elsevier, 1994.
- [68] P. M. Martin, *Handbook of deposition technologies for films and coatings: science, applications and technology*: William Andrew, 2009.
- [69] W. Kern, *Thin film processes II* vol. 2: Access Online via Elsevier, 1991.
- [70] D. Ye, T. Karabacak, B. Lim, G. Wang, and T. Lu, "Growth of uniformly aligned nanorod arrays by oblique angle deposition with two-phase substrate rotation," *Nanotechnology*, vol. 15, p. 817, 2004.
- [71] Y. Cui and C. M. Lieber, "Functional nanoscale electronic devices assembled using silicon nanowire building blocks," *science*, vol. 291, pp. 851-853, 2001.

- [72] V. Poborchii, T. Tada, T. Kanayama, and A. Moroz, "Silver-coated silicon pillar photonic crystals: Enhancement of a photonic band gap," *Applied physics letters*, vol. 82, pp. 508-510, 2003.
- [73] M. H. Huang, S. Mao, H. Feick, H. Yan, Y. Wu, H. Kind, *et al.*, "Room-temperature ultraviolet nanowire nanolasers," *science*, vol. 292, pp. 1897-1899, 2001.
- [74] A. Tao, F. Kim, C. Hess, J. Goldberger, R. He, Y. Sun, *et al.*, "Langmuir-Blodgett silver nanowire monolayers for molecular sensing using surface-enhanced Raman spectroscopy," *Nano Letters*, vol. 3, pp. 1229-1233, 2003.
- [75] Q. Wang, T. Corrigan, J. Dai, R. Chang, and A. Krauss, "Field emission from nanotube bundle emitters at low fields," *Applied physics letters*, vol. 70, pp. 3308-3310, 1997.
- [76] S.-H. Woo, Y. J. Park, D.-H. Chang, and C. K. Hwangbo, "Wideband antireflection coatings of porous MgF<sub>2</sub> films by using glancing angle deposition," *Journal of Korean Physical Society*, vol. 51, p. 1501, 2007.
- [77] R. Sharma, E. Haberer, C. Meier, E. Hu, and S. Nakamura, "Vertically oriented GaN-based air-gap distributed Bragg reflector structure fabricated using band-gap-selective photoelectrochemical etching," *Applied Physics Letters*, vol. 87, pp. 051107-051107-3, 2005.
- [78] S. T. Ho, S. McCall, R. Slusher, L. Pfeiffer, K. West, A. Levi, *et al.*, "High index contrast mirrors for optical microcavities," *Applied physics letters*, vol. 57, pp. 1387-1389, 1990.
- [79] A. Jain, S. Rogojevic, S. Ponoth, N. Agarwal, I. Matthew, W. Gill, *et al.*, "Porous silica materials as low k dielectrics for electronic and optical interconnects," *Thin Solid Films*, vol. 398, pp. 513-522, 2001.

- [80] A. Kundt, "Ueber Doppelbrechung des Lichtes in Metallschichten, welche durch Zerstäuben einer Kathode hergestellt sind," *Annalen der Physik*, vol. 263, pp. 59-71, 1886.
- [81] L. Holland, "The effect of vapor incidence on the structure of evaporated aluminum films," *Josa*, vol. 43, pp. 376-380, 1953.
- [82] D. O. Smith, "Anisotropy in permalloy films," *Journal of Applied Physics*, vol. 30, p. S264, 1959.
- [83] K. Robbie and M. Brett, "Sculptured thin films and glancing angle deposition: Growth mechanics and applications," *Journal of Vacuum Science & Technology A: Vacuum, Surfaces, and Films*, vol. 15, pp. 1460-1465, 1997.
- [84] M. T. Taschuk, M. M. Hawkeye, and M. J. Brett, "Glancing angle deposition," *Handbook of Deposition Technologies for Films and Coatings, 3rd ed.* (Elsevier, 2010), pp. 621-678, 2010.
- [85] N. Kaiser and H. K. Pulker, "Optical interference coatings," *Optical interference coatings/Norbert Kaiser, Hans K. Pulker (eds.). Berlin; New York: Springer, 2003.* (Springer series in optical sciences; 88), vol. 1, 2003.
- [86] B. Movchan and A. Demchishin, "Structure and Properties of Thick Condensates of Nickel, Titanium, Tungsten, Aluminum Oxides and Zirconium Dioxide in Vacuum," *Fiz. Metal. Metalloved.* 28: 653-60 (Oct 1969). 1969.
- [87] J. A. Thornton, "Structure-zone models of thin films," *SPIE vol. 821, Modeling of optical thin films*, vol. 95, 1987.
- [88] R. Messier, A. Giri, and R. Roy, "Revised structure zone model for thin film physical structure," *Journal of Vacuum Science & Technology A: Vacuum, Surfaces, and Films*, vol. 2, pp. 500-503, 1984.
- [89] R. Messier and R. C. Ross, "Evolution of microstructure in amorphous hydrogenated silicon," *Journal of Applied Physics*, vol. 53, pp. 6220-6225, 1982.

- [90] C. Grovenor, H. Hentzell, and D. Smith, "The development of grain structure during growth of metallic films," *Acta Metallurgica*, vol. 32, pp. 773-781, 1984.
- [91] R. Messier, S. Krishnaswamy, L. Gilbert, and P. Swab, "Black a-Si solar selective absorber surfaces," *Journal of Applied Physics*, vol. 51, pp. 1611-1614, 1980.
- [92] J. M. N. a. H. B. Haanstra, "Microfractography of thin films," *Philips Tech.*, vol. Rev. 27, pp. 87-91, 1966.
- [93] F. Liu, M. Umlor, L. Shen, J. Weston, W. Eads, J. Barnard, *et al.*, "The growth of nanoscale structured iron films by glancing angle deposition," *Journal of applied physics*, vol. 85, pp. 5486-5488, 1999.
- [94] L. Abelmann and C. Lodder, "Oblique evaporation and surface diffusion," *Thin Solid Films*, vol. 305, pp. 1-21, 8/ 1997.
- [95] D. Vick, L. J. Friedrich, S. K. Dew, M. J. Brett, K. Robbie, M. Seto, *et al.*, "Self-shadowing and surface diffusion effects in obliquely deposited thin films," *Thin Solid Films*, vol. 339, pp. 88-94, 2/8/ 1999.
- [96] D. Vick, T. Smy, and M. J. Brett, "Growth behavior of evaporated porous thin films," *Journal of Materials Research*, vol. 17, pp. 2904-2911, 2002.
- [97] R. Messier, V. C. Venugopal, and P. D. Sunal, "Origin and evolution of sculptured thin films," *Journal of Vacuum Science & Technology A: Vacuum, Surfaces, and Films*, vol. 18, pp. 1538-1545, 2000.
- [98] B. Dick, M. J. Brett, and T. Smy, "Controlled growth of periodic pillars by glancing angle deposition," *Journal of Vacuum Science & Technology B: Microelectronics and Nanometer Structures*, vol. 21, pp. 23-28, 2003.
- [99] B. Dick, M. Brett, and T. Smy, "Investigation of substrate rotation at glancing incidence on thin-film morphology," *Journal of Vacuum Science & Technology B: Microelectronics and Nanometer Structures*, vol. 21, pp. 2569-2575, 2003.

- [100] R. Messier, T. Gehrke, C. Frankel, V. C. Venugopal, W. Otano, and A. Lakhtakia, "Engineered sculptured nematic thin films," *Journal of Vacuum Science & Technology A: Vacuum, Surfaces, and Films*, vol. 15, pp. 2148-2152, 1997.
- [101] J. Lintymer, N. Martin, J. M. Chappé, P. Delobelle, and J. Takadoum, "Influence of zigzag microstructure on mechanical and electrical properties of chromium multilayered thin films," *Surface and Coatings Technology*, vol. 180, pp. 26-32, 2004.
- [102] S. R. Kennedy and M. J. Brett, "Advanced techniques for the fabrication of square spiral photonic crystals by glancing angle deposition," *Journal of Vacuum Science & Technology B: Microelectronics and Nanometer Structures*, vol. 22, pp. 1184-1190, 05/00/ 2004.
- [103] A. Lakhtakia, R. Messier, and D. K. Paul, "Books - Sculptured Thin Films: Nanoengineered Morphology and Optics," *Physics today.*, vol. 59, p. 67, 2006.
- [104] R. Tait, T. Smy, and M. Brett, "Structural anisotropy in oblique incidence thin metal films," *Journal of Vacuum Science & Technology A: Vacuum, Surfaces, and Films*, vol. 10, pp. 1518-1521, 1992.
- [105] J. A. Thornton, "Influence of apparatus geometry and deposition conditions on the structure and topography of thick sputtered coatings," *Journal of Vacuum Science & Technology*, vol. 11, pp. 666-670, 1974.
- [106] H. van Kranenburg and C. Lodder, "Tailoring growth and local composition by oblique-incidence deposition: a review and new experimental data," *Materials Science and Engineering: R: Reports*, vol. 11, pp. 295-354, 1994.
- [107] A. G. Dirks and H. J. Leamy, "Columnar microstructure in vapor-deposited thin films," *Thin Solid Films*, vol. 47, pp. 219-233, 12/15/ 1977.
- [108] J. Nieuwenhuizen and H. Haanstra, "Microfractography of thin films," *Philips Tech Rev*, vol. 27, pp. 87-91, 1966.

- [109] M. M. Hawkeye and M. J. Brett, "Glancing angle deposition: Fabrication, properties, and applications of micro- and nanostructured thin films," *Journal of Vacuum Science & Technology A: Vacuum, Surfaces, and Films*, vol. 25, pp. 1317-1335, 2007.
- [110] S. Lichter and J. Chen, "Model for columnar microstructure of thin solid films," *Physical Review Letters*, vol. 56, pp. 1396-1399, 1986.
- [111] I. Hodgkinson and J. Hazel, "Empirical equations for the principal refractive indices and column angle of obliquely deposited films of tantalum oxide, titanium oxide, and zirconium oxide," *Applied Optics*, vol. 37, pp. 2653-2659, 1998.
- [112] E. Welsch, H. Walther, D. Schäfer, R. Wolf, and H. Müller, "Correlation between morphology, optical losses and laser damage of  $\text{MgF}_2$ - $\text{SiO}_2$  multilayers," *Thin Solid Films*, vol. 156, pp. 1-10, 1988.
- [113] X. Tang, G. Zhang, and Y. Zhao, "Electrochemical characterization of silver nanorod electrodes prepared by oblique angle deposition," *Nanotechnology*, vol. 17, p. 4439, 2006.
- [114] F. Tang, T. Karabacak, L. Li, M. Pelliccione, G.-C. Wang, and T.-M. Lu, "Power-law scaling during shadowing growth of nanocolumns by oblique angle deposition," *Journal of Vacuum Science & Technology A: Vacuum, Surfaces, and Films*, vol. 25, pp. 160-166, 2007.
- [115] C. Zhou and D. Gall, "Surface patterning by nanosphere lithography for layer growth with ordered pores," *Thin Solid Films*, vol. 516, pp. 433-437, 2007.
- [116] C. Patzig and B. Rauschenbach, "Temperature effect on the glancing angle deposition of Si sculptured thin films," *Journal of Vacuum Science & Technology A: Vacuum, Surfaces, and Films*, vol. 26, pp. 881-886, 2008.
- [117] K. Nagashima, T. Yanagida, K. Oka, M. Taniguchi, T. Kawai, J.-S. Kim, *et al.*, "Resistive switching multistate nonvolatile memory effects in a single cobalt oxide nanowire," *Nano Letters*, vol. 10, pp. 1359-1363, 2010.

- [118] J. Ventura, J. Araujo, J. Sousa, Y. Liu, Z. Zhang, and P. Freitas, "Probing atomic rearrangement events in resistive switching nanostructures," *Applied Physics Letters*, vol. 96, pp. 043505 (1-3), 2010.
- [119] M. Fujimoto, H. Koyama, M. Konagai, Y. Hosoi, K. Ishihara, S. Ohnishi, *et al.*, "TiO<sub>2</sub> anatase nanolayer on TiN thin film exhibiting high-speed bipolar resistive switching," *Applied physics letters*, vol. 89, pp. 223509-223509, 2006.
- [120] M.-F. Chang, C.-W. Wu, C.-C. Kuo, S.-J. Shen, S.-M. Yang, K.-F. Lin, *et al.*, "A Low-Voltage Bulk-Drain-Driven Read Scheme for Sub-0.5 V 4 Mb 65 nm Logic-Process Compatible Embedded Resistive RAM (ReRAM) Macro," 2013.
- [121] Z. Wei, Y. Kanzawa, K. Arita, Y. Katoh, K. Kawai, S. Muraoka, *et al.*, "Highly reliable TaOx ReRAM and direct evidence of redox reaction mechanism," in *Electron Devices Meeting, 2008. IEDM 2008. IEEE International*, 2008, pp. 1-4.
- [122] S. Lee, S. Chae, S. Chang, J. Lee, S. Seo, B. Kahng, *et al.*, "Scaling behaviors of reset voltages and currents in unipolar resistance switching," *Applied Physics Letters*, vol. 93, pp. 212105-212105-3, 2008.
- [123] K. W. Jeong, Y. H. Do, K. S. Yoon, C. O. Kim, and J. P. Hong, "Resistive Switching Characteristics of Unique Binary-Oxide MgO<sub>x</sub> Films," *Journal - Korean Physical Society*, vol. 48, p. 1501, 2006.
- [124] H. Akinaga and H. Shima, "Resistive random access memory (ReRAM) based on metal oxides," *Proceedings of the IEEE*, vol. 98, pp. 2237-2251, 2010.
- [125] A. Sawa, "Resistive switching in transition metal oxides," *Materials today*, vol. 11, pp. 28-36, 2008.
- [126] P. McWhorter, A. Frazier, and P. Rai-Choudhury, "Micromachining and trends for the twenty-first century," *Handbook of Microlithography, Micromachining, and Microfabrication*, vol. 2, pp. 3-39, 1997.

- [127] F. Schellenberg, "A little light magic [optical lithography]," *Spectrum, IEEE*, vol. 40, pp. 34-39, 2003.
- [128] A. Sangiovanni-Vincentelli and G. Martin, "Platform-based design and software design methodology for embedded systems," *Design & Test of Computers, IEEE*, vol. 18, pp. 23-33, 2001.
- [129] W. Kern, "The evolution of silicon wafer cleaning technology," *Journal of the Electrochemical Society*, vol. 137, pp. 1887-1892, 1990.
- [130] Q. Y. Tong, E. Schmidt, U. Gosele, and M. Reiche, "Hydrophobic silicon wafer bonding," *Applied physics letters*, vol. 64, pp. 625-627, 1994.
- [131] K. Wasa, M. Kitabatake, and H. Adachi, *Thin film materials technology: sputtering of control compound materials*: Springer, 2004.
- [132] M. N. Kozicki, M. Balakrishnan, C. Gopalan, C. Ratnakumar, and M. Mitkova, "Programmable metallization cell memory based on Ag-Ge-S and Cu-Ge-S solid electrolytes," in *Non-Volatile Memory Technology Symposium, 2005*, 2005, pp. 7 pp.-89.
- [133] M. N. Kozicki and M. Mitkova, "Resistance-change devices based on solid electrolytes," *Proc. of EPCOS*, 2006.
- [134] M. Mitkova, M. Kozicki, H. Kim, and T. Alford, "Local structure resulting from photo and thermal diffusion of Ag in Ge-Se thin films," *Journal of Non-Crystalline Solids*, vol. 338, pp. 552-556, 2004.
- [135] M. Popescu, *Non-crystalline chalcogenides*. Dordrecht; Boston: Kluwer Academic Publishers, 2000.
- [136] S. O. Kasap, *Principles of electronic materials and devices*. Boston [etc.: McGraw-Hill, 2006.

- [137] M. Ailavajhala, M. Mitkova, and D. P. Butt, "Simulation and process flow of radiation sensors based on chalcogenide glasses for in situ measurement capability," *Physica Status Solidi (c)*, vol. 9, pp. 2415-2419, 2012.
- [138] T. Kang, C. Hong, C. Chong, and T. Kim, "Effects of electric fields on the silver photodoping of  $\text{As}_2\text{Se}_3$  films," *Journal of materials science*, vol. 27, pp. 5620-5622, 1992.
- [139] A. Ganjoo, G. Chen, and H. Jain, "Photoinduced changes in the local structure of a- $\text{GeSe}_2$  by in situ EXAFS," *Physics and Chemistry of Glasses-European Journal of Glass Science and Technology Part B*, vol. 47, pp. 177-181, 2006.
- [140] A. Ganjoo, H. Jain, and S. Khalid, "Atomistic observation of photo-expansion and photo-contraction in chalcogenide films by in situ EXAFS," *Journal of Non-Crystalline Solids*, vol. 354, pp. 2673-2678, 2008.
- [141] B. Singh, S. Rajagopalan, P. Bhat, D. Pandya, and K. Chopra, "Giant photocontraction effect in amorphous chalcogenide thin films," *Journal of Non-Crystalline Solids*, vol. 35, pp. 1053-1059, 1980.
- [142] M. Jin, P. Chen, P. Boolchand, T. Rajagopalan, K. L. Chopra, K. Starbova, *et al.*, "Origin of giant photocontraction in obliquely deposited amorphous  $\text{Ge}_x\text{Se}_{1-x}$  thin films and the intermediate phase," *Physical Review B*, vol. 78, p. 214201, 2008.
- [143] P. Potts, "Energy Dispersive X-ray spectrometry," in *A Handbook of Silicate Rock Analysis*, ed: Springer, 1992, pp. 286-325.
- [144] D. Shindo and T. Oikawa, "Energy Dispersive X-ray Spectroscopy," in *Analytical Electron Microscopy for Materials Science*, ed: Springer, 2002, pp. 81-102.
- [145] C. Raman and K. Krishnan, "A new type of secondary radiation," *Nature*, vol. 121, pp. 501-502, 1928.
- [146] C. Schindler, "Resistive switching in electrochemical metallization memory cells," Universitätsbibliothek, 2009.

- [147] J. Schweitzer. (2014). *Scanning Electron Microscope*. Available:  
<http://www.purdue.edu/rem/rs/sem.htm>
- [148] M. N. Kozicki and M. Mitkova, "Mass transport in chalcogenide electrolyte films—materials and applications," *Journal of non-crystalline solids*, vol. 352, pp. 567-577, 2006.
- [149] I. Fejes and F. Billes, "Investigation of the structural units of germanium sulfide and selenide by quantum chemical methods," *International Journal of Quantum Chemistry*, vol. 85, pp. 85-91, 2001.
- [150] T. Katsuyama, S. Satoh, and H. Matsumura, "Fabrication of high-purity chalcogenide glasses by chemical vapor deposition," *Journal of applied physics*, vol. 59, pp. 1446-1449, 1986.
- [151] C. Cardinaud, G. Turban, B. Cros, and M. Ribes, "X-ray photoelectron spectroscopy analyses of plasma-deposited GeSe<sub>x</sub> films," *Thin solid films*, vol. 205, pp. 165-170, 1991.
- [152] P. Nagels, "Plasma-enhanced chemical vapor deposition and structural characterization of amorphous chalcogenide films," *Semiconductors*, vol. 32, pp. 855-860, 1998.
- [153] P. J. Whitham, D. P. Strommen, L. D. Lau, and R. G. Rodriguez, "Thin Film Growth of Germanium Selenides from PECVD of GeCl<sub>4</sub> and Dimethyl Selenide," *Plasma chemistry and plasma processing*, vol. 31, pp. 251-256, 2011.
- [154] M. Mitkova, Y. Sakaguchi, D. Tenne, S. K. Bhagat, and T. L. Alford, "Structural details of Ge-rich and silver-doped chalcogenide glasses for nanoionic nonvolatile memory," *Phys. Stat. Sol. A: Applications and Material Science*, vol. 207, pp. 621-626, 2010.

- [155] H. Ji, G. S. Was, J. W. Jones, and N. R. Moody, "Effect of ion bombardment on in-plane texture, surface morphology, and microstructure of vapor deposited Nb thin films," *Journal of Applied Physics*, vol. 81, pp. 6754-6761, 05/15/ 1997.
- [156] R. P. Vinci and J. J. Vlassak, "Mechanical behavior of thin films," *Annual Review of Materials Science*, vol. 26, pp. 431-462, 1996.
- [157] I. Valov and G. Staikov, "Nucleation and growth phenomena in nanosized electrochemical systems for resistive switching memories," *Journal of Solid State Electrochemistry*, pp. 1-7, 2012/10/01 2012.
- [158] D. Goldschmidt, T. Bernstein, and P. Rudman, "The kinetics of photodissolution of silver in amorphous  $As_2S_3$  Films," *physica status solidi (a)*, vol. 41, pp. 283-287, 1977.
- [159] T. Wagner, E. Marquez, J. Fernandez-Pena, J. Gonzalez-Leal, P. Ewen, and S. Kasap, "The kinetics of the photo-induced solid-state chemical reaction in Ag/ $As_{33}S_{67}$  bilayers and its reaction products," *Philosophical Magazine B*, vol. 79, pp. 223-237, 1999.
- [160] T. Wagner, G. Dale, P. Ewen, A. Owen, and V. Perina, "Kinetics of the thermally and photoinduced solid state reaction of Ag with  $As_{33}S_{67}$  films," *Journal of Applied Physics*, vol. 87, pp. 7758-7767, 2000.
- [161] J. Rennie, S. Elliott, and C. Jeynes, "Rutherford backscattering study of the photodissolution of Ag in amorphous  $GeSe_2$ ," *Applied physics letters*, vol. 48, pp. 1430-1432, 1986.
- [162] M. Kalyva, A. Siokou, S. Yannopoulos, T. Wagner, J. Orava, and M. Frumar, "Soft x-ray induced Ag diffusion in amorphous pulse laser deposited AsSe thin films: An x-ray photoelectron and secondary ion mass spectroscopy study," *Journal of Applied Physics*, vol. 104, p. 043704, 2008.
- [163] J. Daillant and A. Gibaud, *X-ray and neutron reflectivity: principles and applications* vol. 770: Springer, 2009.

- [164] X. Feng, W. Bresser, and P. Boolchand, "Direct evidence for stiffness threshold in Chalcogenide glasses," *Physical review letters*, vol. 78, p. 4422, 1997.
- [165] D. Drabold and M. Mitkova, "Silver transport in  $\text{Ge}_x\text{Se}_{1-x}$ : Ag materials: Ab initio simulation of a solid electrolyte," *Physical Review B*, vol. 72, p. 054206, 2005.
- [166] M. Kozicki, C. Brown III, M. Mitkova, S. Enderling, J. Hedley, and A. Walton, "Application of Mass Transport in Solid Electrolyte Films in Tunable Microelectromechanical Resonators."
- [167] B. Dick, M. J. Brett, T. J. Smy, M. R. Freeman, M. Malac, and R. F. Egerton, "Periodic magnetic microstructures by glancing angle deposition," *Journal of Vacuum Science & Technology A: Vacuum, Surfaces, and Films*, vol. 18, pp. 1838-1844, 2000.
- [168] K. Robbie, D. J. Broer, and M. J. Brett, "Chiral nematic order in liquid crystals imposed by an engineered inorganic nanostructure," *Nature*, vol. 399, pp. 764-766, 1999.
- [169] O. Toader and S. John, "Proposed square spiral microfabrication architecture for large three-dimensional photonic band gap crystals," *Science*, vol. 292, pp. 1133-1135, 2001.
- [170] K. Kaminska, T. Brown, G. Beydaghyan, and K. Robbie, "Vacuum evaporated porous silicon photonic interference filters," *Applied optics*, vol. 42, pp. 4212-4219, 2003.
- [171] J. X. Fu, A. Collins, and Y. P. Zhao, "Optical properties and biosensor application of ultrathin silver films prepared by oblique angle deposition," *The Journal of Physical Chemistry C*, vol. 112, pp. 16784-16791, 2008.
- [172] D. A. Gish, F. Nsiah, M. T. McDermott, and M. J. Brett, "Localized surface plasmon resonance biosensor using silver nanostructures fabricated by glancing angle deposition," *Analytical chemistry*, vol. 79, pp. 4228-4232, 2007.

- [173] J. J. Steele, M. T. Taschuk, and M. J. Brett, "Nanostructured metal oxide thin films for humidity sensors," *Sensors Journal, IEEE*, vol. 8, pp. 1422-1429, 2008.
- [174] B. Singh, S. Rajagopalan, P. K. Bhat, D. K. Pandya, and K. L. Chopra, "Giant photocontraction effect in amorphous chalcogenide thin films," *Journal of Non-Crystalline Solids*, vol. 35–36, Part 2, pp. 1053-1059, 1/ 1980.
- [175] S. Rajagopalan, B. Singh, P. Bhat, D. Pandya, and K. Chopra, "Photo-induced chemical changes in obliquely deposited amorphous Se-Ge films," *Journal of Applied Physics*, vol. 51, pp. 1768-1772, 1979.
- [176] S. Rajagopalan, B. Singh, P. K. Bhat, D. K. Pandya, and K. L. Chopra, "Photo-induced optical effects in obliquely deposited amorphous Se-Ge films," *Journal of Applied Physics*, vol. 50, pp. 489-492, 01/00/ 1979.
- [177] A. Lakhtakia, *Sculptured thin films: Nanoengineered morphology and optics* vol. 143: SPIE press, 2005.
- [178] D. R. Lide, *CRC Handbook of Chemistry and Physics 2004-2005: A Ready-Reference Book of Chemical and Physical Data*: CRC press, 2004.
- [179] R. Hultgren, P. D. Desai, D. T. Hawkins, M. Gleiser, and K. K. Kelley, "Selected values of the thermodynamic properties of the elements," DTIC Document 1973.
- [180] S. A. Campbell, *Fabrication engineering at the micro and nanoscale*: Oxford University Press, 2008.
- [181] K. Jackson, A. Briley, S. Grossman, D. V. Porezag, and M. R. Pederson, "Raman-active modes of a-GeSe<sub>2</sub> and a-GeS<sub>2</sub>: A first-principles study," *Physical Review B*, vol. 60, p. R14985, 1999.
- [182] S. Sugai, "Stochastic random network model in Ge and Si chalcogenide glasses," *Physical Review B*, vol. 35, p. 1345, 1987.

- [183] Y. Wang, O. Matsuda, K. Inoue, O. Yamamuro, T. Matsuo, and K. Murase, "A Raman scattering investigation of the structure of glassy and liquid  $\text{Ge}_x\text{Se}_{1-x}$ ," *Journal of non-crystalline solids*, vol. 232, pp. 702-707, 1998.
- [184] Y. Wang and K. Murase, "Floppy modes and relaxation in  $\text{Ge}_x\text{Se}_{1-x}$  glasses," *Journal of non-crystalline solids*, vol. 326, pp. 379-384, 2003.
- [185] T. Edwards and S. Sen, "Structure and relaxation in germanium selenide glasses and supercooled liquids: a Raman spectroscopic study," *The Journal of Physical Chemistry B*, vol. 115, pp. 4307-4314, 2011.
- [186] G. Lucovsky, A. Mooradian, W. Taylor, G. Wright, and R. Keezer, "Identification of the fundamental vibrational modes of trigonal,  $\alpha$ -monoclinic and amorphous selenium," *Solid State Communications*, vol. 5, pp. 113-117, 1967.
- [187] M. Cobb, D. Drabold, and R. Cappelletti, "Ab initio molecular-dynamics study of the structural, vibrational, and electronic properties of glassy  $\text{GeSe}_2$ ," *Physical Review B*, vol. 54, p. 12162, 1996.
- [188] P. Boolchand and W. Bresser, "The structural origin of broken chemical order in  $\text{GeSe}_2$  glass," *Philosophical Magazine B*, vol. 80, pp. 1757-1772, 2000.
- [189] V. Georgieva, M. Mitkova, P. Chen, D. Tenne, K. Wolf, and V. Gadjanova, "NO<sub>2</sub> gas sorption studies of  $\text{Ge}_{33}\text{Se}_{67}$  films using quartz crystal microbalance," *Materials Chemistry and Physics*, 2012.
- [190] C. Kügeler, R. Rosezin, E. Linn, R. Bruchhaus, and R. Waser, "Materials, technologies, and circuit concepts for nanocrossbar-based bipolar RRAM," *Applied Physics A: Materials Science & Processing*, vol. 102, pp. 791-809, 2011.
- [191] G. Saffarini, J. Matthiesen, and R. Blachnik, "The influence of mechanical and chemical thresholds on the free volume percentage in Ge-Se-(Fe, In) chalcogenide glasses," *Physica B: Condensed Matter*, vol. 305, pp. 293-297, 2001.

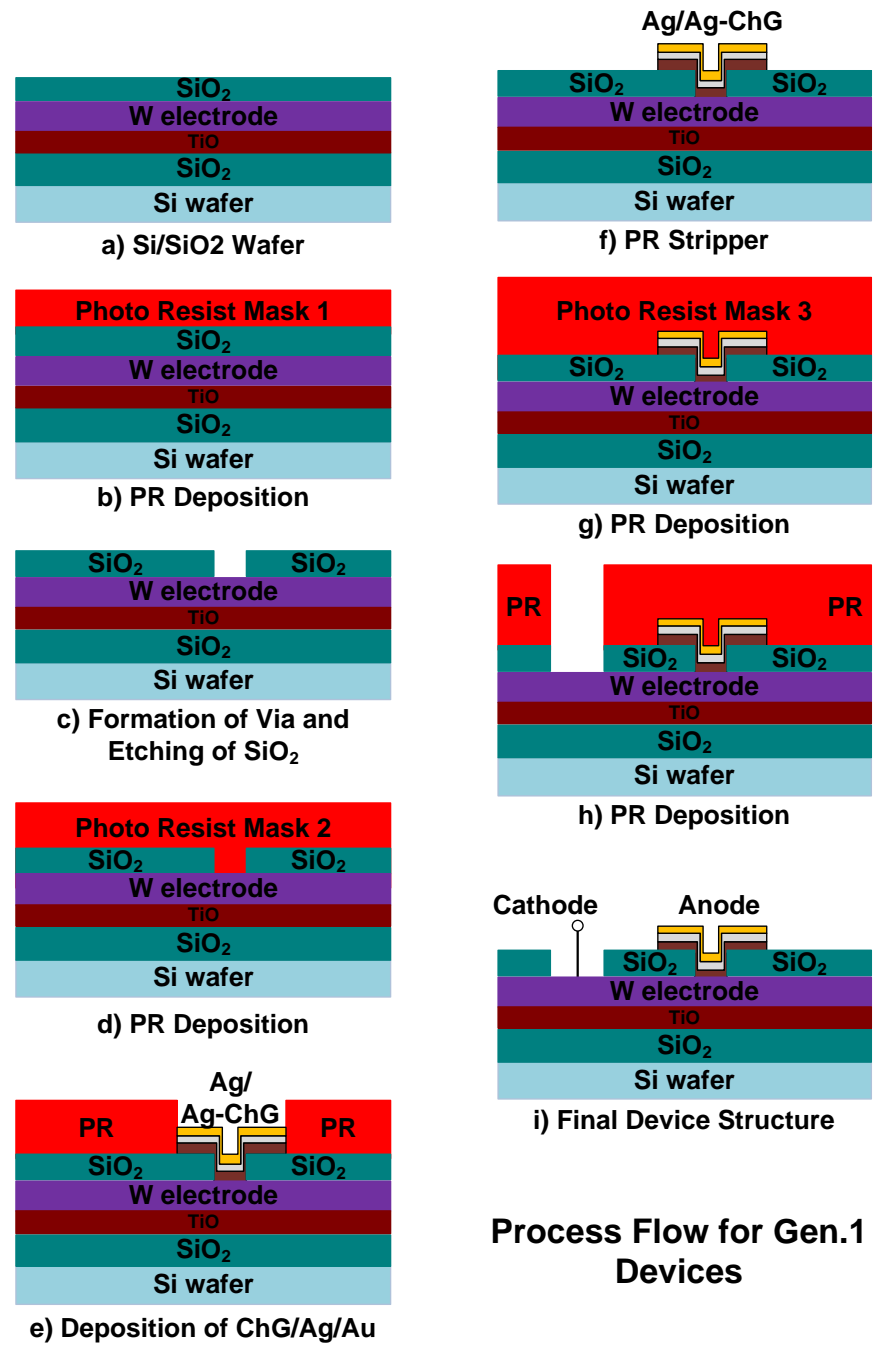
- [192] M. N. Kozicki, "Atoms to go - Ionic Memory and data storage," ed. Boise, ID: 2011 IEEE WMED, 2011.
- [193] Y. Wang, M. Mitkova, D. Georgiev, S. Mamedov, and P. Boolchand, "Macroscopic phase separation of Se-rich ( $x < 1/3$ ) ternary  $\text{Ag}_y(\text{Ge}_x\text{Se}_{1-x})_{1-y}$  glasses," *Journal of Physics: Condensed Matter*, vol. 15, p. S1573, 2003.
- [194] A. Bunde and J. W. Kantelhardt, "Diffusion and conduction in percolation systems," in *Diffusion in Condensed Matter*, ed: Springer, 2005, pp. 895-914.
- [195] K. Rao, *Structural chemistry of glasses*: Elsevier, 2002.
- [196] P. T. Talole and S. T. Sawale, "Performance Enhancement by the Design of Flash Controller for x8 NAND Flash Memory Devices," *International Journal of Computer Applications*, vol. 1, pp. 24-29, 2010.
- [197] D. Sheet, "K9XXG08UXM " 2005.
- [198] D. Sheet, "48F3300L0YDQ0," 2003.
- [199] D. Sheet, "HYB18T1G400," 2006.
- [200] C. Cheng, A. Chin, and F. Yeh, "Novel ultra-low power RRAM with good endurance and retention," in *VLSI Technology (VLSIT), 2010 Symposium on*, 2010, pp. 85-86.
- [201] C. Liaw, M. Kund, D. Schmitt-Landsiedel, and I. Ruge, "The conductive bridging random access memory (CBRAM): A non-volatile multi-level memory technology," in *Solid State Device Research Conference, 2007. ESSDERC 2007. 37th European*, 2007, pp. 226-229.
- [202] N. Derhacopian, S. C. Hollmer, N. Gilbert, and M. N. Kozicki, "Power and energy perspectives of nonvolatile memory technologies," *Proceedings of the IEEE*, vol. 98, pp. 283-298, 2010.

- [203] D. Kamalanathan, U. Russo, D. Ielmini, and M. N. Kozicki, "Voltage-Driven On-Off Transition and Tradeoff With Program and Erase Current in Programmable Metallization Cell (PMC) Memory," *Electron Device Letters, IEEE*, vol. 30, pp. 553-555, 2009.
- [204] C. Schindler, M. Meier, R. Waser, and M. Kozicki, "Resistive switching in Ag-Ge-Se with extremely low write currents," in *Non-Volatile Memory Technology Symposium, 2007. NVMTS'07*, 2007, pp. 82-85.
- [205] C. Schindler, S. P. Therman, R. Waser, and M. N. Kozicki, "Bipolar and Unipolar Resistive Switching in Cu-Doped SiO<sub>2</sub>," *Electron Devices, IEEE Transactions on*, vol. 54, pp. 2762-2768, 2007.
- [206] S. Rahaman and S. Maikap, "Improved Resistive Switching Memory Characteristics Using Novel Bi-layered Ge<sub>0.2</sub>Se<sub>0.8</sub>/Ta<sub>2</sub>O<sub>5</sub> Solid-Electrolytes," in *Proc. IMW*, 2010, pp. 70-73.
- [207] C. Cheng, P. Chen, S. Liu, T. Wu, H. Hsu, A. Chin, *et al.*, "Bipolar switching characteristics of low-power GeO resistive memory," *Solid-State Electronics*, vol. 62, pp. 90-93, 2011.
- [208] B. Govoreanu, A. Ajaykumar, H. Lipowicz, Y.-Y. Chen, J.-C. Liu, R. Degraeve, *et al.*, "Performance and reliability of Ultra-Thin HfO<sub>2</sub> based RRAM (UTO-RRAM)," in *Memory Workshop (IMW), 2013 5th IEEE International*, 2013, pp. 48-51.
- [209] C. Li, S. Minne, B. Pittenger, A. Mednick, M. Guide, and T. Nguyen, "Simultaneous Electrical and Mechanical Property Mapping at the Nanoscale with PeakForce TUNA," *Bruker application note AN132 Rev. A*, 2011.
- [210] K.-H. Kim, S. Gaba, D. Wheeler, J. M. Cruz-Albrecht, T. Hussain, N. Srinivasa, *et al.*, "A functional hybrid memristor crossbar-array/CMOS system for data storage and neuromorphic applications," *Nano letters*, vol. 12, pp. 389-395, 2011.

- [211] R. Kundu, K. Bhatia, N. Kishore, P. Singh, and C. Vijayaraghavan, "Effect of addition of Zn impurities on the electronic conduction in semiconducting  $\text{Se}_{80-x}\text{Te}_{20}\text{Zn}_x$  glasses," *Philosophical Magazine B*, vol. 72, pp. 513-528, 1995.
- [212] R. Lovics, A. Csik, V. Takáts, J. Hakl, K. Vad, and G. Langer, "Depth profile analysis of solar cells by Secondary Neutral Mass Spectrometry using conducting mesh," *Vacuum*, vol. 86, pp. 721-723, 2012.
- [213] M. T. Shatnawi, C. L. Farrow, P. Chen, P. Boolchand, A. Sartbaeva, M. Thorpe, *et al.*, "Search for a structural response to the intermediate phase in  $\text{Ge}_x\text{Se}_{1-x}$  glasses," *Physical Review B*, vol. 77, pp. 094134.1-094134.11, 2008.
- [214] P. Boolchand, P. Chen, D. I. Novita, and B. Goodman, "New perspectives on intermediate phases," *Rigidity transitions and Boolchand Intermediate Phases in nanomaterials*, pp. 1-36, 2009.
- [215] M. Thorpe and M. Chubynsky, "Rigidity and self-organization of network glasses and the intermediate phase," in *Properties and Applications of Amorphous Materials*, ed: Springer, pp. 61-96, 2001.
- [216] D. J. Jacobs and M. F. Thorpe, "Generic rigidity percolation: the pebble game," *Physical review letters*, vol. 75, p. 4051, 1995.
- [217] C. Kügeler, R. Rosezin, E. Linn, R. Bruchhaus, and R. Waser, "Materials, technologies, and circuit concepts for nanocrossbar-based bipolar RRAM," *Applied Physics A*, vol. 102, pp. 791-809, 2011.
- [218] M. Mitkova, Y. Wang, and P. Boolchand, "The dual chemical role of silver as dopant in the Ge-Se-Ag ternary," *Phys. Rev. Lett.*, vol. 83, pp. 3848-3851, 1999.

APPENDIX A

Generation 1 Device's Process Flow



Process Flow for Gen.1 Devices

## APPENDIX B

**Matlab Code for calculating  $V_{th}$ , LRS, HRS**

```

=====
%=          Switching Voltage, LRS, HRS Calculations          =%
%=          M. R. Latif, Nano-Ionic Group                    =%
%=          Electrical Engineering Department                  =%
%=          Boise State University, Boise - ID, USA          =%
=====

%Allocation of input parameters into specific variables
[rows,cols]=size(data());
voltage=data(1:rows,1);
current=data(1:rows,2:cols);
%Variables corresponding to the reverse sweep for LRS
voltage2=data(rows/2:rows,1);
current2=current(rows/2:rows, 1:cols-1);
%Compliance Current
cc=max(current);
negcc=-1*cc;
index=1;
i=1;
%while(index<cols)
    while(index<cols-1)
        %cc_1 is the compliance current corresponding to the threshold voltage
        %The point is to attain a value close to the cc value but less than cc
        cc_1=cc(index)/1.5;
        %Finding the threshold voltage
        [x,y]=find(current(1:rows,index)>cc_1);
        if voltage(min(x))<=0
            index =index+1;
        end

        while i<rows+1
            if current(i,index)==negcc(index)
                index=index+1;
                break
            end
            i=i+1;
        end
        cc_1=cc(index)/1.5;
        [x,y]=find(current(1:rows,index)>cc_1);
        threshold(index)=voltage(min(x));
        if min(x)<8
            x1a=voltage(min(x)-5);
            y1a=current(min(x)-5);
            HRS(index)= abs((x1a)/(y1a));

```

```

else
    %Calculation of the HRS values
    x1a=voltage(min(x)-5);
    x2a=voltage(min(x)-7);
    y1a=current(min(x)-5);
    y2a=current(min(x)-7);
    HRS(index)=abs((x1a-x2a)/(y1a-y2a));
end
%cc_2 is the compliance current to pick the mid point of the LRS slope
%therefore this cc is different from the cc_1
cc_2=cc(index)/2;
[x,y]=find(current2(1:rows/2,index)<cc_2);
x1=voltage2(min(x));
x2=voltage2(min(x)+2);
y1=current2(min(x));
y2=current2(min(x)+2);
LRS(index)=abs((x1-x2)/(y1-y2));
count(index)=index;
index=index+1;
end
%results
threshold=threshold';
LRS=LRS';
HRS=HRS';
count=count';
%This line of code collects all the values together
results=[count threshold LRS HRS];

```